MR imaging of tumors: Approaches for functional and fast morphological characterization

Dissertation zur Erlangung des
naturwissenschaftlichen Doktorgrades
der Bayerischen Julius-Maximilians-Universität
Würzburg

vorgelegt
von

Peter Schmitt

aus
Miltenberg

Würzburg 2013

Eingereicht am:
bei der Fakultät für Physik und Astronomie

1. Gutachter: Prof. Dr. rer. nat. P.M. Jakob
2. Gutachter: Prof. Dr. rer. nat. A. Haase
der Dissertation

1. Prüfer: Prof. Dr. rer. nat. P.M. Jakob
2. Prüfer: Prof. Dr. rer. nat. A. Haase
3. Prüfer: Prof. Dr. rer. Nat. W. Kinzel
im Promotionskolloquium.

Tag des Promotionskolloquiums:

Doktorurkunde ausgehändigt am:

“Felix qui potuit
rerum cognoscere causas“

(Vergil)

„Jedem redlichen Bemühn
sei Beharrlichkeit verliehn.“

(Johann Wolfgang von Goethe)

„Da ist das Ding!
Da ist das Däng!“

(Oliver Kahn)

Table of contents

Introduction

The selection by the Nobel committee of Paul Lauterbur und Sir Peter Mansfield for their discovery in the category of Physiology or Medicine 2003 not only acknowledges the laureates' epoch-making pioneering work in the field of Magnetic Resonance Imaging (MRI), but also reflects the importance that this diagnostic modality has gained during the past decades for the clinical routine. Thanks to the widespread availability of MRI, numerous patients benefit every day from harmless and yet accurate diagnosis, which is helping to select therapy options, while circumventing exposure to radiation or even invasive surgical procedures. The main reason for this success story - and the major advantage of MR in comparison to other imaging modalities - is the wide range of available different soft tissue contrasts. Since the MR signal depends on various intrinsic parameters of tissue such as proton density, relaxation times or magnetization transfer properties, the result of an MR imaging experiment is strongly influenced by the acquisition technique utilized. Many parameters, including (but not limited to) radio frequency (rf) and gradient pulse shapes, flip angles, echo and repetition times, and the acquisition order, allow flexible tailoring of an MR acquisition to the clinical question at hand. MRI is now not only important for clinical diagnostics, but is also a powerful and valuable tool for clinical research. In both contexts, the detection and classification of tumors represents one of the major application areas of MRI.

The road to MR becoming the important tool in clinical science it is today has been long. The beginning of MR dates back to the 1920s, when many scientists were intrigued by the success of quantum physics, which managed to explain phenomena that did not fit into the framework of classical mechanics. In order to interpret the hyperfine structure of atomic spectra, Pauli suggested in 1924 that atomic nuclei might possess an angular momentum and associated magnetic moment [Pau24]. The magnetic moment was quantified a few years later [Fri33, Est33] from molecular hydrogen beam deflection experiments similar to those used in the famous setup by Stern and Gerlach, who had observed – but initially misinterpreted - the existence of the intrinsic electron spin angular momentum with a beam of silver atoms [Ster21].

It was Rabi who, in generalization and refinement of previous work [Gue31, Maj32], theoretically treated transitions between magnetic levels with different quantum numbers, which should occur when an oscillating magnetic field is applied at the Larmor frequency [Rabi37]. He also coined the term "magnetic resonance" when he first reported an experimental realization of this effect in molecular beam experiments [Rabi38, Rabi39]. In condensed phases, the MR phenomenon was first observed independently by two research laboratories in the 1940s. While the group led by Bloch used the term "nuclear induction" to denote

the observation of magnetic resonance in water [Blo46a, Blo46b], Purcell et al. detected the resonance absorption by nuclear magnetic moments in paraffin [Pur46a, Pur46b].

After the introduction of MR in bulk matter, it took almost two decades until the effect was used to study biological samples. Relaxometric experiments conducted on cell water showed that relaxation times are reduced compared to those of distilled water - an effect that was attributed to interaction of water molecules with macromolecular interfaces [Bra65, Cope69, Haz69]. In a study on excised rat tissue, elevated T_1 and T_2 values were reported in malignant tumors in comparison to normal or benign specimens, and it was hypothesized that this discrepancy may be used to differentiate between malignant and benign tissues [Dam71]. Similar findings were obtained in living tumor-bearing mice [Wei72]. Subsequent work, however, revealed considerable overlap between the relaxation times of cancerous, abnormal non-neoplastic and healthy tissue, suggesting insufficient specificity of MR relaxation times for direct cancer diagnosis [Parr74, Egg75]. Only the extension of the arsenal of available methods to spatial encoding via magnetic field gradients [Man73] and to the generation of images [Lau73] in the early 1970s enabled MR to become a clinically valuable diagnostic tool for the exploration of cancer.

Today, MRI is often the modality of choice for the detection of tumors as well as for the delineation of the extent of diseased tissue. Clinical examination protocols typically comprise of standard scans with multiple different contrasts, such as T_1- and T_2- weighted images, additional acquisitions with fluid suppression, and the repetition of T_1-weighted scans after administration of a Gadolinium-based contrast agent. For some contrasts, however (for instance for T_2-weighted imaging), long scan times are required, and the contrast is often influenced by other parameters in addition to the desired weighting parameter (see also end of section 1.2). In this context, an acquisition technique that facilitates the sampling of a pure T_2 contrast in a short acquisition time may be of high value.

In general, in spite of the high sensitivity of MRI for tumor imaging, its specificity is still limited and a differential diagnosis based on MRI can represent a challenge [Reim10]. The contrast in weighted images depends on sequence implementation details and parameter selection. Resulting potential “problems of bias, reproducibility and interpretation” might be mitigated with quantitative assessments [Tof03]. For instance, the acquisition of parameter maps has been shown to yield additional information such as the clinically important distinction between tumor mass and peritumoral edema, as has been demonstrated in animal models [Hoeh92, Eis95]. Furthermore, the malignancy of tumors has been shown to correlate with T_1 [Eng86] and T_2 [Dew90, Tovi93]. At present, however, no study that quantified a single parameter alone has proved reliable for the evaluation of pathologies. Yet, it was hypothesisized that “unique profiles of T_1, T_2 and M_0 may be identified within, for example, individual tumor types”, and that MR could “move from a process of picture-taking ... to a process of measurement” [Tof03]. In this context, a method for efficient quantification of multiple parameters could be a powerful tool for the classification and grading of cancerous tissue.

Besides its important role for identification and morphological assessment of tumors, MR also offers access to functional characterization and analysis of physiological properties, including blood flow, diffusion, tissue perfusion, oxygenation status, among others. Typically, these factors are directly or indirectly related to the metabolism and aggressiveness of a tumor, and hence can provide clinically important prognostic information. In particular, the closely linked phenomena of a disturbed microcirculation and tumor hypoxia, i.e. the pre-

sence of oxygen-deprived regions, directly correlate to a reduced therapeutic efficiency. Consequently, multiple approaches have been developed that aim to manipulate tumor perfusion or oxygen supply, including the administration of vaso-active drugs and breathing gases with increased oxygen and carbon dioxide content. Since MRI is capable of capturing physiological responses to such external stimuli, it might represent an important option for advanced therapy monitoring and stratification.

The goal of this work was to develop, implement, optimize and apply methods for quantitative MR imaging of tumors. In the context of functional characterization, this implied transferring techniques established in tumor model research to human subjects and assessing their feasibility for use in patients. With respect to morphologic parameter imaging, the focus was on the development of novel techniques for fast quantitative parameter measurements and T_2-weighted imaging. The structure of this thesis essentially reflects this scope. Chapter 1 introduces some basics of MR together with fundamental imaging pulse sequences that are used throughout the experimental studies. Important background in tumor physiology and therapy is also covered, and finally the role of MR imaging in the characterization of tumors is reviewed. In the following six central chapters, individual projects are presented that can be assigned to either of two areas – the functional or the fast morphologic imaging of tumors. Each of these six chapters corresponds to a peer-reviewed publication in a scientific journal.

The first part of this thesis, consisting of Chapters 2 and 3, reports studies that describe the implementation and optimization of acquisition techniques for the assessment of functional tumor parameters and their application in patients. Chapter 2 deals with the evaluation of a non-invasive spin-labeling technique for measuring perfusion in head and neck carcinoma patients during radiotherapy. It is shown that repetitive perfusion measurements are possible without any exogeneous contrast agent, which may be helpful for the stratification of vasomodulating therapy options. The subject of Chapter 3 is the implementation of an oxygennation-sensitive multi-gradient-echo technique and its evaluation for dynamic monitoring of the response of head and neck tumors to the administration of breathing gases with high oxygen content.

In addition to these studies, closely related side- and sub-projects were pursued, which also resulted in peer-reviewed conference contributions. These activities included the supervision of a project that dealt with the setup of a respiratory mask system for the administration of high-oxygen-content breathing gases, and experimental analysis of the MR signal response in healthy human subjects [Weig00a, Schm01]. In another project, oxygenation-sensitive and perfusion-related changes of tumors in mice were investigated in response to respiratory challenges, and the results were correlated to histology [Bre02, Kot03]. These studies are not covered within this Ph.D. thesis; the interested reader is referred to the respecttive publications and corresponding diploma theses [Weig00b, Bre01].

In the second portion of this thesis, comprising chapters 4-7, novel theoretical concepts, technical and methodological developments and their numerical verification and experimental application are reported. These projects utilized modifications of the TrueFISP (True Fast Imaging with Steady-state Precession) sequence, which at the time the work was conducted, was not widely established in clinical contexts, but carried high potential due to its high SNR efficiency and unique signal characteristics.

In Chapter 4, an intuitive pictorial description for the TrueFISP transient and steady state signal is presented, and analytical formulations are derived for the respective signal behaviors. The theory is validated in simulations and in phantoms experiments. Chapter 5 deals with the adaption of this theory for the simultaneous quantification of multiple MR parameters. A complete set of analytical solutions is provided for the direct calculation of longitudinal and transverse relaxation times along with spin density, from a single Inversion-recovery TrueFISP acquisition, and the method is verified both in phantom and in-vivo experiments. In Chapter 6, simultaneously acquired parameter maps are used to calculate MR images with contrasts that can either mimic the appearance of standard MR sequences used in a routine clinical exam or that can be freely chosen. Finally, Chapter 7 introduces a novel concept termed T-One-insensitive Steady State Imaging (TOSSI), which facilitates the fast acquisition of purely T_2-weighted images on basis of a TrueFISP sequence. It is shown that TOSSI images obtained in volunteers and tumor patients within less than 2s essentially have the same contrast as T_2-weighted TSE images, which were acquired over minutes.

The projects and studies presented in this thesis were essentially carried out and first presented at international conferences between 2001 and 2005. Nevertheless, the work has lost none of its topicality; this is underscored by the recent acceptance of a manuscript that reports the technique described in Chapter 7 of this thesis for publication in the highly respected peer-reviewed journal *Magnetic Resonance in Medicine* [Schm12]. Fundamental parts of the work compiled in this thesis remain of high relevance for the scientific community, as can be seen from the considerable and still continuously increasing number of citations of these articles in scientific publications. Evidently, various other researchers were inspired by techniques described in this thesis, continued with, and built on them, e.g. by utilizing the presented methods in the context of pre-clinical studies or by developing further technical extensions or refinements. To account for this ongoing evolution, the “Introduction” and “Basics” sections of the individual chapters were formulated to reflect the respective starting points before the projects were carried out, and each chapter is supplemented with a “Conclusion and Retrospect” section that briefly reviews subsequent publications relating to the specific field of research. The thesis concludes with a summary and a “Zusammenfassung”, which represents a translation of the summary into the German language. In an appendix, the referenced literature is found, followed by acknowledgements.

Chapter 1

Basics

This chapter addresses some very fundamental aspects of magnetic resonance and explains several basic MR imaging sequences. Moreover, it covers elementary issues regarding tumor physiology and therapy. Finally, the role of MR in clinical tumor diagnosis is briefly sketched.

1.1 Basic MR physics

In this section, a very brief introduction into MR physics is provided, including elementary properties of nuclei with spin 1/2, the Bloch equations, the use of field gradients for spatial encoding and the concept of k-space.

Nuclear spin ensembles in magnetic fields

Atomic nuclei with unpaired nucleons possess a spin-angular momentum. If a spin ensemble is placed in a static magnetic field $\boldsymbol{B}_0$, each spin is - according to quantum mechanics - confined to discrete energetic states (two for s = 1/2 spins such as ^{1}H). In a semiclassical depiction, these states are defined by fixed components parallel or antiparallel to $\boldsymbol{B}_0$ (per convention assumed as parallel to the z axis). The individual magnetic moments can be considered to precess around $\boldsymbol{B}_0$ at *Larmor frequency* which is defined by

$$\nu_0 = \Delta E / h = \gamma B_0 / 2\pi . \qquad (1.1)$$

Here, ΔE denotes the energy difference between two states, and h is Planck's constant. The gyromagnetic ratio γ depends on the nucleus assessed; for protons, its value amounts to $\gamma = 2\pi \times 42.6$ MHz/T. The possible spin states correspond to different energy levels so that in thermodynamic equilibrium, according to the Boltzmann distribution, an excess of spins is residing in the lower energy level parallel to $\boldsymbol{B}_0$. With an arbitrary distribution of the precession phases, the sum of the transverse components is zero and the population difference results in a small net magnetic momentum $\boldsymbol{M}_0$ - a vector that is parallel to $\boldsymbol{B}_0$. This *magnetization* represents the observable quantity in magnetic resonance.

If a spin ensemble in an external magnetic field is subjected to an additional field $\boldsymbol{B}_1$, applied perpendicular to $\boldsymbol{B}_0$ and oscillating at Larmor frequency, transitions are induced between the different energy states. A semi-classical picture can provide a pictorial interpretation of this excitation process: Spin transitions to a higher energy state are associated with a reduction of the longitudinal magnetization component M_z. By introduction of coherence, however, spins obtain equivalent phase and a transverse component $M_\wedge$ is generated.

The Bloch equations

From a classical point of view, the behavior of a macroscopic magnetic moment $\boldsymbol{M}$ in an external magnetic field $\boldsymbol{B}$ can be expressed by the following equation system, which was derived by Bloch [Blo46b]:

$$\frac{d\boldsymbol{M}}{dt} = \gamma(\boldsymbol{M} \times \boldsymbol{B}) - \left(\frac{M_x}{T_2}\boldsymbol{e}_x + \frac{M_y}{T_2}\boldsymbol{e}_y + \frac{M_z - M_0}{T_1}\boldsymbol{e}_z\right) \tag{1.2}$$

The first term of Eq. 1.2 describes the resonance phenomenon, i.e. the precession of the magnetization vector around an external magnetic field. It also provides a simple explanation of the excitation process: If a transverse field $\boldsymbol{B}_1$, rotating around the z axis at Larmor frequency, is superimposed to $\boldsymbol{B}_0$, the direction of the effective field $\boldsymbol{B}$ changes permanently. In the laboratory system, $\boldsymbol{M}$ is guided onto a spiral trajectory on the surface of a sphere. If transformed into the *rotating frame*, a coordinate system precessing around the z axis at Larmor frequency [Blo46b], the excitation process reduces to a rotation of $\boldsymbol{M}$ away from the $\boldsymbol{B}_0$ direction. If the $\boldsymbol{B}_1$ field is applied for a limited time interval τ (i.e. by means of an *RF pulse* with a finite length τ), $\boldsymbol{M}$ is tilted about the *flip angle*

$$\alpha = \gamma B_1 \tau \,. \tag{1.3}$$

The second term in Eq. 1.2 describes *relaxation*, i.e. the dynamic return of an excited spin system to its thermal equilibrium. This process can be divided up into spin-lattice or longitudinal relaxation and spin-spin or transverse relaxation which independently of each other affect magnetization parallel and perpendicular to the z axis, respectively.

Longitudinal relaxation is attributed to interactions between spins and their environment, referred to as “lattice” in this context. Due to these interactions, the spin system loses energy and the Boltzmann population of the energy states is restored. This process is usually described as an exponential approach of the longitudinal magnetization component to its equilibrium value $\boldsymbol{M}_0$, characterized by the longitudinal relaxation time T_1.

Transverse relaxation originates from mutual interactions between individual spins. The mechanism may be seen in analogy to statistically fluctuating local deviations of the main magnetic field, and it causes an irreversible loss of transverse phase coherence. In consequence, the spins are dephasing and the transverse magnetization component is reduced. According to the Bloch equations, this process can be described by an exponential decay with a transverse relaxation time T_2.

Under practical experimental conditions, potential system imperfections and non-uniform susceptibility distributions within the sample introduce local inhomogeneities of the main magnetic field. Magnetization components that “encounter” a specific value of $\boldsymbol{B}_0$ are

referred to as *isochromats*. If the corresponding frequency deviates from the designated Larmor frequency, an isochromat is referred to as *off-resonant*. Transverse magnetization $M_\perp$ that is composed of different isochromats will show an accelerated decay due to the phase dispersion of its constituents. Assuming a Lorentzian frequency distribution (as justified for randomly distributed microscopic inhomogeneity sources [Brow61, Haac99]) with a FWHM of Dn, this effect may be described by an *apparent transverse relaxation time* T_2^* given by

$$\frac{1}{T_2^*} = \frac{1}{T_2} + \pi\Delta\nu \quad . \tag{1.4}$$

In general, the relaxation times relate to each other as $T_2^* < T_2 < T_1$. While the assumption $T_2 \approx T_1$ is often justified in liquids, biological tissues show a wide range of different T_1 and T_2 values.

The MR signal

The source of the MR signal - and thus the quantity observed in experiments - is the transverse component of magnetization. Its precession around the z axis is accompanied by a rotating magnetic flux which - according to Faraday's law of induction - generates an RF signal in a conducting loop or more sophisticated *RF coils* placed close enough to the sample. As initially predicted by Bloch [Blo46b] and first observed experimentally by Hahn [Hahn50a], a signal "tail" is encountered directly after a short excitation pulse. This *Free Induction Decay* (FID) signal oscillates with Larmor frequency and fades away with the characteristic time constant T_2^*.

The influence of B_0 inhomogeneities can be mitigated by generating spin-echoes, which represent a fundamental phenomenon in the field of MR. In his classic paper, Hahn showed that dephased transverse magnetization can be refocused with a second RF pulse, except for the irreversible losses of coherence caused by spin-spin interactions [Hahn50b]. While any combination of two RF pulses separated by a time delay τ generates a spin-echo after another delay τ, the spin-echo principle is most plastically explained and maximum signal intensity is obtained for the combination of a 90° excitation and a 180° refocusing pulse.

Spatial encoding with magnetic field gradients

The generation of MR images requires that the signal originating from a sample is provided with spatial information so that it is possible to localize individual contributions. This can be achieved by applying magnetic field gradients which - superimposed to the static field B_0 - establish a linear relationship between the local Larmor frequency and the spatial position. While the earliest use of gradients for one-dimensional spatial encoding is claimed by Carr [Carr52, Carr93], the enormous potential of this approach was first recognized by Lauterbur who extended the principle to more dimensions and created the first MR images [Lau73].

Typically, in MRI pulse sequences, slice-selective spin excitation [Gar74] represents a first step of spatial encoding. This is accomplished by applying a *slice selection gradient* G_s and using a shaped RF pulse that has a suitable profile in the frequency domain. As a result, the Larmor condition is only fulfilled for magnetization within a defined slice. Position, thickness and excitation profile of this slice are determined by the gradient strength and by the

carrier frequency, bandwidth and shape of the RF pulse. Due to the impact of G_S during selective excitation, the generated transverse magnetization is dephased - an effect which is commonly compensated with a subsequent gradient lobe of opposite polarity [Hou77].

In conventional imaging experiments, the MR signal is acquired in presence of a *frequency encoding or read gradient* G_R, which causes the excited magnetization components to precess at different rates. A one-dimensional projection of the object in read direction can be obtained by a frequency component analysis of the signal, usually conducted as a Fourier Transformation. If an FID signal is sampled under a read gradient, however, it decays rapidly because of the field inhomogeneities associated with this gradient. In this case, it is beneficial to apply a negative gradient lobe prior to the readout. Hence, when the temporal integral of the gradients in read direction is zero, all magnetization components are in phase and a signal maximum, known as *gradient echo*, occurs within the acquisition window. This effect was probably first described for flow measurements in sea water [Hahn60]. With the advent of MR imaging, the principle was adapted for spatial encoding and started to replace the sampling of FID signals [Man77, Hut78b].

In Lauterburs first publication on MR imaging, multiple projections were sampled in different angular directions and images were calculated using *projection reconstruction techniques* known from computed tomography [Lau73]. While this radial sampling scheme may be advantageous in certain applications, a different concept - that of Fourier imaging - has become the standard technique for MR image formation [Kum75]. It uses the principle of *phase encoding*, which involves the application of an additional gradient pulse prior to signal acquisition. Here, transverse magnetization is modulated with a phase that depends on the position along this gradient. If this experiment is repeated with incrementally varying net integrals of the phase encoding gradient, the spatial origin of the signal along the direction can be resolved with a *Fourier Transformation*.

The concept of k-space

Mathematically, for either read or phase encoding with a gradient $\boldsymbol{G}$, the signal phase observed at a spatial position $\boldsymbol{r}$ after an encoding time t can be written as

$$f(\boldsymbol{r},t) = \gamma \int_0^t \boldsymbol{G}(t')\,\boldsymbol{r}\,dt' = \boldsymbol{kr}\,. \tag{1.5}$$

Here, the wave number k is the integral of the imaging gradients over time:

$$\boldsymbol{k} = \gamma \int_0^t \boldsymbol{G}(t')\,dt'\,. \tag{1.6}$$

With motion and relaxation effects neglected, and assuming a quasi-continuous acquisition, the acquired signal corresponds to the integral of complex signal contributions:

$$S(\boldsymbol{k}) = \int S(\boldsymbol{r}) \times \exp(i f(\boldsymbol{r},t))\,d\boldsymbol{r} = \int S(\boldsymbol{r}) \times \exp(i\boldsymbol{kr})\,d\boldsymbol{r}\,. \tag{1.7}$$

Here, $S(\boldsymbol{r})$ denotes the spatially varying MR signal. Evidently, the signal acquired in a frequency- and phase-encoded MR experiment represents the complex Fourier inverse of

the MR image. Each of its coordinates corresponds to a defined spatial frequency, quantified by the corresponding values of the wave numbers *k*. Hence, the raw data domain is commonly referred to as *k-space* [Twi83].

The various MRI methods available today not only differ with respect to signal generation, but also in how the k-space data are sampled. An MR signal acquired in presence of a constant read gradient directly corresponds to a single line of k-space. Due to the discrete nature of the digitization process, the signal is sampled at N_R distinct data points. If - like in 2D Fourier imaging - N_P parallel lines are obtained with different phase encoding steps, the experimental k-space is represented by an $N_R \times N_P$ matrix, and an image with an identical matrix size is obtained via discrete Fourier Transformation. According to the Nyquist Theorem, the distance of adjacent k-space points determines the *field-of-view* (FOV) of the image, while the extent of k-space reflects the in-plane pixel size, i.e. the nominal resolution.

The discrete nature of acquired k-space data and potential signal changes during acquisition, e.g. due to relaxation, are equivalent with a multiplication of k-space with respective functions (boxcar, exponential decay etc). In image space, these effects correspond to a convolution with the Fourier inverse of these functions (i.e. sinc function, Lorentzian line etc). Hence, certain acquisition schemes may lead to image blurring, limit the actual resolution or even introduce image artifacts (also see analysis of *point-spread function* in chapter 7).

SNR and signal normalization

Besides the desired signal, any physical data acquisition also captures a certain amount of noise signal. The *signal-to-noise ratio* (SNR) is a key quantity that defines the sensitivity of an MR experiment and represents a measure for image quality. It is a function of various sequence-independent factors such as the main magnetic field strength B_0, hardware setup (RF coil sensitivity and receiver chain), encoding strategy and geometry, voxel size, number of averages, sampling bandwidth, data filtering, reconstruction algorithm and others.

While these aspects were considered in the design of the experimental parts of this thesis (in that the data acquisitions were adjusted to yield desired SNR and image quality), their influence is not included in the theoretical considerations. Since the MR signal is directly proportional to the equilibrium magnetization and to the amount of ^{1}H nuclei per volume, it is expressed as the transverse magnetization component and normalized to a parameter M_0, which is referred to as *spin density*. With this convention, the initial FID signal that is generated with an infinitesimally short 90° excitation pulse would amount to $S = M_0$.

1.2 Basic MR imaging sequences

In this section, some fundamental MR imaging sequences are introduced, including the gradient-echo, FLASH, spin-echo, CPMG, and turbo-spin-echo sequence. Other, more specific sequences are covered in the “basics” sections of the later chapters (e.g. the IR snapshot FLASH technique for T_1 quantification in section 2.2, or the multi-gradient-echo sequence for determining T_2* in section 3.2). The TrueFISP sequence, basis for several methodological developments presented in this thesis, is the subject of section 4.2. The FLAIR technique, part of many neuroradiological exams, is explained in section 6.2.

Basic Fourier imaging sequences

Fig 1.1 schematically shows a basic gradient echo sequence that uses the concepts explainned above. Originally published as “spin-warp” imaging [Ede80], it combines the generation of gradient echoes with the principle of Fourier reconstruction and can be considered the forerunner of various imaging sequences available today. The timing of the sequence is determined by the *echo time TE* and the *repetition time TR*, which denote the time intervals from an excitation pulse to the echo maximum and to the subsequent excitation, respectively.

After RF excitation, transverse magnetization components decay with T_2*, and hence the echo amplitude is weighted with this parameter. The concept of Fourier imaging can also be realized with a spin-echo type of sequence, where a refocusing RF pulse is inserted between excitation and signal reception, so that the echo amplitude is dependent on T_2. Over *TR*, until the subsequent RF pulse, the longitudinal components increase due to T_1 relaxation. Hence, the sequence type and the selected parameters such as *TE*, *TR* and flip angles directly influence the image contrast, and differently weighted images can be obtained by varying these degrees of freedom.

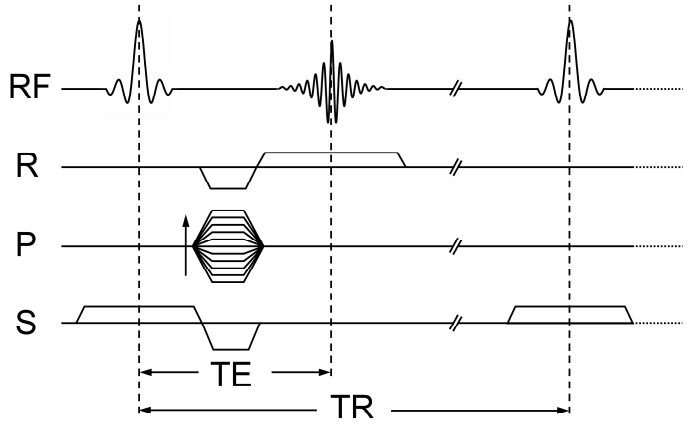

Fig. 1.1: Basic gradient echo sequence timing scheme for excitation and signal reception (RF), and for imaging gradients in read (R), phase (P) and slice encoding direction (S).

FLASH

The FLASH (Fast Low Angle SHot) imaging sequence [Haa85, Haa86] represents a specific realization of the gradient-echo principle in that low flip angle excitation pulses are used in combination with short *TR* intervals. Usually, additional spoiling mechanisms are inserted for eliminating residual transverse magnetization or higher-order coherences.

In the mid-eighties, spin-echo-based techniques were commonly used for MR imaging, typically realized with 90° excitation pulses, 180° refocusing pulses and long *TR* times. The introduction of FLASH, combining the gradient echo concept with low flip angles in the context of imaging, was a revolutionary step - for the first time, the acquisition of single images became possible within less than a second. With a small flip angle excitation, considerable transverse magnetization is generated, while the longitudinal component is largely preserved. During the subsequent *TR* cycle, this remaining portion of M_z increases again due to longitudinal relaxation. After a sufficient number of *TR* intervals, a steady state is established. Under the assumption that any transverse magnetization is eliminated when the next excitation is played out, the FLASH signal intensity may be calculated as [Wau70]

$$S = \frac{M_0(1- E_1)\ \sin a\ \exp(-TE/T_2^*)}{1- E_1 \cos a} \times\ , \tag{1.8}$$

with $E_1 = \exp(-TR/T_1)$. Evidently, different image contrasts can be generated with the FLASH technique. With increasing *TE*, the resultant images are more and more dependent on the effective transverse relaxation time T_2*. For short *TE* values, this influence is reduced and a T_1-weighted contrast is obtained for larger flip angles, while the use of very small flip angles yields spin-density-weighted images. From compartments with a specific T_1 value, maximum signal is achieved at the Ernst Angle given by [Ern66, Kai74]

$$a_{Ernst} = \arccos(E_1)\ . \tag{1.9}$$

RF spoiling

The expression of Eq. 1.8 is obtained under the condition that residual transverse magnetization components disappear completely at the end of a *TR* interval. However, transverse coherences can be partially refocused by RF pulses in subsequent repetition cycles as spin-echoes, stimulated or higher-order echoes [Woe61], adding T_2-weighted contributions to the signal. This phenomenon can be evaluated with the Extended-Phase-Graph algorithm, which itself is based on general partition analysis [Kai74] but takes advantage of symmetries encountered in imaging sequences [Henn91b]. For the elimination of RF-refocused signal components, approaches using gradient spoiler schemes were suggested [Fra87, Wood87, Wang90]. However, it was also shown that the influence of incremental phase encoding gradients may disturb the steady state and cause image artifacts [Cra88, Wood88]. This problem can be avoided with additional rewinder gradient pulses that retract the impact of phase encoding between the acquisition window and the following RF pulse (see Fig.1.2) [Fra87, Hawk87, Gyn88].

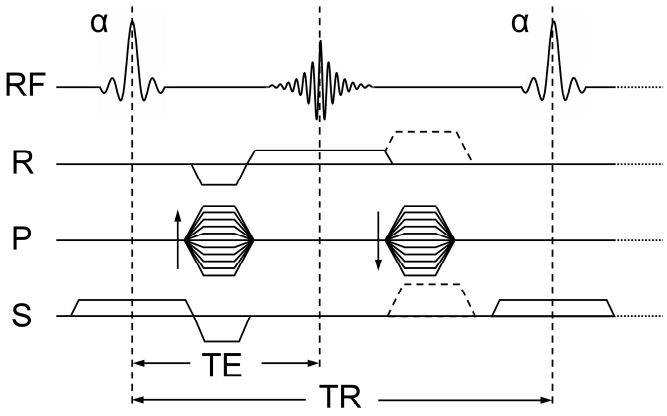

Fig. 1.2: FLASH sequence with rewinder gradients and optional spoiler gradients in read and slice encoding direction. RF-spoiling is achieved by appropriate RF phase lists.

The resulting rewinded FLASH sequence, also named GRASS [Utz86], FAST [Gyn88] and (conventional) FISP [Haac90], provides a contrast that is strongly influenced by T_2-weighted contributions [Zur88, Gyn89]. However, the echo interferences can be additionally adjusted by applying subsequent RF pulses with dedicated phase shifts. In so-called rf-spoiled FLASH

sequences, a constant signal is generated by applying the excitation pulses with linearly increasing phase differences [Zur87, Cra88]:

$$f_{RF}(n) = \sum_{0}^{n} df_{RF} \qquad \text{with n = 0, 1, 2, 3, …} \tag{1.10}$$

The contrast behavior of Eq 1.8 is reproduced for specific values of df_{RF}. Common phase lists use values of 50° or 117°, and others were recommended in the case of flow or non-steady-state conditions [Duyn97, Bus01].

The spin-echo sequence

The use of refocusing pulses and, hence, of spin-echoes was proposed early in the context of MRI [Man77], and represents a fundamental basis of many MRI techniques. A diagram of a plain spin-echo sequence is shown in Fig. 1.3. For arbitary excitation and refocusing pulse flip angles, the analytic description of the spin-echo contrast is rather complex [Vin90], but for the simple standard scheme 90° - TE/2 - 180° - TE/2 - ACQ, the expected signal is simply [Dix82, Weh84]:

$$S = M_0\left[1 - 2\exp\left(-(TR - TE/2)/T_1\right) + \exp(-TR/T_1)\right]\exp\left(-TE/T_2\right). \tag{1.11}$$

In the case of TE/2 << TR, by Taylor expansion of the exponential terms and neglection of higher order terms of TE/TR [Lee86], this expression reduces to:

$$S = M_0\left[1 - \exp(-(TR - TE)/T_1)\right]\exp\left(-TE/T_2\right). \tag{1.12}$$

It reflects the assumption that the longitudinal magnetization is first saturated with the 90° excitation, starts to relax until the 180° pulse and is inverted, so that its recovery effectively starts from zero again at a time close to the spin echo. The standard contrasts available with spin-echo sequences are spin-density, T_1 or T_2 weighting. As with gradient-echo acquisitions, the desired contrast can be adjusted by using appropriate combinations of *TE* and *TR*. Even though spin-echo sequences are associated with comparatively long imaging times, particularly if used with long *TR* for generation of spin-density- or T_2-weighted images, they still find application in routine clinical exams.

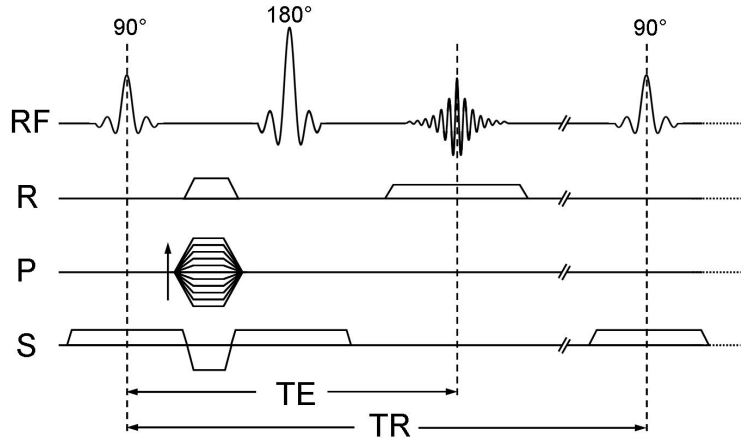

Fig. 1.3: Schematic display of a simple spin-echo sequence with a 90° excitation and 180° refocusing pulse.

The CPMG sequence

In the CPMG (Carr-Purcell-Meiboom-Gill) experiment, a train of 180° refocusing pulses is applied after a 90° excitation pulse. Multiple spin-echoes are generated, which - in the ideal case - decay with T_2. After the initial publication of this principle [Carr54], it was found that potential flip angle inaccuracies are efficiently compensated for if a phase difference of p/2 is introduced between excitation and the subsequent refocusing pulses [Mei58]. Originally proposed for spectroscopic assessment of transverse relaxation characteristics, different realizations of CPMG sequences were presented for the purpose of MR imaging [Schn83, Gra86b; Cra87, Mul90a]. In Fourier-based imaging, each echo within an echo series receives identical phase encoding and is used for an individual image so that a series of images showing progressive T_2 dependence is obtained. For many applications, CPMG imaging sequences are considered the gold standard method for mapping of T_2.

The TSE sequence

In the TSE (turbo-spin-echo) sequence, originally presented as RARE (Rapid Acquisition with Relaxation Enhancement) and also named FSE (fast spin-echo), the CPMG concept is adapted for fast imaging in that the individual echoes of a multi-spin-echo train are acquired with different phase encoding and contribute to the k-space of the same image [Henn84, Henn86]. In conventional TSE imaging, multiple echo trains are acquired with interleaved phase encoding steps, each train providing a segment of the k-space. The main image contrast is determined by the low-order k-space lines, so that the order of phase encoding is important [Henn86].

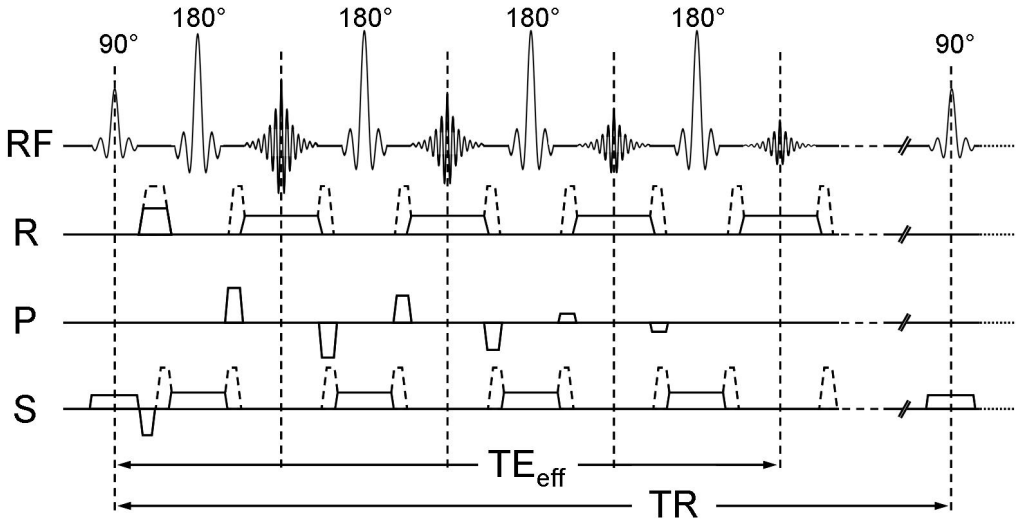

Fig. 1.4: Timing diagram of a TSE sequence with 90° excitation, a train of 180° refocusing pulses and rewinded phase encoding. In this example, the fourth echo corresponds to a line close to the center of k-space, and defines the effective echo time TE_{eff}. Optional spoiler gradient to elimiate FID signals or higher order echo pathways are sketched with dashed lines.

The TSE signal behavior can be described by means of an effective echo time TE_{eff} [Mul91]:

$$S = M_0\left[1 - \exp\left(-\left(TR - TE_{Last}\right)/T_1\right)\right]\exp\left(-TE_{eff}/T_2\right), \quad (1.13)$$

Here, TE_{Last} denotes the echo time of the last echo of the train. In analogy to Eq. 1.12, this formulation reflects the approximation that M_z starts its recovery at the end of the echo train [Lee86]. Principally, the resulting contrast can also vary from T_1-, over spin-density- to T_2-weighted, depending on the values of TR and TE_{eff}.

Factors that influence the TSE signal

For the derivation of Eq. 1.13, the underlying assumption is that ideal 90° and 180° pulses are applied across the whole slice, so that the signal simply decays with the transverse relaxation time. Whenever the refocusing pulse angle is different from 180°, however, higher-order echoes can form over different coherence pathways. This effect, which is best analyzed and illustrated with the Extended-Phase-Graph formalism [Henn88, Henn91], leads to an additional T_1 dependency of the signal evolution.

If slice-selective refocusing pulses are used, pulse profile imperfections inevitably yield low-angle contributions at the edges of the slice and FID signals as well as higher-order echoes will occur. These signals may cause image artifacts which can be avoided with appropriate phase cycling schemes [Gra86b, Bar89, Zur91] and additional gradient lobes that rewind the phase encoding within the echo cycle [Henn86, Henn88a, Mul90, Zur91]. With the latter approach, RARE sequences using low flip angle pulses became feasible, which have the advantage of avoiding the high SAR associated with a series of 180° pulses [Hen88a, Henn88b, Nor91]. In this case, however, stimulated echo contributions may be expected to alter the echo decay significantly [Cra87, Poon92, Wil96]. Thus, in TSE acquisitions, the image contrast is not solely determined by T_2, and with CPMG-based imaging sequences aiming at T_2 mapping, falsified T_2 estimates may be obtained. Improvements are possible by using non-selective refocusing pulses [Mul90a, Whi97] or by introducing spoiler gradients such unwanted echo pathways are eliminated [Cra87, Henn88a, Bar89, Poon92]. Besides higher-order echo effects, the appearance of TSE images may also be influenced by phenomena such as magnetization transfer, decoupling of J-modulation effects and diffusion [Con92, Henk92]. Nevertheless, the TSE sequence is of high clinical value and can be considered a standard component of various examination protocols.

1.3 Tumors: Classification, physiology and therapy

In this section, a brief overview on tumor classification and therapy is given. The tumor micromilieu and, in specific, tumor hypoxia is introduced as important factor influencing treatment outcome. Therapeutical options are addressed which aim at manipulating microenvironmental parameters and may have potential to improve prognosis on an individual basis.

Tumors and their classification

A tumor, also referred to as neoplasm, is an abnormal mass of tissue, formed by mutated cells which proliferate out of control. Benign tumors are associated with high tissue differen-

tiation and slow growth, and are usually restricted to the primary site. Malignant, i.e. cancerous tumors are less differentiated and often develop in rapid and aggressive fashion. Their cells are likely to invade surrounding tissue or to travel via blood vessels or lymph streams, spreading to near lymphatic nodes or more distant parts of the body where new tumors, called metastasis, might form.

Tumors are classified histologically according to the type of tissue they arise from (*Typing*). For instance, carcinomas - the most commonly diagnosed cancers - originate in epithelial tissue, like skin, mucous membranes, lungs, breast and other organs. The malignancy of a tumor is an important prognostic factor, and it is usually indicated from G1 (low) up to G4 (highest) (G*rading*). The growth spectrum of a tumor is commonly classified by means of the TNM system with T describing the extension of the primary lesion, N indicating if regional lymph nodes are affected, and M specifying the evidence for hematogeneously induced metastasis (*Staging*) [Spi72, Ric02].

Standard therapy options

The three most important tools of tumor therapy are surgery, radiation, and chemotherapy. Additional treatment forms like laser therapy or hyperthermia may be added to improve or complement the effect. Each modality aims at removing or killing cancerous cells and can either be used to cure the patient or to alleviate symptoms. Generally, the choice of treatment depends on the type of the lesion and its stage. Surgery and radiation destroy tumors locally while in chemotherapy, drugs are administered to eliminate malignant cells spreading through the body. Surgery may be successful in treating primary tumors but is inefficient in curing metastatic cancer. Radiation therapy - frequently applied in combination with chemotherapy - is often used to reduce tumor size before surgery, or to minimize the risk of recurrence after tumor resection. However, it is also an important option as a primary therapy, particularly for malignancies that can not be removed surgically [Ric02].

Radiotherapy is based on exposing the tumor to ionizing radiation in order to destroy the cells or to prevent further growth. Different kinds of radiation are used such as X-rays, g-rays (e.g. of ^{60}Co or ^{137}Cs), electrons, neutrons, protons or p-meson beams. While the primary effect of radiation is the ionization of molecules, its impact is predominantly determined by secondary effects. These are, for instance, caused by the formation of radicals, result in a damage of DNA molecules and finally in death of the cells. The effectiveness of radiation is dependent on multiple parameters, like the cell cycle phase, the efficiency of cellular self-repairing processes [Lea96] and others (see next paragraphs). Radiation is most harmful to rapidly reproducing cells so that malignant lesions tend to be damaged more than normal tissue. Moreover, cancer cells are provided with less efficient repair mechanisms than cells of surrounding healthy tissues. Thus, the latter can be partly prevented from damage and tumors can be targeted more specifically if the total radiation dose is applied in fractions. For instance, a total dose of 70 Gy might be given over about six weeks as single daily doses of 2 Gy [Sau10].

Tumor micromilieu and perfusion

Even within tumors of identical site, type and stage, treatment outcomes may vary enormously between patients. Both the responsiveness to nonsurgical therapy and the metastatic

potential are known to be influenced by various physiological factors such as tumor vascularisation and perfusion, interstitial transport, nutrient supply, oxygenation, bioenergetic status and pH value. These parameters are closely linked and define the so-called metabolic microenvironment, as sketched in Fig. 1.5 [Vau89, Mol98].

In solid tumors, the micromilieu tends to differ considerably from that of surrounding normal tissue, mainly due to morphological and functional abnormalities of the tumor vascularity. While pre-existing host vessels can also be incorporated into a growing tumor, new tumor vessels will arise from neovascularization. Typically, these form chaotic microvessel networks, characterized by increased vascular permeability, lacking smooth muscle cells, missing vessel hierarchy and organization, and deficient perfusion [Vau98a].

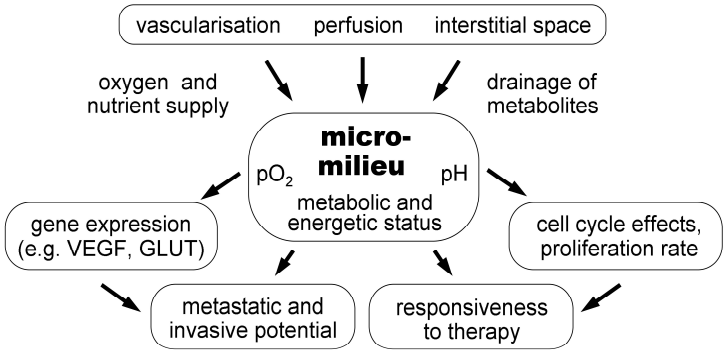

Fig. 1.5: The metabolic micromilieu of tumors, schematic depiction of the interplay between physiological parameters and their consequences (simplified from [Mol98]).

Clinical investigations on tumor microcirculation have been performed using a variety of techniques, including radioisotope clearance techniques, thermal washout procedures, laser Doppler flowmetry, color Doppler ultrasound, tracer-based positron emission tomography (PET) and dynamic computed tomography (CT), and MRI techniques (overviews in [Fel98, Fel99, Was01]). Despite methodological problems and inevitable inaccuracies, all these methods proved to be applicable in the assessment of tumor perfusion or vascularization. In general, tumors can exhibit very high as well as very low blood flow rates, and perfusion can vary considerably between tumors of identical site and classification. Both the distribution of vessels and the temporal course of microcirculation may show substantial temporal heterogeneity within a tumor, resulting in considerably anisotropic distribution of blood flow [Vau98]. A relation between weak perfusion or perfusion changes during therapy and poor treatment outcome was demonstrated by several patient studies, thus suggesting prognostic relevance of tumor microcirculation [Ked94, Pir95, Mayr96, Hawi97, Her99, deVri01].

Tumor oxygenation: Characteristics and clinical importance

A key factor of the tumor microenvironment is the tissue oxygenation which refers to the distribution of partial oxygen pressure. Hypoxia, i.e. the presence of oxygen deprived regions, is a characteristic property of solid tumors [Vau90, Vau01a, Vau01b]. It may originate from various pathogenic mechanisms such as a raised oxygen demand in rapidly proliferating tumor cells or an inadequate oxygen transport capacity of the blood due to tumor- or therapy-associated anemia. A major cause of tumor hypoxia, however, is an insufficient arterial oxygen supply, which is predominantly attributed to two different effects: diffusion-limited (“chronic”) hypoxia, resulting from large intravascular distances [Tho55] and perfusion-limited

("acute") hypoxia [Brow79], caused by spontaneous fluctuations in tumor blood flow or even by vessel disclosure on the microregional level [Cha87].

The oxygenation status of different tumor entities has been investigated in a number of clinical studies (overviews in [Vau98b, Fel99]). Generally, in correspondence to the results of studies on microcirculation, marked intra- and interindividual heterogeneities were observed, even in tumors of the same stage and grade. As a common rule, median pO_2 values lower than those of surrounding normal tissue were found in primary, in metastatic and in recurrent tumors. It has been known for long time from radiobiological studies that the radiation doses required to destroy hypoxic cells are two to three times higher than for well-oxygenated cells [Gray53, Wri57]. Besides this general treatment resistance, tumor hypoxia and micro-environment can have impact on patient prognosis by other mechanisms. These include an stronger tendency to form metastasis or an increase of the tumor malignancy [Wou02]. Clinical studies were able to show that the oxygenation status of a tumor is a decisive factor for long-term local control and patient survival [Hoe93, Nor96, Bri97, Fyl98, Stad99, Fel99, Nor00, Rud00, Vau01a, Vau01b].

Methods to assess tumor oxygenation

Various methods have been described for assessment of tumor tissue oxygenation (reviews in [Hor98a, Hor98b, Dew00, Bus03]). In many studies, data were acquired with a polarographic technique, also referred to as "Eppendorf" histography [Vau89, Kal90]. Here, quantitative pO_2 values are obtained by a needle electrode which is inserted into the tissue of interest. Since oxygen is consumed at the tip of the electrode, data has to be acquired while the probe is driven through the tissue in several tracks. This renders the technique highly invasive, and the monitoring of time-dependent oxygenation changes at a certain location is not possible. The latter limitation may be overcome by the "Oxylite" system, a fiber-optic oxygen-sensing device that remains at a fixed position [Col97]. At the cost of limited volume coverage, it can provide continuous readout of tissue pO_2, and it offers the additional advantage of MR compatibility [Grif99].

Besides these methods, different endogeneous and exogeneous markers are available for the assessment of tumor oxygenation [Bus03]. While endogeneous markers are genes or gene products that are upregulated under oxygen-deficient conditions, exogeneous markers are substances that must be administered and then accumulate in hypoxic tissue [Bus03]. Typical examples are nitroimidazole-based compounds such as EF-5 or pimonidazole, which preferentially metabolize in oxygen-deprived cells and can be detected by immunohistochemical analysis [Ral96]. Particularly pimonidazole has found application in studies on human tumor biopsies [Ken97, Kaa02, Nor03]. The role of MR is discussed in chapter 1.4.

Targeting hypoxia

Tumor hypoxia is not only an important prognostic parameter, but it can also represent a key factor for the development of targeted, tumor-specific therapies. There are two fundamentally different strategies to enhance treatment in the presence of poor oxygenation [Wou02]. The first approach is to exploit unique aspects of hypoxia itself, e.g. by the administration of bioreductive drugs (such as Tirpazamin) that are exclusively toxic to hypoxic cells or by other means that target distinctive properties of tumor blood vessels or biological responses to

hypoxia. The second approach is to combat hypoxia - either by administering chemical compounds (such as Nimorazole) that mimic the influence of oxygen during radiotherapy and can restore radiosensitivity or by aiming at improvements of oxygenation directly.

Manipulation of perfusion and oxygenation

Strategies to increase tumor perfusion and the availability of oxygen during radiotherapy include means to increase the microvascular oxygen content in order to overcome restrictions caused by diffusion-limited O_2 availability or to improve the microcirculation in order to enhance perfusion-limited O_2 delivery [Vau98c].

The administration of Erythropoietin (EPO), a hormone that stimulates the production of erythrocytes (red blood cells), seemed to be a promising approach to increase the oxygen transport capacity of blood, in particular in patients with anemia. This condition is characterized by a low hemoglobin concentration in blood and represents a prevalent condition connected to cancer and its therapies [Bush86]. However, clinical studies with EPO finally yielded disappointing results or even adverse effects [Hen03], and EPO treatment in tumor patients is subject of controversial discussions.

An increased arterial oxygen supply (*hyperoxia*) can also be achieved by administering breathing gases with high oxygen content. In practice, the breathing of *carbogen*, a mixture of 95% O_2 and 5% CO_2, shows to be efficient in raising the level of oxygen dissolved in the blood plasma. The rationale for the combination with an excess of carbon dioxide (*hypercapnia*) lies in its ability to counteract potential oxygen-induced vasoconstriction [Roj91]. Though it was found that carbogen breathing before and during radiation can lead to both increases and decreases of tumor perfusion [Robi95, Hill96, Pow96], it was shown to improve tumor pO_2 values in animal models [Stü98, Bus99] as well as in patients, albeit with heterogeneous response [Pow99, Aqu00]. A futher observation was that carbogen enhances the radiosensitivity of tumor cells more than pure oxygen [Roj91, Hill98].

In clinical trials, carbogen was combined with the vasoactive agent nicotinamide, the amide derivative of vitamin B3, and accelerated fractionated radiation in order to improve the outcome of radiotherapy, in particular in patients with tumors of the head and neck region and of the bladder (ARCON) [Kaa98, Kaa02a, Kaa02b]. Since the breathing of carbogen is supposed to primarily have an effect on chronic hypoxia, the rationale behind the addition of nicotinamide is to reduce acute hypoxia, most probably via a reduction of the intermittent shutdown of vessels and an improvement of tumor perfusion. However, it was not possible to achieve a statistically significant improvement. Presumably, the heterogeneous selection of patients hampered a statistical prove of an efficient radiosensitizing effect [Ber00].

During the breathing of carbogen gas, patients experienced discomfort and intolerance to the 5% CO_2 content [Grif97, Hos99a, Kaa02b], whereas lower concentrations of 2% or 2.5% showed to be tolerated much better [Pow99, Aqu99, Bad00]. In preclinical studies, neither oxygenation improvements nor radiosensitizing effects were compromised when such lower CO_2 concentrations were used instead of 5%, both without [Hill98] or with the addition of nicotinamide [Hor04]. In patients, blood gas analyses revealed that carbogen with 2% CO_2 - also known as *carbogen light* - enhances arterial oxygen levels to a similar extent as 3.5% or 5% [Bad00]. Studies with the Eppendorf histograph showed that a CO_2 fraction of 2% or

2.5% significantly increased the tumor pO_2 when compared to pure oxygen, and no significant differences were found in comparison to the effects achieved with 5% [Pow99, Aqu00].

1.4 Assessment of tumors with MRI

This section briefly addresses the role of MRI for the examination of tumors. Besides the topics of clinical standard imaging and the use of contrast agents, it touches the relevance of dynamic contrast-enhanced studies and discusses aspects of parameter quantification for tissue characterization. Promising investigative approaches that are explored in the context of this thesis, such as spin-labeling methods for the investigation of tumor perfusion and oxygenation-sensitive techniques, are discussed in chapters 2 and 3, respectively.

Tumor imaging

In case of suspected cancerous disease, different modalities such as MRI, CT, PET and others are available that allow for an image-based examination. In general, the preferred initial choice of imaging modality typically depends on the body part in question as well as on the symptoms and on the suspected cause [Cas99]. For investigating head and neck tumors, MRI is considered helpful in answering specific questions, but CT is the more frequently used initial modality, also due to its widespread availability. For ruling out intracranial mass lesions, MRI is generally accepted as the technique with highest sensitivity [Reim10]. Once the presence of a tumor has been diagnosed, it is important to evaluate its extension in order to determine the site for stereotactic biopsy and to plan surgical resection or radiotherapy. In this context, CT und MRI can be considered as complementary techniques. CT may be advantageous in depiction of calcified lesions and bony anomalies, and often is the method of choice for target volume planning in radiation oncology. In many cases, however, MRI is considered superior in determining the true extent of tumors [Reis08].

Clinical tumor MRI

In a clinical MRI exam, a set of sequences is used that provide differently weighted images. The composition of the protocol will depend on the part of the body to be assessed and on the suspected lesion, but also on the age and physical condition of the patient. Typically, both T_1- and T_2-weighted imaging are included, usually performed with spin-echo or turbo-spin-echo (TSE) sequences. In some cases, spin-density-weighted images can yield supplementary information. The inclusion of 3D gradient-echo techniques is recommended if the acquisition of thin slices or sensitivity to hemorrhage is desired. While fat suppression can be beneficial in the head and neck region, the suppression of cerebrospinal fluid (CSF) signal may help to increase the conspicuity of certain lesions in neurological exams. In the brain, a diffusion-weighted scan is often added. An essential element of most clinical MRI exams is the acquisition of (predominantly T_1-weighted) images after intravenous administration of contrast agent, typically containing Gd-chelate complexes. For direct comparability, slice position and orientation of a post-contrast scan are chosen identically to that of an equivalent pre-contrast acquisition. More details on sequences and protocols used in clinical exams can be found in section 6.2.

Contrast-enhanced imaging

The majority of clinical protocols include the administration of MR contrast agents, which alter tissue relaxation times, and the acquisition of pre- and post-contrast images. In most tissues, the common Gd-based contrast agents with low molecular weight are distributed in the extra-cellular space, and strong enhancement occurs due to high intrinsic vascularity. In the healthy brain, however, MR contrast agents reside in the intravascular compartment. Only in the case of a blood-brain barrier disruption - as encountered in tumors or other lesions - they diffuse into the interstitial space and lead to a local signal enhancement. In many cases, post-contrast images provide better lesion conspicuity, and improved distinction between tumor tissue and edema [Run97], but enhancing margins do not necessarily delineate the histological tumor boundaries [Kel87, Ear88] and it may remain difficult to discriminate between radiation necrosis and recurrent disease [Tof03]. In general, the presence of a local enhancement reflects a combination of several parameters, including regional blood volume, microvessel permeability and properties of the interstitial space.

Dynamic contrast-enhanced imaging

A separation of the parameters mentioned above is possible with dynamic contrast-enhanced (DCE) MRI. In these techniques, the kinetics governing the accumulation of contrast agent is assessed by acquisition of a time-resolved series of images, either T_1-weighted or - predominantly used in the brain - T_2*-weighted (reviews in [Grie97, Tof99, Pet00, Tho00, Barb01, Pad02, Cho03]). Based on tracer kinetic models, physiological quantities such as the capillary permeability-surface area product, regional blood volume, perfusion or mean transit time can be estimated. In human tumors, correlations were found between kinetic MR parameters and microvessel density [Hawi97, Buck97], oxygenation [Coo00, Lyng01a], grading [Aro94, Knop99, Lud00, Lud01, Robe00, Robe01, Shin02] or treatment outcomes [Pard94, Wenz96, Mayr96, Mayr99, Hawi98b, Hos99, DeVri01, Ess03].

Quantitative MRI in tumors

In the brain, due to edema, necrosis or cyst formation, the majority of pathological processes is associated with elevated water content. This is typically linked to an increase of spin density and of T_1, which is also related to macromolecule concentration and water binding. Moreover, T_2 is also elevated due to the increase in motional freedom of tissue water molecules. Most tumors show hyposignal in T_1-weighted and hypersignal in T_2-weighted images, which helps to recognize them. Due to wide biologic variations, however, the relaxation times of normal and abnormal tissues overlap, and the determination of tumor type and stage is not always possible. Nevertheless, quantitative MRI has a long tradition and attracted attention of many researchers. The following paragraphs briefly review the dependencies of MR parameters on physiology and the experience for characterization of tumors. Many aspects were extracted from [Tof03].

Spin density

The spin or proton density of tissue - here named M_0 - is a paradoxical parameter. On the one hand, its influence is implicitly present in all MR acquisitions. On the other hand, its dynamic range is rather small and there may be a lack of experience of using it clinically. It should be noted that M_0 not necessarily refers to all protons that are present, but rather to the amount of MR-observable spins, i.e. to “mobile protons” with transverse relaxation that is sufficiently slow to be captured by the utilized sequences. Some tissues exhibit a considerable amount of nonaqueous protons, primarily in lipids, proteins and nucleic acids. In non-lipid compartments, most mobile protons are in water, so that spin density might represent the tissue water content. Hence, spin density changes are often closely linked to T_1 changes [Fato99]. From a study in patients with brain tumors, for instance, an elevated spin density was reported in comparison to white matter [Just88].

Longitudinal relaxation time T_1

The longitudinal relaxation time T_1 represents an intrinsic biophysical property of tissue. It is linked to the concentration of macromolecules as well as on water binding and content. In healthy brain tissue, the presence of myelin leads to shortened T_1 of within white matter and is responsible for the typical T_1 contrast. The presence of pathology can induce alterations of T_1. As an example, inflammatory lesions and edema around tumors are typically associated with an increase in T_1. Also within tumors, T_1 values were found that were significantly prolonged in comparison to that of white matter, while there was some overlap with gray matter values [Eng86, Just88, Kur95]. With respect to the tumor type, some marked differences were observed. For instance short T_1 values were observed in meningiomas, while longest were found in glioblastomas [Nar86, Kur95]. Although a correlation was found between T_1 values and the malignancy of astrocytomas [Eng86], the differentiation of tumor types seems not possible on relaxation time measurements alone.

Transverse relaxation time T_2

The transverse relaxation time T_2 of white matter is shorter than that of gray matter. This difference is attributed to various factors such as discrepancies in water compartmentalization, vascularity or iron concentration [Vym95] as well as lower water content [Broo80], smaller regional blood volume [Kos99], and the presence of water that has very short T_2 since it is embedded in myelin lamellae [Whi97]. Studies in animal tumor models revealed a correlation between measured T_2 values and tumor cell nuclei fraction within cancerous tissue [Kur95] and distribution T_2 characteristics from edema with highest, tumorous tissue with intermediate and healthy brain with lowest values [Hoeh94, Eis95]. T_2 maps only, however, showed not to be sufficient for identifiction of different tumor types [Just88, Hoeh94, Eis95, Wilm93]. Also from experimental tumor studies, T_2 quantification was reported to improve the detection of tissue affected by irradiation [Mio96] and to facilitate the detection of early response to chemotherapeutic drugs - before its impact manifests on T_1 images due to volume reduction [Pop98].

Quantification of multiple parameters

An early clinical study explored the feasability of using texture measures to discriminate tissues on the basis of T_1 maps, T_2 maps and spin density-weighted images. It achieved an excellent identification of CSF, white matter and gray matter, and very good results with respect to the discrimination between tumor and edema [Lerski93]. Besides the combination of multiple parameters in general, the inclusion of diffusion-weighted images [Eis95], and the use of feature space analysis [Sol98] have been shown helpful for tissue characterization. Despite individual encouraging results, the quantification of multiple parameters remains a research approach and is not an element of clinical routine.

Retrospect

Since the studies for this thesis were planned and conducted, the field of tumor imaging has experienced a continuous evolution. In the field of MR, most prominent advances include MR spectroscopy, magnetization transfer imaging, susceptibility-weighted imaging, vessel size imaging, diffusion-weighted, diffusion tensor imaging and the availability of whole-body imaging techniques (reviews in [Hern10]). Moreover, emerging molecular and metabolic imaging methods such as 18F-FDG-PET have gained importance [Tre12]. Multi-modal imaging with integrated systems such as PET/CT and, more recently, MR/PET have become available [Buch12]. A discussion of these techniques and developments, however, is beyond the scope of this thesis.

Chapter 2

Quantification of perfusion in patients with head and neck tumors

In the study presented in this chapter, a spin-labeling technique was evaluated for the assessment of tumor perfusion in head and neck carcinoma patients. Eleven patients were investigated; five of them were examined twice during radiotherapy. For perfusion quantification, T_1 was measured with IR-Snapshot-FLASH imaging after slice-selective and non-selective inversion, respectively. Perfusion maps were obtained on the basis of a two-compartment-model. Tumor perfusion and perfusion changes during therapy were found to behave heterogeneously. Tumors with high initial perfusion tended to be smaller in size and to show better response to radiotherapy than those showing weak pretreatment perfusion. Without the need for exogenous contrast agent, the repetitive characterization of tumor perfusion was feasible. The presented technique may be useful for stratification of vasomodulating treatments. This chapter reflects the contents of a corresponding peer-reviewed journal article [Schm03a].

2.1 Introduction

The responsiveness of tumors to non-surgical treatment modalities such as irradiation and chemotherapy is substantially influenced by tumor blood flow, tumor tissue perfusion and oxygen supply [Fel99b, Res01]. Chronic and acute tumor hypoxia have been the target of different approaches which aim to modify tumor oxygenation and perfusion [Kje91, Hor94, Sie94, Roj96, Nor97, Pow99, VanD99, Aqu00, Ber00, Jor00, Kaa02a, Kaa02b]. Hence, a non-invasive method for evaluation of tumor tissue perfusion and perfusion changes as a predictive factor for treatment response would be of considerable clinical value.

Clinical investigations on tumor blood flow have been performed using a variety of modalities such as Positron Emission Tomography (PET) [Bac00], dynamic CT [Fel93, Herm99] and dynamic MR imaging ([Fel93, Wong00, deVri01]. A comprehensive overview is given by Feldmann et al. [Fel99b]. Most techniques require the administration of a contrast agent and have been hampered by a lack of quantification (SPECT, PET) or limited coverage

(Doppler ultrasound). In dynamic CT studies, high doses of ionizing radiation have to be applied. Generally, the use of contrast agents renders repetitive measurements difficult due to a lack of true intravascular selectivity during the equilibrium phase. Moreover, a dynamic contrast-enhanced acquisition can typically not be directly repeated, so that it is not ideally suited for monitoring the influence of vasoactive substances.

Based on MR spin-labeling methods, tissue perfusion can be assessed non-invasively, without the injection of exogeneous contrast agents. In this concept, blood water is magnetically marked and used as an endogenous tracer. It induces magnetization changes in the tissue it flows into, which are indicative for local perfusion. Spin-labeling perfusion methods inherently offer a potential advantage if compared to methods based on contrast injection. With spin-labeling, examinations could be performed repeatedly or continuously, which might be useful for visualizing the influence of vasomodulating agents.

At the time the study presented in this chapter was prepared, however, only very few publications were available that dealt the assessment of tumor perfusion with spin-labeling methods. In a rat glioma model, a spin-labeling technique was successfully used for quantitative tumor perfusion measurements [Sil00b]. Besides an early report that showed the feasibility of such investigations in tumor patients [Kwo95], only a single other study in human subjects was found. It demonstrated that it is possible to assess cervical uterine perfusion with spin-labeling and it found that blood flow in malignant tissue was stronger and faster than in normal cervical tissue [Hawi98a].

The aim of this study was the evaluation of a non-invasive MR spin-labeling technique for the assessment of tumor tissue perfusion in head and neck carcinoma patients during radiotherapy.

2.2 Basics - spin-labeling, tissue model and quantification

With the aid of MR spin-labeling, imaging of tissue perfusion can be accomplished non-invasively, without the administration of exogenous contrast agents. In the study presented here, a FAIR-type (Flow-sensitive Alternating Inversion Recovery) labeling scheme was employed in combination with an IR (Inversion Recovery) FLASH signal readout for quantitative T1 measurements. From the resulting data, based on a two-compartment tissue model, quantitative perfusion maps can be calculated.

Spin-labeling

In MR spin-labeling methods, the blood is magnetically prepared before it flows into the volume of interest. In comparison to a reference scan, this yields detectable signal differences that depend on local capillary blood flow. Typically, these differences are rather small, and long scan times are required to obtain sufficient SNR. This represents a general limitation of these techniques. While spin-labeling methods were also used in humans for the quantification of myocardial perfusion [Bel98, Wac99, Wall00], their main application in human subjects is the measurement of brain perfusion. Specifically, spin-labeling techniques have proven useful for visualization of qualitative or relative cerebral blood flow changes in functional activation experiments [Kim95, Sil00a, Pre01]. Another potential clinical application

is the assessment of ischemic disease, e.g. for identification of weakly perfused regions in acute stroke [Cha00, Hun02]. Exemplary cancer patient data had been shown early [Kwo95], and a subsequent spin-labeling study on human tumors reported a correlation between the perfusion of tumors and their malignancy [Hawi98a].

The FAIR spin labeling scheme

The FAIR spin labeling scheme was proposed in the mid-90s by several groups (Kim95, Kwo95, Schw96). It is schematically illustrated in Fig. 2.1. The basic idea is to combine acquisitions after (a) non-selective and (b) slice-selective inversion preparation, respectively. Stationary magnetization as present in non-perfused areas encounters the 180° RF pulse in both cases, so that the signal evolutions during the subsequent recovery period are identical. In the case of non-selective inversion, spins flow into the slice, which also relax towards the positive z direction. With slice-selective inversion, however, the magnetization that enters the slice due to tissue perfusion already is in its thermal equilibrium. This leads to an apparent acceleration of longitudinal relaxation, which can either be captured as modified contrast in a fast image acquisition or measured quantitatively.

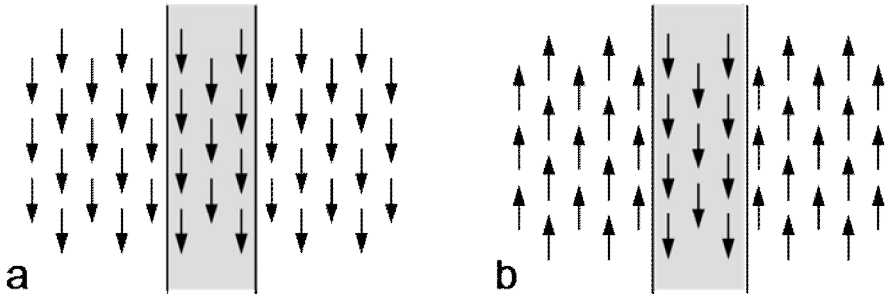

Fig. 2.1: The FAIR spin labeling scheme: The plane of interest (gray) is imaged after (a) non-selective and (b) slice-selective inversion.

The two-compartment tissue model

For a quantitative determination of tissue perfusion, data has to be assessed on the basis of a mathematical model that accounts for the physiological processes on capillary level in simplified fashion. For this purpose, a two-compartment model was proposed [Bau92, Bau96], based on an early model for capillary tissues [Kro18]. The basic concept is illustrated in Fig. 2.2.

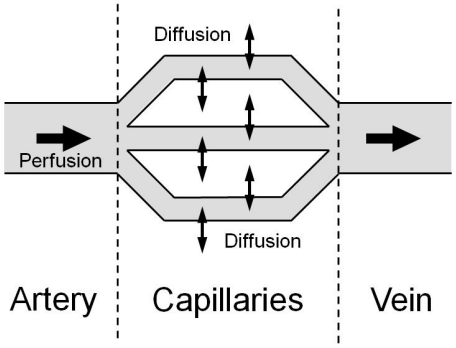

Fig. 2.2: Schematic display of the the two-compartment tissue model

In this model, tissue is supposed to be composed of two homogeneous compartments, the intracapillary and extravascular space. Two major transport processes are considered: The permanent transfer of magnetization from the arterial system to the capillary space due to tissue perfusion, and the exchange between the two compartments caused by diffusion. For the latter, water is assumed to be freely diffusible, with fast exchange between the two compartments. Typically, any relaxation between spin labeling and entrance to the capillary regime is neglected, i.e. the effective transit time is assumed to be short.

Perfusion quantification

In the two-compartment model, the temporal evolution of the magnetization depends on the amount of arterial blood supply and the kinetics of water diffusion exchange. The mathematical formulation of these aspects leads to an inhomogeneous differential equation, which has a bi-exponential expression as a general solution for the signal evolution. Using the so-called *mean relaxation time approach* [Bau92], i.e. an approximation with a mono-exponential formulation, and solving the equation for the combination of non-selective and selective inversion, the following formula is obtained for the tissue perfusion [Bel98]:

$$P = \frac{\lambda}{T_{1,Blood}} \left(\frac{T_{1,nonsel}}{T_{1,sel}} - 1 \right) \qquad (2.1)$$

Here, λ denotes the blood-tissue partition coefficient, which is defined as the ratio of the quantity of water per gram of tissue and the quantity of water per milliliter of blood. $T_{1,\mathrm{Blood}}$ is the longitudinal relaxation time of blood, and $T_{1,\mathrm{nonsel}}$ and $T_{1,\mathrm{sel}}$ are the apparent tissue T_1 values after non-selective and selective inversion, respectively. With the assumption that λ and $T_{1,\mathrm{Blood}}$ are constant and known, tissue perfusion can be determined quantitatively by measuring the subtle difference between $T_{1,\mathrm{sel}}$ and $T_{1,\mathrm{glob}}$, i.e. by conducting to measurements of the longitudinal relaxation time of tissue.

T_1 quantification with IR Snapshot FLASH

The concept of Snapshot FLASH imaging may be understood as fast sampling of a parameter-selected image that reflects a state generated by a preceding magnetization preparation experiment [Haa90]. This approach became feasible by improvements of the MR system hardware and the associated high speed of FLASH imaging. Various contrasts are possible, for instance by T_1-, T_2- or chemical-shift-selective preparations.

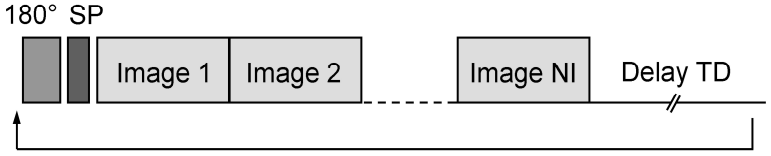

Fig. 2.3: IR snapshot FLASH: Continuous sampling of the inversion recovery curve with a train of FLASH images.

In an IR snapshot FLASH experiment, the magnetization recovery period following a 180° inversion pulse is continuously sampled with a series of FLASH images [Haa89, Haa90].

This concept is depicted schematically in Fig. 2.3. It is based on the principle published for spectroscopic T_1 quantification by Look and Locker [Look76], which had also been reported to be useful in the context of imaging [Gra86a]. After spin inversion, the signal starts with $S_0 = M_0 \sin a$ and evolves exponentially towards its steady state value given by Eq. 1.8. The continuously applied a pulses, however, have noticeable influence on the evolution of the longitudinal magnetization so that the signal evolution does not correspond to free relaxation. Instead of the true T_1, a shorter apparent relaxation time T_1^* is observed. For small flip angles, it can be described by [Kap76, Dei91]:

$$T_1^* = \left(\frac{1}{T_1} - \frac{\ln(\cos a)}{TR} \right)^{-1} \quad . \tag{2.2}$$

The resultant signal time course can be described by a 3-parameter fit function:

$$S(t) = S_{ss}(1 - INV \exp(-t / T_1^*)) \quad , \tag{2.3}$$

where the inversion factor INV is a measure for the ratio between the initial and the steady state signal:

$$INV = 1 + S_0 / S_{ss} \, . \tag{2.4}$$

For $TR << T_1^*$, the true T_1 can be determined from the fit parameters as [Dei92]

$$T_1 = (INV - 1) \times T_1^* \quad . \tag{2.5}$$

Along the recovery curve, a sufficient number of sampling points and an adequate temporal distance between adjacent images can be achieved with a segmented acquisition, i.e. by acquiring only a part of the image k-space per shot. After a waiting delay *TD*, allowing for complete return to equilibrium, the experiment has to be repeated for sampling the remaining phase encoding steps. If the phase encoding lines sampled within each shot are distributed evenly over the whole k-space in a comb-like pattern, a smooth signal behavior is obtained along the phase encoding direction. With a linear phase encoding pattern, it is justified to assign each image to the time when its central phase encoding step is acquired [Dei95].

For sequence optimization, multiple parameters have to be considered such as the flip angle, the RF pulse slice profile, the acquisition bandwidth and - depending on the latter - the *TR*, the segmentation scheme, the number of images and the subsequent waiting period. All these factors should be adjusted with regard to the tissue of interest or a specific range of T_1 values. With respect to SNR efficiency, the optimal flip angle for most biological tissues is expected between 5° and 10° [Dei92]. The formula of Eq. 2.1.6, however, is independent of the flip angle, which reflects an inherent robustness of the method against potential local flip angle deviations.

2.3 Methods

Subjects and experimental setup

A total of 11 patients with histologically proven head and neck carcinoma and/or lymphatic node metastases were investigated. Five patients were examined twice: once at the beginning of primary radiation therapy and once more after at least 54Gy. All patients gave informed consent, and the protocol was approved by the local ethics committee.

The MR imaging experiments were performed on a 2T whole body MR scanner (TOMIKON S200, Bruker Medizintechnik, Ettlingen, Germany). The system body coil was used for excitation and a receive-only quadrature head coil was employed for signal detection. For fast depiction of anatomy and as a basis for the slice positioning, FLASH localizer images were acquired. Explicit care was taken in the second examinations to reproduce the slice positions of the first examinations. Foam pads were used to minimize head or neck movements.

Data acquisition

Tissue perfusion was determined quantitatively with the FAIR-type spin labeling technique introduced in section 2.2: Two series of segmented Snapshot-FLASH images were acquired after slice-selective and after non-selective spin inversion, respectively.

The scans were performed within a slice of 10mm thickness, positioned through the center of the main lesion. The chosen FOV of 24cm x 18cm and matrix size of 128 x 64 pixels (zerofilled to 128 in phase encoding direction) yielded an in-plane resolution of 1.9mm x 2.8mm. For quantitative perfusion imaging, a sufficiently high SNR is required to detect very small differences in T_1 precisely. Hence, a low acquisition bandwidth of 5.5kHz was used. Imaging parameters were TE = 13.3ms, TR = 25.9ms, flip angle = 6°. For the T_1 measurement, a train of 16 IR snapshot FLASH images was acquired in segmented fashion: After the inversion pulse, 16 temporal frames were sampled consecutively, each comprising 8 of the 64 required phase encoding steps, so that a total of 8 IR experiments resulted in a single T_1 measurement. This acquisition scheme yielded a TI time of 108ms for the first image and an interval of 208ms between the 15 subsequent differently T_1-weighted images, i.e. the respective TI times were 108ms, 316ms, ..., 3228ms. With a shortened recovery delay of 2s prior to each subsequent inversion, the time required for sampling the complete data of two IR image series was 1:25min. Data of 6 subsequent series were averaged to obtain high SNR, which resulted in a total scan time of 8:30min for a perfusion experiment.

Prior to the patient study, both excitation and inversion slice profiles had been optimized in phantom experiments in order to ensure consistency between T_1 values obtained after global and slice selective inversion and to establish perfusion sensitivity while avoiding erroneous results. The calibration of the technique had also been controlled in volunteer experiments, where reproducible results were obtained in excellent agreement with literature values [Weig00a, Weig00b, Schm01].

Data evaluation

The corresponding longitudinal relaxation time maps for $T_{1,nonsel}$ and $T_{1,sel}$ were calculated with a pixel-wise fit of the 16 magnitude image intensities to a three-parameter exponential function (using a least square fitting routine and a computing algorithm described in [Nek92]), and subsequent correction for the influence of the continuously applied RF pulses according to Eq. 2.5 [Dei92]. From these maps, a perfusion map was calculated according to the formula given in Eq. 2.1. For the blood-tissue-coefficient and the longitudinal relaxation time of blood, values of λ =0.9 ml/g [Rai76] and $T_{1,blood}$ = 1650ms were used.

Two typical types of artifacts were addressed that are described in literature for spin labeling experiments: Regions with unphysiologically high perfusion values and pixels showing negative perfusion [Ye96]. The first generally arise from bulk motion in slice direction, e.g. blood flow in large vessels, but are also found in regions tainted by unavoidable movement, e.g. at the throat or the tongue. The second may be caused by statistical variation in regions of no or very weak perfusion. Thresholds were used to eliminate both types of artifacts: Pixels in which the difference between $T_{1,nonsel}$ and $T_{1,sel}$ exceeded 150ms and/or pixels showing negative or unphysiologically high perfusion values of P>150ml/100g/min were excluded from the map, i.e. the corresponding perfusion values were set to zero and not considered during subsequent postprocessing.

For further evaluation, the distributions of quantitative perfusion values within the tumor region were visualized in cumulative histograms. Values of 5ml/100g/min and 60ml/100g/min were introduced as boundaries for low and high perfusion, respectively, and the fraction of pixels with perfusion lower and higher than those boundaries were calculated. In addition, a semi-quantitative analysis of the perfusion maps was also performed by comparing the perfusion pattern of the tumor to that of the sternocleid muscle of the contralateral side.

2.4 Results

In this study, a standardized MRI protocol was employed for measuring tissue perfusion quantitatively with a spin-labeling technique. First results in patients with advanced head and neck cancer were obtained. Ten of the 11 patients were successfully studied, five of them both at the beginning and the end of their radiotherapy course. In one subject, data had to be omitted from further assessment because of severe motion due to claustrophobic anxiety in the magnet bore.

Among the investigated subjects, tumor perfusion and changes in perfusion during radiotherapy were heterogeneous, as was the response to radiotherapy. An overview over all patient characteristics is given in Tables 2.1 and 2.2. Considerable intratumoral heterogeneity was found, and marked differences were observed between the studied patients. In 4/10 patients, a visual difference between a better perfused periphery and a central core was observed. This characteristic, however, was not seen in the remaining patients. In the course of treatment, not only the perfusion but also the volumes of the studied lesions changed, as can be seen from Table 2.1. In 4/5 patients that were examined twice, a decrease of tumor perfusion after radiation doses >54 Gy was seen, while one patient showed increased perfusion in the tumor center and a moderate size reduction.

Patient no. and total dose		Tumor site and stage	Volume in ml	P_{rel} [1)] (core of lesion)	P_{rel} [1)] (rim of lesion)	Voxel fraction with weak perfusion [2)]	Voxel fraction with high perfusion [3)]
1	0 Gy	Oropharynx T2N2b	24	+	+	28 %	50 %
	54 Gy		2	=	=	2 %	7 %
2	0 Gy	Hypopharynx T2 N3	80	-	+	59 %	21 %
	54Gy		48	+	+	45 %	31 %
3	2 Gy	Hypopharynx T4N2a	40	-	+	67 %	8 %
	62 Gy		40	-	+	76 %	4 %
4	0 Gy	Base of tongue T3N2c	15	+	+	38 %	31 %
	69 Gy		2	-	-	81 %	12 %
5	0 Gy	Hypo-Oropharynx T4N2c	7	=	+	43 %	34 %
	58 Gy		<1	-	=	78 %	8 %

Table 2.1: Characteristics of patients studied before and at the end of their radiotherapy course. Indicator lesions (cervical lymphnode metastasis) are analyzed semi-quantitatively relative to the sternocleido muscle and quantitatively using the cumulative perfusion histograms.

1) Perfusion relative to contralateral musculature: + increased; = equal; - less
2) Percentage of Voxels with P < 5 ml/100g/min
3) Percentage of Voxels with P > 60 ml/100g/min

Patient no. and lesion		Tumor site and stage	Volume in ml	P_{rel} [1)] (core of lesion)	P_{rel} [1)] (rim of lesion)	Voxel fraction with weak perfusion [2)]	Voxel fraction with high perfusion [3)]
6	PT	Hypo-Oropharynx T3N2b	13	+	+	41 %	39 %
	node		1	+	+	36 %	36 %
7	PT	Paranasal sinus T4N0	45	+	+	19 %	53 %
8	node	Oropharynx T2N3	83	-	=	42 %	8 %
9	node	Oropharynx T2 N2b	33	=	=	37 %	26 %
10	PT	Hypopharynx T3N2c	9	+	+	34 %	48 %
	node		21	=	=	45 %	8 %

Table 2.2: Characteristics of patients studied before radiotherapy. Indicator lesions (cervical lymphnode metastasis and/or the respective primary tumor) are analyzed semiquantitatively relative to the sternocleido muscle and quantitatively using the cumulative perfusion histograms.

1) Perfusion relative to contralateral musculature: + increased; = equal; - less
2) Percentage of Voxels with P < 5 ml/100g/min
3) Percentage of Voxels with P > 60 ml/100g/min

In Figs. 2.4 and 2.5, representative data of two patients are shown. Both had lymphatic node metastasis and were examined twice. In patient #1 the tumor shows a rather homogeneously high perfusion pattern before therapy (Fig. 2.4b). After 54 Gy a considerable size reduction is observed (Fig. 2.4d), and perfusion in the lesion is lower but still demonstrable (Fig. 2.4e). Areas with low perfusion P < 5ml/100g/min have increased, as is shown in the cumulative histogram (Fig 2.4f). In this patient complete clinical remission was achieved after a total radiation dose of 69.5 Gy.

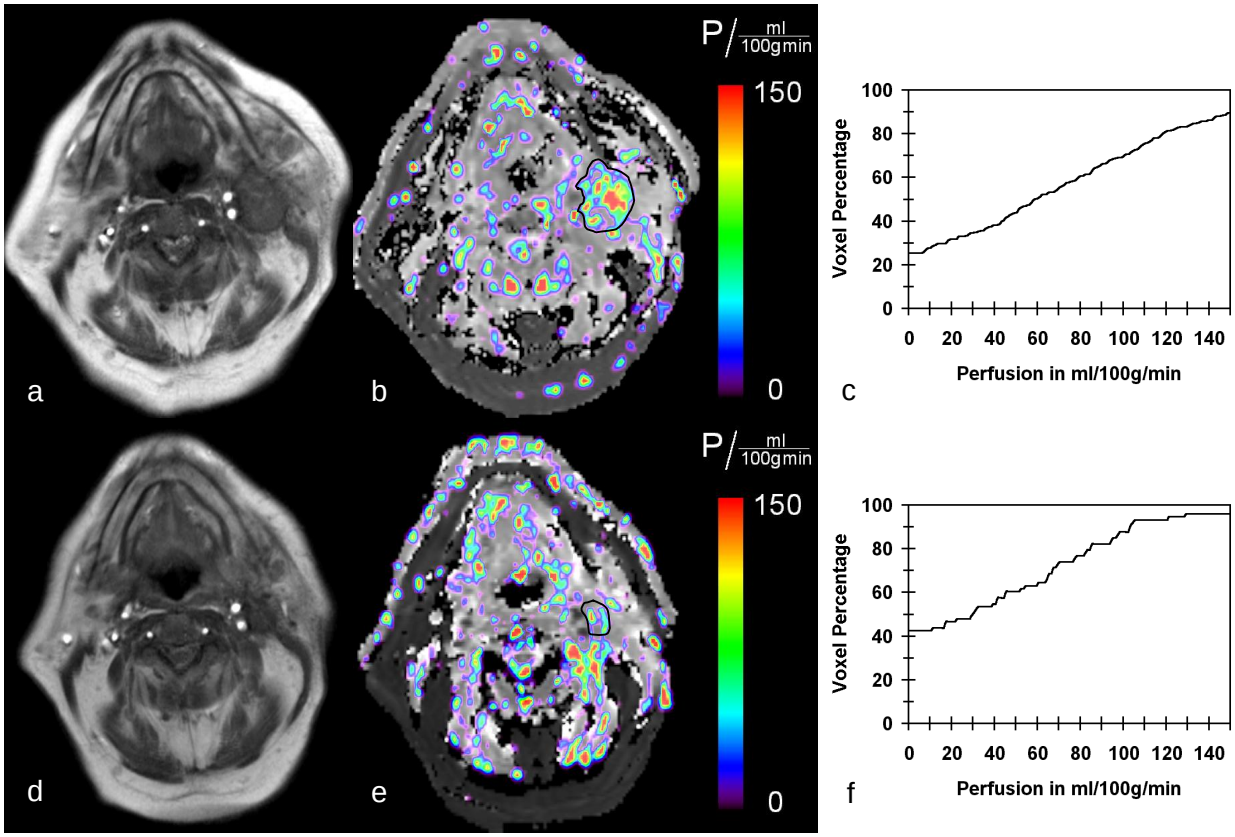

Fig. 2.4: Patient #1 with left sided jugular lymph node metastasis. Before therapy rather homogeneously high perfusion pattern (b). After 54 Gy, considerable size reduction (d) and lower perfusion (e). Increase of areas with low perfusion <5ml/100g/min (f). In this patient, complete clinical remission after a total dose of 69.5 Gy.

Figs.2.4-2.6: FLASH images for anatomical reference (a,d); Tissue perfusion maps as calculated with Eq. (2.1), depicted in a rainbow-colored scale over the corresponding grey-scaled $T_{1,\text{nonsel}}$ maps (b,e); Cumulative frequency histograms of perfusion value distribution (ml/100g/min) within the tumor regions (c,f). In Figs. 2.4 and 2.5, results at the start and at the end of treatment are shown in the upper and lower row, respectively.

In patient #2, the lesion appears with homogeneous signal intensity in the FLASH image before therapy (Fig. 2.5a). The perfusion map shows enhanced perfusion values in the periphery of the tumor mass (Fig. 2.5b). The effect of the threshold postprocessing is demonstrated by the suppression of high perfusion values in the clearly visible carotid arteries. After 54 Gy, there is a moderate size reduction (Fig. 2.5d) and areas of high perfusion are seen also in the center of the lesion (Fig. 2.5e). The respective cumulative perfusion histograms show a decrease of poorly perfused areas (Figs. 2.5c, 2.5f).

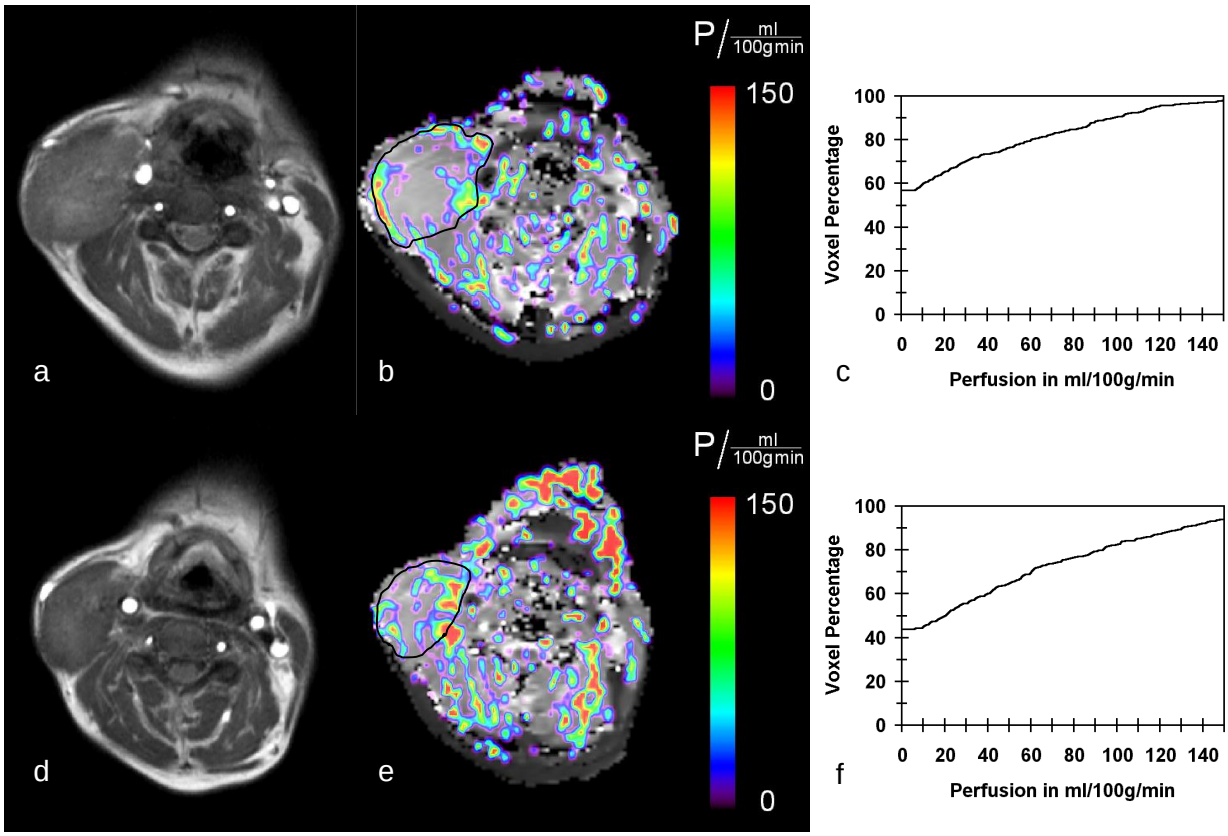

Fig. 2.5: Patient #2 with a right-sided lymph node metastasis of the neck. Before therapy, homogeneous appearance of the lesion in the FLASH image (a). Enhanced perfusion values at the periphery of the tumor mass (b). After 54 Gy, moderate size reduction (d) and areas of high perfusion also in the center of the lesion (e). Decrease of poorly perfused areas (c,f).

As a further example, data from patient #7 is provided in Fig. 2.6, showing a squamous cell carcinoma located at the paranasal sinus. The extent of the lesion before therapy is clearly delineated on the FLASH image (a). The corresponding perfusion map shows a large asymmetrically located hyperperfused region (b).

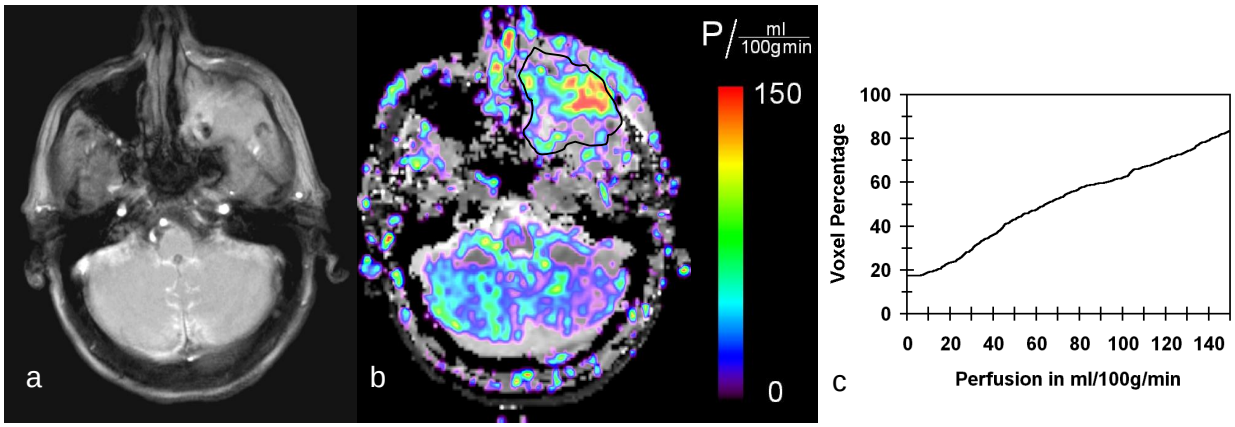

Fig. 2.6: Patient #7 with a squamous cell carcinoma located at the paranasal sinus, examined before therapy. FLASH image showing extent of the lesion (a). Large asymmetrically located hyperperfused region in the corresponding perfusion map (b).

2.5 Discussion

In the presented MR perfusion imaging technique, magnetically labeled blood water acts as an endogenous tracer. After slice-selective spin inversion, the inflow of fully relaxed spins causes measurable shortening of the longitudinal relaxation time T_1. Tissue perfusion can be calculated on a pixel-by-pixel basis under the assumption of a two-compartment model. With this approach, no administration of an exogenous contrast agent is required as in first-pass perfusion experiments, rendering the method completely non-invasive in nature. As a further advantage, repetitive perfusion measurements could be feasible over short time intervals, for instance to visualize the effect of vasomodulating agents. This would be difficult to accomplish with contrast-enhanced perfusion techniques.

The method appeared suitable in different kinds of tumors and localisations. To date, it was used for the examination of head and neck tumors as well as for brain lesions. Despite the use of foam pads during patient positioning and thresholds for perfusion calculation, it was not possible to completely avoid motion artifacts in regions of the larynx or the tongue.

The determination of tissue perfusion is based on several assumptions. A basic point is that a two-compartment model with fast diffusion exchange between capillary and extravascular space is applicable, which may not be the case for all tumors, especially those with necrotic tissue. Nevertheless, this problem should not be a general obstacle - since no inflow takes place in necrotic tissue, no perfusion should be measured. Accordingly, the results in a tumor with centrally cystic necrosis showed no perfusion in this area. For perfusion determination, the blood-tissue-partition coefficient was assumed to be constant as 0.9ml/g. This value may be not exactly correct for all tumor tissues, but according to Eq. 2.1, any deviation in l would scale linearly with the calculated result and only lead to a corresponding slight under- or overestimation of absolute perfusion values.

For perfusion quantification, it is essential to resolve small differences between T_1 values after global and slice-selective inversion very accurately. Therefore, both a high SNR

and sufficient temporal resolution of the single images are indispensable. Although these requirements were considered by using a low acquisition bandwidth and segmented image acquisition, six averages over identical images were performed in order to achieve reliable results. Nevertheless, tumor perfusion could be assessed within a reasonable timeframe of 8:30min.

Several publications demonstrated that spin labeling approaches yield very good results for applications such as in vivo perfusion measurements in rat brain [Schw96] or myocardium [Bel98], where measured alterations in perfusion were also validated by microsphere perfusion measurements [Wall00, Hil01]. Human applications are described for the quantification of perfusion in heart [Wac99] and in brain tissue [Pre01]. The technique has also been shown to be capable of detecting the influence of oxygen and carbogen breathing on brain tissue perfusion in a volunteer study [Weig00b, Schm01]. Under hyperoxic conditions, however, the oxygen dissolved in blood plasma leads to a reduction of $T_{1,blood}$ [Sil03], which in turn has a direct influence on perfusion results. This effect should be monitored and considered in the data evaluation [Weig00b].

In the presented study, tumors with high initial perfusion showed the tendency to be smaller in size and to show better response to radiotherapy than those showing weak pretreatment perfusion. This trend was also observed in a dynamic CT perfusion study on head and neck tumor patients, although a significant correlation could not be established [Her99].

Several MRI perfusion studies investigated carcinoma of the cervix, using dynamic acquisition of T_1-weighted images or rapid T_1 quantification after a bolus injection of contrast agent. Various results were obtained: One study concluded that the method may not facilitate differentiation between aggressive and non-aggressive tumors [Pos99]. Others were able to show that parameters from dynamic CE MRI correlated with pO_2 values as measured with polarographic needle electrodes [Coo00, Lyng01a]. Results of a study by Mayr et al. suggest that cervix tumors with higher tissue perfusion may have a lower incidence of local recurrence than those with lower perfusion. Moreover, an increase of perfusion during early therapy showed to be strongly correlated to treatment outcome [Mayr96].

In the presented study, a perfusion increase after a dose of 54Gy was seen in 1/5 patients examined twice. This finding may be associated with local reperfusion effects due to the considerable size reduction of the initially large, but moderately responding tumor. In 4/5 patients a decreased tumor perfusion was measured in the second examination. A similar observation is reported from the above-mentioned study on cervical carcinoma, where parameters indicating lowered perfusion were measured as a general trend after therapy [Mayr96]. All in all, the presented data may be in accordance with the assumption that high pretreatment perfusion is associated with positive treatment response. To date, however, the number of investigated cases is too small to allow for meaningful clinical correlations.

Recent work supports increasing evidence for a correlation between tumor oxygenation and treatment outcome [Fyl98, Nor00]. Furthermore, in studies using histographic needle measurements it was shown that human tumor oxygenation can be elevated by carbogen breathing [Aqu00, Pow99]. The potential of carbogen to enhance radiosensitivity was validated in various experimental tumor models [Nor97, Sie94], with potential further improvement in combination with nicotinamide injection [Hor94, Kje91] and accelerated radiation schedules [Roj96]. Subsequent clinical trials have reported various results [Kaa02], like high local

control rates in tumors of the larynx and oropharynx [Kaa02] or the lack of significant improvement in clinical outcome as observed for unselected groups of patients with locally advanced head and neck tumors [Ber00]. In that context, a non-invasive technique for repetitive perfusion measurements might be useful to select patients that show response to vasomodulators and may benefit from an according individualized therapy.

2.6 Conclusion and retrospect

This study showed that the localized quantification of the perfusion rate of head and neck tumors is feasible with the presented MRI spin-labeling technique. Tumor perfusion, perfusion changes during radiotherapy and treatment response were found to be heterogeneous among the investigated patients. In 4 of 10 patients, a visual difference between a better perfused tumor periphery and a central core was detected. In 4 of 5 patients examined both before therapy and after doses of at least 54 Gy, a significant decrease in tumor perfusion was found. However, more patients have to be investigated to examine a potential correlation between perfusion rate and local treatment failure.

The spin-labeling technique is completely non-invasive and does not require the administration of any contrast agent. Hence, repetitive characterization of tissue perfusion changes may be possible, e.g. for the investigation of blood flow effects induced by vasomodulating agents. Both measured tumor perfusion and its response to vasoactive drugs may be of prognostic value and useful to preselect patients for individual treatments based on vasomodulation or anti-angiogenic agents.

Since this study was conducted, a considerable variety of spin labeling methods has been described in literature (technical overviews in [Pet06, Liu07, Mar10]). Over the last years, the availability of this approach to clinicians has improved, also because the major MR system vendors started to distribute spin labeling packages. Clinical studies have been perfomed on different clinical applications, including the assessment of tumors. In a study on patients with intracranial gliomas, for instance, spin-labeling results showed close linear relation with perfusion data from dynamic CE susceptibility-weighted experiments, and allowed distinction between high- and low-grade gliomas [War03]. Another study showed that perfusion measures from spin-labeling scans - in combination with diffusion imaging - significantly improved the diagnostic accuracy of glioma grading if compared with conventional imaging [Kim07]. While there is a certain focus on neuroimaging (reviews in [Brow07, Wolf07, Tou08]), spin-labeling methods are not restricted to the brain. Their application to tumors of other organs or body regions such as the kidneys [Boss06] or, most recently, the breast [Kaw12] were also explored. Hence, the study presented in this chapter can be seen as one of the first pioneering studies in a continuing vivid field of research.

Chapter 3

Monitoring tumor oxygenation changes in patients breathing hyperoxic gases

The study presented in this chapter was aimed at implementing and evaluating a non-invasive functional MR technique for monitoring tumor tissue oxygenation changes in 13 patients with head and neck carcinoma. Different breathing gases - air, carbogen light (2% CO_2 + 98% O_2) and 100% oxygen - were administered to induce oxygenation changes. A multi-gradient-echo (MGE) sequence was used for quantification of the apparent transverse relaxation time T_2*. For both hyperoxic gases, the tumor T_2* values showed a shift of the mean towards higher values, corresponding to an increase of oxygenation. This increase correlated with a median shift for ΔT_2* towards positive values in the majority of the patients. For oxygen, in comparison to carbogen light, a slightly stronger T_2* increase and a significantly higher heterogeneity of the response were observed. The presented MR technique showed to be feasible for monitoring oxygenation changes in head and neck tumor patients and should be helpful for the selection of patients who might benefit from carbogen-induced radiosensitation. This chapter reflects the contents of a corresponding peer-reviewed journal article [Kot09].

3.1 Introduction

The major pathophysiological mechanisms leading to tumor hypoxia are structural and functional abnormalities in tumor microvasculature and anemia, which lead to increased oxygen diffusion distances and reduced oxygen transport capacity of the blood [Bush86, Mol98, Gil99]. Sustained tumor hypoxia enhances various cellular and molecular responses that perpetuate malignant progression. Different studies show evidence for a correlation between tumor oxygenation and treatment outcome [Hoe93, Nor96, Bri97, Fyl98, Stad99, Fel99, Nor00, Rud00, Vau01a, Vau01b].

Since hypoxic cells also show reduced radiosensitivity, different strategies were evaluated for improving tumor oxygenation during irradiation. These include the administration of carbogen (95% O_2 and 5% CO_2) as a breathing gas. While a high oxygen content leads to an

increase of the amount of oxygen dissolved in the blood plasma, the addition of CO_2 aims at counteracting vasoconstriction as caused by the oxygen [Roj91].

Although studies reported inconsistent effects of hyperoxic and hypercapnic breathing gases on tumor blood flow [Lan98, Dunn99], carbogen led to an improvement of tumor oxygenation in experimental settings [Stü98, Bus99]. The same observation was made in patients, but with heterogeneous response [Pow99, Aqu00]. The administration of carbogen was involved in the clinical ARCON trials, which were aimed at improving the radiotherapy treatment outcome in patients with tumors of the head and neck and bladder (ARCON) [Kaa98, Kaa02a, Kaa02b]. The observed radiosensitizing effect, however, was statistically not significant, most probably due to a heterogeneous selection of patients [Ber00]. In this context, a tool to assess the response to carbogen on an individual basis might be helpful for determining patients who might benefit most from carbogen breathing.

With MR, images can be acquired that are sensitive to changes in the concentration of paramagnetic deoxyhemoglobin, so that tissue oxygenation and changes in oxygenation can be assessed non-invasively. A brief review of the basic underlying mechanisms is found in section 3.2. At the time the study presented in this chapter was prepared, a variety of reports could be found that described results obtained animal tumor models. However, only two studies had been published that explored the effect of carbogen in human subjects [Grif97, Tay01]. In both, T_2*-weighted imaging was used to monitor the tumor response and in each on, an enhancement was observed in more than half of the examined patients, consistent with an increased oxygenation and perfusion.

Another common finding was a high number of technical failures, mainly due to patient motion. This could be attributed to the respiratory discomfort caused by the high level of CO_2 [Pow99]. Other studies using carbogen with lower levels of CO_2 showed similar improvements of tumor oxygenation and less distress for patients [Aqu00, Pow99, Schu02]. Blood gas analysis, infrared spectroscopy and MRI measurements indicated that carbogen light, a mixture of 98% O_2 and 2% CO_2, was sufficient for maximum oxygenation [VanD99, Robi01].

This study describes a standardized MRI-protocol to investigate tissue oxygenation and oxygenation changes in head and neck tumors as induced by the inhalation of oxygen and carbogen light.

3.2 Basics - BOLD imaging in tumors and T_2^* quantification

This section provides a brief review of the BOLD effect, reviews literature application to investigate the response to breathing gases, with a focus on tumor imaging, and finally illustrates the multi-gradient-echo sequence

The BOLD effect

MR also offers access to the oxygenation of blood and tissue. The underlying contrast mechanism is referred to as blood oxygenation level dependent (BOLD) effect [Oga90a, Oga90b]. It is based on the magnetic properties of hemoglobin - oxygenated hemoglobin is a diamagnetic molecule, while deoxygenated hemoglobin is paramagnetic in nature [Pau36]. This implies a dependency of the bulk susceptibility of blood on its oxygenation level [Wei92]

and, hence, of the phase of its MR signal. Moreover, with decreasing hemoglobin saturation of blood, a reduction of its transverse relaxation rates T_2 [Thu82, Wri91] and T_2* [Chi94, Bart97, Li98] is observed. In principle, these properties can be exploited for a direct assessment of the oxygen saturation of blood [Haac97, Li98].

In tissue, the situation is more complex: Due to its different magnetic susceptibility, the venous intravascular compartment induces microscopic magnetic field gradients that extend beyond the vessel wall. Even if water spins can be considered as stationary, i.e. in the *static dephasing regime*, their resonance frequencies are position-dependent, which leads to signal dephasing and faster transverse relaxation [Oga93, Yab94]. In situations when the diffusion of water molecules through the extravascular field inhomogeneities cannot be neglected, their precession phases depend on their individual trajectories, which in turn causes an additional loss of phase coherence in the extravascular compartment. The overall tissue signal can be considered as the complex sum of intra- and extravascular signals. It depends on the interplay of multiple physiological factors such as hematocrit, venous blood oxygenation, regional blood volume, vessel size and morphology, as well as diffusion and water exchange kinetics. The contributions of the different compartments depend on the used imaging sequence and the main magnetic field strength and can be modelled or analyzed with the aid of different tissue models [Wei94, Ken94, Box95, Zho98, Bau99].

Since its discovery, the BOLD effect has emerged as an important contrast mechanism for functional fMRI, which provides access to the localization of neuronal activity and represents a basic tool for the field of human brain mapping. The underlying physiological mechanism is complicated, but can briefly be summarized as follows: The neuronal activity of a certain brain area leads to a transient increase of regional perfusion. The increased supply of oxygen, however, is not balanced with a commensurate increase of the local oxygen consumption rate [Fox86]. Consequently, this leads to a net increase of oxyhemoglobin in the capillary bed and, hence, to a transient local signal increase in T_2*-weighted imaging. Besides its use for functional studies, the BOLD effect was also exploited to monitor oxygenation changes in the human skeletal muscle [Leb98a, Leb98b] and in other organs such as the kidney [Pra97] or the heart [Wac99].

Respiratory challenges and BOLD MRI in tumors

BOLD signal changes are not only be observed as the result of external paradigms such as visual stimulation or functional task execution, but also in response to the inhalation of hyperoxic and/or hypercapnic gases, as was reported in early papers [Oga90a, Oga90b]. Pure oxygen was proposed as MR contrast agent [Berthezene] and shown that relaxation times of various tissues are altered by pure oxygen [Tad97]. In healthy volunteers, the response of brain tissues and blood flow was assessed for elevated contents of CO_2 [Ros94, Ros00] or O_2 [Wat00, Pel02, Weig00a, Weig00b].

In the context of tumor imaging, the signal response to a combination of both, the administration of carbogen gas, is of particular interest, since the latter represents a promising option to enhance the sensitivity to irradiation (see section 1.3). Various studies investigated the response of rodent tumor models to oxygen or carbogen breathing [Robi95, Howe96, Robi97, Al-H98, Howe99, Robi99, VanD99, Al-H00, Robi00, Howe01, Robi01, Al-H02, Baud02, Dunn02, Robi03, Baud03]. Results were heterogeneous - ranging from

considerable signal increases on T_2*-weighted images or prolonged quantitative T_2* values, both consistent with improved blood flow and oxygenation, to an absence of any significant changes during carbogen breathing.

A signal response observed in conventional T_2*-weighted gradient echo images may not only result from changes in hemoglobin saturation, but also from changes in flow [Men93, Duyn94, Kim94]. Since in tumors, this might include physiological effects that are different to those responsible for BOLD effects in cerebral tissue, some investigators introduced the term “flow and oxygenation dependent” (FLOOD) contrast [Robi99, Howe99, Howe01]. Others, however, employed T_2* quantification instead of T_2*-weighted imaging, given this parameter is rather insensitive to changes in blood flow [Lebon98]. Moreover, it was found in an animal study that cerebral T_2* responses showed direct correlation to variations in the deoxyhemoglobin concentration as measured with near infrared spectroscopy (NIRS) [Pun98]. Moreover, in a study on rat tumors, Al-Hallaq et al. reported a close correlation between T_2* alterations caused by carbogen breathing and oxygenation, determined with microelectrodes [Al-H98].

Multi-gradient-echo (MGE) sequences and quantification of T_2*

A quantification of T_2* is typically accomplished with a multi-gradient-echo sequence, which essentially represents an extension of the gradient-echo concept. In this technique, an alternating read gradient is used so that a train of multiple echoes is generated at different echo times [Men93, Chen96]. Typically, only the odd echoes under a positive readout gradient are acquired, which helps to avoid echo shifting problems associated with inhomogeneities of the main magnetic field [Rei97]. In this approach, the echo distances ΔTE can be reduced by playing out the negative gradient lobes with higher amplitude and shorter duration, as shown in Fig. 3.1.

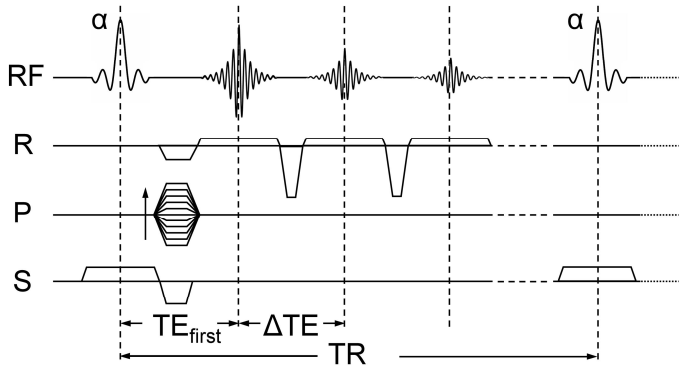

Fig. 3.1: Multi-gradient-echo sequence: An alternating readout gradient is used to generate a train of multiple gradient echoes

A multi-gradient-echo acquisition results in a series of images at different echo times. From this series, a T_2* map of the object can be calculated by fitting the data to an mono-exponential curve on a pixel-by-pixel basis:

$$S(TE) = S_0 \exp(- TE / T_2^*) \quad . \tag{3.1}$$

3.3 Methods

A total of 14 patients (12 male, 2 female, mean age 58 ± 8 years) with histologically proven head and neck carcinoma with or without lymphatic node metastases were included in the study. The MR examinations were performed on a clinical MR scanner at 1.5T (MAGNETOM Vision, Siemens AG, Healthcare Sector, Erlangen, Germany), using the standard neck coil of the system. During the examination, different breathing gases (air, carbogen light, oxygen) were administered via a soft face mask system (B+P Beatmungsprodukte GmbH, Neunkirchen-Seelscheid, Germany). A continuous gas flow of 15l/min and an elastic reservoir bag with a volume of 2l ensured sufficient breathing gas supply, and separate in/out valves prevented re-breathing of exhaled gas. During the MR exam, the mask was attached with elastic straps and additionally fixed in place by the frame of the RF coil.

Prior to the actual examination, the homogeneity of the main magnetic field was optimized using the 3D shim routine provided with the scanner. Localizer images that encompassed the whole lesion were acquired using a T_1-weighted multi-slice TSE acquisition (TE = 14ms, TR = 500ms).

During this setup and preparation phase, room air was administered through the breathing mask. Over the course of the actual experiment, breathing gases were supplied according to the following scheme: air (3min), carbogen light (5min), air (4min), and oxygen (4min). An MGE sequence was used for quantification of the apparent transverse relaxation time T_2*. An axial slice was positioned through the center of the lesion, and a series of 32 acquisitions was conducted, each lasting 30s. Further imaging parameters were: Flip angle = 25°, N_{Echoes} = 8, ΔTE = 12ms, TR = 110ms, matrix = 256^2, FOV = (192x192)mm^2, slice thickness = 8mm, spatial resolution = (0.75x0.75)mm^2.

In the localizer images, regions of interest (ROIs) were drawn which encompassed the lesion. The tumor volume was estimated from the total number of pixels obtained over all slices. In the MGE data, T_2* values were calculated for each scan on a pixel-by-pixel basis by fitting the signal intensities to a mono-exponential decay as given in Eq. 3.1. The first 2min after changing the breathing gas were considered as transition time and the respective data were discarded from further post-processing. For the individual breathing periods, the characteristic T_2* results were calculated by averaging over the values obtained after these transition phases. Color-encoded maps were generated for visualizing the spatial distributions of T_2* values and of corresponding changes.

3.4 Results

Thirteen of fourteen patients (12m, 1f) with a total of 16 lesions were successfully studied. In one patient, the examination had to be aborted because of claustrophobia in the magnet bore. All other patients finished without side effects or expression of discomfort. Except for a single case with stage T2, all primary tumor stages were T3 or T4. Twelve of thirteen patients had macroscopic lymph node involvement. MRI measurements were obtained from primary tumor in seven, from both PT and lymphatic nodes in three and from cervical nodes alone in other three patients. An overview of the successfully investigated tumors and lesion locations is provided in Table 3.1.

#	PT type	Site of PT	Stage	Lesion
1	SCC	Base of tongue	cT2 cN3	Node
2	SCC	Oropharynx / Hypopharynx	cT3-4 cN3	PT / Node
3	SCC	Oropharynx	cT4c N2b	PT
4	SCC	Base of tongue	cT4 cN2c	PT / Node
5	SCC	**Larynx** / Hypopharynx	cT4 cN2b	PT
6	SCC	Larynx	cT3 cN0	PT
7	SCC	Base of tongue	cT4 cN2a	Node
8	SCC	Hypopharynx	cT4 cN2c	Node
9	SCC	Oropharynx / Base of tongue	cT4 N2c	PT / Node
10	SCC	Hypopharynx	cT4c N2b	PT
11	Adenoid-cystic Ca.	Nasal Sinus / Nasopharynx	cT4c N0	PT
12	SCC	Oropharynx	cT4 cN2b	PT
13	SCC	Nasopharynx	cT2 cN2b	PT

Table 3.1: Characteristics of investigated patients and lesions (primary tumor (PT) or lymphatic node); SCC (squamous cell carcinoma)

An analysis of the T_2* maps revealed considerable spatial differences. Inter- and particularly intratumoral tissue signal changes suggesting oxygenation effects were heterogeneous for both breathing gases, carbogen light and oxygen. A pixel-by-pixel analysis of the T_2* values within the tumors, sampled at equilibrium before and after change of the breathing gases, showed a shift towards higher values, consistent with an increased oxygenation. This finding correlated with a median shift towards positive values for ΔT_2* under carbogen light and oxygen in most but not all patients (data shown in Table 3.2). Any changes induced by carbogen light breathing were reversible, i.e. the T_2* time courses reached their baseline level again during the subsequent period using air breathing.

While the changes in median T_2* were consistent, no statistically significant change for the median or mean ΔT_2* was seen. Moreover, while there was a trend for higher T_2*-values during pure oxygen breathing, no significant differences for changes of mean T_2* values or mean ΔT_2* values were found between carbogen light or oxygen. However, heterogeneity in T_2* within the tumor was larger under oxygen breathing, as represented by the standard deviation of the mean ΔT_2* in the individual patients derived from the pixel by pixel analysis (data shown in Table 2). In Figs. 3.2 and 3.3, ΔT_2* maps and T_2*/ΔT_2* histograms are displayed for patient 5 and patient 11, respectively. While patient 5 shows a strong response in the tumor region, such a marked signal change is not observable in patient 11.

In Fig. 3.4, a scatter plot is shown for the ΔT_2* standard deviations for carbogen light and oxygen on a patient per patient base. There was a statistically significant ($p = 0.0016$; t-

student test) difference between T_2* changes induced by the two different breathing gases. This finding suggests that in the studied tumors oxygenation changes induced by carbogen light are spatially less heterogeneous than those induced by oxygen.

Patient	Node / PT	Air	Carbogen		O_2	
		T_2*	ΔT_2*	Median ΔT_2*	ΔT_2*	Median ΔT_2*
1	node	37.5 ± 8.8	3.2 ± 5.0	3.4	1.0 ± 8.7	1.7
2	PT	27.1 ± 5.9	1.1 ± 3.6	1.7	2.8 ± 4.9	2.4
2	node	37.7 ± 9.5	2.2 ± 2.6	2.3	1.0 ± 3.6	1.3
3	PT	52.3 ± 10.9	-0.4 ± 4.9	-0.5	-1.1 ± 5.7	-1.1
4	PT	49.0 ± 7.8	-2.2 ± 5.8	-2.5	0.3 ± 6.8	-0.6
4	node	50.3 ± 11.0	0.7 ± 5.6	0.7	1.7 ± 11.0	1.7
5	PT	38.9 ± 15.8	4.3 ± 6.0	5.5	3.3 ± 7.0	4.5
6	PT	35.9 ± 9.2	-1.4 ± 6.9	-2.2	1.7 ± 7.6	1.1
7	node	40.8 ± 6.7	4.0 ± 6.7	4.4	8.4 ± 19.3	5.1
8	node	45.4 ± 13.7	-0.5 ± 4.0	-0.2	1.5 ± 6.2	1.4
9	PT	33.3 ± 5.9	0.0 ± 3.8	0.3	0.9 ± 5.1	1.0
9	node	45.7 ± 9.5	-0.3 ± 2.9	-0.2	1.2 ± 6.4	1.0
10	PT	42.3 ± 13.7	-1.5 ± 7.4	-1.6	2.2 ± 11.5	1.1
11	PT	27.4 ± 12.1	0.9 ± 4.6	0.6	-1.5 ± 9.8	-1.7
12	PT	32.9 ± 8.6	-0.1 ± 4.9	-0.4	0.8 ± 7.2	0.1
13	PT	31.5 ± 12.5	-0.3 ± 2.1	-0.2	-1.0 ± 3.2	-1.2

Table 3.2: ΔT_2* values with SD and median ΔT_2* values breathing carbogen light or oxygen in primary tumors or lymphatic nodes in patients investigated.

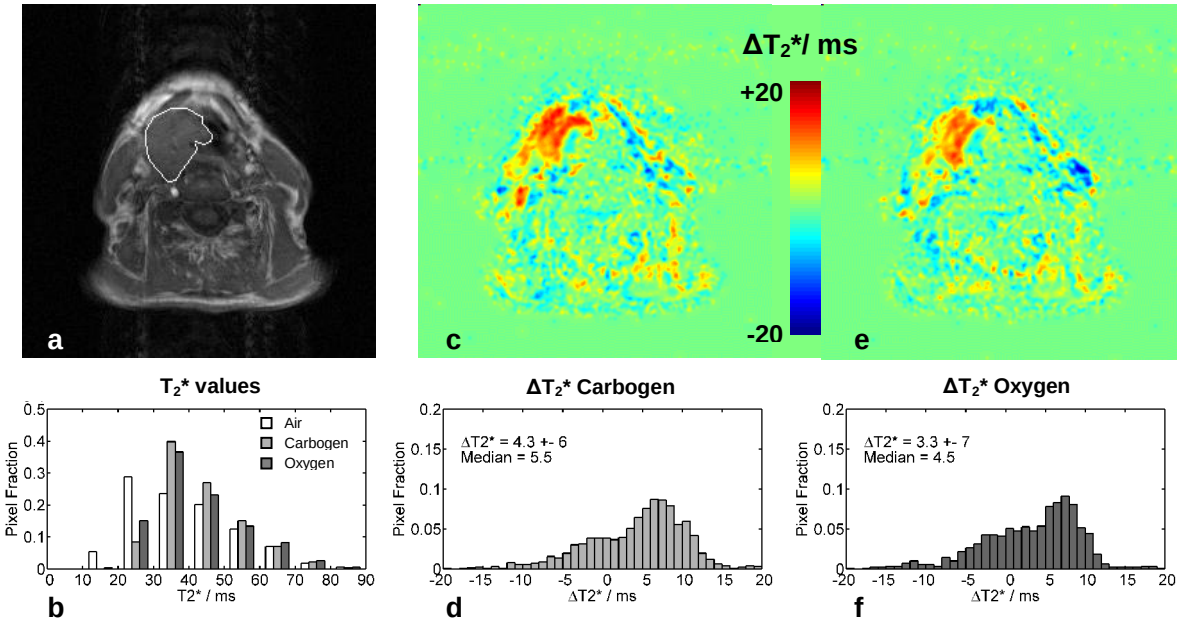

Fig. 3.2: Patient #5 (with Larynx/hypopharynx carcinoma) showing strong response; (a) Segmented tumor on TSE localizer image; (b) distribution (in % of pixels) of T_2* values under air, carbogen, and oxygen breathing; (c,e) ΔT_2* maps for carbogen/oxygen breathing, and (d,f) corresponding distributions of ΔT_2* values (also in % of pixels).

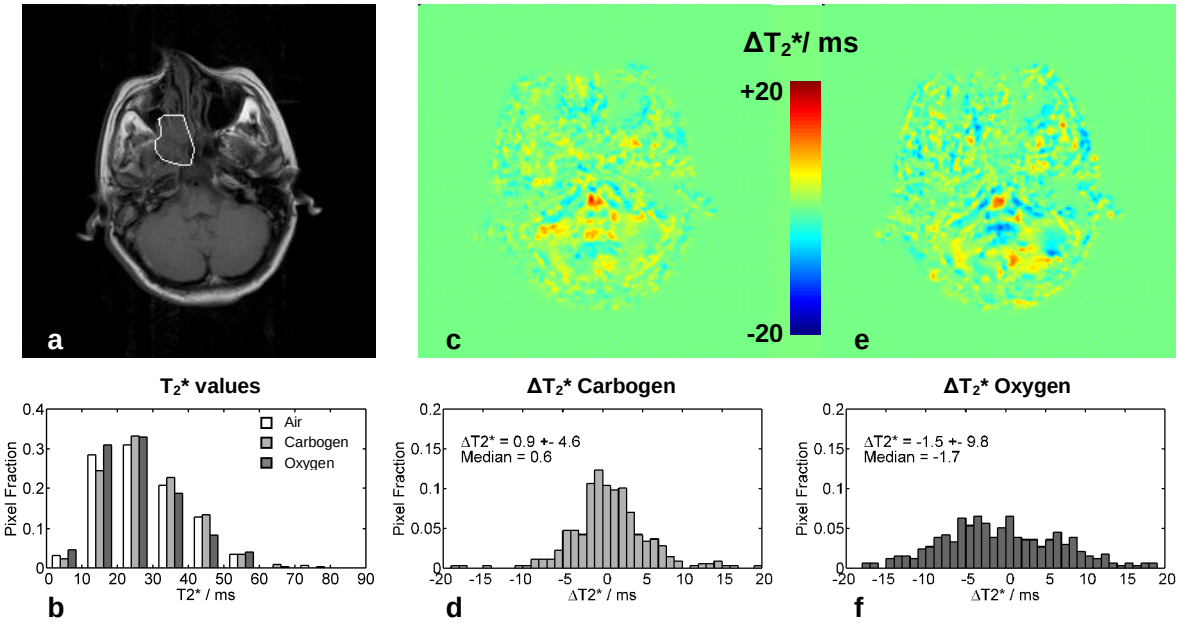

Fig. 3.3: Patient #11 (with nasal sinus/nasopharynx carcinoma) showing weak response; (a) Segmented tumor on TSE localizer image; (b) distribution (in % of pixels) of T_2* values under air, carbogen, and oxygen breathing; (c,e) ΔT_2* maps for carbogen/oxygen breathing, and (d,f) corresponding distributions of ΔT_2* values (also in % of pixels).

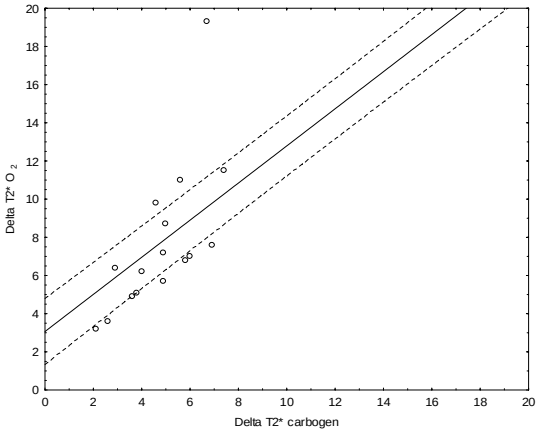

Fig. 3.4: Scatter plot of ΔT_2* standard deviations for carbogen light or oxygen breathing.

3.5 Discussion

The majority of studies that attempt to assess oxygenation or oxygenation changes to characterize tumor tissue are using non-MR methods. These include positron emission tomography (PET), optical approaches and polarographic needle electrode techniques [Milo04]. The latter represent the broadly accepted gold standard for in vivo measurements of tumor tissue oxygenation. It was applied in experimental tumor models and patients. A good correlation was found between the hypoxic tumor fraction and radiotherapy outcome in cervix carcinoma and head and neck tumors [Fyl98, Bri99, Kno99, Lyng99]. Despite its reliability, this procedure has several drawbacks. It is invasive, causing pain to the patient and tissue injury at the sites of electrode insertion. The injury and probable bleeding may result in a perturbation of the tissue pO_2. Its use is limited to accessible areas which can tolerate multiple needle punctures, so that it might be difficult to evaluate small lesions. The length of the probe and the necessary insertion limit the size of the tumor or lymphatic node to be investigated..

The presented MRI technique offers the capability to monitor oxygenation changes in tumors completely non-invasively, with high spatial and temporal resolution. The total exam time amounted to 30-45 minutes, which was tolerated well by the examined patients. It can be easily repeated and since it is non-invasive, the risks of bleeding, infection and pain associated with pO_2 histography are avoided.

This study has been the first to assess oxygenation changes for both oxygen and carbogen in tumor patients with MR imaging and to describe a statistically significant difference between the intratumoral responses induced by the two different gases. It is presumed that tumor oxygenation and carbogen response depend at least partly on perfusion and its changes. Due to differences in vascular density, relative proportions of perfused and necrotic areas, regions of tumor show varying responses to carbogen- or oxygen-breathing [Dunn02]. High oxygen concentrations may lead to vasoconstriction in host vessels and thereby change perfusion patterns. This phenomenon may explain the marked spatial heterogeneity of T_2* changes seen in the present study and is probably at least partly counterbalanced by the addition of CO_2. A more detailed analysis of these interconnections could be achieved by combining oxygenation-sensitive MR acquisitions with methods that are sensitive to tissue perfusion, e.g. spin labelling techniques. Nevertheless, the method used in the present study is qualitative in nature, i.e. an absolute measure of pO_2 is not obtained. Such estimates would have to be based on complex tissue models, and besides blood flow, additional

quantities such as regional blood volume, vessel size or density, and diffusion coefficients might be required.

While the study was prepared and conducted, other reports were published that explored the effect of carbogen light on different types of tumors in patients, and combined T_2* quantification with dynamic contrast-enhanced MRI. In a study on patients with head and neck tumors, a significant T_2* increase was found in seven of 11 cases, but no changes in tumor blood flow or vascularity was observed [Rij02]. Another study found improved tumor blood oxygenation in 6 out of 10 meningioma patients, and correlations between T_2* and contrast uptake rate [Rij04]. Well-perfused tumors tended to show reduction of both T_2* and uptake rate in response to hypercapnic hyperoxia.

Several clinical studies tried to improve tumor oxygenation by offering a hyperoxic hypercapnic gas mixture like carbogen parallel with vasoactive drugs like nicotinamide. Particularly in head and neck tumors, a number of phase I and II studies have shown the feasibility and tolerability of this strategy. Promising results have been reported and phase III studies are underway (review in [Kaa02]). In these trials, a positive overall effect on treatment outcome has been reported. For unselected groups of patients with locally advanced head and neck tumors, however, a lack of significant improvement in clinical outcome was observed [Kaa02]. The importance of an individualized approach is highlighted by the heterogeneous and in some patients paradox effect seen in the presented data and in the imaging studies discussed earlier. Non-invasive techniques for monitoring of tissue oxygenation and oxygenation changes might be useful to select patients that show a positive response to breathing hyperoxic hypercapnic gas mixtures.

3.6 Conclusion and retrospect

With the presented MRI technique, the demonstration of oxygenation changes in head and neck tumor patients is feasible. Tumor oxygenation and oxygenation changes were heterogeneous both inter- and intraindividually among a group of patients with advanced head and neck cancer. This effect is smaller for breathing of carbogen light in comparison to pure oxygen. Corresponding prospective clinical trials would be warranted to examine the prognostic value of the presented MRI technique and a possible benefit in terms of a preselection of patients.

Since this study was carried out, a range of publications appeared that added more information to this field of research. In an experimental study in two different tumor lines in mice, a correlation was found between changes of T_2* and irradiation efficiency as induced by carbogen breathing. In the tumors that had a shorter baseline T_2* and showed a strong response with carbogen, the administration of carbogen during irradiation showed to improve the therapeutic response significantly. In the tumors with a longer T_2* and negligible T_2* changes, only small growth inhibition was achieved with carbogen [Rod2004]. In studies on patients with prostate carcinoma, the observed responses were very heterogeneous. While Alonzi et al. reported that 64% of the examined patients showed positive T_2* response during carbogen, Diergarten et al. noticed in their data that enhancements in carcinoma were lower than those in normal prostate tissue, which might also be attributed to steal effect [Die05].

An exciting area of research is the recent development of a quantitative BOLD approach. It requires multiple separate measurements of tissue features that influence T_2*, including T_2 and regional blood volume fraction, which was determined from measurements before and after the injection of a *USPIO* contrast agent (ultrasmall super-paramagnetic iron oxide). If these data are combined according to a dedicated mathematic model, the quantitative mapping of blood oxygen saturation in tumors becomes possible [Chr11, Chr12].

For a more detailed understanding of the connection between observed phenomena and physiology, it should be useful to correlate non-invasive tumor imaging approaches with endogeneous tumor markers and functional imaging [Zips07]. For instance, markers such as HIF-1α have high potential as predictors of clinical outcome [Del08]. In this context, a multi-institutional research project to evaluate the impact of hypoxia and the metabolic microenvironment on radiotherapy of solid tumors has been introduced [Zips04]. It applies different imaging techniques including MR imaging and spectroscopy, metabolic mapping, histological multiparameter analysis of biochemical hypoxia, perfusion and vasculature and immunohistochemistry of factors related to angiogenesis, invasion and metastases. As part of this study, it was demonstrated that pretreatment lactate concentration and T_2* response to carbogen represented predictive markers independent from pathophysiological changes induced during fractionated irradiation [Mör10].

Chapter 4

A simple geometrical description of the TrueFISP signal

In this chapter, a pictorial approach is presented for describing the TrueFISP transient phase and steady state signal. It is based on simple geometrical considerations, without the need for an abstract mathematical treatment. Brief formulations are derived that define the direction of the magnetization vector for which a smooth exponential decay is obtained even at considerable off-resonance frequencies. Analytic expressions are developed that describe the signal evolution as a function of T_1, T_2, flip angle and frequency offset. The theory is verified by numerical simulations and MR experiments. This chapter reflects the contents of a corresponding peer-reviewed journal article [Schm06].

4.1 Introduction

The TrueFISP MR sequence is commonly referred to as a steady state imaging technique. However, useful information may also be obtained from TrueFISP-based signal acquired under non-steady-state conditions. It was described early that initial samples can be associated with prominent signal fluctuations [Patz89], and that a simple a/2 preparation scheme can help to reduce unwanted oscillations [Deim94]. In this context, an inversion-prepared TrueFISP acquisition had been proposed for rapid T_1-weighted imaging [Deim94]. This principle later gained renewed interest and was presented as a promising tool for fast relaxometry. In analogy to the IR snapshot FLASH technique (described in section 2.2), a TrueFISP image series was acquired after preparation with an inversion pulse, and the observed signal intensities were reported to follow the free longitudinal relaxation curve very closely, even at high flip angles of 50° [Sche01a].

Own attempts to reproduce these results and to utilize such an IR TrueFISP sequence for T_1 quantification yielded contradictory results. With both numerical simulations and phantom experiments, it was also found that the signal recovery during a TrueFISP acquisition can be described by mono-exponential behavior. The signal evolution, however, showed not to be solely dependent on T_1. Instead, apparent relaxation times T_1^* were observed that strongly depended on the flip angle and on both T_1 and T_2 [Schm02].

While a matrix-based treatment of the transient signal was used as a tool for designing elaborate sequence preparation schemes [Har01], a corresponding description of the achievable signal time course that also included off-resonance effects was not available. The discrepancy between literature and own results and the lack of a theoretical explanation generated the motivation to embark on a more detailed analysis of the transient signal behavior in TrueFISP acquisitions. Beforehand - given that the TrueFISP sequence represents the basis for several methodological developments presented in this thesis - some basic aspects of the technique are illuminated in the next section.

4.2 Basics - the TrueFISP technique

The sequence

Technically, the TrueFISP sequence (also referred to as balanced or fully-refocused SSFP, balanced FFE or FIESTA) can be considered as a specific derivate of FLASH. As illustrated in Fig. 4.1, rephasing gradients are added in all spatial directions and RF pulses are applied with alternating phase. It provides the capability of rapid imaging while preserving a high SNR efficiency, in particular for compartments with a high T_2/T_1 ratio.

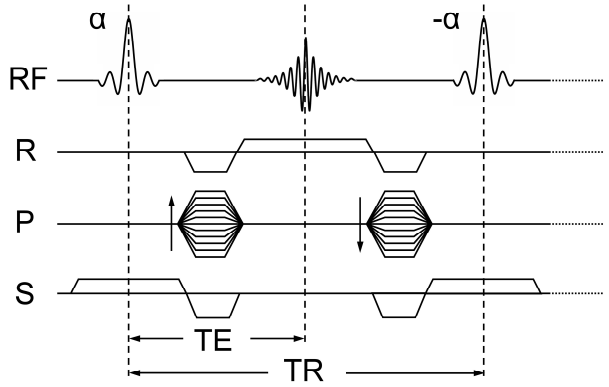

Fig. 4.1: The TrueFISP sequence: In each encoding direction, the net gradient integral amounts to a value of zero. Typically, the RF pulses are applied with alter phase, and the echo time is chosen as $TE = TR/2$.

The TrueFISP technique represents the imaging analogue of the SSFP principle initially described by Carr. In his early paper, contrary to preceding work on FIDs and echoes, a series of closely spaced RF pulses was applied. For the first time, it was recognized as important that “the oscillating RF field be phase coherent from pulse to pulse” [Carr58]. The TrueFISP sequence was first proposed in the mid-eighties, originally named FISP (Fast Imaging in Steady Precession) [Opp86]. For a considerable time span, its use was hampered by insufficient hardware capabilities [Zur88, Henn91b] but thanks to technical advances in magnet design as well as gradient and receiver performance, the TrueFISP was ‘remembered’ [Due98] and has since then generated much renewed interest for various applications.

The steady state signal

In the TrueFISP sequence, the net integrals of all gradients within a *TR* cycle are zero and ideally, no position-dependent dephasing takes place. Thus, it is appropriate to describe a certain isochromat by a single vector so that the theoretical analysis of the TrueFISP signal is

rather straightforward in comparison to that of spoiled SSFP or multi-spin-echo sequences. Usually, signal calculations are performed by means of a matrix formalism, which was introduced as an early tool for the assessment of the signal behavior in periodic pulse sequences [Jay55]. With its use, an analytic expression can be derived for the steady state signal of TrueFISP sequences. It is a complex function of the parameters involved (T_1, T_2, M_0, TR, flip angle and frequency offset) [Ern66, Fre71, Kai74, Hin76, Sek87, Zur88, Zur90, Haac90, Haac99], here expressed for sequences with alternating RF phase:

$$S_{ststst} = \frac{M_0(1- E_1)\sin a\sqrt{1+E_2^2+2E_2\cos f}}{(1- E_1\cos a)(1+E_2\cos f) - (E_1 - \cos a)(E_2+\cos f)E_2}. \qquad (4.1)$$

In this expression, the frequency offset of the considered isochromat is expressed by the *off-resonance angle* f which indicates the extent of the dephasing process in the rotating frame over the complete TR interval (i.e. the rotation around the z axis). Relaxation is included as $E_{1,2} = \exp(-TR/T_{1,2})$. For on-resonant isochromats and for $TR << T_{1,2}$, the formula can be reduced to [Hin76, Zur88, Haac90, Haac99]:

$$S_{ststst} = \frac{M_0 \sin a}{(T_1/T_2+1) - \cos a\times(T_1/T_2 - 1)}. \qquad (4.2)$$

This result reflects the often-cited dependence of the TrueFISP steady state signal on the ratio T_2/T_1. For a fixed flip angle a, the steady state signal is an increasing function of the ratio T_2/T_1, so that high signal is obtained from fluid compartments with a long T_2. In tissue with specific values of T_1 and T_2, maximum signal is obtained for a flip angle that fulfills the following condition [Opp86, Haac99, Sche03c]:

$$\cos(a_{opt}) = \frac{T_1/T_2 - 1}{T_1/T_2 + 1}. \qquad (4.3)$$

Commonly, comparatively high flip angles between 50° and 70° are used. The optimum angle is generally higher than the Ernst angle of a FLASH sequence with same TR, but it can reduce to about 30° in brain matter with $T_2/T_1 \approx 0.1$. For $T_2 = T_1$ and a = 90°, a maximum signal of $M_0/2$ is achieved - which is a remarkable value given that it is continually available even at shortest TR values as long as the steady state is conserved.

The combination of its speed, high SNR efficiency and a good contrast between fluids and other tissues renders the technique beneficial for various applications such as the evaluation of cardiac function [Bark01, Carr01] and perfusion [Schr01, Fen04] or coronary angiography [Des01, Spu02]. Due to a poor image contrast between gray and white matter and a low conspicuity of neurological lesions, however, TrueFISP images were rated as not well-suited for examination of the human brain [Sche03c].

Influence of frequency offsets

An important property of the TrueFISP technique is its sensitivity to off-resonances. Following Eq. 4.1, the steady state signal tends towards zero if the dephasing angle approximates odd multiples of p. In TrueFISP images, regions at corresponding frequency offsets appear as dark banding artifacts. Thus, while the sensitivity to off-resonances can be minimized by

choosing *TR* as short as possible, the reduction of B_0 field inhomogeneities (shim) is of particular importance in TrueFISP applications.

As a particular property of TrueFISP, the phase of the steady state signal is almost constant within the individual transmission bands, while adjacent bands show opposite signal phase. Evidently, the TrueFISP sequence reveals refocusing properties similar to those of spin-echo sequences and, as a consequence, it can be beneficial if an echo time of *TE* = *TR*/2 is used [Sche03a].

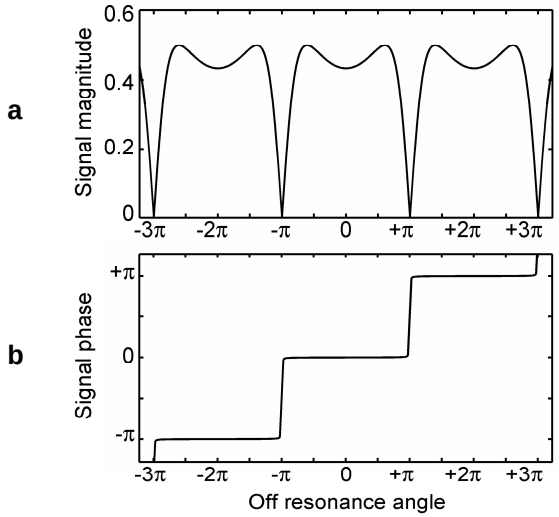

FIG. 4.2: The TrueFISP steady state signal response: (a) magnitude and (b) phase of the signal as a function of the off-resonance angle f, here simulated for $T_1 = T_2 = 1000$ ms, *TR* = 6 ms and a = 60°. The signal phase is depicted as a monotonously increasing function. Phases of -p and +p, however, can be considered equivalent.

Sequence preparation

In a TrueFISP acquisition, the magnetization reaches its steady state after a certain transition period. Without appropriate magnetization preparation, the transient signal can be characterized by strong fluctuations and, consequently, be not useful for imaging. A common technique for preventing these signal oscillations is to apply an additional RF pulse with flip angle -a/2, preceding the imaging sequence at a time *TR*/2 before the first a pulse [Deim94]. With this approach, a smoother transition towards the steady state can be achieved and the signal stemming from early *TR* intervals may be used for filling of k-space.

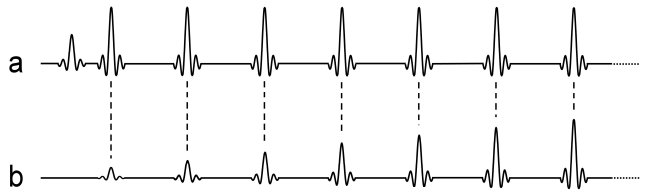

FIG. 4.3: TrueFISP preparation schemes: (a) a/2 prepulse, (b) Series of pulses with linearly increasing flip angle

While the a/2 pre-pulse is ideally suited for magnetization at Larmor frequency, it is less efficient with increasing off-resonance, and it fails completely for off-resonant signal bands with opposite signal phase. Alternative preparation schemes have been developed that help to avoid initial signal fluctuations even for off-resonant magnetization. As a general rule, these solutions require the application of more than a single preparing RF pulse. A frequently used approach is to play out a series of pulses with linearly increasing flip angles [Nis00, Des03].

Other more elaborate preparation schemes were presented such as the solution proposed by Hargreaves et al., who used the Shinnar-LeRoux (SLR) algorithm for selective RF pulse design [Pau91] in combination with a preceding magnitude calibration [Har01].

4.3 Theoretical considerations

In the following calculations, RF pulses with alternating phase are considered that flip the magnetization vector ***M*** around the x axis of the rotating frame.

Frequency offset dephasing and the ideal zenith angle

In a TrueFISP sequence, an off-resonant isochromat is driven towards a state in which its precession phase oscillates between approximately -f /2 and +f /2. RF excitations are encountered when these minimum or maximum phase values are reached, and the tip of ***M*** crosses the y-z-plane at a time close to $t = TR/2$ [Patz89, Deim94]. This picture, illustrated in Fig. 4.4, directly explains the spin-echo-like refocusing properties of the TrueFISP technique outlined previously. For the sake of clarity, the effect of relaxation is neglected and a dephasing angle f < p is used but the principles apply to larger off-resonances as well.

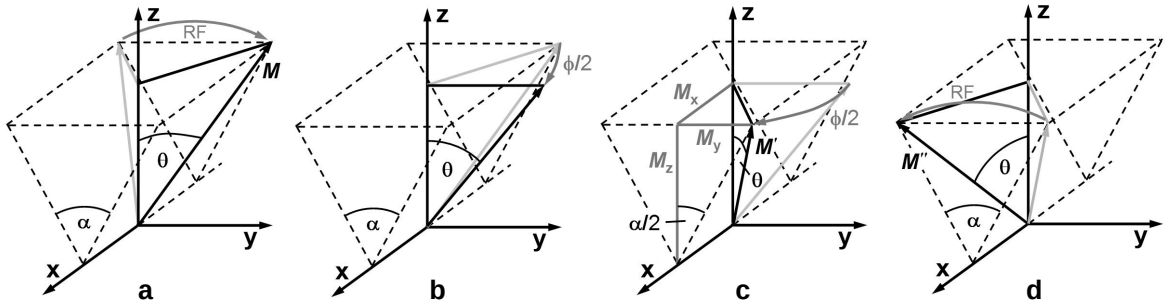

FIG. 4.4: Off-resonant magnetization with benign phase behavior (relaxation neglected)

Just before an a pulse, the tip of the magnetization vector resides on the surface of a wedge with an opening angle a and its vertex being formed by the x axis. By the RF pulse, ***M*** is flipped to the other side of the wedge (a). From here, it starts rotating around the z axis on a circular cone with an inner angle q which remains constant since relaxation is neglected. From this point on, this angle q between the magnetization and the z axis will be referred to as *ideal zenith angle*. After a time *TR*/2, the phase is zero (b), and at the end of the *TR* cycle, the vector ***M'*** is located where the q cone crosses the a wedge again (c). Now, the magnetization is flipped to the state ***M''***, a position equivalent to ***M*** but with opposite phase (d). For times directly before or after the RF pulses, the following geometrical relationships can easily be extracted from Fig. 4.4:

$$\tan(a/2) = \frac{M_y}{M_z}\ , \tag{4.4}$$

$$\cos(f/2) = \frac{M_y}{M_\wedge}\ . \tag{4.5}$$

Here, $M_\wedge$ is the length of the transverse component of ***M***. The ideal zenith angle q is defined by both the longitudinal and transverse component of ***M*** and can thus be expressed as a function of the flip angle and the off-resonance dephasing angle f :

$$\tan(q) = \frac{M_\wedge}{M_z} = \frac{\tan(a/2)}{\cos(f/2)} \quad . \tag{4.6}$$

In the on-resonant case (or for f = ±2p, ±4p, ...etc.), q is equal to a/2, and for a dephasing angle of f = ±p, ±3p, …etc., it approaches a value of 90°, independently of the flip angle.

The TrueFISP signal phase

If both longitudinal and transverse relaxation processes are considered, a slight asymmetry of the dephasing trajectory is observed. This is explained in Fig. 4.5, where the dynamics of ***M*** are sketched as projections in the x-y-plane. Here, relaxation is neglected as before, corresponding to the symmetric course of Fig. 4.4. If relaxation is included, as illustrated with exaggerated appearance in Fig. 4.5b, the longitudinal component M_z increases between RF pulses (not visible directly in this diagram) while the transverse component $M_\wedge$ decreases, leading to a slightly distorted trajectory.

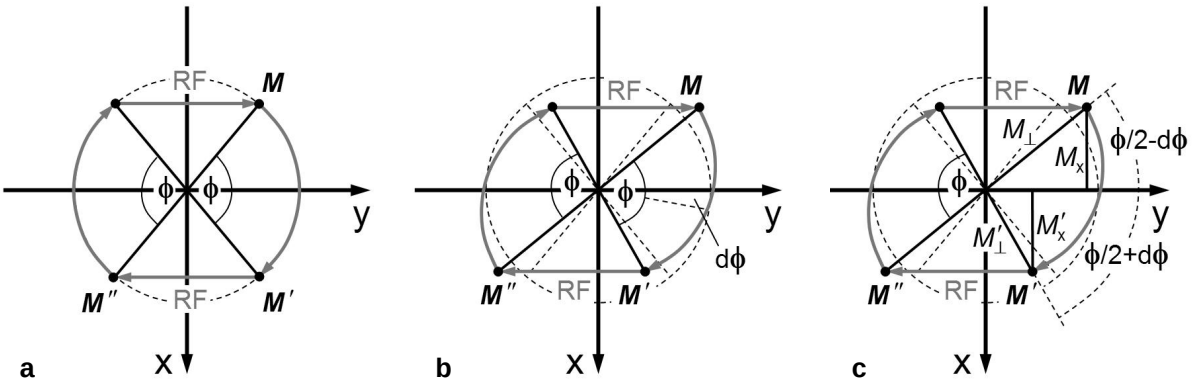

FIG. 4.5: Off-resonant magnetization in the transverse plane with benign phase behavior: (a) Relaxation neglected (b) Relaxation included (c) Derivation of the signal phase *d*f

Due to this asymmetric phase behavior, the MR signal exhibits a small phase *d*f if the echo center is acquired at *TE* = *TR*/2. Based on this simple picture, this phase can be calculated easily. During the *TR* cycle, the transverse magnetization component $M_\wedge$ decreases towards a value $M_\wedge' = M_\wedge E_2$, with $E_{1,2} = \exp(-TR/T_{1,2})$. Since the state ***M"*** should be equivalent to ***M*** and the RF pulses should not change the x component, it can be assumed that $M_x' = -M_x$. According to Fig. 4.5c, the following relations can directly be extracted:

$$\sin(f/2 - df) = \frac{|M_x|}{M_\wedge} \quad , \tag{4.7}$$

$$\sin(f/2 + df) = \frac{|M_x|}{M_\wedge E_2} \quad . \tag{4.8}$$

Combining these two equations yields:

$$\tan(d\varphi) = \frac{1 - E_2}{1 + E_2} \tan(\varphi / 2) \ . \qquad (4.9)$$

Again, this formulation was derived for $\varphi < \pi$, but a general solution is obtained for $d\varphi$ if the resultant arctangent term is solved to yield values of $-\pi < d\varphi < \pi$. The signal phase is close to zero for a wide range of frequencies, reflecting the refocusing properties of the TrueFISP sequence [Sche03a] even when relaxation is considered. Evidently, $d\varphi$ is a function of TR, T_2 and the off-resonance angle φ, but it is independent of T_1 and the flip angle.

The direction of the steady state magnetization at a time $t = TR/2$ is determined by the zenith angle given in Eq. 4.6 and the phase defined in Eq. 4.9. This direction is of particular importance for obtaining smooth signal evolution, as will be discussed later. From here on, if the dephasing process takes place approximately as discussed, the magnetization will be described as showing *benign phase behavior*. It is observed not only in the steady state but may also be achieved during the transient phase, with the length of $\boldsymbol{M}$ evolving towards its steady state value.

Relaxation in the magnetization vector plane

In the following analysis, the evolution of $\boldsymbol{M}$ is separated into dephasing, relaxation and RF influence. This is accomplished by using a two-dimensional coordinate system where the magnitude of the transverse magnetization component $M_\perp$ is assigned to the abscissa and the longitudinal component M_z is shown on the ordinate. This coordinate frame corresponds to the plane defined by the z axis and the tip of the magnetization vector, i.e. it "follows" the direction of $\boldsymbol{M}$ and will thus be referred to as the *magnetization vector plane*.

With relaxation between successive pulses included, both the actual zenith angle and the length of $\boldsymbol{M}$ change during the TR interval, since T_1 relaxation leads to an increase of M_z while T_2 relaxation causes a decrease of $M_\perp$. This situation is illustrated schematically in Fig. 4.6a. For $TR << T_{1,2}$, it is appropriate to assume that the change $\Delta\boldsymbol{M}$ is small compared to the length of $\boldsymbol{M}$, with respective components ΔM_z and $\Delta M_\perp$ which depend on the relaxation times as well as on the actual values of M_z and $M_\perp$. According to the Bloch equations, with $M_0 = 1$, these changes can be written as

$$\Delta M_z = M_z' - M_z = M_0 - E_1(M_0 - M_z) - M_z = (1 - E_1)(M_0 - M_z) \qquad (4.10)$$

and

$$\Delta M_\perp = M_\perp' - M_\perp = M_\perp E_2 - M_\perp = M_\perp (E_2 - 1) \ . \qquad (4.11)$$

RF pulses and magnetization at Larmor frequency

As a first step, the influence of RF pulses is evaluated for on-resonant magnetization for which the M_x component stays zero and $M_\perp$ equals $|M_y|$. If a magnetization vector $\boldsymbol{M'}$ right before the following RF excitation is considered with an arbitrary angle ψ to the z axis, the α pulse causes a rotation of $\boldsymbol{M'}$ onto the z axis and, since the quantity $M_\perp$ is always positive, a subsequent backward rotation over an angle $|\alpha - \psi|$. As shown in Fig. 4.6b, this corresponds to a rotation of $\boldsymbol{M'}$ over an angle $2|\psi - \alpha/2|$ towards the line where $\psi = \theta = \alpha/2$, i.e. the tip of the magnetization after the pulse (named $\boldsymbol{M''}$) is obtained by mirroring the tip of $\boldsymbol{M'}$ across the line defined by the angle θ, so that the change $\Delta\boldsymbol{M}_{RF}$ is perpendicular to this direction.

Generally, the application of an RF pulse train with alternating phase can result in fluctuations of the transverse component of ***M***. With an increasing number of excitations, due to relaxation in between the RF excitations, the situation will tend towards a steady state of the actual angle J. In this state, J continuously decreases from a value J_{max} directly after an a pulse, crosses the value q = a/2 around the center of the *TR* interval and finally reaches a value J_{min}, just before it is flipped back to J_{max} by the next a pulse. Both J_{min} and J_{max} are located symmetrically around q = a/2 - a property determined by the impact of the RF pulses in the magnetization vector plane. For $TR << T_{1,2}$, this periodic deviation from the q cone is small and the magnetization vector evolves closely along the a/2 line. As shown in Fig. 4.6c, this steady state situation for J does not necessarily correspond to the TrueFISP steady state, and the length of ***M*** may still change. Since the echo is usually detected at *TE* = *TR/2* and hence approximately at the angle q, a smooth signal time course can be anticipated.

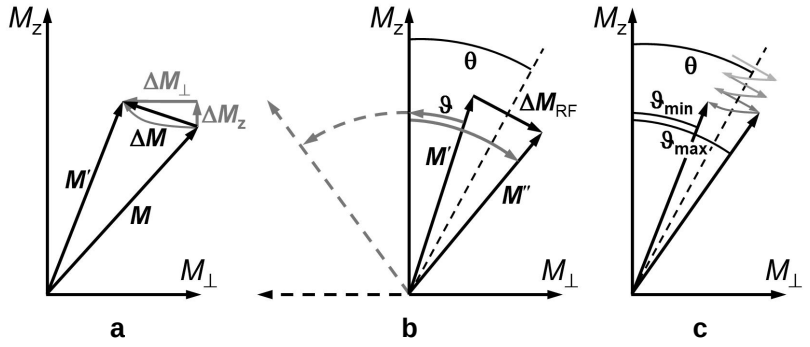

FIG. 4.6: Relaxation and excitation observed in the magnetization vector plane: (a) Influence of relaxation (b) RF pulses cause mirroring of ***M*** across the line defined by q (c) Smooth evolution along the q cone

Off-resonance influence and smooth evolution along the q cone

For off-resonant isochromats which encounter a rotation around the z axis between RF pulses, the situation will tend towards a very similar condition as in the on-resonant case. In close analogy, the RF pulse train drives ***M*** towards a state with the zenith angle J evolving along its steady state value q. This angle is generally not equivalent to a/2, since it also depends on the off-resonance angle according to Eq. 4.6. As soon as ***M*** has reached the q cone and the benign phase condition of Fig. 4.5b and Eq. 4.9 is met, an a pulse has the approximate effect of mirroring ***M*** across the q line in the magnetization vector plane, and the evolution of J is kept balanced close to the q direction by consecutive RF excitations, yielding a signal time course without fluctuations. Thus, Figs. 4.6a-c also describe the off-resonant case in good approximation. This behavior is easily demonstrated with Bloch simulations, as shown later in Fig. 4.8. However, it may also be anticipated directly from Figs. 4.5b, where it is directly visualized that an RF pulse lengthens $M_\wedge$ and M_x, and hence, shortens M_z.

Implications for TrueFISP sequence preparation schemes

The previous section implies that a smooth signal time course can be achieved from the start of the sequence on if, at a time *TR*/2 before the first TrueFISP pulse, the magnetization vector is brought close the steady state direction. This finding is in agreement with previous work on TrueFISP transient phase evolution where the ideal initial direction of ***M*** was defined in abstract manner as the solution of an extensive matrix equation [Har01].

Evidently, for magnetization at Larmor frequency, the a/2 prepulse represents the optimal solution. In off-resonant conditions, ideal preparation is easily accomplished by using a preparation pulse of flip angle q and phase *d*f (results in Fig. 4.11). For simultaneous preparation over a substantial range of different isochromats, however, more time-consuming multi-pulse approaches are required such as those mentioned in section 4.2.

Now, the common goal of these preparation schemes has firstly been formulated with two novel but simple equations: They all aim at placing the magnetization vector approximately into the steady state direction determined by the ideal zenith angle q and phase of Eqs. 4.6 and 4.9. The following treatment is based on the assumption that the magnetization vector is oriented in this direction, resulting in a smooth signal evolution.

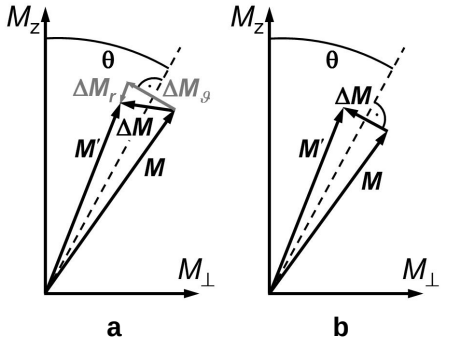

FIG. 4.7: Assessment of the steady state in the magnetization vector plane: (a) Separation of DM into its radial and zenith components DMr and DMJ (b) In the steady state, the condition DMr = 0 is fulfilled

The steady state

For further analysis, it is useful to separate the small change D***M*** caused by relaxation into two components, as depicted in Fig. 4.7a: (1) a change D$\boldsymbol{M}_\vartheta$ in zenith direction which, for |D***M***| << |***M***|, can be assumed to be perpendicular to ***M*** and may also be interpreted as a rotation around the origin in the magnetization vector plane, and (2) the component D$\boldsymbol{M}_r$ in radial direction indicating alterations in the length of ***M***. With $\boldsymbol{e}_M = \boldsymbol{e}_\wedge \sin q + \boldsymbol{e}_z \cos q$ as the unity vector approximately parallel to ***M***, D$\boldsymbol{M}_r$ can be calculated as the projection of D***M*** onto the direction of ***M***:

$$D\boldsymbol{M}_r = (D\boldsymbol{M} \cdot \boldsymbol{e}_M)\,\boldsymbol{e}_M \quad . \tag{4.12}$$

The steady state magnetization can be derived with a simple assumption: When the steady state is reached, the "gain" originating from longitudinal relaxation must counterbalance the "loss" caused by transverse relaxation. Hence, the length of ***M*** at the end of a *TR* interval should be identical to that at the beginning, and the relaxation should result in a directional change only which is compensated by the subsequent RF excitation. As illustrated in Fig. 4.7b, this is the case if D***M*** = D$\boldsymbol{M}_\vartheta$, or equivalently, if D$\boldsymbol{M}_r$ = 0. From this approach, together with Eqs. 4.4-4.6, 4.10 and 4.11, all components of ***M*** can directly be calculated for the steady state, from here on denoted by $\boldsymbol{M}_{stst}$. The following solution is obtained for the transverse component $M_{stst,\wedge}$ which closely approximates the detectable MR signal S_{stst}:

$$M_{stst,\wedge} = S_{stst} = \frac{M_0(1-E_1)\tan(a/2)\cos(f/2)}{(1-E_1)\cos^2(f/2)+(1-E_2)\tan^2(a/2)} \quad . \tag{4.13}$$

Despite its comparative compactness, this expression is a good approximation for the formulation given in Eq. 4.1, and for f = 0 and *TR* << $T_{1,2}$, it also directly collapses to Eq. 4.2.

The transient phase

For assessment of the transient phase of the TrueFISP sequence, it is useful to analyze the vector representing the difference between the actual and the steady state magnetization [Har01]. This can be accomplished using the equation

$$\boldsymbol{M}'' - \boldsymbol{M}_{stst} = \lambda\,(\boldsymbol{M} - \boldsymbol{M}_{stst}) \tag{4.14}$$

which is found in similar form early in the literature [Jay55]. As before, ***M"*** denotes the magnetization vector after relaxation, dephasing *and* RF pulse, i.e. after a complete *TR* cycle. In the general case, λ would have to be replaced by a diagonal matrix ***A*** which is a function of the relaxation and sequence parameters involved [Har01]. For magnetization prepared towards the proper direction, however, an almost purely exponential decay is observed and ***A*** reduces to a real value λ as indicated above. A corresponding apparent relaxation time T_1^* can be calculated according to

$$\lambda = \exp(-T_1^*/TR). \tag{4.15}$$

Following Figs. 4.6 and 4.7, $\Delta\boldsymbol{M}_J$ is compensated by $\Delta\boldsymbol{M}_{RF}$ in the magnetization vector frame due to the impact of the subsequent RF pulse. Thus, it is justified to replace ***M"*** by $\boldsymbol{M} + \Delta\boldsymbol{M}_r$ and Eq. 4.14 reduces to

$$\boldsymbol{M} + \Delta\boldsymbol{M}_r - \boldsymbol{M}_{stst} = \lambda\,(\boldsymbol{M} - \boldsymbol{M}_{stst})\,. \tag{4.16}$$

For the transverse component of $\boldsymbol{M}_{stst}$, the approximation given in Eq. 4.13 can be inserted, and the longitudinal and transverse components of ***M*** and $\boldsymbol{M}_{stst}$, respectively, can be related to each other using Eq. 4.6. Consequently, the equation system represented by Eq. 4.16 can directly be solved for λ. Besides $\lambda = 1$ which describes the trivial case $\boldsymbol{M} = \boldsymbol{M}_{stst}$, the following solution is obtained:

$$\lambda = \frac{\cos^2(\varphi/2)\cdot E_1\cos^2(\alpha/2) + E_2\sin^2(\alpha/2)}{\cos^2(\varphi/2)\cdot\cos^2(\alpha/2) + \sin^2(\alpha/2)}\,. \tag{4.17}$$

With increasing frequency offset, λ decreases and in the extreme limit of $\varphi = \pm\pi$, it tends towards a minimum value of $\lambda = E_2$ (see also Fig. 4.9b in the results section). For the on-resonant condition, Eq. 4.17 reduces to a weighted average of E_1 and E_2 with respective weighting factors which are simple functions of the flip angle:

$$\lambda = E_1\cos^2(\alpha/2) + E_2\sin^2(\alpha/2)\,, \tag{4.18}$$

The ideal signal time course

The findings developed above can be combined to yield an ideal exponential signal time course. With M_0 as the maximal possible signal, the signal decay can be assumed to start at $S(t = 0) = M_0 \sin\theta$, and it will exponentially develop towards the steady state signal. This signal evolution can be expressed as

$$S(t) = S_{stst} + (M_0\sin\theta - S_{stst})\exp(-t/T_1^*)\,, \tag{4.19}$$

where $S_{stst,\wedge}$ can be approximated by Eq. 4.13, the ideal zenith angle θ is defined by Eq. 4.6, and the apparent relaxation time T_1^* can be calculated according to Eqs. 4.15 and 4.17.

4.4 Methods

For verification of the theory and for illustration and visualization of the underlying concepts, numerical simulations based on the Bloch equations were carried out using Matlab (The MathWorks, Natick, MA, USA). The measured signal was modeled for a continuous train of TrueFISP pulses with alternating phase, after preceding preparation with a single RF pulse or with different multi-pulse preparation schemes. Both RF pulses and data acquisition durations were assumed to be infinitesimally short, and various sequence parameters, relaxation times and off-resonance angles was assessed.

Simulation results are shown for T_1 = 1035 ms, T_2 = 92 ms, TR = 5.95 ms, TE = TR/2, and a = 20°, 60°and 100°. These relaxation and acquisition parameters correspond to those of the phantom and sequence used in the experimental part of this study. To illustrate T_2 dependencies, additional values of T_2 = 250 ms and 900 ms were also included.

Experiments were performed on a clinical scanner at 1.5 T (MAGNETOM Vision, Siemens AG, Healthcare Sector, Erlangen, Germany), using the built-in body coil for both excitation and signal reception to ensure a homogeneous B_1 field. A cylindrical phantom with an inner diameter of 68 mm was examined, containing water doped with an SPIO contrast agent (Endorem^{TM}, Guerbet, France) at a concentration of 0.06 mmol(Fe)/l. This solution was expected to provide a ratio T_2/T_1 of approximately 0.1, similar to the value of biological tissues.

The longitudinal relaxation time of the phantom was measured with an inversion recovery HASTE sequence. A total of 15 images were acquired, with TI ranging from 25 ms to 15 sec. For assessment of transverse relaxation, a train of 16 spin-echoes was sampled with a CPMG sequence (DTE = 25 ms, TR = 6 sec). From the corresponding magnitude image series, T_1 and T_2 values were calculated by exponential fitting.

Prior to the TrueFISP experiments, the homogeneity of the main magnetic field was optimized using the automatic 3D shim routine provided with the scanner. After shimming, an additional gradient of G_z = 0.04 mT/m was applied in z direction so that a position-dependent frequency offset was created which varied linearly with the z coordinate, along the axis of the cylinder, while the isocenter of the gradient system stayed at resonance frequency.

For rapid visualization of the frequency distribution, TrueFISP images were acquired in coronal orientation, with the read direction placed parallel to the z axis. Non-selective block pulses with alternating phase were used for RF excitation so that the signal in each pixel originated from the whole width of the phantom. Imaging parameters included TR = 5.95 ms, TE = TR/2, a square matrix of 256 pixels and a field-of-view of 256 mm. By averaging over the last six of twelve consecutively sampled images, it was ensured that the steady state was reached and a sufficiently high signal-to-noise ratio was obtained.

The transient signal was investigated using a one-dimensional TrueFISP sequence. All timing parameters were identical to those utilized in the imaging experiments. However, no phase encoding gradients were applied so that with each echo, a one-dimensional projection was acquired along the z axis. Starting with the first excitation at t = TR/2 after a single preparation pulse, the signal decay was sampled for more than 15 sec with a total of 2560 TR intervals. This experiment was performed using flip angles of 20°, 60° and 100°. In each case, it was repeated with different preparation pulses, designed to guide to magnetization onto the corresponding q cone for dephasing angles of f = 0, p/2, 3p/4 and p.

In the steady state images, the applied frequency gradient resulted in dark bands with minimum signal. The corresponding spatial positions were assigned to dephasing angles of $f = \pm p$ so that the z axis was linearly transformed to an axis indicating the off-resonance angle. The decay curves measured with different flip angles at different frequency offsets were normalized to a maximum possible signal of one by dividing by an identical factor so that they could be directly compared to the theoretical predictions provided by Eq. 4.16.

4.5 Results

In Fig. 4.8, representative results of Bloch simulations are depicted for $a = 60°$. In the upper row, trajectories of the tip of ***M*** are shown in the magnetization vector plane, while the corresponding time courses of the transverse components (solid black) are plotted in the lower row, together with the ideal exponential signal decay calculated from Eq. 4.16 (single dots). In the on-resonant case of $f = 0$, and after an a/2 preparation pulse, a course close to and balanced around the a/2 cone is observed as predicted in Fig. 4.6c. The corresponding signal decay curve reveals a smooth monoexponential approach towards the steady state value, with a continuously decreasing length of ***M*** (a). For magnetization with a dephasing angle of $f = p/2$, the a/2 preparation proves to be suboptimal in that initial oscillations are encountered while ***M*** evolves towards its steady state (b). If a preparation pulse of 39° and according small phase (as calculated from Eqs. 4.3 and 4.6) is assumed for the same isochromat, a trajectory is observed which stays balanced around the q cone in the magnetization vector plane, yielding a purely monoexponential signal recovery curve (c).

These observations confirm that the concept of Fig. 4.6c is also valid in the off-resonant situation. In all cases, even with considerable signal fluctuations present, the simulated time courses follow the ideal exponential decays predicted by theory. With increasing deviation of the prepared magnetization direction from the optimal one, however, signal fluctuations continuously become more and more pronounced. The same findings were obtained with various other relaxation time combinations, flip angles and off-resonances.

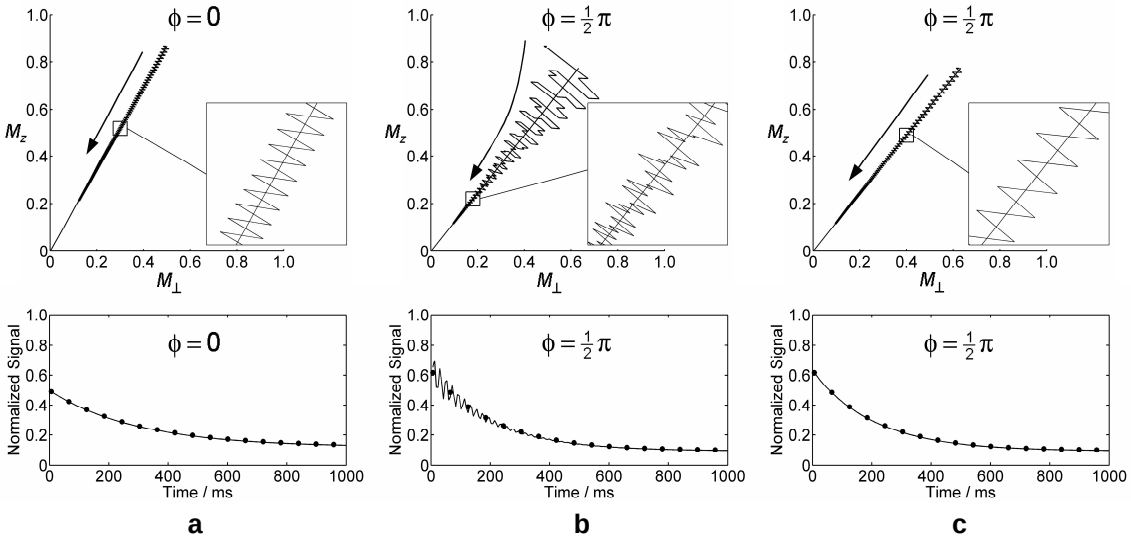

FIG. 4.8: Simulations of the TrueFISP transient phase: Trajectories of ***M*** in the magnetization vector plane (upper row) and corresponding simulated (solid) and ideal theoretical (dots) signal time courses (lower row): (a) f = 0 and a/2 preparation (b) f = p/2 and a/2 preparation (c) f = p/2 and preparation to the q cone.

In Fig. 4.9, theoretical values of the zenith angle (a) and the signal phase (b,c) are plotted versus off-resonance frequency (dots). For comparison, numerical results of Bloch simulations are shown for both parameters, as found for the first TrueFISP signal directly after preparation (solid gray) and when the steady state has been reached (solid black). For preparation, a series of RF pulses with increasing flip angles was modeled (n = 7). The flip angle of the k^{th} pulse was calculated as $a_k = (k - 0.5)\, a_{target}/n$, yielding equidistant linear steps for the designated zenith angles of on-resonant magnetization towards the target of $q = a/2$ [Paul04]. It can be seen that the preparation approach is rather efficient over wide range of frequencies, with only small periodic deviations, and that the steady state direction is reflected by Eqs. 4.6 and 4.9 with high accuracy.

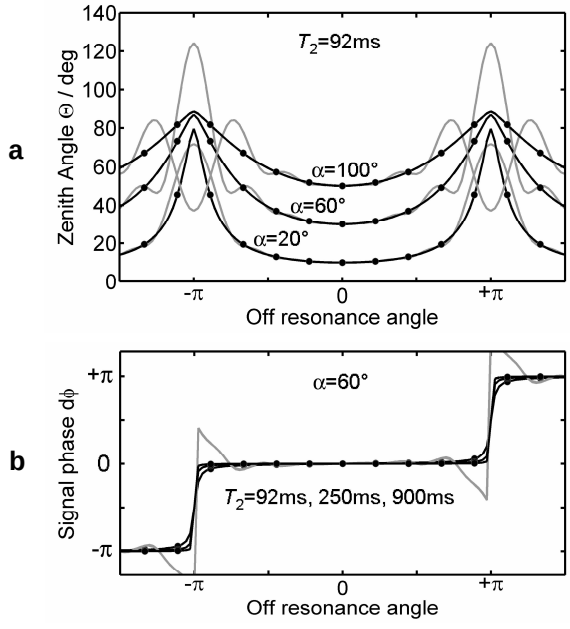

FIG. 4.9: The parameters defining the direction of ***M*** plotted vs. the off-resonance angle f : (a) The ideal zenith angle q; (b) the signal phase df . Theoretical values (single dots) and results of Bloch simulations are plotted, as obtained directly after preparation with an increasing flip angle series (solid gray) and in the steady state (solid black).

In Fig. 4.10, both the steady state signal (a) and the apparent relaxation time T_1^* (b), calculated from Eqs. 4.13, 4.15 and 4.17 are plotted for the various values of T_2 and flip angle as functions of the off-resonance angle (solid black), in comparison to expressions obtained with simulations based on the Bloch equations (single dots). As described previously, T_1^* lies between T_1 and T_2, depending on the flip angle [Schm02]. It is further shortened due to off-resonance, reaching a theoretical minimum of $T_1^* = T_2$ at complete off-resonance of f = ±p. Throughout, there is very good agreement between the analytical expressions and the numerical results.

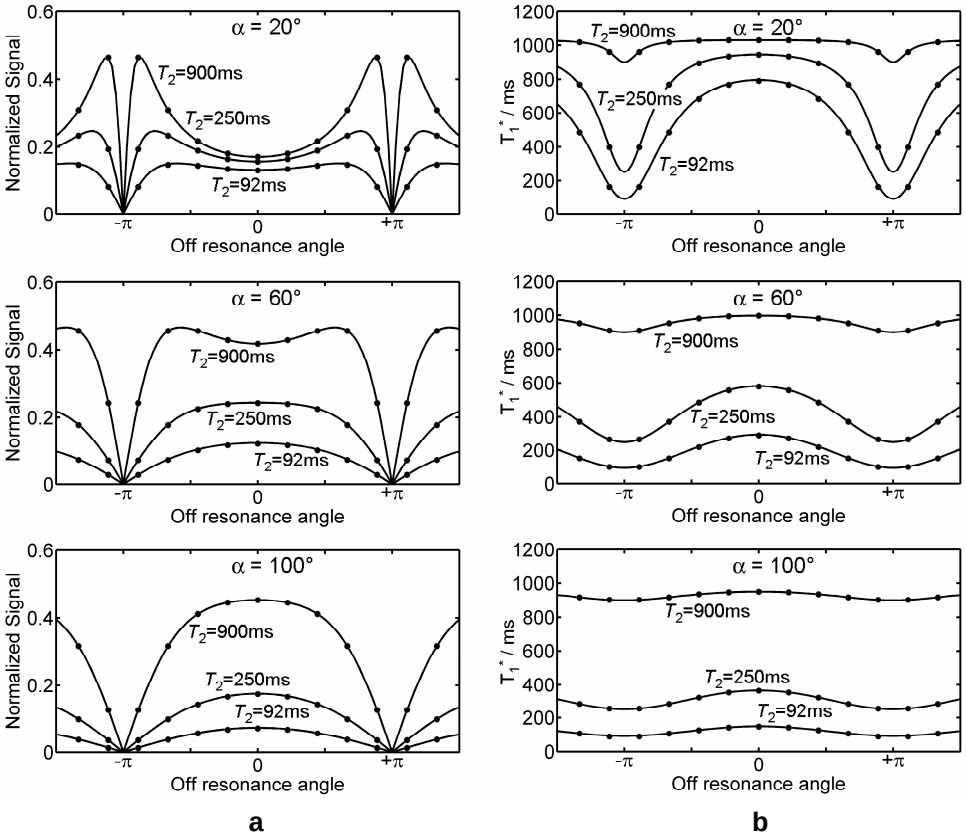

FIG. 4.10: (a) Steady state signal and (b) the apparent relaxation time T_1^* plotted for flip angles of 20° (upper row), 60° (middle row) and 100° (lower row) vs. off-resonance.

In Fig. 4.11, representative experimental results are shown for the flip angles of 20° (a), 60° (b) and 100° (c). The TrueFISP images acquired in the steady state (upper row) exhibited the expected frequency response profile with low signal bands perpendicular to the z axis, indicating the position of ±p dephasing over *TR*. This appearance was reproduced in the data obtained with the dynamic one-dimensional sequence, where the total sampling time of more than 15 sec proved to be long enough to reach the steady state in all cases. For pixels at dephasing angles of 0, p/2, 3p/4 and 19p/20 (rows 2-5, respective spatial positions indicated with arrows in the images), the first second of the acquired signal recovery curve is plotted after a conventional a/2 preparation (solid gray) as well as after ideal preparation onto the q cone (solid black), together with the respective ideal signal decay as calculated from Eq. 4.19 (single dots).

Significantly different time courses are obtained for the various flip angles and frequency offsets. As expected, for magnetization at resonance frequency, the a/2 preparation scheme is ideally suited for avoidance of signal fluctuations and essentially pure exponential decays are observed. With increasing off-resonance, the a/2 prepulse is suboptimal and initial oscillations are more and more prominent, while the q prepared signal time courses reveal smooth behavior, except in the case of a low flip angle and an off-resonance angle that is extremely close to ±p. For all flip angles and resonance offsets, the signal time courses are well described by the ideal monoexponential decay functions which were calculated using $S(0) = \sin q$, the decay rate calculated according to Eq. 4.17, and the expression for the steady state given in Eq. 4.13. It can be concluded that these approaches and the developed formulas are well reflected by the experiments.

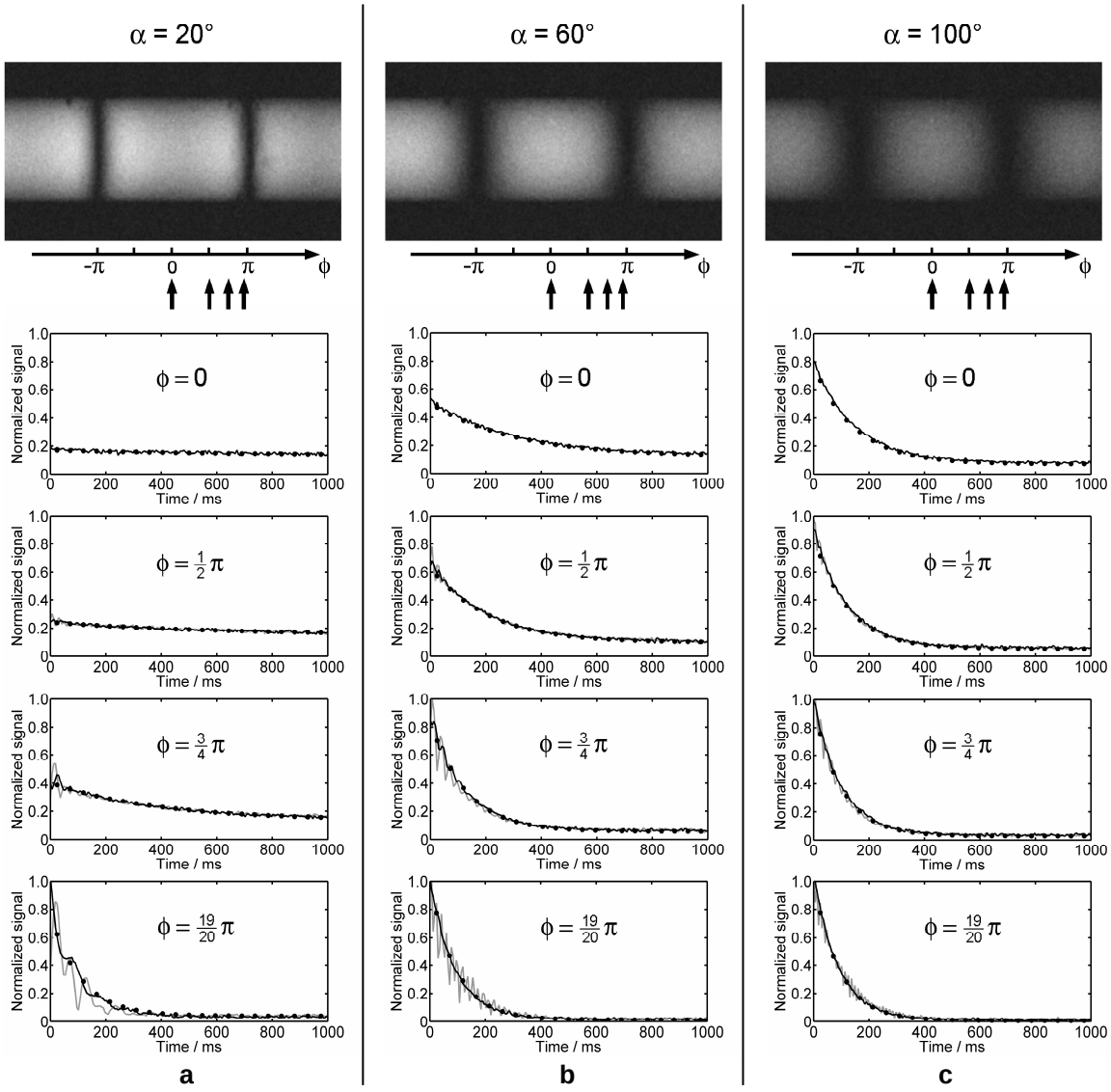

FIG. 4.11: TrueFISP steady state images (upper row) and transient signal curves (lower rows) acquired with flip angles of (a) 20°, (b) 60° and (c) 100°. Signal curves are displayed for off-resonance angles of f = 0, p/2, 3p/4 and 19p/20 (corresponding spatial positions are marked in the images with arrows). Ideal theoretical curves (dots) are shown together with the signal evolution sampled after a/2 preparation (solid gray) and after a preceding q pulse (solid black).

4.6 Discussion

In this chapter, the dynamics of the magnetization vector during a TrueFISP sequence was assessed using basic geometrical considerations instead of formal matrix-based mathematical formulations. The treatment relies on prior knowledge about the TrueFISP sequence, such as the dephasing and refocusing properties of off-resonant isochromats [Deim94] or the principle of analyzing the transient phase via the difference between actual and steady state magnetization vector [Jay55, Har01].

Building on these insights, the trajectory of $\boldsymbol{M}$ was described by means of a cone with an opening angle q. With simple sketches, two yet unpublished compact analytical expressions were derived for the ideal zenith angle q and the signal phase. If these benign conditions are fulfilled, a signal decay without fluctuations towards the steady state is observed even for considerably off-resonant magnetization.

As another novel concept, the magnetization vector plane was introduced, providing separation of the dephasing process from relaxation and RF excitation. In this reference frame, if $\boldsymbol{M}$ is guided into the proper direction, an a pulse has the approximate effect of mirroring $\boldsymbol{M}$ at the q line. This finding may be rather astonishing, but offers a simple explanation of the magnetization trajectory in SSFP experiments. With a close look at the relaxation and excitation processes, a pictorial explanation is obtained as to how the corresponding small changes of $\boldsymbol{M}$ govern the signal in the steady state and the preceding transient phase.

In an intermediate step, a novel compact expression was obtained for the TrueFISP signal steady state. Though this formula is simpler than the one available for many years [Ern66, Fre71], it appears to be a good approximation and has proven to be valuable for further analysis. With its use, an analytical formula was derived for the decay rate of the signal time course in the transient TrueFISP phase. It is worthwhile noting that the analytical formulas calculated from this approach result directly from simple rearrangement of terms, without any need for further approximations.

The validity of the theory was assessed with Bloch simulations and phantom experiments, both giving equivalent and consistent results. For various parameter combinations, a preparation towards the ideal direction resulted in smooth signal decay, and the signal time courses were well reflected by the corresponding theoretical prediction. This behavior was observed even for dephasing angles very close to $\varphi = \pm\pi$. All these results underline the validity of the conceptual framework and the developed analytical expressions.

The TrueFISP signal evolution is characterized by an apparent relaxation time T_1^* which lies in between T_1 and T_2, as had first been reported in [Schm02]. With decreasing flip angle, the value of T_1^* tends towards the true T_1. When flip or off-resonance angle approach values of 180° or $\pm\pi$, respectively, it converges towards T_2. This behavior is directly explained by the geometrical relation between these quantities illustrated in Fig. 4.4: For higher values of α or φ, the ideal zenith angle q becomes larger, resulting in a more pronounced role of transverse relaxation and an increasing T_2 influence.

Other authors used a more formal matrix-based treatment - in combination with rather abstract mathematical procedures based on spinor formalism and perturbation theory - for investigations of the TrueFISP signal decay. These approaches, mathematically more exact but potentially less pictorial in nature, led to similar results and confirm the theory and the

results presented in this chapter [LeR03, Gan04]. The same holds true for the compact expression for the transient decay rate which is obtained in the special case of zero frequency offset: The formula provided in Eq. 4.18 corresponds to the result of a recent publication wherein an elegant simplifying calculation was presented for on-resonant magnetization evolving along the a/2 cone [Sche03b].

4.7 Conclusion and retrospect

In conclusion, a simple picture has been presented for description of the ideal TrueFISP signal behavior in the transient phase. Simple analytic expressions were presented for the ideal zenith angle q and phase $d\mathrm{f}$. These angles define the target direction for the various preparation schemes published which aim at suppression of initial signal fluctuations. Without the need for advanced mathematical treatment, formulations were derived for the apparent relaxation time and the steady state signal which determine the TrueFISP signal evolution. Thus, a basis is provided for contrast calculation and sequence optimization when TrueFISP sequences are employed for signal acquisition outside the steady state, as it is the case in magnetization-prepared experiments. Moreover, the results should provide a theoretical foundation for TrueFISP-based relaxometry studies.

Since this study was carried out and published, the family of b-SSFP techniques has continued to be of high interest for many applications and its signal behavior has been subject of further theoretical analyses. For instance, by decomposing coherences into irreducible subpaths, Ganter derived an exact solution to describe the transient phase signal also for unbalanced SSFP sequences [Gan09]. Other publications investigated the influence of magnetization transfer effects [Bie06] or finite RF pulses [Bie09, Bie10] and analyzed the signal response in presence of intra-voxel frequency distributions [Gan06, Mill10].

Chapter 5

IR TrueFISP: Quantification of T_1, T_2 and spin density

Based on the theoretical description provided in the previous chapter, a complete set of analytical solutions is derived for the direct measurement of T_1, T_2 and spin density with a single Inversion-Recovery TrueFISP acquisition. The influence of off-resonance effects is analyzed with numerical simulations, and the feasibility of the technique for fast acquisition of parameter maps as well as its accuracy are demonstrated with phantom experiments. Moreover, an in-vivo study on the human brain is presented, where T_1, T_2 and spin density maps were obtained that are in very good agreement with literature values. This chapter essentially reflects the contents of a corresponding peer-reviewed journal article [Schm04a].

5.1 Introduction

In an IR TrueFISP scan, a series of images is sampled continuously after a preceding inversion pulse. As reported in the introduction of the previous chapter, and as can be understood from the developed theory, own experiments with such a sequence yielded apparent relaxation times T_1^* that depended on both T_1 and T_2.

In a first approach, these T_1* values had been compared to a look-up table of values as obtained from numerical simulations based on the Bloch equations. It became clear that different combinations of T_1 and T_2 can correspond to the same specific T_1^*. In analogy to signal of an IR FLASH acquisition (see section 2.2, however, a three-parameter exponential curve is required for a full description of the recovery curve. By taking these specific characteristics of the signal evolution into consideration, it became feasible to determine a unique combination of T_1 and T_2 from an IR TrueFISP acquisition [Schm02].

This insight was the motivation to investigate whether there is an analytical solution for the quantification of relaxation parameters from the signal curve. The results are summarized in the following section: Based on the theory presented in the preceding chapter, compact analytical expressions are derived for the direct calculation of T_1, T_2 and relative spin density from a single IR TrueFISP signal time course.

5.2 Theoretical considerations

In the following treatment, off-resonance effects are neglected and magnetization is considered to be at Larmor frequency, which is valid in case of a high homogeneity of the main magnetic field as typically encountered in MR experiments on homogeneous phantoms or in the human brain. In order to present a complete and consistent derivation, some equations of chapter 4 are repeated.

It was shown in section 4.3 that, for on-resonant magnetization evolving along the a/2 direction during a TrueFISP sequence, a decay rate is expected which can be described by

$$\mathrm{I} = E_1 \cos^2(\mathrm{a}/2) + E_2 \sin^2(\mathrm{a}/2) \quad . \tag{5.1}$$

Using $\mathrm{I} = \exp(-T_1^*/TR)$, $E_{1,2} = \exp(-T_{1,2}/TR)$, and $TR << T_{1,2}$, this formulation reduces to a direct relation for the apparent relaxation time T_1^*:

$$T_1^* = \left(\frac{\cos^2(\mathrm{a}/2)}{T_1} + \frac{\sin^2(\mathrm{a}/2)}{T_2} \right)^{-1} \quad . \tag{5.2}$$

With the origin of time positioned at the first imaging pulse and with T_1 relaxation between spin inversion and this pulse neglected, the TrueFISP signal value extrapolated to $t = 0$ can be described in good approximation by

$$S_0 = M_0 \sin(\mathrm{a}/2) \quad , \tag{5.3}$$

where M_0 denotes the proton density. For $TR << T_{1,2}$, the TrueFISP steady state signal at resonance frequency can be written as:

$$S_{stst} = \frac{M_0 \sin \mathrm{a}}{(T_1/T_2 + 1) - \cos \mathrm{a} \times (T_1/T_2 - 1)} \quad . \tag{5.4}$$

Generally, the steady state signal S_{stst} is lower than the initial signal S_0. Thus, in close analogy to the case of an IR FLASH experiment described in chapter 2.2, three parameters are required for a complete description of an IR TrueFISP signal time course from S_0 to S_{stst}, for instance using the fit function:

$$S(t) = S_{stst} \left[1 - INV \times \exp(-t/T_1^*) \right] \quad . \tag{5.5}$$

Here, the inversion factor *INV* indicates the ratio between S_0 and the steady state signal S_{stst}. Using Eqs. 5.3 and 5.4, *INV* can be expressed as

$$INV = 1 + \frac{S_0}{S_{stst}} = 1 + \frac{\sin(\mathrm{a}/2)}{\sin \mathrm{a}} \left[\left(\frac{T_1}{T_2} + 1 \right) - \cos \mathrm{a} \left(\frac{T_1}{T_2} - 1 \right) \right] \quad . \tag{5.6}$$

Evidently, *INV* only depends on the flip angle and on the ratio T_1/T_2, and it approaches $INV = 2$ for the limit of a small flip angle. Together with Eq. 5.2, the following expressions can be derived:

$$T_1 = T_1^* (INV - 1) \cos(\mathrm{a}/2) \tag{5.7}$$

$$T_2 = T_1^* \left(1 - \frac{\cos(\alpha/2)}{INV - 1} \right)^{-1} \sin^2(\alpha/2) \quad . \tag{5.8}$$

If T_2 relaxation in between the a/2 preparation pulse and the first a pulse is neglected, the relative spin density M_0 may be estimated directly from:

$$M_0 = \frac{S_{SS}(INV - 1)}{\sin(\alpha/2)} \quad . \tag{5.9}$$

In summary, from the time course of an IR TrueFISP acquisition, three parameters T_1^*, S_{stst} and *INV* can be measured, and from these, unique solutions can be analytically calculated for T_1, T_2 and M_0.

5.3 Methods

In order to assess both the accuracy of the approximate equations given in the theory section and the influence of off-resonance effects, IR TrueFISP experiments were modeled with numerical simulations on basis of the Bloch equations with Matlab (The MathWorks, Natick, MA, USA). Various values of T_1, T_2 and flip angle were included, and as before, RF pulses and signal acquisition were assumed to be infinitesimally short.

Experimental data were acquired on a 1.5 T whole body scanner (MAGNETOM Vision, Siemens AG, Healthcare Sector, Erlangen, Germany), using a standard quadrature head coil. A total of 18 phantom bottles with a diameter of 60 mm were examined. Fifteen bottles were filled with 0-2% agarose (Agar-Agar, Carl Roth GmbH & Co. KG, Karlsruhe, Germany), doped with Gd-DTPA (Magnevist™, Bayer Schering AG, Berlin, Germany) at concentrations of 0-0.259 mmol/l. Three phantoms consisted of water doped with a SPIO contrast agent (Endorem™, Guerbet, France) at concentrations of 0.025, 0.050 and 0.100 mmol(Fe)/l. With these phantoms, a wide range of T_1 and T_2 values was covered as well as different ratios T_2/T_1.

For reference, the longitudinal relaxation times of the phantoms were measured with a spin-echo sequence. After adiabatic inversion, spoiling of residual transverse magnetization and a subsequent delay *TI*, a single line of k-space was acquired, followed by a delay of 15 sec before the next inversion. Images were acquired at 14 different inversion times, ranging from *TI* = 25ms to *TI* = 9s. Transverse relaxation was assessed with a CPMG-sequence. After a 90° excitation, a total of 16 echoes were acquired with an inter-echo distance of D*TE* = 50 ms. To minimize T_1 influence, a long *TR* of 10 sec was used. Reference values of T_1 and T_2 were calculated from the corresponding magnitude image series by three-parameter and two-parameter fitting routines, respectively.

IR-TrueFISP experiments were performed on the phantoms arranged in groups with a segmented imaging sequence (*TR* = 6.46 ms, bandwidth = 488 Hz/pixel) at flip angles between 10° and 130°. After adiabatic inversion, a train of 38 image segments was acquired. Each segment comprised 21 phase encoding steps, equally distributed over k-space with spacing of 12 steps. Thus, the recovery curve was sampled for more than 5 sec. A delay of 5 sec was introduced to allow for longitudinal relaxation before the next inversion. A square field of view of 256 mm was covered with a matrix of 252 x 256 pixels, yielding a total time of

2:08 min for the complete acquisition of 38 images. A sinc-shaped RF pulse was used, which had been optimized for a rectangular slice profile with thickness 8 mm. The same sequence was used for parameter measurements in the human brain. Healthy volunteers as well as patients with brain tumors were examined after giving informed consent. After shimming, IR TrueFISP image series were acquired with different flip angles in axial slices.

The acquired IR TrueFISP magnitude image series were fit on pixel-by-pixel basis to the three-parameter function given in Eq. 9.5, using a least square fitting routine and dedicated computing algorithm [Nek92]. From the resulting fit parameter maps, T_1, T_2 and M_0 maps were calculated using Eqs. 5.7 - 5.9. In the phantom data, values were taken from regions of interest (ROIs) placed within the bottles and compared to the corresponding results obtained in the same manner from SE and CPMG sequences. In the in-vivo data, T_1, T_2 and M_0 values were evaluated in ROIs positioned in white matter, gray matter, cerebro-spinal fluid (CSF) and muscle tissue, each ROI comprising at least 25 pixels.

5.4 Results

For magnetization at zero or small off resonance frequency, the simulated temporal signal curves revealed essentially pure monoexponential behavior and could thus be completely characterized by three fit parameters T_1^*, S_{SS} and *INV*. This is demonstrated in Fig. 5.1a, where three temporal signal courses, simulated for a flip angle of 50° and different ratios of T_2/T_1, are depicted together with the corresponding monoexponential fits. In Fig. 5.1b and 5.1c, results for T_1^* and *INV* are shown for different T_2 values as a function of the flip angle, obtained with numerical simulations and analytic calculations according to Eqs. 5.2 and 5.6. At small flip angles, the value of T_1* equals the true T_1, and in the multi-spin-echo limit of a = 180°, it approaches T_2 (b). *INV* equals 2 at small flip angles and is even close to 2 for higher flip angles, when $T_2 \gg T_1$. Both T_1^* and *INV* as calculated from Eqs. 5.2 and 5.6 correspond to the results from Bloch simulations very closely (c). For brain tissue (e.g. white matter with T_1 = 700 ms and T_2 = 75 ms), a rather short T_1^* of 287 ms and an inversion factor of *INV* = 3.63 would be expected with a flip angle of 50°.

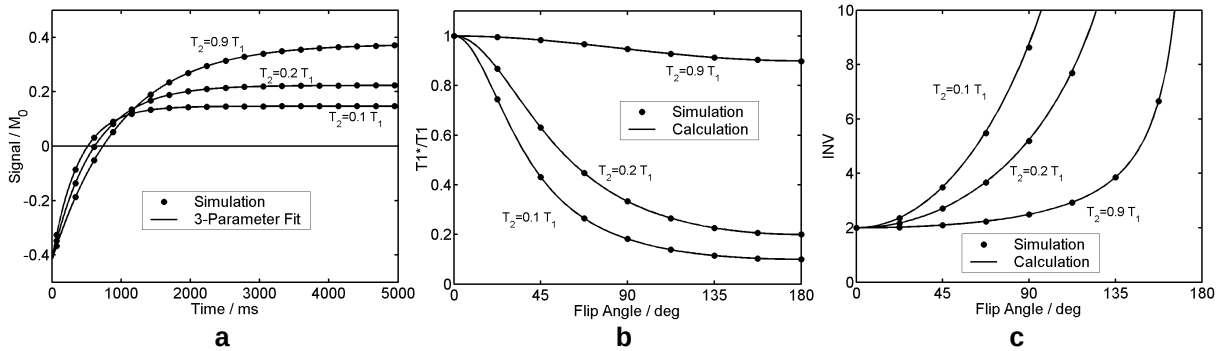

FIG. 5.1: Simulations and calculations: (a) signal time courses with a flip angle of 50° for different ratios T_2/T_1. (b) ratio of apparent T_1^* to true T_1 and (c) inversion factor *INV* vs. the flip angle.

For spins not on resonance, more and more distinctive initial signal oscillations are observed as well as a subtle persistent deviation from the respective on-resonant time course. The

signal curves still fit well to monoexponential functions but errors are introduced in the calculation of T_1, T_2 and M_0 values. This is illustrated in Fig. 5.2, where the parameter values determined at different flip angles are plotted against the off-resonance angle f, i.e. the dephasing angle during the *TR* interval. For the depicted simulations, a T_1 of 1000 ms and a T_2 of 100 ms were used, but the relative deviations from the true values were largely independent of T_1 or of the ratio T_2/T_1, i.e. the depicted results represent estimates for various tissues. For example, with a flip angle of 50° and at an off resonance angle of p/3 which corresponds to a frequency offset of 26 Hz for the *TR* of 6.46 ms used here, T_1 and M_0 are overestimated by less than 4% and by roughly 12%, respectively, while the measured T_2 values are about 20% too high. However, off resonance appeared not to be a problem in the studies conducted in phantoms and the human brain.

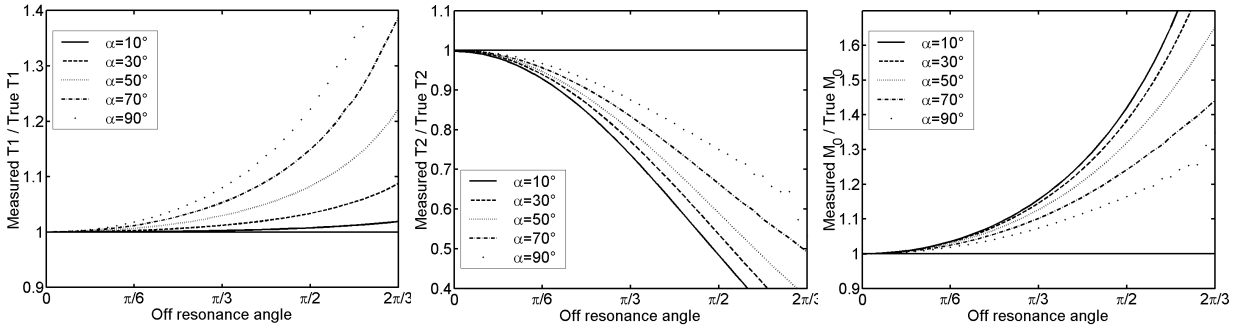

FIG. 5.2: Simulated off-resonance influence: ratio of measured parameter value to true value at flip angles from 10° to 90° vs the off resonance angle: (a) T_1 (b) T_2 (c) M_0.

In the phantom experiments, the single pixel signal courses were well characterized by the monoexponential three-parameter fit function according to Eq. 5.5. The complete T_1, T_2 and M_0 parameter maps obtained with a flip angle of 50° are shown in Fig. 5.3a-c. The gray scales of the T_1 and T_2 map were truncated at 3500 ms and 1400 ms, respectively. The spin density values were normalized to the average value of all phantoms, and indicated in arbitrary units. In some phantoms, thin fluid films have formed between the agar matrix and the bottle wall. In the T_2 map, they appear as bright rings at the phantom rims, corresponding to long T_2 values. They are not visible in the T_1 map, since T_1 is mainly determined by the Gd concentration which can be expected to be essentially identical for the agar gel and the surrounding fluid. Rather similar M_0 values are observed in the differently doped bottles, as may have been expected since spin density should not show strong dependence on the concentration of contrast agent or agarose.

An overview of all phantom results at a = 50° is given in Figs. 5.3d-f. Here, the T_1, T_2 and M_0 values measured with the TrueFISP sequence are plotted vs. the corresponding reference values. The excellent agreement with the single point values for all phantoms covering wide ranges of T_1 and T_2 is apparent in the high correlation coefficients of $r^2 = 0.999$ and $r^2 = 0.996$ for the T_1 and T_2 data and in the clustering of all M_0 values near to 1, as expected. Equivalent results were obtained with flip angles between 30° and 90°. With a smaller flip angle of 10°, the measured T_1^* values were similar to the calculated T_1 and the reference T_1 values. However, the obtained T_2 and M_0 maps had a noisy appearance and the reference

values were not reproduced precisely (data not shown). With flip angles higher than 90°, short T_1^* values and limited accuracy for the determination of all parameters were observed.

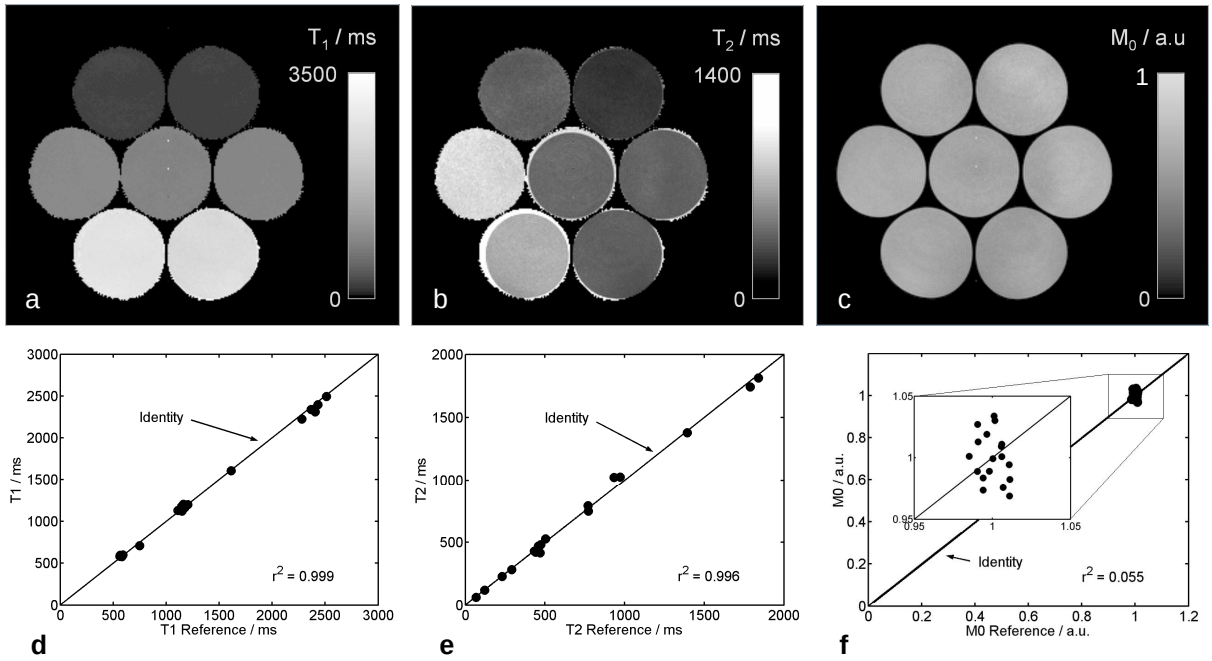

FIG. 5.3: Phantom results: (a) T_1, (b) T_2 and (c) M_0 map of grouped phantoms, (d) T_1 and (e) T_2 and (f) M_0 of all phantoms vs. the corresponding reference values.

In the in-vivo study, a similar impact of the choice of the flip angle was observed. Accurate measurements were shown to be feasible at flip angles between 30° and 70°. A low flip angle of 10° resulted in noisy T_2 maps and high flip angles of 90° and above lead to very short T_1* values which could not be recorded precisely. In Fig. 5.4, representative in vivo results of a volunteer brain are shown, measured with an IR TrueFISP experiment at a flip angle of 50°. The calculated T_1, T_2 and spin density parameter maps are depicted in Figs. 5.4a-c. For better visualization, the gray scales of the relaxation time maps were truncated at 3500 ms and 250 ms, respectively. The spin density map was normalized to M_0 = 1 for the maximum value found in CSF.

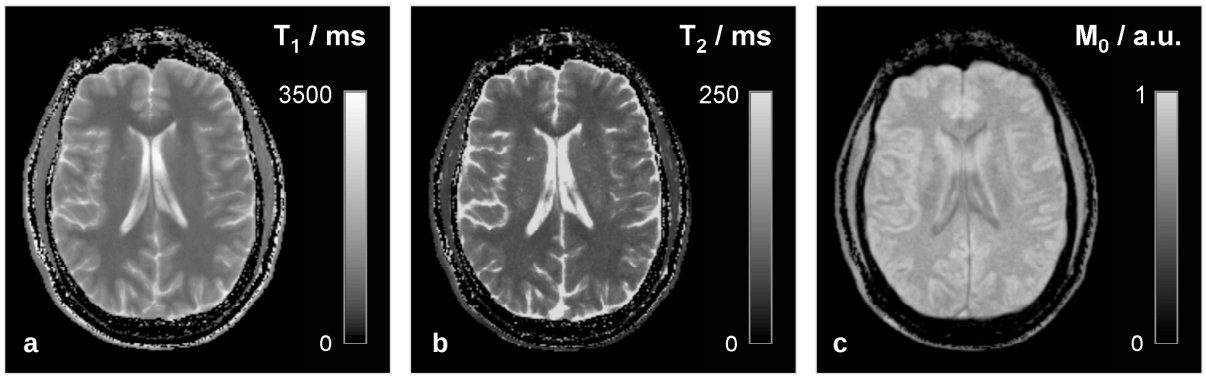

FIG. 5.4: Volunteer results: Parameter maps measured with an IR TrueFISP experiment at a flip angle of 50°: (a) T_1, (b) T_2 and (c) M_0.

In Table 5.1, average parameter results are given, obtained within ROIs positioned in gray matter, white matter, CSF and muscle tissue. With the exception of comparatively low spin density of CSF, the measured values fit well into the range of literature values and were be reproducible in the same subject. Similar results were obtained in all volunteers.

	T_1 / ms	T_2 / ms	M_0 / a.u.
White matter	719 ± 33	73 ± 6	0.81 ± 0.03
Gray matter	1165 ± 88	92 ± 11	0.98 ± 0.07
CSF	3337 ± 111	2562 ± 123	1.00 ± 0.07
Muscle	963 ± 78	60 ± 12	0.79 ± 0.05

Table 5.1: Volunteer data: parameter values obtained from ROIs positioned in different tissues (mean ± SD).

Figs. 5.5 and 5.6 show examples for quantitative multi-parameter maps in patients with brain tumors. Acquisition parameters and gray scales are identical to those of Fig. 5.4.

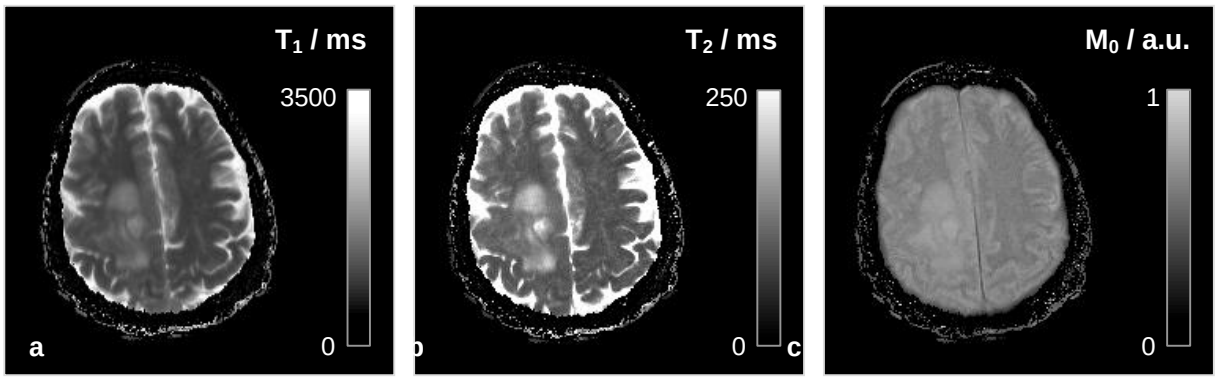

Fig. 5.5: Results from a patient with glioblastoma (male, 69y). Parameter maps measured with a single IR TrueFISP experiment: (a) T_1, (b) T_2 and (c) M_0.

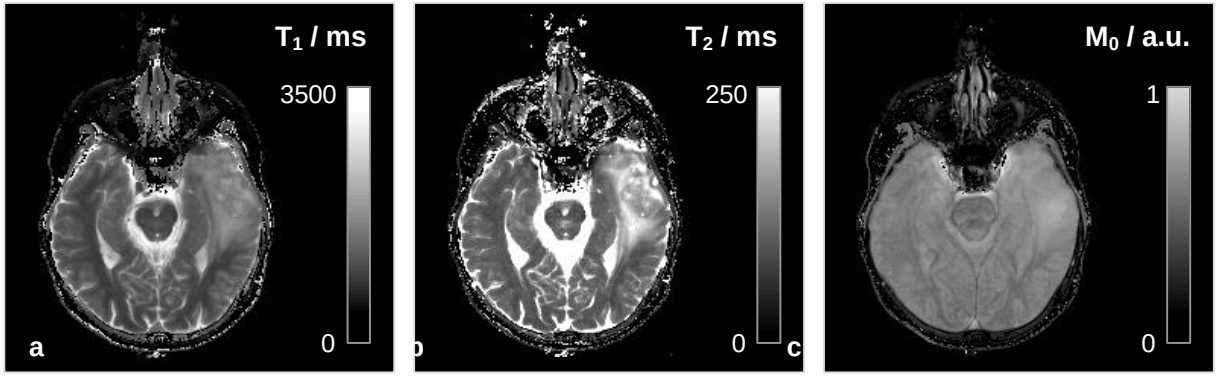

Fig. 5.6: Results from a patient with glioblastoma (male, 73y). Parameter maps measured with a single IR TrueFISP experiment: (a) T_1, (b) T_2 and (c) M_0.

5.5 Discussion

The idea of acquiring a series of TrueFISP images after spin inversion had been proposed early for T_1-prepared steady state imaging [Deim94]. From a later study on phantoms doped with Gd-DTPA, it was reported that the measured IR TrueFISP time course with a flip angle of 50° reflected free longitudinal relaxation very closely [Sche01]. However, Gd-doped phantoms were used in which T_2 should be close to T_1, so that the apparent TrueFISP T_1^* may have been equal to the true T_1 merely for coincidental reasons.

In this context, it is worth noting that the idea of using the transient response of the SSFP sequence for relaxation time measurements was reported long ago. It was stated that "…during the continuous pulse train, the T_1 recovery of the magnetization after a 180° pulse can be directly observed and plotted" and that this „…suggests a method for measuring T_1 in liquids where $T_1 = T_2$" [Hin76]. The limitation included in this statement reveals an early insight that in most biological tissues, where T_2 is substantially shorter than T_1, an apparent relaxation constant T_1^* is expected which is much shorter than the real T_1. In this chapter, however, it was shown that if the complete recovery time course information is incorporated, e.g. using a three parameter fit according to Eq. 5.5, it is possible to extract T_1 and T_2 as well as relative spin density. Both the phantom and in-vivo results of this study confirm the feasibility and accuracy of the technique.

Although several simplifying assumptions underlie the proposed calculations, the results correspond very closely to those of numerical Bloch simulations. These still can not reflect real experimental conditions, since for example, the duration or potential inaccuracies of RF pulses and signal reception are not accounted for. In vivo, blood or CSF flow into the imaging slice may affect the results. These were not considered, nor were diffusion effects which may generally influence the signal in TrueFISP imaging [Bux93].

A direct comparison of quantitative relaxation constants with literature is difficult, as various values for T_1 and T_2 of brain parenchyma are reported from previous studies. While both lower and higher values can be found, most reported T_1 values of white matter lie between 633 ms and 758 ms, while those of cortical gray matter range between 998 ms and 1304 ms [Bre89, Whi97, Hen99, Vym99, Sri03]. Whereas transverse relaxation in the brain may be characterized best with a multi-exponential decay [Poon92], a reasonable range of T_2 values for a mono-exponential model is 69.0 ms to 81.1 ms in white and 77.9 ms to 93.3 ms in gray matter [Bre89, Poon92, Whi97, Vym99]. The values given in Table 5.1 are in close agreement with these reports from literature. The spin density ratio between gray and white matter determined here is very close to previously reported values between 0.84 and 0.88 [Brix90, Rob96, Whi97]. Reasonable results were obtained in muscle and CSF, except spin density values of CSF, which may be underestimated due to incomplete relaxation during the five-second waiting periods before the subsequent inversion pulses.

An important point to discuss is the sensitivity of TrueFISP to off resonance. The typical banding artifacts can be avoided when the off resonance dephasing angle during *TR* is less than ±p, a condition that could easily be fulfilled over a phantom group or over a human brain, even for the moderate *TR* of 6.46 ms. Furthermore, the theoretical approximation used for data evaluation is only valid for on resonant spins. With Bloch simulations, it was possible to demonstrate the sensitivity of the technique to off resonance. In particular, for magnetization at frequencies considerably off resonance, the sequence preparation with the preceding

a/2 pulse would not be perfect. Oscillations in the first echoes would be expected, inevitably associated with image artifacts, particularly in the present case of segmented acquisition. However, artifacts were not encountered in this study, not even in the first image after inversion, which is acquired with only the first 21 echoes after preparation. Consequently, it may be assumed that serious problems with off resonant magnetization did not occur. Both the phantom and volunteer studies demonstrate the feasibility of the technique and that it is possible to measure three different parameters with a single IR TrueFISP experiment.

With a low flip angle of 10°, an apparent T_1^* was obtained that is close to the real T_1. This is due to the fact that in that case the magnetization vector remains essentially parallel to the main magnetic field and therefore predominantly follows longitudinal relaxation. Consequently, the component of the magnetization vector which is subjected to transverse relaxation and the resulting influence of T_2 on the signal time course are too small for precise quantification of T_2. With a larger flip angle, e.g. of 70°, the transverse magnetization component, and thus the precision of measuring transverse relaxation, is increased. On the other hand, the steady state signal may be maximal for flip angles of only 30° in brain tissue, suggesting that the chosen flip angle should not be chosen too large. In addition, the apparent relaxation time decreases for increasing flip angle. At a flip angle of 90°, a T_1* of only 138 ms is expected for white matter (T_1 = 700 ms, T_2 = 75 ms), which is in the range of the temporal distance between two consecutive images in this study. In this case, the temporal resolution used here proved to be too small for precise sampling of the signal recovery curve. At high flip angles, the images would have to be divided into smaller segments and, consequently, the total scan time would be increased. For these reasons, the optimum excitation angle as well as the best segmentation scheme for this angle will depend on the expected T_1 and T_2 values. The question is not trivial and should be subject of further investigations.

For the presented data evaluation, the inversion factor *INV* has to be measured precisely. For a accurate fit of the steady state signal value, the recovery curve should ideally be sampled at least until the steady state condition is reached. In the present study, the signal time course was observed for more than 5 sec, by far long enough to reach the steady state in brain tissue, but too short for CSF. Thus, if the focus is on parenchyma only, the recovery sampling time could be substantially shortened, also leading to shorter total scan times. For optimized measurements in CSF, it may be beneficial to acquire more images. Furthermore, any loss of longitudinal magnetization due to incomplete recovery before inversion or an imperfect inversion pulse will lead to errors. With the use of an adiabatic hyperbolic secant inversion pulse the second influencing factor may be minimized, at least when a coil with homogeneous B_1 field is used. However, for complete recovery, a long delay is required before inversion. The delay of 5 sec used in the experiments was shown to be sufficiently long to give reasonable results for gray and white matter, but errors may be introduced for the results in voxels with long T_1, such as CSF.

With a saturation recovery sequence, no delay would be required and the total scan time could be significantly reduced. However, additional information would be necessary to obtain a unique solution of T_1 and T_2. This may be accomplished with two experiments at different flip angles and a postprocessing procedure similar to that proposed previously [Schm02]. Whether this approach is beneficial for the efficiency of T_1 and T_2 quantification has yet to be determined.

The *TR* of the TrueFISP sequence used in the presented studies was 6.46 ms, which is quite moderate compared to the short *TR* values below 3 ms which are available on clinical scanners. It was possible to use a long RF pulse which could thus be optimized for slice profile effects. With a shorter *TR*, potential influence of off resonance effects is minimized and a higher temporal SNR efficiency may be achievable. On the other hand, very short RF pulses have to be used which leads to an inevitably poor slice profile. With a broad flip angle distribution over the slice, the complex integral over different recovery curves will be measured, each with its own apparent relaxation constant. This will lead to a more complicated recovery curve which will probably not be described adequately by a mono-exponential function. However, the flip angle distribution along the slice profile can easily be measured and this information may also be included into the theory. This problem may be avoided with a 3D sequence.

5.6 Conclusion and retrospect

In conclusion, the presented results show that it is possible to derive T_1 and T_2 as well as relative spin density from a single IR TrueFISP experiment. The optimization of all sequence parameters and a thorough comparison with conventional techniques regarding SNR, T_1 and T_2 accuracy should be subject of further research. No problems with off-resonance and imperfect pulse profiles occurred in this study, but the robustness of the technique with respect to these effects has to be explored.

Since the work of this chapter was published, the IR TrueFISP concept for parameter quantification approach presented in this chapter has drawn the attention of many research groups. For instance, the approach was applied to various tissues such as the rat brain [Blau09], placenta specimen [Van05], as well as to human cartilage [New05a], blood [Wu08], myocardium [Wang07], and sceletal muscle [DeSou11]. It was also used in animal tumor models [Weid06, Walk09], and for SPIO quantification [Elk09]. The technique was analyzed with respect to its flip angle dependency [New05b] and the influence of MT effects [New08, Blu09]. It was extended to a single-shot version [Steh07], to a method that compensates for B1 inhomogeneities [New07], and to a 3D implementation [New10]. It was combined with an MGE acquisition to map T_2* as a further parameter [Steh08], and with a patient-driven model calibration [Loe09], and a modified low-flip angle version was proposed for faster T1 quantification [Gai09]. Recently, a radial IR TrueFISP technique with an optimized radial sampling pattern and MT effect compensation [Ehs12] was presented.

Chapter 6

Synthetic multiple-contrast images based on a single IR TrueFISP acquisition

In this chapter, a study is presented that aims at reconstructing synthetic images with different contrasts from parameter maps obtained with a single IR TrueFISP acquisition. It is shown that any desired contrast can be obtained that is based on T_1, T_2 and spin density, including T_1-weighted, T_2-weighted, spin-density-weighted, and FLAIR images. The feasibility of the approach is demonstrated in volunteers and patients with brain tumors. The image signal intensities for the calculated images are shown to correlate very well with those of traditionally obtained images, which require the acquisition of a number of different data sets using multiple imaging sequences. This chapter essentially reflects the contents of a corresponding peer-reviewed journal article [Gul04].

6.1 Introduction

The major strength of MRI is the wide range of contrast mechanisms available. A standard clinical neurological examination typically comprises T_1 and T_2 weighting, fluid attenuated inversion recovery (FLAIR) sequences (CSF-nulled, T_2-weighted), and occasionally spin-density-weighted acquisitions. Images with these different types of contrast information have to be obtained using separate acquisitions, with is associated with two problems: A long scan time - resulting in patient discomfort, reduced potential for collecting alternative contrasts, etc. - as well as the possibility of misregistration of clinically relevant anatomical information between different types of images. The latter problem can be caused by motion between the scans, but also by slice profile discrepancies of the different sequences.

In this study, it is shown that some of these problems can potentially be alleviated with the help of the approach presented in the preceding chapter - data acquisition with a single IR TrueFISP sequence and subsequent calculation of three independent fundamental parameter maps. Such maps provide quantitative information about the MR properties of the tissue anatomy, and can potentially add information if included in a conventional exam. However, this would require radiologists to become accustomed to reading T_1, T_2, and spin

density maps instead of traditional contrast images. This might be problematic because these maps are presently not integrated in standard MRI examinations. Moreover, in view of the wide range of parameter values found in human tissue, it might be difficult to interpret parameter maps alone. However, they open up the intriguing possibility of calculating images with unique contrast properties, which cannot be obtained with routine standard MR sequences.

In this chapter, a method is proposed to reconstruct images with clinically relevant spin density, T_1, and T_2 weighting as well as images resembling those obtained with a FLAIR sequence. These resulting contrasts are shown to be very similar to experimentally acquired routine clinical contrasts. Thus, a method is provided that yields perfectly registered synthetic multiple contrast MR images as well as underlying quantitative T_1, T_2, and spin density maps from a single IR TrueFISP acquisition.

6.2 Basics - clinical standard protocol

Although the imaging strategy in a clinical MRI exam is typically tailored to the questions to be answered and the available clinical information, it is fair to say that a set of standard imaging protocols constitutes the basis for common indications. While section 1.4 provided a general introduction on MRI of tumors, this section provides a brief overview on the basic elements of a clinical exam, using intracranial imaging as an example.

Overview

Besides the mere necessity to discover a mass lesion, the essential questions to be answered by the imaging protocol include the following [Reim10]: Is the mass lesion a tumor? Where is it located? What is the amount of mass effect and edema? What is the most likely diagnosis? To assess these questions, images with multiple different contrasts are acquired. Table 6.1 provides a brief overview of a typical protocol for evaluation of the adult brain.

Sequence	Contrast	*TE*	*TR*	*TI*
SE	T_1-weighted	10-20	500-700	-
TSE / SE	T_2-weighted	90-130	3000-6000	-
TSE / SE	SD-weighted	10-30	2000-5000	-
FLAIR	CSF-nulled	100-150	6000-10000	1800-2200
Diffusion-weighted EPI	Diffusion-weighted	~40 (EPI) or 100-140 (SE-EPI)	optional	-

Table 6.1: Clinical standard protocol for imaging of the adult brain (extracted from [Reim10]).

Because of their robustness and the well-established contrast behavior, standard spin-echo techniques are still widely used, despite the long total scan times needed. T_1-weighted

acquisitions are often implemented as spin-echo-based acquisitions, while T_2-weighted and FLAIR scans are typically performed using TSE sequences.

Many exams include intravenous contrast injection and subsequent repetition of the T_1-weighted acquisitions. At first hand, for comparison, the slice geometry should be identical to that of the pre-contrast T_1-weighted scans, but eventually different orientations can also be helpful. In the head and neck region, it can be helpful to acquire the post-contrast T_1-weighted images with fat suppression, and TSE-based sequences instead of EPI might be useful for DWI, due to their lower susceptibility to artefacts.

Most tumors show hypointense signal in T_1-weighted images, while their appearance on T_2-weighted images is hyperintense. Hence, T_2-weighted images facilitate direct detection of many lesions, which renders them clinically highly relevant. However, since edema might also obscure underlying lesions, the T_1-weigthed contrast can be better suited for anatomical definition of the latter. Moreover, T_1-weighted data is deemed the basis for "assessing the gross anatomy and structure of the brain" [Reim10]. Most protocols are complemeted with a FLAIR acquisition, which generates high contrast at interfaces between and brain parenchyma and CSF, and thus facilitates the conspicuity of small lesions located in white matter.

FLAIR

In the FLAIR technique, the inversion recovery principle is employed for achieving a dark appearance of CSF. The basic sequence is composed of an initial 180° inversion pulse, an inversion delay *TI* and subsequent signal acquisition, classically carried out with a spin-echo readout. For an optimized combination of *TI* and *TR*, the z component of magnetization with a specific T_1 value amounts to zero in the moment of data acquisition. As a result, the signal of corresponding compartments is efficiently suppressed.

The clinical value of IR sequences was recognized early [Byd85], and the approach showed to be of particular importance for the elimination of CSF signal in neurological MR imaging [Haj92a, Haj92b]. A major drawback of FLAIR was the long scan times associated with the spin-echo acquisition at long *TR*. The efficiency of the technique was increased significantly by employing the RARE/TSE sequence for readout [Ryd94]. This rendered FLAIR applicable in the clinical setting. The sequence diagram is illustrated in Fig. 6.1. The corresponding signal can be described by the following formula [Ryd95]:

$$S = M_0\left[1 - 2\exp(-TI/T_1) + \exp(-(TR - TE_{last})/T_1)\right]\exp(-TE_{eff}/T_2) \qquad (6.1)$$

FLAIR images are typically acquired with a sequence that provides a strongly T_2-weighted contrast. Since CSF appears dark, tissue abnormalities with prolonged T_2 exclusively show up as bright objects. Consequently, various lesions are demonstrated with higher conspicuity than with conventional T_2-weighted imaging, predominantly in the brain stem and areas adjacent to ventricles or subarachnoid spaces, i.e. close to CSF [Haj92b, DeC92, DeC93]. Although disadvantages were reported in the depiction of lesions with long T_1 as encountered in multiple sclerosis [VanW96], the high value of the technique could be demonstrated for various pathologies, including brain tumors and metastases [Ess98, Ess99].

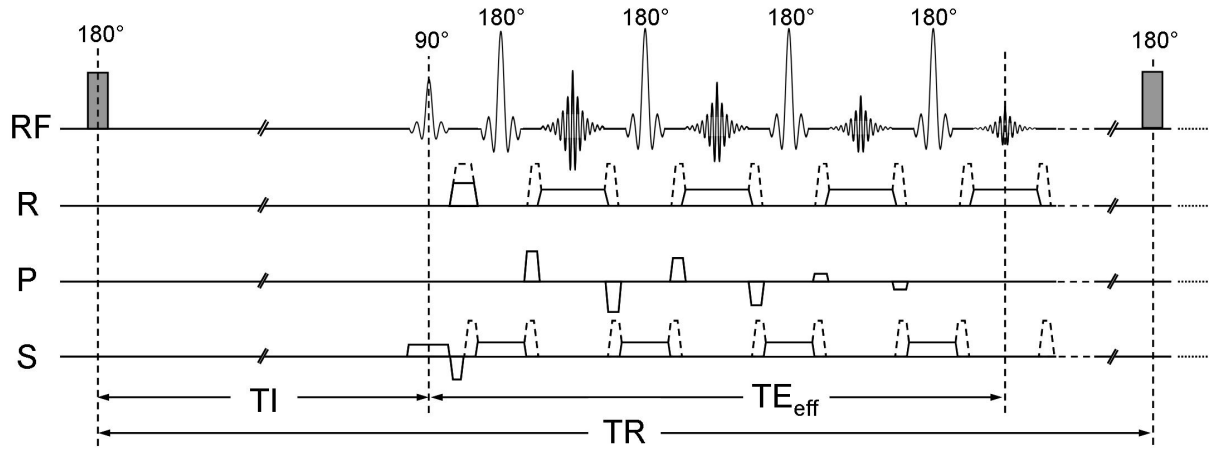

Fig. 6.1: FLAIR sequence with TSE acquisition.

6.3 Theoretical considerations

This section extends the theoretical treatment of section 5.2. It introduces a correction term that accounts for imperfect estimation of M_0 due to incomplete T_1 relaxation during the repetition period. The previously derived formulas are repeated in order to preserve consistency within this chapter.

Generation of T_1, T_2, and M_0 maps

It was shown that it is possible to derive T_1, T_2, and spin density maps directly from the signal time course acquired with an IR TrueFISP sequence [Schm04a]. Specifically, the IR TrueFISP signal at a time t after the inversion preparation pulse can be described by an exponential three-parameter equation as follows:

$$S(t) = S_{stst}\left[1 - INV \cdot \exp(-t / T_1^*)\right] \quad . \tag{6.2}$$

Here, S_{stst} denotes the TrueFISP steady state signal and T_1^* is the apparent longitudinal relaxation constant. The inversion factor INV characterizes the relation between the signal right after inversion and S_{stst}. From these three fit parameters, T_1, T_2, and M_0 maps can be obtained by using the following simplified equations:

$$T_1 = T_1^*(INV - 1)\cos(\alpha / 2) \tag{6.3}$$

$$T_2 = T_1^*\left(1 - \frac{\cos(\alpha / 2)}{INV - 1}\right)^{-1} \sin^2(\alpha / 2) \quad . \tag{6.4}$$

$$M_0 = \frac{S_{stst}(INV - 1)}{\sin(\alpha / 2)} \quad . \tag{6.5}$$

Correction for incomplete relaxation during the repetition period

The formulas presented in Eqs. 6.3-6.5 for calculation of T_1, T_2, and M_0 were derived under the assumption that - in an IR TrueFISP sequence that is played out in segmented fashion - the longitudinal magnetization reaches its equilibrium value before the inversion pulse that precedes each shot [Schm04a]. In practice, however, this condition is not fulfilled for all tissues. Particulary, compartments with long T_1 encounter incomplete relaxation during the waiting delay after an acquisition, so that only an effective longitudinal magnetization M_{eff} is reached until the subsequent inversion. This results in a systematic underestimation of the respective spin density values. The situation is illustrated in Fig. 6.2, which shows the simulated temporal courses of the longitudinal magnetization component for gray matter and CSF. In this scenario, the IR TrueFISP signal is assumed to be sampled over t_{scan} = 5 s, followed by a waiting delay of t_{wait} = 5 s. For T_1 and T_2, values of 1150/90 ms and 3350/2250 ms were used for the two tissues, respectively. The simulations show that M_{eff} = 0.99 M_0 in gray matter, but M_{eff} = 0.88 M_0 in CSF for the imaging parameters used in the present study.

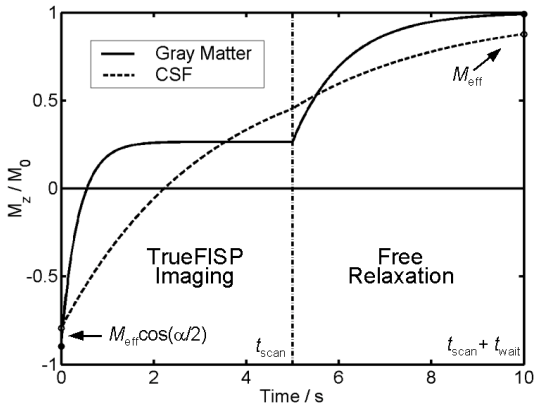

Fig. 6.2: Time course of effective longitudinal magnetization under conditions of incomplete T_1 relaxation.

The signal acquried at the end of the recovery curve at $t = t_{scan}$ can be written as

$$S(t_{scan}) = S_{stst}\,[1 - INV \exp(-t_{scan} / T_1^*)] \ . \tag{6.6}$$

Since the magnetization vector ***M*** evolves along a cone with azimuth angle a, its longitudinal component $M_z(t_{scan})$ is related to $S(t_{scan})$ by

$$M_z(t_{scan}) = S(t_{scan})\cot(a/2). \tag{6.7}$$

After the time t_{scan}, this component of ***M*** relaxes along the z-axis for the waiting time t_{wait}, while the transverse magnetization becomes zero due to T_2 relaxation as long as t_{wait} is long enough or if additional spoiler gradients are applied. M_{eff}, the value of M_z after t_{wait}, can be calculated as

$$M_{eff} = M_0 - [M_0 - M_z(t_{scan})]\exp(-t_{wait} / T_1) \ . \tag{6.8}$$

Based on Eqs. 6.6-6.8, a corrected M_0 value can be calculated from

$$M_0 = \frac{M_{eff} - S_{stst}\,[1 - INV \exp(-t_{scan} / T_1^*)]\cot(a/2)\exp(-t_{wait} / T_1)}{1 - \exp(-t_{wait} / T_1)} \ . \tag{6.9}$$

6.4 Methods

Imaging

All experiments were performed on a 1.5 T whole body scanner (MAGNETOM Vision, Siemens AG, Healthcare Sector, Erlangen, Germany), equipped with a standard quadrature head coil. Results were obtained from six healthy volunteers and from two brain tumor patients to demonstrate the feasibility of the approach.

The segmented IR TrueFISP imaging sequence consisted of a non-selective adiabatic 180° inversion pulse, a gradient spoiler in order to dephase any residual transverse magnetization, an a/2 preparation [Deim94] and subsequent acquisition of 38 images. Acquisition parameters included a flip angle of 50°, *TR* of 6.46 ms, 21 k-space lines per image and shot, 136 ms per image, a total of 12 shots, a data matrix of 252 x 256, a 5 s waiting delay between the last acquisition and the subsequent inversion pulse, and a total data acquisition time of 2 minutes per slice.

For comparison, T_1-weighted images were acquired with a spin-echo sequence (*TE* = 14 ms, *TR* = 500ms), T_2- and spin-density-weighted images with a TSE sequence (TE_{eff} = 16/98 ms, *TR* = 4000 ms). FLAIR images were obtained with *TR* = 6500 ms, TE_{eff} = 105 ms, and *TI* = 2200 ms. All reference datasets were acquired with a slice thickness of 8 mm, a FOV of 256x256 mm^2, and a data matrix of 250-252 x 256. The images were zero-filled to a matrix of 256 x 256. The total imaging time for the comparison data set (T_1-, T_2-, and spin-density-weighted plus FLAIR images) was just over 15 minutes, with actual data acquisition constituting 13 minutes of this time.

Generation of synthetic images

The TrueFISP signal recovery curves were fit to Eq. 6.2, and parameter maps were calculated using Eqs. 6.3-6.5. The small error that arises from incomplete T_1 relaxation during the waiting delay, however, which particularly affects the estimation of M_0 for compartments with long T_1, was corrected according to Eq. 6.9. Using these parameter maps, synthetic T_1-, T_2-, and spin-density-weighted images were generated to either match the contrast of a corresponding spin-echo or turbo spin echo (TSE) experiment, or to contain “pure” T_1, T_2, or spin-density contrast (by removing the weighting of all other contrast mechanisms). These images were calculated using the following expression derived from the Bloch equations [Mul91]:

$$S = M_0\left[1 - \exp\left(-\left(TR - TE_{Last}\right)/T_1\right)\right]\exp\left(-TE_{\text{eff}}/T_2\right), \qquad (1.13)$$

where TE_{eff} is the effective echo time for the TSE sequence (i.e. the echo time for the central lines of k-space), *TR* the repetition time, and TE_{last} the length of the entire echo train, i.e. the time from the center of the 90 degree pulse to the center of the last echo. The FLAIR signal intensity was calculated according to Eq. 6.1.

Comparison between synthetic and acquired contrast images

Besides a visual inspection of result images, a correlation analysis was conducted for the volunteer data. For each of the subjects, and for each of the different image contrasts, the relationship between acquired and calculated images was evaluated numerically by means of a pixel-based correlation. The regression analysis was carried out for a first region of interest (ROI) that encompassed the whole brain, but excluded the surrounding subcutaneous fat signal, and also for a second ROI that amounted to 7 cm x 3 cm in size and was chosen to cover the occipital region of the brain. Signal values from the acquired contrast images were normalized so that the minimum and maximum signal intensities from the whole brain corresponded to 0 and 1, respectively. The intensity values from the synthetic images were regressed against the separately acquired images. For the regression plots, the data was subjected to a linear transform such that the slope of the regression between the two signal intensities (in arbitrary units) was unity. Finally, correlation coefficients r and the corresponding p values were calculated to assess the similarity of synthetic and experimental images.

6.5 Results

All participating subjects were studied successfully. In following, image data are shown for a representative volunteer (subject #1 in Table 6.2). In Fig. 6.3, the T_1, T_2 and spin-density maps obtained from the IR TrueFISP data set are shown. The corresponding synthetic T_1-weighted, T_2-weighted, spin-density-weighted, and FLAIR images, which were calculted from the maps, are displayed in Fig. 6.4 (a-d), above their experimental counterparts as acquired with the individual sequences (e-h).

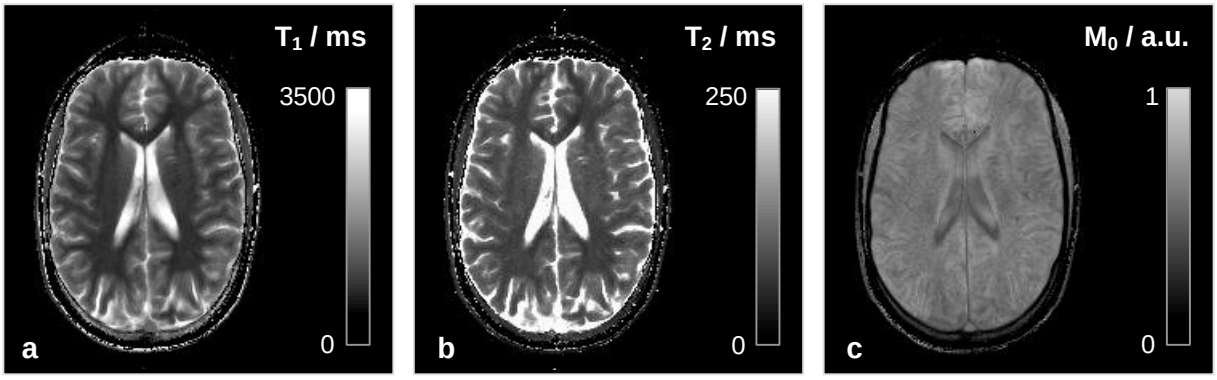

Fig. 6.3: (a) T_1 map (b) T_2 map (c) spin density maps calculated from the IR TrueFISP data.

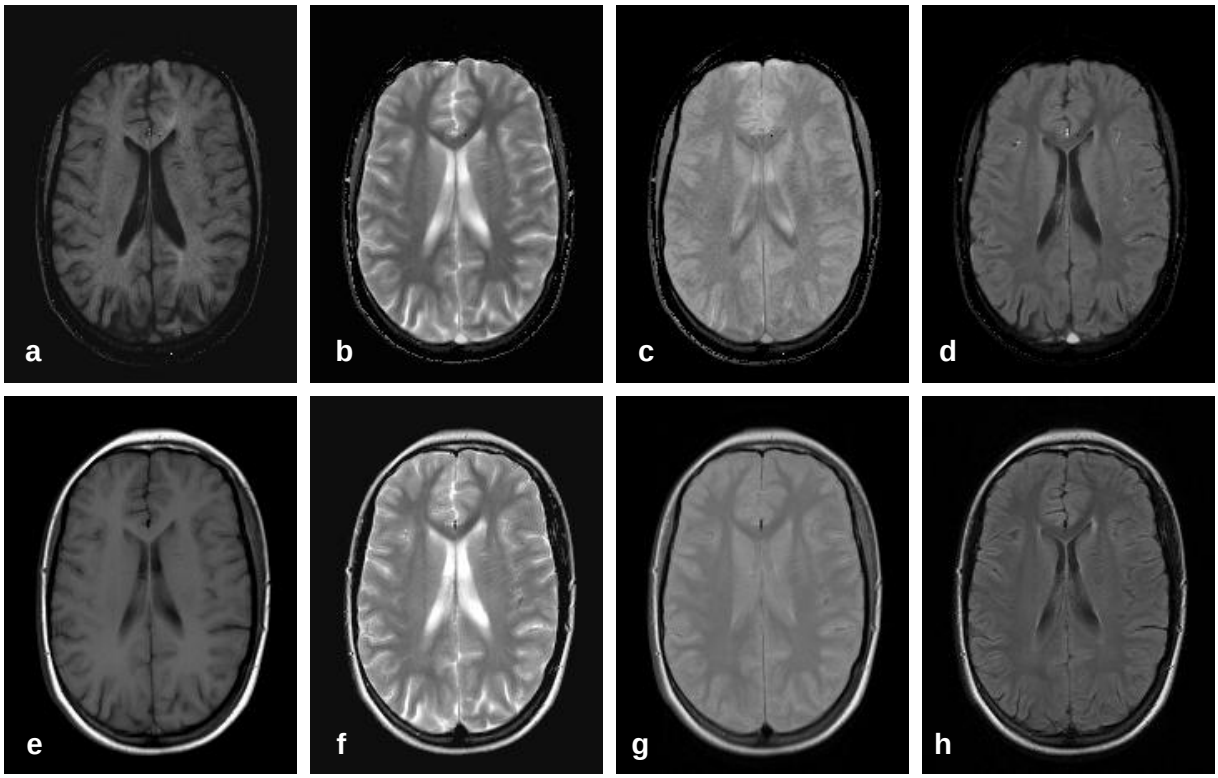

Fig. 6.4: Representative results obtained in subject #1 of Table 6.2. Synthetic images: (a) T_1-weighted with TE/TR = 14/500 ms, (b) T_2-weighted with TE/TR = 98/4000 ms, (c) spin density-weighted with TE/TR = 16/4000 ms, and (d) FLAIR with $TE/TI/TR$ = 105/2200/6500 ms; (e-h) corresponding acquired images from separate imaging sequences.

Fig. 6.5 illustrates the ROI that was used for analysis of the same volunteer as in Figs. 6.3 and 6.4. Figs. 6.6a-d show the scatter plots and regression lines for T_1-weighted, T_2-weighted, spin-density weighted, and FLAIR images, respectively. The regression values and corresponding p values for all volunteers are provided in Table 6.2.

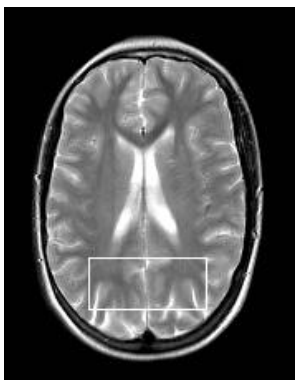

FIG. 6.5: ROI chosen for regression analysis, here shown on subject #1.

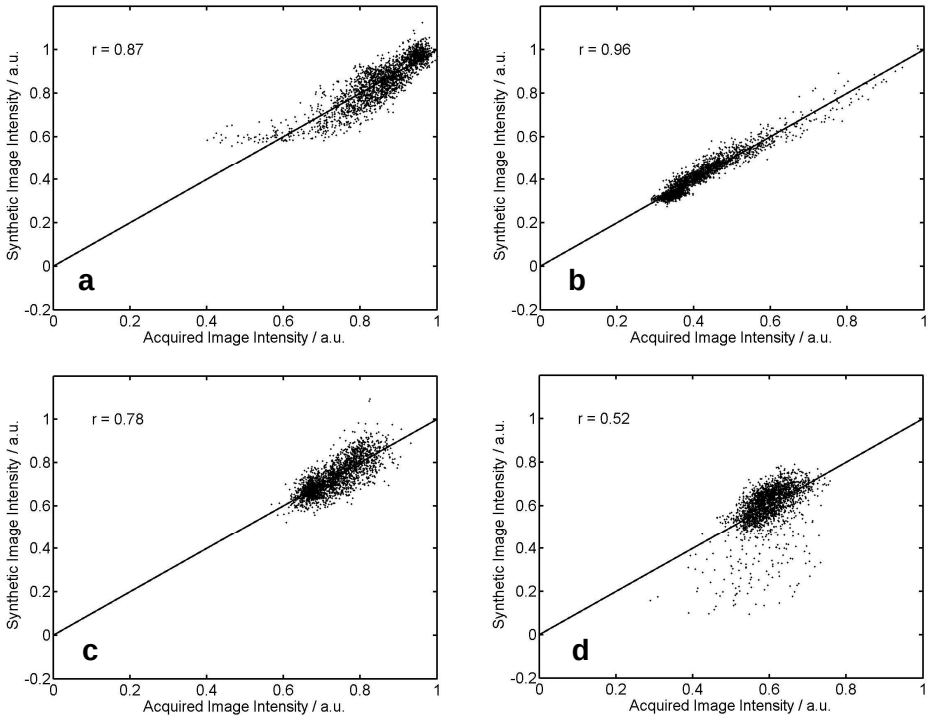

FIG. 6.6: Regression analysis for subject #1 for (a) T_1-weighted, (b) T_2-weighted, (c) spin-density weighted and (d) FLAIR images. The number of pixels was 2100 and p<<0.000001 for all cases.

	Whole brain ROI (15909 < n_{pix} < 17384)				ROI depicted in Fig. 6.5 (n_{pix} = 2100)			
Contrast (à)	T_1-w.	T_2-w.	M_0-w.	FLAIR	T_1-w.	T_2-w.	M_0-w.	FLAIR
Subject #	r	r	r	r	r	r	r	r
1	0.83 *	0.95 *	0.65 *	0.63 *	0.87 *	0.96 *	0.78 *	0.52 *
2	0.75 *	0.93 *	0.70 *	0.56 *	0.81 *	0.93 *	0.81 *	0.40 *
3	0.81 *	0.81 *	0.58 *	0.62 *	0.74 *	0.84 *	0.74 *	0.70 *
4	0.78 *	0.82 *	0.52 *	0.49 *	0.79 *	0.65 *	0.61 *	0.24 **
5	0.69 *	0.95 *	0.74 *	0.71 *	0.77 *	0.92 *	0.78 *	0.43 *
6	0.83 *	0.94 *	0.53 *	0.65 *	0.90 *	0.94 *	0.78 *	0.62 *

Table 6.2: Regression analysis for whole brain and occipital ROI (as shown in Fig. 6.5) for each of six subjects (* p<<0.000001, ** p<0.0001).

In Figs. 6.7a and 6.7b, images bearing “pure” T_1-weighted and T_2-weighted contrast (i.e., the weighting of all other contrast mechanisms removed) are displayed. The perfectly spin-density weighted image as shown in Fig. 6.7c is identical to the spin-density map of Fig. 6.3c.

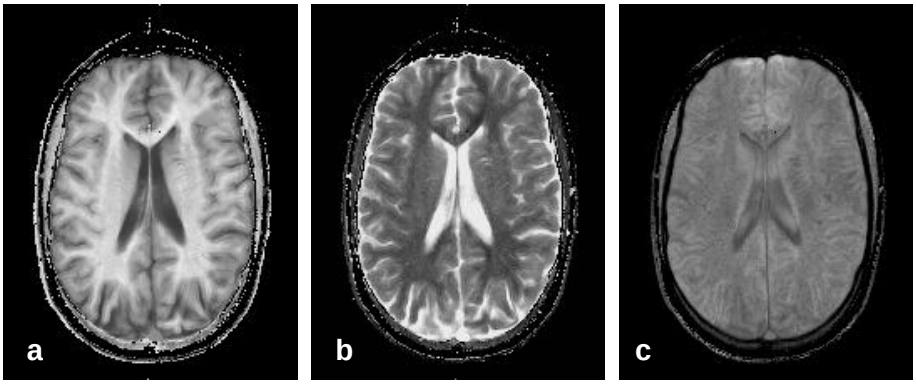

Fig. 6.7: Images generated to depict pure contrasts: (a) T_1-weighted with TR = 500 ms, (b) T_2-weighted with TE = 98 ms, and (c) pure spin-density-weighted contrast.

Figs. 6.8 and 6.9 illustrate the synthetic and acquired image results for the two patients investigated. The composition of both figures corrsponds to that of Fig. 6.4.

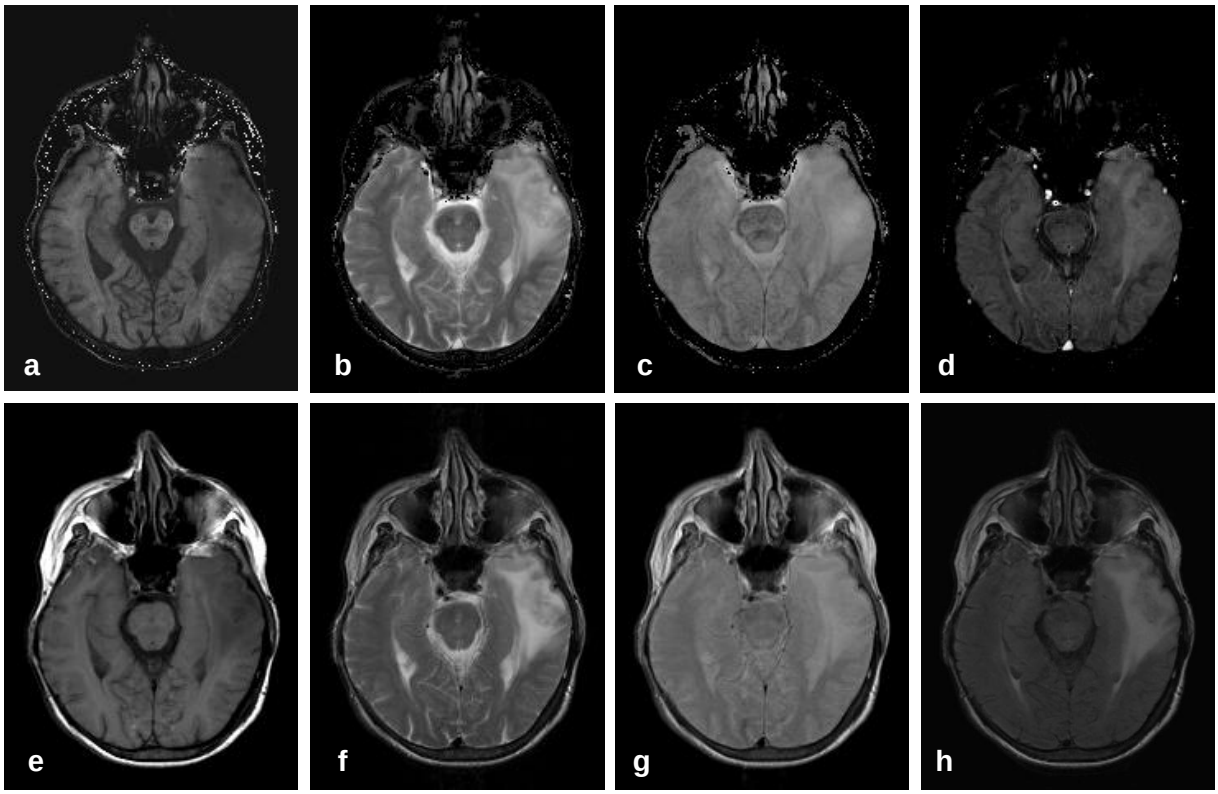

Fig. 6.8: Patient (male, 73 years) with glioblastoma; Synth. images: (a) T_1-w. with TR/TE = 500/14 ms, (b) T_2-w. with TR/TE = 4000/98 ms, (c) spin density-w. with TR/TE = 4000/16 ms, and (d) FLAIR with TR/TI/TE = 6500/2200/105 ms; (e-h) corresponding acquired images from separate sequences.

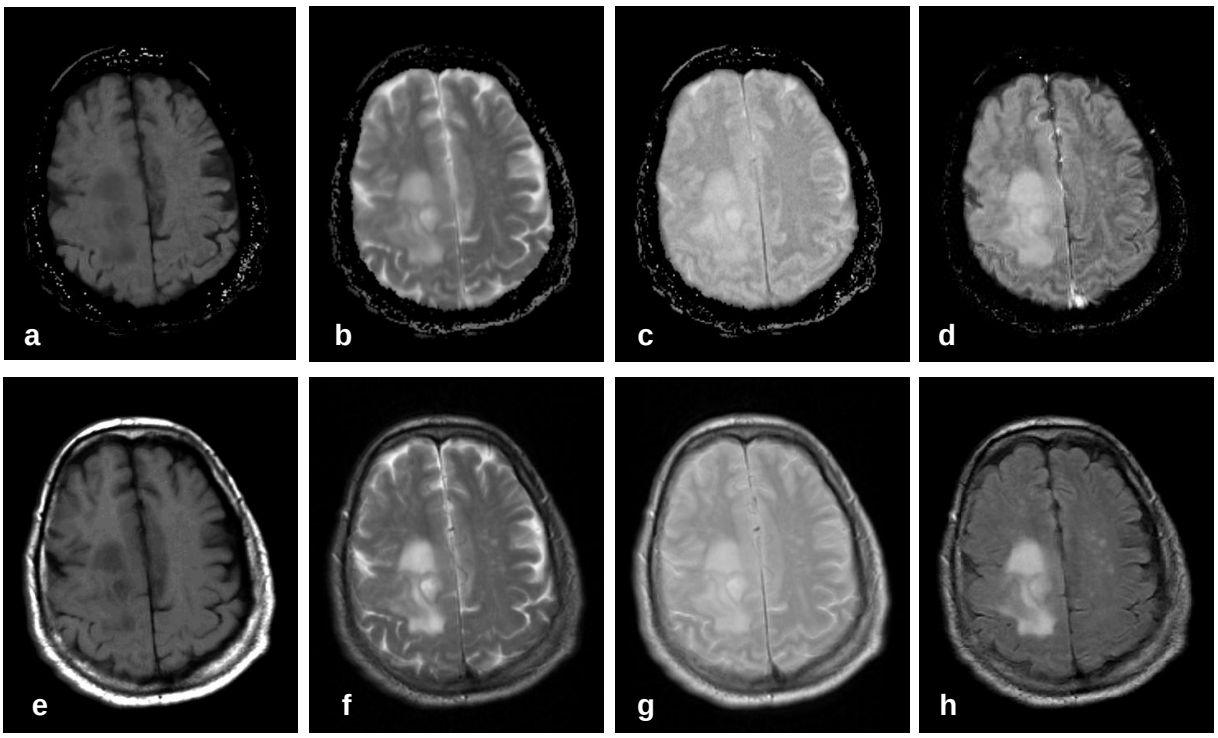

Fig. 6.9: Patient (male, 69 years) with glioblastoma; Synth. images: (a) T_1-w. with TR/TE = 500/14 ms, (b) T_2-w. with TR/TE = 4000/98 ms, (c) spin density-w. with TR/TE = 4000/16 ms, and (d) FLAIR with $TR/TI/TE$ = 6500/2200/105 ms; (e-h) corresponding acquired images from separate sequences.

6.6 Discussion

The contrast information for the images constructed from the IR TrueFISP data closely resembles that of a standard clinical MRI exam (T_1-weighted, T_2-weighted, spin-density weighted, and FLAIR), as can be seen from Fig. 6.4. In particular, the contrast between gray and white matter is very similar for the two image sets. Moreover, the regression analysis in Fig. 6.6 and Table 6.2 shows that there clearly is a linear relationship between the intensities from the images generated from the IR TrueFISP experiment and their acquired counterparts, even though the two sets of images can be expected to have different slice profiles, and correlation should be additionally degraded by potential motion between the multiple scans. The linear relationship between the signal intensities indicates that the two sets of images can be made to equal each other by employing a simple linear transform, validating the assertion that there is close agreement in generated contrast and that images calculated from the TrueFISP data can be used in lieu of the traditional images of corresponding contrast.

Minor differences are observed between the calculated and directly acquired data sets as shown in Fig. 6.4. In particular, CSF spaces in the calculated FLAIR image (Fig. 6.4d) are more prominent than in the experimental image (Fig. 6.4h). This can be attributed to partial volume effects. In a traditionally acquired image, a pixel that contains both CSF and gray matter has a signal intensity that depends approximately linearly on the fraction of CSF in the

voxel. A comparison betwen this signal behavior and the one expected from the new method is shown in Fig. 6.10, using simulated FLAIR data with varying fractions of CSF and gray matter. The simulations show that this signal behavior is more complex for images derived from the IR TrueFISP data sets, as the intensity is dependent largely on an apparent T_1 for that voxel and therefore is not linearly related to voxel volume fraction of CSF as would normally be the case. This behavior results in lower signal intensity compared to a normal FLAIR image for a large range of CSF fractions in the voxel and, hence, leads to a slightly larger appearance of CSF spaces. The remaining CSF/gray matter mixtures show higher signal with the new method. These subtle differences might actually prove to be an advantage during image interpretation, because the CSF and gray matter parenchyma are sometimes more clearly demarcated. The above-described behavior is also the reason that in Fig. 6.6d, a number of pixels are seen to lie below the regression line. These pixels essentially lie within the CSF spaces.

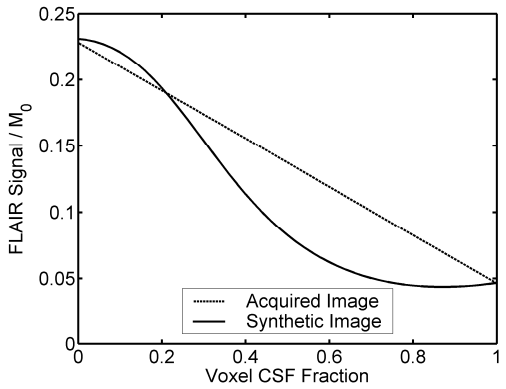

Fig. 6.10: Simulated data depicting FLAIR image signal intensity with various voxel volume fractions of CSF and gray matter. T_1/T_2 were assumed to be 4000/2500 ms for CSF and 1100/90 ms for gray matter, respectively.

The inherent flow sensitivity of the single slice TrueFISP sequence could introduce minor differences between the two sets of images. This phenomenon may potentially be encountered in the ventricles and it is clearly visible in the venous sinuses, which are brighter in the images from the TrueFISP data than in the standard images. A final difference between the two groups of images is that the bright rims arising from the fat within the skin are darker in the data sets derived from the IR TrueFISP data. The fat signal experiences off-resonance effects in the TrueFISP sequence itself, and therefore the parameter fits for fat are less reliable than for water. Also, it is well documented in the literature that fat has high signal on TSE images compared to single-echo spin echo due to modulation of j-coupling and decreased diffusive signal loss [Henk92, Stab99, Fau00]. The intensity difference therefore arises primarily because the TSE images give bright fat rims as compared to standard single spin echo images.

The synthetic images highlight the wealth of contrast information that can be derived from the data. These reconstructed “standard” T_1, T_2, spin density weighted, and FLAIR images can be provided to the interpreting physician, along with images where a desired amount of various kinds of contrast can be “dialed in,” depending on the clinical question at hand. While contrasts from T_1-, T_2-, and spin-density-weighted TSE images have been reproduced, this inherently may not be the ideal way to exploit all of the information, as TSE images are typically not purely T_1, T_2, or spin-density weighted, diluting the maximum contrast available due to a given parameter. For example, since gray matter has a longer T_1 but

also a higher spin-density than white matter, the intrinsic contribution from the spin-density parameter in T_1-weighted images decreases gray-white matter contrast. From the quantitative maps, however, one can construct perfectly T_1, T_2, and spin-density weighted images instead, as shown in Fig. 4 (a-b). As can be seen, this provides improved image contrast, particularly in the T_1-weighted image. In theory, an endless array of additional contrast possibilities exists. This possibility might be particularly useful in tumor imaging, where both an elevated spin density or an increased T_2 can counteract a signal reduction within a lesion due to a prolonged T_1, so that the origin of the contrast can remain unclear [Tof03].

Additionally, the quantitative T_1, T_2, and spin density information can be made available to the physician. Thus, all contrast characteristics can be evaluated and indeed, quantified. An analogy can be drawn to CT image display, where the underlying quantitative Hounsfield Units measurement is used to display the images in numerous windows. Similarly, one can envision radiologists using various “windows” with many different weightings, plus quantitative information to fully characterize lesions. Finally, another major advantage of the proposed method is that since the images constructed are derived from the same data set, they are perfectly registered, and thus the physician is not required to perform this important step while interpreting the images. Lesion/anatomical structure contrast characteristics in multiple “windows” can thus be determined precisely without inter-image misregistration, again as in the CT analogy.

In the present implementation of the method, images are acquired in the axial plane only, as single slices. Therefore, the used implementation presently does not provide a reduction in data acquisition time over traditional imaging. For a data set with ten slices, the acquisition time using the new method is roughly 21 minutes, while that using separate sequences is roughly 15 minutes. The problem of patient motion, therefore, will not be alleviated, although with the presented method motion artifacts would be limited to a single slice rather than the entire data set of a single contrast type. However, this is inherently a limitation of the used scanner setup and it can be expected that the required imaging time will be decreased significantly with a state-of-the-art MR system. Multi-slice interleaved acquisition is possible on present generation scanners (a two-fold time savings), and also the rather long *TR* used here (6.5 ms) can be shortened to 4-5 ms. Additionally, radial sampling with echo-sharing reconstruction has recently been applied along with IR TrueFISP to derive parameter maps, resulting in per-slice imaging times on the order of T_1, i.e. a few seconds [Gris99]. Partially parallel imaging [Pru99, Gris02] can also be used to reduce imaging time in general.

An important consideration with TrueFISP imaging in general is the influence of off-resonance effects. As noted previously, these may contribute to the difference in signal intensities of the subcutaneous fat between the two sets of images. Besides this aspect, however, no significant off-resonance artifacts were observed and an off-resonance correction of intracranial signal was not necessary. Off-resonance effects may pose greater difficulty in the implementation of this method in the body, where it would likely be necessary to estimate the exact frequency for each pixel, probably requiring alterations in the imaging scheme.

6.7 Conclusion and retrospect

In this study, a method was presented for generation of perfectly registered images with any desired T_1, T_2, or proton density weighting from a single sequence examination along with quantitative parameter maps. The generated images were comparable to those obtained for a routine clinical exam. In the future, it can be expected that it becomes possible to acquire the images faster (as detailed in the previous section) and in three-dimensional fashion, by adding a slice encoding dimension. As a result, clinical images could be reconstructed in coronal, sagittal, or axial orientation, allowing the radiologist to characterize T_1, T_2, spin density, and additonal contrasts in any planes of choice. Future experiments should investigate the method after administration of contrast agent, particularly in patients with brain pathology.

After this study was published [Gul04], the universal concept of using a single MR sequence for generation of quantitative multi-parameter maps was pursued by other research groups [War07]. This approach was also combined with the calculation of synthetic multi-contrast MR images [War08], which yielded the basis for foundation of an awarded start-up company (http://www.syntheticmr.se). Later investigations in a clinical setting demonstrated that synthetic images could be obtained in short scan times and corresponded to the clinical diagnoses as well as acquired differently weighted images [Bly12].

Chapter 7

T-One-insensitive steady state imaging (TOSSI)

A novel concept called T-One-insensitive Steady State Imaging (TOSSI) is proposed for fast generation of purely T_2 -weighted MR images. This is achieved by imaging between non-equally spaced inversion pulses, with the magnetization vector alternatively residing in states parallel and anti-parallel to B_0 for durations TP_i and TA_i, respectively. With TP_i and TA_i adequately chosen, identical signal time courses can be obtained for different T_1 values, i.e. T_1 contrast can efficiently be removed from resultant images. As a specific realization of this principle, TOSSI sequences are presented that use TrueFISP readout blocks between the inversion pulses. While the standard TrueFISP signal time course would be determined by both T_2 and T_1, a pure T_2 dependence is realized with successfully suppressed influence of longitudinal relaxation, and images with essentially T_2 contrast alone are obtained. Analytical expressions are provided for the description of the ideal signal behavior, which help in creating pathways for sequence parameter optimization. The performance of the technique is analyzed with Bloch equation simulations. In-vivo results are presented that were obtained in healthy volunteers and brain tumor patients. This chapter reflects the contents of a corresponding peer-reviewed journal article [Schm12].

7.1 Introduction

According to Eq. 4.2, the steady state signal of a TrueFISP acquisition with $TR << T_1,T_2$ can be approximated as dependent on the ratio of T_2 and T_1. This contrast, however, is not useful in many applications. For example, in brain imaging, the TrueFISP contrast between CSF and parenchyma is high, but it is rather poor between gray and white matter [Haac90], and it might be difficult to detect lesions with both elevated T_1 and T_2. Though TrueFISP was used in studies that were aimed at obtaining "T_2-like" contrast, the authors implied that it should actually be considered dependent on T_2/T_1 [Due98, Chu00].

While these findings hold true for the steady state, a mixed contrast is generated in situations when central k-space data are acquired before the steady state is reached, as for instance in 2D imaging with short imaging times. For this situation, it was observed that the

contrast changes in a smooth way from spin-density-weighted to T_2/T_1-weighted [Hua02]. Specifically, it is determined by the transient TrueFISP signal, which - after suitable preparation or catalyzation to avoid signal oscillations [Deim94, Nis00, Har01] - shows exponential behavior and dependence on T_1, T_2 and the flip angle [Schm02] and can be described by closed mathematical formulations [LeR03, Sche03b, Gan04, Schm06]. Since it would clearly be useful to achieve (or increase) T_2-weighted contrast in many clinical situations, researchers have proposed sequences that are not pure TrueFISP acquisitions and show modified contrast behavior. For example, a T_2 preparation module - first reported in the context of coronary imaging [Brit95] - was used prior to the TrueFISP acquisition [Shea02, Hua07]. This leads to a situation where pure T_2 contrast is generated directly after the preparation, at the expense of reduced SNR. Additionally, while the initial contrast ideally is T_2-weighted, the evolution during the subsequent acquisition is also significantly influenced by T_1. In a different approach, called T_2-TIDE, T_2 contrast is created within a TrueFISP sequence: A 90 and a series of 180 degree pulses are used at the beginning of the acquisition and thereafter, the flip angle is ramped down to a predetermined target value [Paul06]. Here, the signal evolution begins with a fast T_2 decay (as would be expected from the similarity to a TSE or HASTE sequence). With decreasing flip angle, however, the T_1 influence becomes increasingly prominent during the evolution to the TrueFISP steady state of the target flip angle. In both cases, the early introduction of T_2 contrast induces a quick loss of signal, and T_1 effects become more evident during the subsequent signal evolution, so that an acquisition interval of only limited duration can be used if T_2 contrast is desired.

Contrary to these approaches which essentially aim to increase T_2 weighting, this chapter presents a method called T-One-insensitive steady state imaging (TOSSI), which aims at reducing or eliminating T_1 contrast [Schm03b, Schm04b]. In this concept, signal from longitudinal relaxation is allowed to enter the imaged signal, but T_1 contrast is eliminated throughout the acquisition via a train of non-equally spaced 180°-pulses that are inserted into the sequence. Thus, when applied to TrueFISP imaging, images with essentially pure T_2 contrast can be obtained in a short, high SNR acquisition.

The general principle of the TOSSI concept is explained below and analytic expressions are derived for both the ideal signal evolution and the calculation of optimal delays between inversion pulses, which can be used as a basis for further sequence optimization. The behavior of the magnetization is modelled using numerical simulations of the Bloch equations. Moreover, data acquired in healthy volunteers and patients with brain tumors demonstrate that TrueFISP images with T_2 contrast comparable to traditional TSE approaches can be acquired within short imaging times.

7.2 Theory

In this section, basic considerations and simulations based on the Bloch equations are used to introduce the fundamentals of the TOSSI concept. First, in order to introduce properties of a train of inversion pulses, separated by alternating intervals *TP* and *TA*, and to prepare the concept of a continuously varying *TP*/*TA* pattern, a general description is derived from a situation of free relaxation: It is shown that such a pulse series efficiently locks the longitudinal magnetization around a value M_z that is independent of T_1, which in turn means that T_1 effects can be removed in medium term for a certain value of M_z by using the appropriate

TP/*TA* ratio. Hence, if M_z changes during a TOSSI acquisition due to non-T_1 influences, a *TP*/*TA* ratio continuously adapted to the corresponding evolution of M_z can maintain T_1 independence. Moreover, the concept of inserting TrueFISP as a readout module in between the inversions is proposed and analyzed. Starting from the transient TrueFISP signal behavior and incorporating the assumption that T_1 influence can be efficiently eliminated, a function is developed for the ideal TOSSI signal evolution. Finally, using a close-up look at both this idealized function and a real TOSSI signal curve, optimized temporal inversion patterns are derived. In this project, the analytic description is confined to on-resonant behavior.

Basic concept:

The central concept behind TOSSI involves a basic mechanism of longitudinal relaxation: If a magnetization vector M resides in an orientation with negative longitudinal component M_z, i.e. anti-parallel to B_0, the magnitude of M_z will be reduced during longitudinal relaxation. If, however, ***M*** is oriented parallel to B_0, the magnitude of M_z will grow in amplitude until it equals M_0. Hence, it should be feasible to compensate the respective changes in the magnitude of M_z by alternately keeping ***M*** in anti-parallel and parallel orientations, and to eliminate the mid-term influence of T_1.

For a magnetization vector of a specific length, the rate of relaxation is “faster” when M_z is negative when compared to a situation with positive M_z. Hence, it might intuitively be expected that the goal of T_1 insensitivity may be achieved when ***M*** resides in the anti-parallel state for a longer time when compared to the parallel direction. The simplest way this condition can be created is by using a train of non-equally spaced inverting RF pulses.

Train of non-equidistant inversion pulses: Bloch Simulations

A train of 180° inversion RF pulses applied to a magnetization ***M*** (for now without any additional spin excitation or signal acquisition), alternately separated by delays *TP* and *TA*, leads to a remarkable behavior: After a sufficiently high number of pulses, the temporal evolution of ***M*** converges towards a dynamic steady state of the magnitude of its longitudinal component M_z that is essentially independent of T_1. The magnitude remains close to a mean value M_m, and relaxation takes place around this value with identical time courses within each of the intervals *TA* and *TP*, respectively. For $TP > TA$, M_z will point in the direction of B_0 during *TP* (“parallel”) and in the opposite direction during *TA* (“anti-parallel”), as expected.

This concept was tested with numerical simulations of the Bloch equations using Matlab (MathWorks, Inc.). Specifically, the dynamics of M_z after 1000 inversion pulses - used to ensure that the “locked” condition is established - was modelled for a wide range of physiologically relevant T_1 times and various ratios $R = TA/TP$. In Fig. 7.1, simulation results are plotted for two considerably different T_1 times of 200 ms and 3000 ms. Comparable simulations for intermediate T_1 times would give rise to curves which fall between the two examples presented. Different *R* values were generated by keeping the sum of *TA* and *TP* constant at 48 ms, while adapting *TP* and *TA* accordingly.

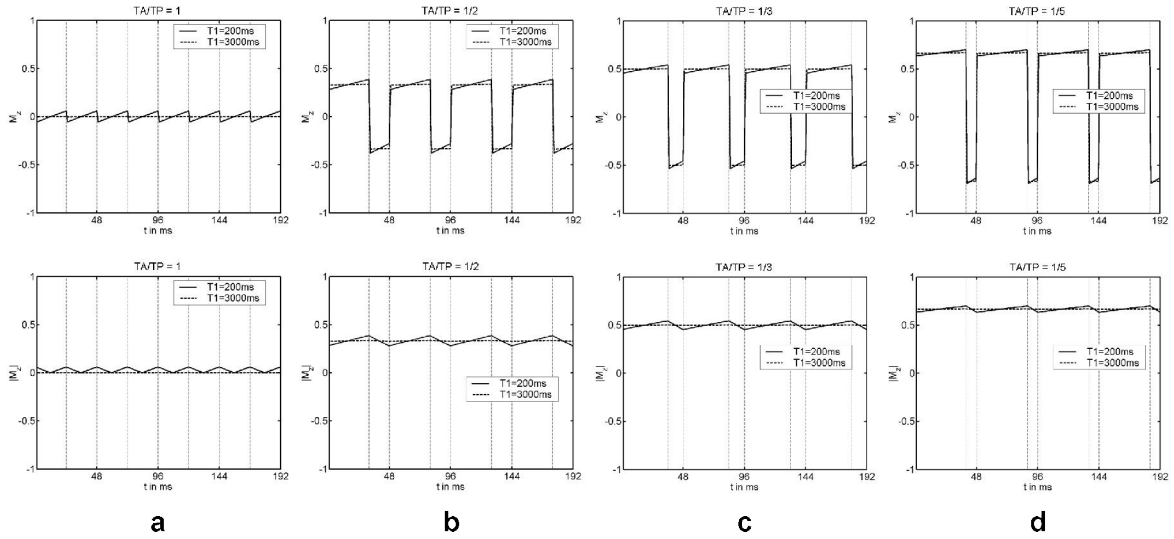

Fig. 7.1: Bloch simulations: Dynamic steady state of the evolution of M_z for a train of inversion pulses that are alternately separated by delays *TP* and *TA*. Time courses of (top) M_z and (bottom) $|M_z|$ are shown for (a) $R = 1$ ($M_m = 0$), (b) $R = 1/2$ ($M_m = 1/3\ M_0$), (c) $R = 1/3$ ($M_m = 1/2\ M_0$), (d) $R = 1/5$ ($M_m = 2/3\ M_0$).

As can be seen, the magnetization approaches the same M_m values for each *TA*/*TP* ratio, even for considerably different T_1 times. Small differences in the curves exist as faster relaxation with shorter T_1 gives rise to more prominent “zigzag” pattern around M_m. However, these results highlight the basic principle of TOSSI: Even though the T_1 values of these two species differ by a factor of 15, most of the difference (i.e., the contrast) between them has been removed while maintaining high magnetization throughout the pulse sequence.

Train of non-equidistant inversion pulses: Basic considerations

The findings described above can easily be formulated in an analytical manner. The dynamic steady state is established when the loss of $|M_z|$ during *TA* and the gain of $|M_z|$ during *TP* compensate each other. This situation is illustrated in Fig. 7.2.

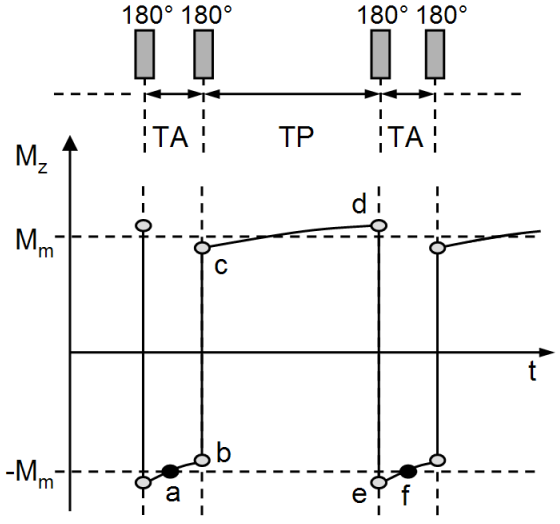

Fig. 7.2: Schematic display: Dynamic steady state of the evolution of M_z for a train of inversion pulses that are alternately separated by delays *TP* and *TA*.

With the assumption that M_m in good approximation corresponds to the value of $|M_z|$ in the center of the intervals *TA* and *TP*, respectively, the evolution of M_z can be described by the following steps:

a - b (relaxation): $$M_b = M_0 - (M_0 - M_a) \exp(-TA/(2T_1)) \quad (7.1)$$

b - c (inversion): $$M_c = -M_b \quad (7.2)$$

c - d (relaxation): $$M_d = M_0 - (M_0 - M_c) \exp(-TP/T_1) \quad (7.3)$$

d - e (inversion): $$M_e = -M_d \quad (7.4)$$

e - f (relaxation): $$M_f = M_0 - (M_0 - M_e) \exp(-TA/(2T_1)) \quad (7.5)$$

Here, *TP* and *TA* represent the evolution times in the antiparallel and parallel orientations as shown in Fig. 7.2 while M_f and M_a represent the magnitude of the longitudinal magnetization at the times “a” and “f”. The equlibrium state sketched in Fig. 7.2 is reached when the condition $|M_f| = |M_a| = M_m$ is fulfilled. From Eqs. 7.1-7.5, the following expression can be obtained for M_m:

$$M_m = -M_0 \frac{1 - 2\exp\left(-\frac{TA}{2T1}\right) + 2\exp\left(-\frac{TA+2TP}{2T1}\right) - \exp\left(-\frac{TA+TP}{T1}\right)}{\exp\left(-\frac{TA+TP}{T1}\right) - 1} \quad . \quad (7.6)$$

For $TA << T_1$, the approximation $\exp(-TA/T_1) \approx 1 - TA/T_1$ can be substituded into Eq. 7.6 (as can $1 - TA/TP$, by analogy for the exponential terms involving *TP*), and M_m becomes

$$M_m \approx M_0 \frac{-T1 \times TA + T1 \times TP - TA \times TP}{T1 \times TA + T1 \times TP - TA \times TP} \quad . \quad (7.7)$$

Since *TA* and $TP << T_1$, the second-order term *TA***TP* may be eliminated, and M_m can be rewritten as:

$$M_m \approx M_0 \frac{1 - (TA/TP)}{1 + (TA/TP)} \quad (7.8)$$

Under these conditions, and if the approximations are valid, M_m is independent of T_1.

Optimum *TA*/*TP* ratio for T_1 compensation

From the analyses above, a reciprocal conclusion can be drawn by inverting the explanation: If the longitudinal magnetization component has a specific value M_z, this amount of longitudinal magnetization can be conserved by a train of non-equidistant inversion pulses, independent of T_1. The optimum *TA*/*TP* ratio, R_{opt}, to remove the long-term influence of T_1 relaxation on the magnitude of M_z can be determined by inverting Eq. 7.8:

$$R_{opt} = \frac{M_0 - M_z}{M_0 + M_z} \quad . \quad (7.9)$$

This expression is in very good correspondence with the simulations shown in Fig. 7.1. Though it had been derived graphically for *TP* > *TA*, it also correctly reflects the special case of $R = 1$, where M_z passes the zero axis during each relaxation period, and is turned back into anti-parallel orientation by each inversion pulse.

Moreover, if the concept is used with imaging sequence readout blocks in between the inversions, the magnetization is additionally subjected to the influence of the RF pulses and transverse relaxation, and will change over time. Hence, the optimum ratio *TA*/*TP* that serves to eliminate the influence of longitudinal relaxation, will also become time-dependent:

$$R_{opt}(t) = \frac{M_0 - M_z(t)}{M_0 + M_z(t)} \quad . \tag{7.10}$$

If a temporal signal course is considered that is independent of T_1, the image contrast will be generated by the remaining parameters that determine the contrast behavior of the sequence, e.g. transverse relaxation. With the $M_z(t)$ of a specific target T_2 time inserted in Eq. 7.10, a function $R(t)$ value should be obtained that should provide an efficient separation of T_2 components close to the chosen target T_2 value. In the following, this hypothesis is analyzed for an implementation that uses TrueFISP as the readout sequence during *TA* and *TP*.

TrueFISP: Signal behavior in the transient phase

In standard TrueFISP imaging, the on-resonant magnetization vector approximately evolves on a cone with angle a/2 to the z axis, where it is flipped from one side to the other by successive RF pulses [Deim94, Sche01b, Sche03c]. The transient signal can be expressed by [Schm04a]:

$$S_{TrueFISP}(t) = S_{stst} + (S_0 - S_{stst}) \exp(-t / T_1^*) \quad . \tag{7.11}$$

Here, after preparation of the magnetization vector to the cone with angle a/2 with respect to the z axis [Deim94], the signal time course starts at

$$S_0 = M_0 \sin(\mathrm{a}/2) \quad , \tag{7.12}$$

and evolves smoothly with an apparent relaxation time constant T_1^* [Sche03, Schm04a, Schm06] given by

$$T_1^* = \left(\frac{\cos^2(\mathrm{a}/2)}{T_1} + \frac{\sin^2(\mathrm{a}/2)}{T_2} \right)^{-1} \quad . \tag{7.13}$$

It converges towards its steady state signal S_{stst}, which can be approximated by:

$$S_{stst} = \frac{M_0 \sin \mathrm{a}}{(T_1/T_2 + 1) - \cos \mathrm{a} \times (T_1/T_2 - 1)} \quad . \tag{7.14}$$

In the TrueFISP steady state, the loss of magnetization caused by transverse relaxation within each TR interval is compensated by a corresponding gain originating from longitudinal relaxation. For an actual signal smaller than the steady state signal, the evolution towards S_{stst} is part of the TrueFISP signal time course in an inversion recovery experiment, with a

180° pulse preceding the α/2 preparation [Deim94]. It is also described by Eq. 7.11, if a value of

$$S_0 = -M_0 \sin(\alpha/2) \tag{7.15}$$

is inserted for the initial signal. Per convention, negative signal values are used in this paper to describe TrueFISP signal with negative M_z.

TOSSI: Idealized signal curve with TrueFISP readout blocks

For a TrueFISP-based TOSSI implementation, inversion pulses are inserted into the TrueFISP sequence in non-equally spaced fashion in order to remove the influence of longitudinal relaxation, with imaging data acquisition alternatively taking place in states that are oriented parallel and anti-parallel to B_0. Hence, starting with parallel orientation, the resulting signal evolution ideally would reflect the transient signal of a TrueFISP experiment, but with its T_1 dependence removed. To derive an idealized (albeit not realizable) function for such a signal evolution, the hypothesis must be incorporated that longitudinal relaxation is eliminated completely. This assumption can be mathematically introduced into Eq. 7.11 by setting T_1 to infinity (i.e. T_1 ® ¥) in Eqs. 7.13 and 7.14. As a result, the first term in Eq. 7.13 vanishes and the steady state signal in Eq. 7.14 becomes zero, so that the following simple expression is obtained for the idealized TOSSI signal time course:

$$|S_{TOSSI}(t)| = |M_0 \sin(\alpha/2) \exp(-(t/T_2)\sin^2(\alpha/2))|, \tag{7.16}$$

From this equation, it can be seen that the transverse magnetization decays significantly slower for TOSSI as compared to free relaxation or an ideal TSE acquisition with 180° refocusing pulses. While the signal of a TOSSI acquisition is scaled with an additional factor sin(α/2), its contrast with a specific effective TOSSI echo time $TE_{eff,TOSSI}$ (i.e. the time span between the start of the echo train and the acquisition of k-space center) should correspond to that of a TSE acquisition with an echo time of

$$TE_{TSE} = TE_{eff,TOSSI} \sin^2(\alpha/2) \quad . \tag{7.17}$$

In TrueFISP-based TOSSI, the signal should evolve closely along the idealized curve given by Eq. 7.16. In analogy to the case of free relaxation shown in Figs. 7.1 and 7.2, however, and since M_z is alternately oriented towards positive and negative z direction, the real signal will show fluctuations around the idealized time course. It will be constituted of “pieces” that alternately originate from the corresponding transient TrueFISP and IR-TrueFISP curves and cross the idealized function from below and from above. If the real signal curve is supposed to cross the idealized curve at an arbitrary time *t*', its slope at this point is solely determined by the actual magnetization state. Specifically, it will correspond to the slope of the transient TrueFISP or IR-TrueFISP signal time curve in exactly the same state, i.e. at the identical signal value (Fig. 7.3). These slopes can be graphically obtained from points in time where the respective signal values amount to $S_{TrueFISP} = S_{TOSSI}(t')$ (Fig. 7.3, arrow A) or $S_{IR\text{-}TrueFISP} = -S_{TOSSI}(t')$ (Fig. 7.3, arrow B), depending on whether ***M*** is in the parallel or anti-parallel phase, respectively. Within each short *TP* and *TA* section, the signal dynamics will be driven by both relaxation and RF pulses, leading to a subtle oscillatory pattern. One might expect that differ-

rent values for the *TA/TP* ratio may be optimal along the TOSSI curve, but its dependency on parameters such as T_1, T_2 and flip angle is yet to be determined.

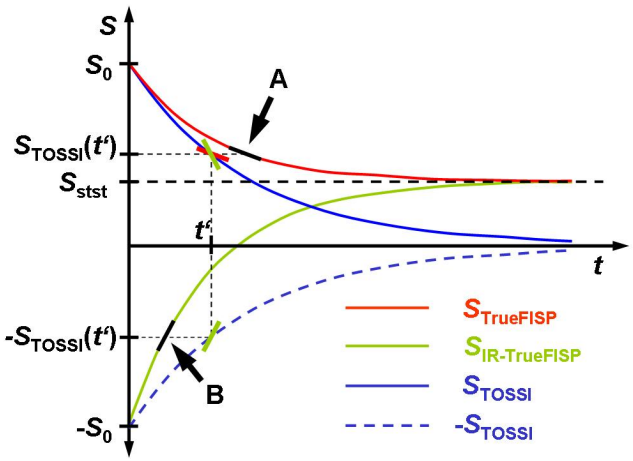

Fig. 7.3: Schematic display of an idealized TOSSI signal time course (blue & solid). At a specific time *t'*, where the real signal curve is supposed to cross the idealized curve, the true evolution (i.e. its slope) is determined by the behavior of the corresponding transient TrueFISP (red & solid) or IR TrueFISP (green & solid) curves, depending on whether M_z is oriented in positive or negative z direction. In specific, the slope can be graphically obtained as the tangents of these curves at time points with identical signal magnitudes, i.e. where the values of $S_{TrueFISP}$ (arrow A) or $S_{IR\text{-}TrueFISP}$ (arrow B) are equal to those of $S_{TOSSI}(t')$ or $-S_{TOSSI}(t')$.

Derivation of optimized temporal patterns

Based on the considerations above, optimized temporal schemes can be determined by analyzing the slopes of the ideal TOSSI function and the transient TrueFISP signal evolutions. The question is which combination of *TA* and *TP* would lead to complementary deviations at a specific point in time. With the assumption that the intervals *TA* and *TP* are short compared to the relaxation times, a linear approximation of the exponential signal evolution is valid and the ideal TOSSI function as well as the real signal during *TA* and *TP* may be approximated by linear functions over time. If both possibilities of a parallel or anti-parallel orientation are assessed simultaneously at a specific time point *t'* of the idealized TOSSI curve, the real signal curves (i.e. the tangents from $S_{TrueFISP}$ and $S_{IR\text{-}TrueFISP}$), can be considered to cross the TOSSI curve in the middle of either the *TA* or *TP* interval. This is sketched in Fig. 7.4., which represents a close-up view of Fig. 7.3 at time *t'*.

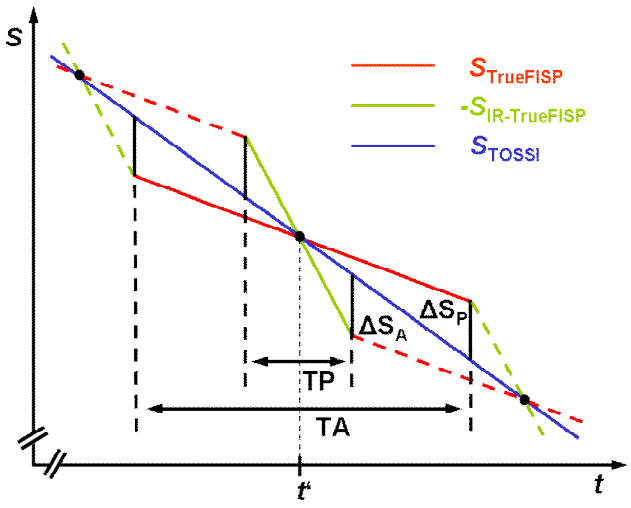

Fig. 7.4: Schematic close-up view of an idealized TOSSI function (blue) and two corresponding "pieces" of actual signal courses as they would occur around a time point *t'* in a real TOSSI signal evolution during a parallel (red) or anti-parallel (green) phase. The slopes of these real signal curves match those of corresponding transient TrueFISP or IR-TrueFISP evolutions at identical signal values. An optimal ratio of TP/TA can be derived by inserting the condition that the deviations DS_P and DS_A compensate each other.

The slope of each linear function will be determined by the first derivation of the respective exponential time course. In specific, the slope of the TrueFISP evolution amounts to

$$dS_{TrueFISP}(t)/dt = -\left[(S_0 - S_{stst})/T_1^*\right]\exp(-t/T_1^*) = (S_{stst} - S_{TrueFISP}(t))/T_1^* \quad . \qquad (7.18)$$

This formulation is valid irrespective of the value of S_0, i.e. Eq. 7.18 holds true for both TrueFISP as well as other schemes such as IR TrueFISP. For the ideal TOSSI curve, the slope can be calculated as

$$m_{TOSSI}(t) = \frac{dS_{TOSSI}(t)}{dt} = -\frac{M_0 \sin^3(a/2)}{T_2}\exp(-(t/T_2)\sin^2(a/2)) = -\frac{\sin^2(a/2)}{T_2}S_{TOSSI}(t) \ . \quad (7.19)$$

The slopes during m_A und m_B correspond to slopes of TrueFISP curve, but not to those at the time t of interest, but for those times where the signal matches that of the TOSSI signal at time t. Hence, m_P is retrieved by inserting $S_{TOSSI}(t)$ in Eq. 7.18, which results in

$$m_P(t) = \left.\frac{dS_{TrueFISP}}{dt}\right|_{S_{TrueFISP}=S_{TOSSI}(t)} = \frac{(S_{stst} - S_{TOSSI}(t))}{T_1^*} \quad , \qquad (7.20)$$

The slope m_A, however, is retrieved by inserting the negative value $-S_{TOSSI}$ to consider the TrueFISP situation with negative M_z, and after multiplication with -1 in order to treat the signal curve as mirrored into the positive range:

$$m_A(t) = -\left.\frac{dS_{TrueFISP}}{dt}\right|_{S_{TrueFISP}=-S_{TOSSI}(t)} = -\frac{(S_{stst} - (-S_{TOSSI}(t)))}{T_1^*} = -\frac{(S_{stst} + S_{TOSSI}(t))}{T_1^*} \quad (7.21)$$

It can easily be shown that the relation

$$m_P(t) < m_{TOSSI}(t) < m_A(t) \quad , \qquad (7.22)$$

holds true for a/2 < 90°, i.e. that the real evolution is steeper than that of the ideal TOSSI curve when ***M*** is anti-parallel, and that it is less steep when parallel to B_0. The deviations of the real signal evolution from the ideal TOSSI signal (before and after crossing it) induced in parallel state and in the anti-parallel state can be expressed by

$$\Delta S_P = m_P TP/2 - m_{TOSSI} TP/2 \quad \text{and} \qquad (7.23)$$

$$\Delta S_A = m_A TA/2 - m_{TOSSI} TA/2 \quad . \qquad (7.24)$$

The ideal TA/TP ratio, R_{opt}, for balancing the signal along the ideal TOSSI curve is found when both signal deviations match:

$$\Delta S_A = \Delta S_P \quad , \qquad (7.25)$$

so that R_{opt} can be written as

$$R_{opt} = TA/TP = \frac{(m_A - m_{TOSSI})}{(m_B - m_{TOSSI})} \quad . \qquad (7.26)$$

After insertion of Eqs. 7-19-7.21, and using Eqs. 7.13-7.14 for S_{stst} and T_1^*, this expression reduces to

$$R_{opt}(t) = \frac{1 - \cos(a/2)\exp(-(t/T_2)\sin^2(a/2))}{1 + \cos(a/2)\exp(-(t/T_2)\sin^2(a/2))} \quad . \tag{7.27}$$

For magnetization on the a/2 cone, its transverse and longitudinal component relate to each other as

$$M_{xy}\cos(a/2) = M_z \sin(a/2) . \tag{7.28}$$

Hence, the longitudinal component of *M* can be expressed as

$$M_z(t) = M_0 \sin(a/2)\exp(-(t/T_2)\sin^2(a/2)) . \tag{7.29}$$

The comparison of Eq. 7.27 with the ideal TOSSI curve yields:

$$R_{opt}(t) = \frac{M_0 - M_{Z,TOSSI}(t)}{M_0 + M_{Z,TOSSI}(t)} \quad . \tag{7.30}$$

This directly corresponds to Eq. 7.10 which had been derived in a more general fashion from the free relaxation situation. With Eq. 7.27, it is now possible to derive optimized temporal schemes for subsequent times *TP* and *TA* at a certain flip angle for components with T_2 times around a certain T_2 of interest.

7.4 Methods

From the analytical calculations of relaxation characteristics, temporal patterns were derived for the design of TOSSI acquisition schemes. Typically, values between 75 ms and 125 ms were used as the target range for T_2, corresponding to values expected for brain parenchyma. Numerical simulations of the expected signal evolutions, based on the Bloch equations, helped to investigate and further optimize the magnetization time course behavior of specific sequence embodiments. As before, for simplification, both RF pulses and signal acquisition were assumed infinitesimally short.

In order to assess the influence of the resulting signal curves on spatial encoding and image resolution, and to investigate the influence of the off-resonant behavior, additional simulations were carried out for gray matter (GM) and fat. For these tissues, T_1 / T_2 values were assumed to be 1165 ms / 92 ms [Schm04a] and 343 ms / 58 ms [deB04], respectively. For fat, an off-resonance frequency of 220 Hz was used (assuming 1.5T), which corresponds to a dephasing angle of 152° over the TR interval of 6.46 ms. From the simulated signal curves, corresponding point spread functions (PSFs) were calculated by zero-filling the data to 4096 points, a subsequent Fourier transformation and a normalization to a maximum value of 1 for the PSF of GM.

For a first actual implementation, multiple TOSSI sequence variants were implemented on a 1.5T clinical MR system (Magnetom Vision, Siemens Healthcare Sector, Germany). The basis for the imaging blocks was a standard TrueFISP sequence, with *NA* and *NP* acquisition

intervals during the anti-parallel and parallel imaging block, respectively. As illustrated in Fig. 7.5, each block was prepared with an α/2- and concluded with a -α/2-pulse [Deim94, Sche01b] in order to maintain smooth transient state conditions on either side of the inversion pulses. Due to software constraints on the scanner used in these experiments, it was only possible to implement the TOSSI concept with constant values for *NA* and *NP*, i.e. with constant *TA*/*TP* ratios. Single-shot TOSSI sequences with linearly incrementing phase encoding steps were realized and tested with different timing schemes. To account for the inverted state of the magnetization vector during the *TA* periods, the respective data were scaled by -1.0 before reconstruction.

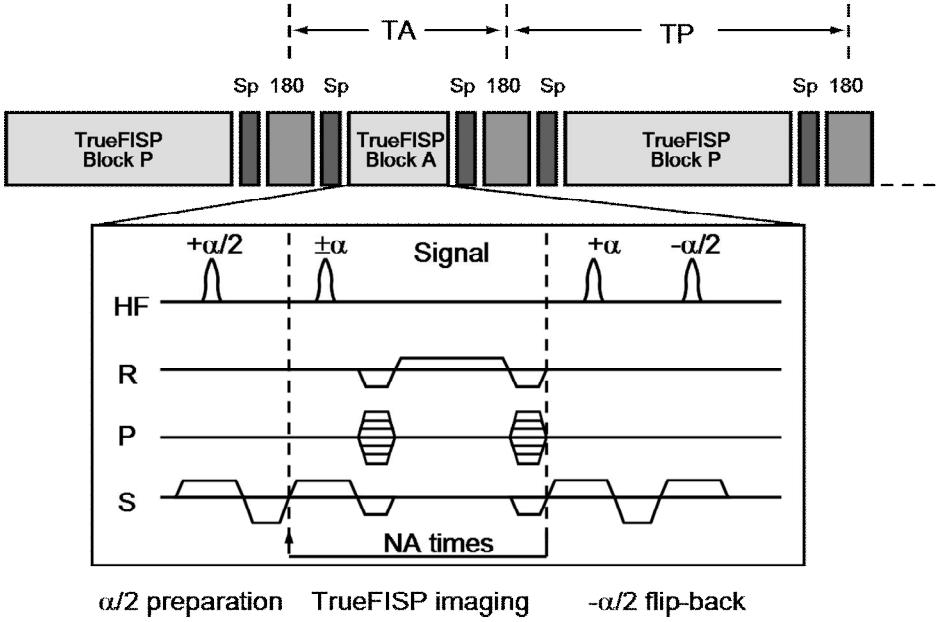

Fig. 7.5: TOSSI sequence implementation: Schematic display of the general pattern of *TA* and *TP* periods, with inversions pulses (180°) in between, surrounded by gradient spoilers (Sp). The timing of a single TrueFISP imaging block with α/2 preparation and flip-back modules is illustrated. Note that *NA* acquisitions take place during *TA*, while *NP* acquisitions are carried out during *TP* (not shown for the latter).

To demonstrate the contrast achievable with TOSSI, the method was tested and optimized in healthy volunteers, and a small study was conducted in patients with brain tumors. All human studies were performed in accordance with the local ethics committee. Informed consent was obtained from all subjects. In all experiments, the standard head coil of the system was used for both RF pulse transmission and MR signal reception.

In the patient study, images with standard TrueFISP and T2-weighted TSE sequences were acquired as contrast references. The most important imaging parameters are listed in Table 7.1. For TOSSI, a scheme with NP = 23 and NA = 8 was selected which corresponded to TP and TA values of 169 ms and 72 ms, respectively. This pattern was replicated eight

times to acquire a total of 8 * (23 + 8) = 248 phase-encoding steps, so that a singleshot TOSSI image was acquired in an imaging time of 8 *241 ms = 1928 ms. The center of k-space was sampled in the middle of the third TP interval which corresponded to an effective echo time of 586 ms. For the standard TrueFISP and TSE acquisitions, linear and linear segmented phase-encoding schemes were used, yielding effective echo times of 824 ms and 98 ms, respectively.

Parameter	TrueFISP	TOSSI	TSE
Excitation/refocusing angle	50°	50°	180°
Slice thickness	8 mm	8 mm	8 mm
FOV	256 mm	256 mm	256 mm
Reconstructed matrix (zerofilled)	256	256	256
Acquired matrix	256	248	242
PE lines per shot	256	248	11
Number of shots	1	1	22
Receiver bandwidth / (Hz/pix)	488	488	130
Echo distance / ms (*)	6.46	6.46	16.54
Effective TE / ms (*)	824	586	98
Echo train duration / ms	1654	1928	192
TR / ms (*)	n.a.	n.a.	3000
Scan time / s	1.654	1.928	66

Table 7.1: Imaging parameters of the TrueFISP, TOSSI and T_2-weighted TSE protocols. (*) Please note that generic terms are used in this table in order to compare corresponding quantities. The effective echo time TE_{eff} describes the temporal distance between the start of the echo train to the acquisition of k-space center, as introduced in section 1.2 for TSE sequences. The time between adjacent RF pulses is referred to as “echo distance” also for TrueFISP and TOSSI, since the term *TR* is utilized to denote the time from shot to shot here, which is the standard nomenclature in TSE sequences.

7.5 Results

Simulations and optimizations

In Fig. 7.6, TrueFISP and TOSSI signal time courses are depicted for a flip angle of 50°, together with the corresponding *TA*/*TP* ratio evolutions. Data are shown for different T_2 values: For short T_2 times between 75 ms and 125 ms as encountered in the brain, and for a longer value of 1000 ms which could represent a fluid compartment. For each T_2, a considerable

range of T_1 values was simulated (800 ms, 1200 ms, 3000 ms). While Fig. 7.6a shows simulated signals for TrueFISP, Fig. 7.6b depicts the ideal TOSSI curve given in Eq. 7.16. In Figs. 7.6c and 7.6d, results of Bloch simulations are displayed for a TOSSI scheme with constant *TA*/*TP* ratio as described in the methods section, and for a flexible scheme that was designed for the separation of signals with different short T_2 values, like those of white and gray matter of the human brain. Evidently, the standard TrueFISP signal time courses shown in Fig. 7.6a depend on both T_2 and T_1, and curves with an identical T_2 but different T_1 cross each other. The TrueFISP acquisition can be interpreted as a special case of TOSSI with just a single P block. This corresponds to $TA = 0$ or $TA/TP = 0$, which is displayed as a single black dot on the right side of Fig. 7.6a. This value is far away from the ideal *TA*/*TP* ratio evolutions of Eq. 7.27 that are visualized in the same colors as the signal curves on the left. In Fig. 7.6b, the ideal TOSSI signal evolutions as given in Eq. 7.16 are plotted over time. Here, the different T_2 components are clearly separated throughout the plot, independent of T_1.

In Fig. 7.6c, the TOSSI signal time courses are plotted for a scheme with constant *TA*/*TP* of $NP = 23$ and $NA = 8$ - the same as implemented on the MR system and used for the in-vivo experiments. As can be seen, this scheme is suboptimal in that considerable fluctuations of the signal amplitude are created. However, different T_2 values are reasonably separated and T_1 influence is reduced in comparison to the TrueFISP curves. On the right side of Fig. 7.6c, the used *TA*/*TP* is plotted over time. Here, the time points were attributed to the middle of the intervals spanned by each pair of adjacent *TA* and *TP* or *TP* and *TR*. For the start of the curves at $t = 0$, the assumption was made that all signals start with a common value, which corresponds to a point where the ideal TOSSI curve and the actual signal course intersect. Hence, the first *TP* was doubled, leading to a reduced value for first *TA*/*TP* ratio. From the simultaneous display of ideal continuous and used discrete *TA*/*TP*, it becomes apparent that this scheme is not optimal throughout the complete time course.

In Fig. 7.6d, simulation results are displayed for a flexible TOSSI scheme with varying *TA*/*TP* that was optimized for a T_2 value of approx. 100 ms. Specifically, the scheme for $\{NP_1/NA_1, NP_2/NA_2, NP_3/NA_3, \ldots NP_i/NA_i\}$ was {20/4, 19/4, 12/4, 10/4, 9/4, 8/4, 7/4, 7/4, 6/4, 6/4, 6/4, 5/4, …, 5/4}. A constant *TA* was used to render a monotonously increasing evolution of *TA*/*TP* possible, and - as illustrated on the right side of Fig. 7.6d - *TP* was chosen such that the successive discrete *TA*/*TP* values (black dots) matched the continuous ideal *TA*/*TP* (colored lines) as well as possible. Since the latter appear to be very similar for the different short T_2 times, an optimization for an intermediate T_2 shows to work well for a wider range of similar T_2 times. As shown in the left, the ideal signal curve is closely reproduced by simulated curves with optimized varying *TA*/*TP*, and the fluctuations are significantly reduced in comparison to the pattern of Fig. 7.6c. The T_2 values are separated effectively independent of the respective T_1, and essentially pure T_2 contrast is generated.

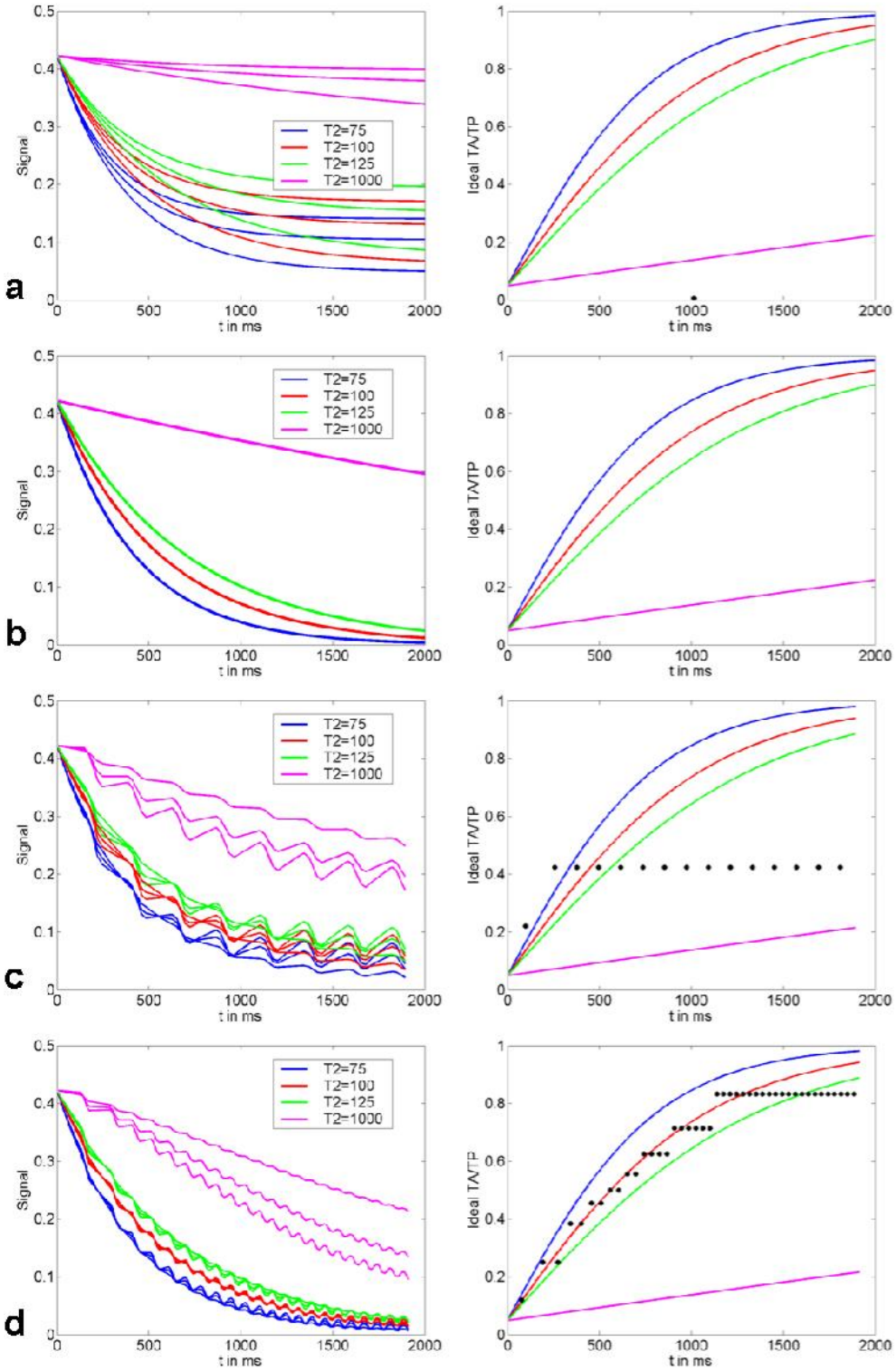

Fig. 7.6: Results of simulations and optimizations: Signal evolutions (left, colored), ideal *TA*/*TP* functions (right, colored) and actually simulated *TA*/*TP* (right, black dots) for Standard TrueFISP (a), ideal TOSSI according to Eq. 7.16 (b), TOSSI with constant *TA*/*TP* (c), and TOSSI with varying *TA*/*TP* (d).

In Fig. 7.7, calculated and simulated signal evolutions and corresponding PSFs are shown for GM and fat. For both, the idealized signal curves according to Eq. 7.16 show smooth exponential signal decay (Fig. 7.7a, top) and hence the related PSFs are reflected by Lorentzian functions (Fig. 7.7b,c, top), with a full width at half maximum (FWHM) of 1.94 pixels for GM. The corresponding real signal curve features small fluctuations (Fig. 7.7a, bottom), but these do not have a substantial negative impact on the PSF. Here, the FWHM amounts to 1.86 pixels, i.e. some degree of spatial blurring is expected for single-shot TOSSI acquisitions. For fat, however, the considerable off-resonance dephasing leads to a disturbed signal curve with prominent oscillations (Fig. 7.7a, bottom) and, hence, to notable irregularities and sidebands in the corresponding PSF (Fig. 7.7b,c, bottom, arrows). These imply a spatial dislocation of a fraction of the fat signal, which could lead to image artifacts.

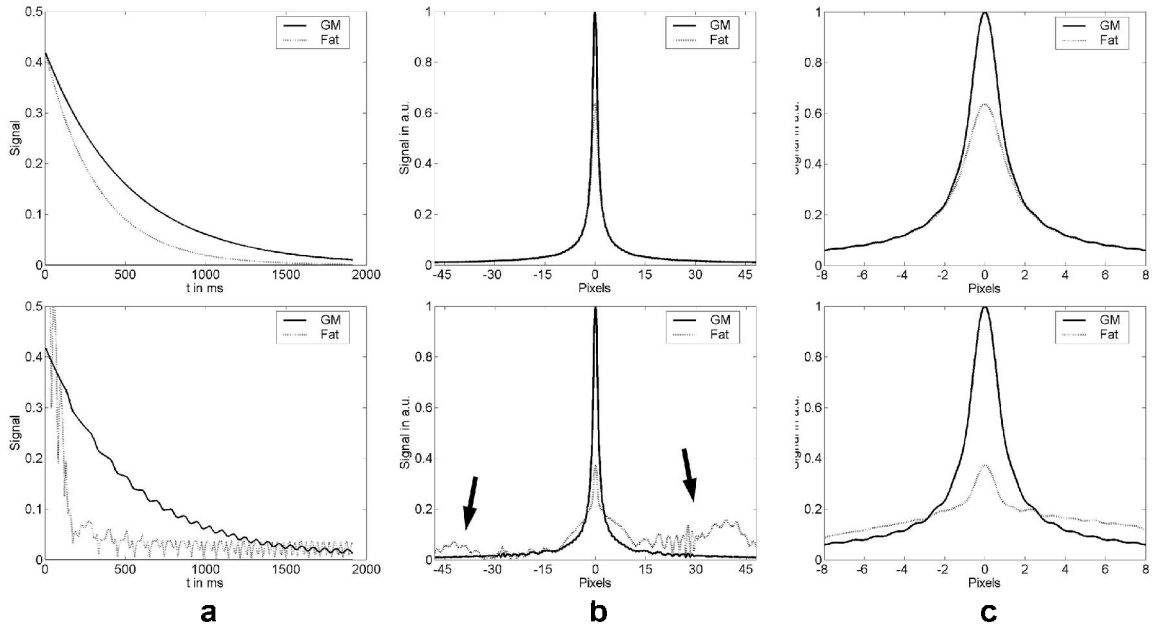

Fig. 7.7: Results of simulations for gray matter (GM, solid line) and fat (dotted line). Signal time courses (a) and corresponding point spread functions (PSF) plotted over different pixel ranges (b,c) for the idealized TOSSI behavior of Eq. 7.16 (top) and for TOSSI with varying *TA*/*TP* (bottom). While the fluctuations in the GM signal curves show not to have a prominent effect on the PSF, the disturbed signal curve for fat is associated with markable problems in the PSF (arrows).

In-vivo studies

In Figs. 7.8 and 7.9, in-vivo results obtained in tumor patients are shown. In each case, the TrueFISP image is shown on the left, the single-shot TOSSI image in the middle, and the T_2-weighted TSE image on the right, respectively. While gray and white matter show nearly uniform amplitude in the standard TrueFISP image, the TOSSI image exhibits essentially pure T_2 contrast, very similar to the corresponding T_2-weighted TSE image. Specifically, blood is dark and subcutaneous fat appears artificially bright in the TSE images, as known from literature [Henk92]. In the TOSSI data, however, blood is shown with comparatively high and fat with low signal, a result which more correctly reflects the T_2 values of these compartments.

Fig. 7.8 shows images of a patient with cystic brain metastasis. A large metastatic tumor in the occipital white matter is visible in all images. However, the surrounding edema and a much smaller lesion in the fronto-parietal white matter are hardly visible in the TrueFISP image. However, both are clearly delineated in the TOSSI image, corresponding to their appearance in the T_2-weighted TSE image (arrows). In Fig. 7.9, images of a patient with a glioblastoma are displayed. While the TOSSI image is sensitive to susceptibility effects in regions with inhomogeneous magnetic field distribution such as the nasal sinuses, it reveals fine structural details within the core of the lesion, and its contrast closely resembles that of the T_2-weighted TSE image.

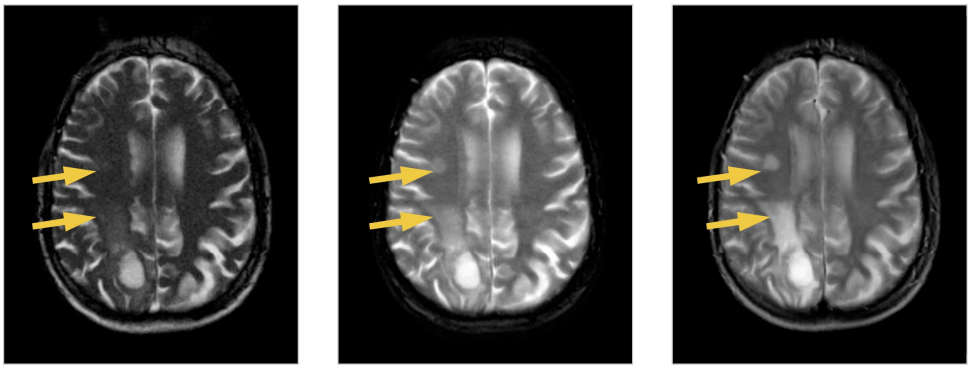

Fig. 7.8: Images obtained in a patient with cystic brain metastases (primary tumor ovarian carcinoma): TrueFISP (left, TA < 2 s), TOSSI (middle, TA < 2 s), and T_2-weighted TSE (right, TA = 66 s).

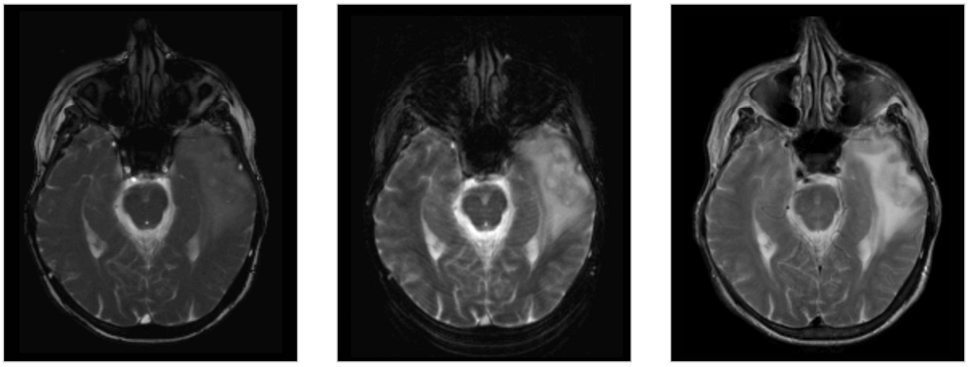

Fig. 7.9: Images obtained in a patient with a glioblastoma: TrueFISP (left, TA < 2 s), TOSSI (middle, TA < 2 s), and T_2-weighted TSE (right, TA = 66 s).

7.6 Discussion

The calculations and simulations presented in this work demonstrate that the influence of longitudinal relaxation can be efficiently compensated with the TOSSI concept and that signal evolutions can be created which essentially depend solely on T_2. With an effective

elimination of T_1, however, the sole mechanism for gaining back longitudinal magnetization is removed, so that the signal evolves towards zero but not towards the original TrueFISP steady state value.

The derivation of the idealized TOSSI function was based on the assumption that $TA << T_1$ and $TP << T_1$, a condition that cannot be easily realized in practice. Consequently, the real curves show some deviation from the idealized curve, which becomes evident as signal fluctuations. For on-resonant magnetization, however, it could be shown that the real curves evolve closely around the idealized curve and that the small fluctuations do not critically contaminate the PSF or impede spatial encoding.

From the shape or width of the PSF, it can be directly deduced that some degree of signal blurring is expected in phase-encoding direction for single-shot TOSSI. However, with flip angles significantly smaller than 180°, the resulting apparent decay times are much longer than the true T_2 values. Consequently, the signal decay is less steep and the blurring is less severe than it would be expected in a corresponding single-shot TSE-based acquisition. In fact, the TOSSI signal behavior renders the use of very long echo trains feasible, and makes it possible to capture the center of k-space at rather long effective echo times to capture maximum T_2 contrast. In terms of image contrast, for example, the TE of 98 ms as used in this work for the TSE acquisitions corresponds to a TE_{eff} of 549 ms for TOSSI with a flip angle of 50°, as can be calculated from Eq. 7.17. Hence, single-shot imaging proved to be possible even for comparatively large matrices, even with only moderate TR values and no use of parallel imaging.

For off-resonant magnetization such as fat, however, the situation can become problematic in that the signal curve shows oscillations and the PSF indicates considerable spatial mis-encoding. This might not be unexpected with the used α/2 preparation scheme that is suboptimal in off-resonant situations. It should be noted, however, that the PSFs were (per definition) calculated for object with a size of a single pixel. Hence, the intensity of the PSF corresponds to the integral of the signal curve. With increasing object size, the amplitude of the PSF will more and more correspond to the signal acquired at the k-space center. Hence, with the chosen effective echo time of 586 ms, it can be deduced from the signal curve that fat will appear with very low signal. This could be a disadvantage in situations where the presence or absence of lipids in a lesion helps in the differential diagnosis However, there should still be plenty of situations where a rapid T_2-weighted scan would be useful even without an accurate fat signal visualization.

The technique presented here has the intrinsic requirement that inversion pulses have to be inserted within the imaging sequence, which means that a certain amount of time is not directly spent for the generation of MR signal. This leads to a slight reduction of the scan efficiency of the method if compared to a standard TrueFISP acquisition. Moreover, these pulses may be sensitive to inhomogeneities of B_0 and B_1, which could lead to local image contrast variations, and crosstalk effects might play a role in multi-slice imaging. Finally, these additional RF pulses lead to an increased power deposition during the data acquisition, which might be problematic at higher field strengths. Also the calculations and simulations presented here have some general limitations. Within the scope of this work, several factors were neglected that are known to have impact on the TrueFISP signal. These include flow and diffusion [Gud95] as well as magnetization transfer effects [Bie06]. Also the influence of finite RF pulse durations [Bie09, Bie10] was not considered.

On the other hand, good results were obtained in the small patient study presented in this paper, but there is potential for further improvements of the method. Although essentially purely T_2-weighted single-shot images were obtained even without the use of optimized varying *TA*/*TP* values, a more precise separation of similar T_2 values and smoother signal time courses should be possible with a realization of optimized temporal patterns that reflect the ideal *TA*/*TP* for a specific range of T_2 values. Due to the discrete nature of the *TA* and *TP* intervals, given these are composed of discrete excitations, *TR* intervals, and spoiler times, the ideal course of *TA*/*TP* can not be reproduced exactly. According to the simulations presented in this work, however, approximate discrete approaches should nonetheless have high potential. Although specific implementations will never be optimal for all possible T_2 times, a wide range of values can be covered and it should be possible to find optimized schemes for various applications.

Further approaches to optimize the technique might include using variations of the flip angle within the up- and down-periods, or the combination of the TOSSI principle with a preceding T_2 preparation module, such that T_2-weighting is already created before the signal acquisition, at the expense of some SNR loss. Other aspects that remain to be investigated are the general robustness of TOSSI against off-resonance effects and the feasibility and usefulness for fast T_2 imaging in more challenging applications such as cardiac imaging and interactive real-time imaging, where TOSSI was suggested as a promising approach [Yut08].

7.7 Conclusion and retrospect

In this work, a novel concept was presented for the generation of pure T_2 contrast. Both calculations and simulations showed that it is possible to remove the influence of longitudinal relaxation from the magnetization evolution by means of non-equidistant inversion pulses, and to generate signal time courses that are solely determined by transverse relaxation. Both the initial signal and the apparent decay rate are influenced by the choice of flip angle, which makes it possible to use long echo trains, late effective echo times, and, hence, to realize purely T_2-weighted single-shot imaging with the complete signal evolution being governed by T_2. These findings were confirmed by the results of a small study in patients with brain tumors: Single-shot TOSSI images acquired within less than two seconds revealed a contrast essentially identical to that of T_2-weighted TSE acquisitions in brain parenchyma.

Since the TOSSI concept was first proposed and published, other researchers adopted the approach and continued to develop the technique. In a first study using a further optimized approach, an optimized inversion spacing was used in combination with parallel imaging and adiabatic inversion pulses that facilitated multi-slice imaging [Der06]. In order to achieve an improved point-spread function and to enhance the resolution of TOSSI, it was proposed to combine an initial TOSSI acquisition with a later standard TrueFISP phase within a single echo train. This approach showed to be beneficial for fast T2-weighted imaging in the human abdomen and in other body regions [Der07, Der12].

Summary

The subject of this work was to develop, implement, optimize and apply MR imaging methods for functional and morphological characterization of tumors. In the first chapter of this thesis, the basic physics of magnetic resonance was introduced, and some simple MR imaging sequences were explained, followed by some fundamentals of tumor physiology and therapy, and a brief overview on the role of MRI for the characterization of cancerous tissue. In the following six chapters, individual projects were presented, each relating to either the functional (Chapters 2-3) or the fast morphologic imaging of tumors (Chapters 4-7). The content of each chapter essentially reflects a corresponding peer-reviewed publication in a scientific journal.

With respect to the characterization of tumor function and physiology, techniques that had mainly been utilized in animal studies before were adapted for an examination of human subjects, and their feasibility for the assessment of tumors was investigated in patients.

In Chapter 2, a study was presented that dealt with the evaluation of a spin-labeling technique for measuring tumor perfusion in patients with carcinoma of the head and neck. A total of eleven patients were examined, five of them twice during the course of radiotherapy. For the assessment of tumor perfusion, a spin-labeling method was implemented that utilized an Inversion Recovery Snapshot-FLASH imaging sequence for data acquisiton. Quantitative perfusion maps were generated on the basis of a two-compartment tissue model. It was found that both baseline tumor perfusion and perfusion changes during therapy behaved heterogeneously. In particular, tumors with high pretreatment perfusion values tended to be smaller in size and to show stronger response to radiation therapy than tumors with low initial perfusion. Since the presented technique does not require the administration of an exogenous contrast agent, it facilitates the repetitive characterization of tumor perfusion, and it may be useful for stratification of vasomodulating treatment options.

The subject of Chapter 3 was the implementation and evaluation of a non-invasive functional MR technique for monitoring tumor tissue oxygenation changes. In this study, 13 patients with head and neck carcinoma were included. Different breathing gases - air, “carbogen light” (2% CO2 + 98% O2) and 100% oxygen - were administered in order to induce oxygenation changes. Wie a multi-gradient-echo sequence, the apparent transverse relaxation time T_2* in the tumor was quantified, which is directly correlated to tissue oxygenation. For both hyperoxic gases, a shift of the mean towards higher values was observed for the tumor T_2*, which corresponds to an increase in oxygenation. For oxygen, in comparison to carbogen light, a slightly stronger elevation of T_2* and a significantly higher heterogeneity of the response were observed. The developed MR technique proved to be feasible for monitoring

of oxygenation changes in head and neck tumor patients. Hence, it has potential for the selection of patients who can benefit from a carbogen-induced radiosensitation.

In the context of the morphologic assessment and parameter imaging of tumors, novel concepts and techniques were developed, which facilitated the simultaneous quantification of multiple MR parameters, the generation of “synthetic” MR images with various contrasts, and the fast single-shot acquisition of purely T_2-weighted images.

In Chapter 4, an intuitive pictorial approach was introduced in order to analyze the signal dynamics of TrueFISP sequences in the so-called transient phase and in the steady state. Based on the Bloch equations and elementary geometrical dependencies, the magnetization vector dynamics during a *TR* interval was separated into different components. This procedure made it possible to derive a new, compact formula for the TrueFISP steady state signal, and a closed form expression for the signal decay rate during the transient phase of the TrueFISP sequence, each as a function of T_1, T_2, flip angle and resonance frequency offset. The validity of the concept and the analytical results was verified by numerical simulations as well as with MR phantom experiments. The theory can be used for contrast calculations and has potential to facilitate improved parameter quantification with magnetization-prepared TrueFISP experiments.

Building on the previous chapter, Chapter 5 reported a novel technique that was developed to extract parameter maps for T_1, T_2 and relative spin density simultaneously from data acquired with a single inversion recovery TrueFISP scan. In general, the signal time courses obtained with this sequence can in good approximation be described by a three-parameter monoexponential function. From the results of the preceding chapter, a comprehensive set of analytical formulas was derived, which directly relates the the three fit parameters to the target quantities T_1, T_2 and M_0. The influence of off resonance frequency effects was analyzed with numerical simulations, and the feasibility of the technique for fast acquisition of parameter maps was demonstrated in phantom experiments and in an in-vivo study on the human brain. The results obtained in phantoms with different combinations of T_1 and T_2 showed excellent agreement with reference measurements. In healthy volunteers, high quality T_1, T_2 and spin density maps were obtained, which were in excellent agreement with literature values.

In Chapter 6, a method was proposed to reconstruct “synthetic” MR images with a wide range of contrasts, based on quantitative parameter maps as calculated from a single IR TrueFISP acquisition. It was shown that it becomes possible to realize a wide range of contrasts, including T_1-weighted, T_2-weighted, spin-density-weighted, or FLAIR images. The feasibility of this approach was verified in volun-teers and brain tumor patients. It was demonstrated that the “synthetic” weighted images as calculated from the maps essentially matched the contrast behavior of the corresponding “traditional” MR images, which were acquired separately as individual data sets using multiple imaging sequences such as spin-echo, TSE or FLAIR. Moreover, an exciting new possibility was identified: The calculation of images with novel contrast properties that are different from those available with routine MR sequences. As an example, images with “pure” T_1, T_2, or spin-density contrast were calculated - a promising new possibility with unexplored potential clinical utility.

Finally, in Chapter 7, a novel conceptual framework named T-One-insensitive Steady State Imaging (TOSSI) was presented for fast MR imaging with pure T_2 contrast. Here,

imaging modules are played out between non-equally spaced inversion pulses, with the magnetization vector alternatively residing in states parallel and anti-parallel to the main magnetic field. With adequately chosen temporal periods between these pulses, identical signal evolutions are generated for compartments with different T_1 values, so that T_1 contrast can efficiently be removed from resultant images. A specific realization of the general TOSSI idea was presented, which used TrueFISP readout blocks between the inversion pulses. By deriving a mathematical description of the ideal signal behavior, pathways for sequence parameter optimization were created. The performance of the technique was analyzed with simulations based on the Bloch equations, and using in-vivo studies. While the conventional TrueFISP signal evolution is a function of both T_2 and T_1, the influence of longitudinal relaxation was successfully suppressed with TOSSI, and an essentially pure T_2 dependence was realized. In both healthy volunteers and brain tumor patients, single-shot TOSSI images obtained within less than two seconds essentially contained the same contrast as conventional T_2-weighted TSE images, which required a scan time of several minutes.

In the presented projects, novel MR imaging techniques were developed, analyzed, optimized and applied, which showed high potential for functional and fast morphological characterization of tumors.

Zusammenfassung

Gegenstand dieser Arbeit war die Entwicklung, Implementierung, Optimierung und Anwendung von MR-Bildgebungsmethoden für die funktionelle und morphologische Charakterisierung von Tumoren. Im ersten Kapitel wurden die physikalischen Grundlagen der Magnetresonanz dargestellt und einige einfache MR-Bildgebungssequenzen erklärt, gefolgt von einer kurzen Einführung in die Tumorphysiologie und -therapie, sowie einer Übersicht bzgl. der Rolle der MR-Bildgebung für die Charakterisierung von Tumorgewebe. In den folgenden sechs Kapiteln wurden einzelne Projekte vorgestellt, die entweder im Zusammenhang mit der funktionellen (Kapitel 2 und 3) oder mit der schnellen morphologischen Bildgebung von Tumoren (Kapitel 4 bis 7) stehen. Der Inhalt eines jeden Kapitels entspricht im Wesentlichen einer entsprechenden, durch Experten begutachteten Publikation in einer wissenschaftlichen Fachzeitschrift.

In Bezug auf die Charakterisierung von Tumorfunktion und -physiologie wurden Verfahren, die zuvor vor allem an Tiermodellen eingesetzt worden waren, für Messungen am Menschen adaptiert, und ihre Anwendbarkeit zur Untersuchung von Tumoren wurde an Patienten erforscht.

In Kapitel 2 wurde eine Studie vorgestellt, die sich mit der Evaluierung einer Spin-Labeling-Methode zur Messung der Tumorperfusion bei Patienten mit Karzinomen des Kopf-Hals-Bereichs befasste. Dabei wurden insgesamt elf Patienten untersucht, fünf davon zweimal während des Verlaufs einer Strahlentherapie. Zur Bestimmung der Tumorperfusion wurde eine Spin-Labeling-Methode implementiert, bei der die Datenakquisition auf einer Inversion-Recovery-Snapshot-FLASH-Bildgebungssequenz beruht. Basierend auf einem Zwei-Kompartimente-Gewebemodell wurden quantitative Perfusionskarten berechnet. Es stellte sich heraus, dass sich sowohl die Tumorperfusion im Ausgangszustand als auch deren Änderungen während der Therapie heterogen verhielten. Insbesondere wiesen Tumoren mit hohen prätherapeutischen Perfusionswerten tendentiell eine geringere Größe auf und zeigten ein stärkeres Ansprechen auf die Bestrahlungstherapie als Tumoren mit niedriger anfänglicher Perfusion. Da die vorgestellte Technik keine Gabe eines exogenen Kontrastmittels erfordert, ermöglicht sie eine wiederholte Charakterisierung der Tumorperfusion, und kann somit hilfreich sein zur Stratifizierung vasomodulierender Behandlungsansätze.

Gegenstand von Kapitel 3 war die Implementierung und Erprobung eines nicht-invasiven funktionellen MR-Verfahrens zur Erfassung von Oxygenierungsänderungen in Tumorgewebe. Für diese Studie wurden 13 Patienten mit Karzinomen im Kopf-Hals-Bereich untersucht. Ihnen wurden verschiedene Atemgase - Luft, “Carbogen light” (2% CO_2 + 98% O_2) und 100% Sauerstoff - verabreicht, um Oxygenierungsänderungen zu erzeugen. Mittels einer

Multi-Gradientenecho-Sequenz wurde dabei die effektive transversale Relaxationszeit T_2* im Tumor quantifiziert, welche direkt mit der Gewebeoxygenierung korreliert. Mit beiden hyperoxischen Gasen war für T_2* im Tumor eine Verschiebung des Mittelwerts zu höheren Werten zu beobachten, was einer Erhöhung der Oxygenierung entspricht. Für Sauerstoff wurden im Vergleich zu Carbogen light ein etwas stärkerer Anstieg von T_2* und eine signifikant höhere Heterogenität der Reaktion beobachtet. Das entwickelte MR-Verfahren erwies sich als gut geeignet, um bei Patienten mit Kopf-Hals-Tumoren Änderungen der Oxygenierung darzustellen. Somit birgt es Potential für die Selektion von Patienten, die von einer Carbogen-induzierten Radiosensitivierung profitieren können.

Im Bereich der morphologischen Untersuchung und Parameterbildgebung an Tumoren wurden neue Konzepte und Verfahren entwickelt, welche die simultane Quantifizierung mehrerer MR-Parameter, die Generierung „synthetischer“ MR-Bilder mit unterschiedlichen Kontrasten, sowie die schnelle „Single-Shot“-Akquisition rein T_2-gewichteter Bilder ermöglichen.

In Kapitel 4 wurde ein intuitiver, bildhafter Ansatz eingeführt, um das Signalverhalten von TrueFISP-Sequenzen in der sog. „Transient Phase“ und im Steady State zu analysieren. Auf Basis der Bloch-Gleichungen und elementarer geometrischer Zusammenhänge wurde die Dynamik des Magnetisierungsvektors über ein TR-Intervall in verschiedene Komponenten separiert. Dies ermöglichte die Herleitung einer neuen, kompakten Formel für das TrueFISP-Steady-State-Signal sowie eines geschlossenen Ausdrucks für die Änderungsrate des Signals während der „Transient Phase“ einer TrueFISP-Sequenz, jeweils in Abhängigkeit von T_1, T_2, dem Flipwinkel und dem Offset der Resonanzfrequenz. Die Validität des Konzepts und der analytischen Ergebnisse wurde mittels numerischer Simulationen sowie mit MR-Experimenten an Phantomen nachgewiesen. Die Theorie kann für Kontrastberechnungen genutzt werden und birgt Potential für eine verbesserte Parameter-Quantifizierung mit magnetisierungspräparierten TrueFISP-Experimenten.

Aufbauend auf dem vorherigen Kapitel wurde in Kapitel 5 ein neuartiges Verfahren vorgestellt, mit dem sich aus den Daten eines einzigen Inversion-Recovery-TrueFISP-Scans gleichzeitig Parameterkarten für T_1, T_2 und die relative Spindichte extrahieren lassen. Generell kann der Signalverlauf, den man mit dieser Sequenz erhält, in guter Näherung mittels einer dreiparametrigen mono-exponentiellen Funktion beschrieben werden. Aus den Ergebnissen des vorherigen Kapitels wurde ein umfassender Satz von analytischen Formeln hergeleitet, welcher eine direkte und eindeutige Beziehung zwischen den drei Fitparametern und den Zielgrößen T_1, T_2 und M_0 herstellt. Der Einfluss von Off-Resonanz-Effekten wurde mittels numerischer Simulationen analysiert, und die Anwendbarkeit der Methode zur schnellen Akquisition von Parameterkarten wurde in Phantomexperimenten und in einer In-vivo-Studie am menschlichen Gehirn demonstriert. Die Ergebnisse, die in Phantomen mit unterschiedlichen Kombinationen von T_1 und T_2 erzielt wurden, wiesen eine exzellente Übereinstimmung mit Referenzmessungen auf. Bei gesunden Probanden ergaben sich T_1-, T_2- und Spindichte-Karten von hoher Qualität, welche exzellent mit Literaturwerten übereinstimmten.

Kapitel 6 handelte von einer Methode, mit der - auf der Basis quantitativer Parameterkarten aus einer einzigen IR-TrueFISP-Akquisition - „synthetische“ MR-Bilder rekonstruiert werden können. Es wurde gezeigt, dass damit eine weite Bandbreite an Kontrasten realisierbar wird, wie z.B. Bilder mit T_1-, T_2-, Spindichte- oder FLAIR-Kontrast. Die Funktionstüchtigkeit dieses Ansatzes wurde in Probanden und Tumorpatienten verifiziert. Es wurde demonstriert, dass die synthetischen, aus den Karten berechneten Bilder weitgehend das Kontrast-

verhalten der entsprechenden „traditionellen“ MR-Bilder widerspiegelten, welche separat mittels verschiedener Bildgebungssequenzen - wie z.B. Spin-Echo, TSE oder FLAIR - in Form von einzelnen Datensätzen aufgenommen wurden. Darüberhinaus wurde eine interessante weitere Option identifiziert: Die Berechnung von Bildern mit neuartigen Kontrasteigenschaften, welche mit Routine-MR-Sequenzen nicht direkt verfügbar sind. So wurden beispielsweise Bilder mit „reinem“ T_1-, T_2-, oder Spindichtekontrast generiert - eine vielversprechende neue Möglichkeit mit noch unerforschtem klinischem Nutzen.

Schließlich wurde in Kapitel 7 ein neuartiges Konzept mit der Bezeichnung „T-One-insensitive Steady State Imaging“ („TOSSI“) zur schnellen MR-Bildgebung mit reinem T_2-Kontrast vorgestellt. Hierbei werden Bildgebungsmodule zwischen ungleich beabstandeten Inversionspulsen ausgespielt, wobei sich der Magnetisierungsvektor abwechselnd in Zuständen parallel und anti-parallel zum Hauptmagnetfeld befindet. Mit geeignet gewählten Zeitintervallen zwischen diesen Pulsen lassen sich damit für Kompartimente mit verschiedenen T_1-Werten identische Signalverläufe erzeugen, sodass in den resultierenden Bildern Anteile von T_1-Kontrast auf effiziente Weise eliminiert werden. Es wurde eine spezifische Realisierung dieser generellen TOSSI-Idee präsentiert, bei der TrueFISP-Ausleseblöcke zwischen den Inversionspulsen zu Einsatz kommen. Über die Herleitung einer mathematischen Beschreibung des idealen TOSSI-Signalverhaltens wurden Anhaltspunkte für die Optimierung der Sequenzparameter gewonnen. Die Leistungsfähigkeit des Verfahrens wurde mit Bloch-Simulationen und in In-vivo-Studien analysiert. Während sich der konventionelle TrueFISP-Signalverlauf als Funktion sowohl von T_2 als auch von T_1 darstellt, wurde mit TOSSI der Einfluss der longitudinalen Relaxation erfolgreich unterdrückt und somit eine weitgehend reine T_2-Abhängigkeit realisiert. Sowohl bei gesunden Probanden als auch bei Patienten mit Hirntumoren zeigten Single-Shot-TOSSI-Bilder, die in weniger als zwei Sekunden aufgenommen wurden, im Wesentlichen den gleichen Kontrast wie konventionelle T_2-gewichtete TSE-Bilder, deren Messdauer mehrere Minuten betrug.

In den vorgestellten Projekten wurden neue MR-Bildgebungsverfahren entwickelt, analysiert, optimiert und angewandt, welche hohes Potential bergen für die funktionelle und schnelle morphologische Charakterisierung von Tumoren.

Literature

[Aqu00] Aquino-Parsons C, Green A, Minchinton AI. Oxygen tension in primary gynaecological tumours: the influence of carbon dioxide concentration. Radiother Oncol 57(1): 45-51 (2000).

[Al-H98] Al-Hallaq HA, River JN, Zamora M, Oikawa H, Karczmar GS. Correlation of magnetic resonance and oxygen microelectrode measurements of carbogen-induced changes in tumor oxygenation. Int J Radiat Oncol Biol Phys 41: 151-159 (1998).

[Al-H00] Al-Hallaq HA, Zamora M, Fish BL, Farrell A, Moulder JE, Karczmar GS. MRI measurements correctly predict the relative effects of tumor oxygenating agents on hypoxic fraction in rodent BA1112 tumors. Int J Radiat Oncol Biol Phys 47(2): 481-488 (2000).

[Al-H02] Al-Hallaq HA, Fan X, Zamora M, River JN, Moulder JE, Karczmar GS. Spectrally inhomogeneous BOLD contrast changes detected in rodent tumors with high spectral and spatial resolution MRI. NMR Biomed 15(1): 28-36 (2002).

[Aro94] Aronen HJ, Gazit IE, Louis DN, Buchbinder BR, Pardo FS, Weisskoff RM, Harsh GR, Cosgrove GR, Halpern EF, Hochberg FH, et al. Cerebral blood volume maps of gliomas: comparison with tumor grade and histologic findings. Radiology 191(1): 41-51 (1994).

[Bac00] Bacharach SL, Libutti SK, Carrasquillo JA. Measuring tumor blood flow with H(2)(15)O: practical considerations. Nucl Med Biol 27(7): 671-676 (2000).

[Bad00] Baddeley H, Brodrick PM, Taylor NJ, Abdelatti MO, Jordan LC, Vasudevan AS, Phillips H, Saunders MI, Hoskin PJ. Gas exchange parameters in radiotherapy patients during breathing of 2%, 3.5% and 5% carbogen gas mixtures. Br J Radiol 73(874): 1100-1104 (2000).

[Barb01] Barbier EL, Lamalle L, Decorps M. Methodology of brain perfusion imaging. J Magn Reson Imaging 13(4): 496-520 (2001).

[Bar89] Barker GJ, Mareci TH. Suppression of artifacts in multiple-echo magnetic resonance. J Magn Reson 83(1): 11-28 (1989).

[Bark01] Barkhausen J, Ruehm SG, Goyen M, Buck T, Laub G, Debatin JF. MR evaluation of ventricular function: true fast imaging with steady-state precession versus fast low-angle shot cine MR imaging: feasibility study. Radiology 219(1): 264-269 (2001).

[Bart97] Barth M, Moser E. Proton NMR relaxation times of human blood samples at 1.5 T and implications for functional MRI. Cell Mol Biol (Noisy-le-grand) 43(5): 783-791 (1997).

[Baud02] Baudelet C, Gallez B. How does blood oxygen level-dependent (BOLD) contrast correlate with oxygen partial pressure (pO2) inside tumors? Magn Reson Med 48(6): 980-986 (2002).

[Baud03] Baudelet C, Gallez B. Cluster analysis of BOLD fMRI time series in tumors to study the heterogeneity of hemodynamic response to treatment. Magn Reson Med 49(6): 985-990 (2003).

[Bau92] Bauer WR, Schulten K. Theory of contrast agents in magnetic resonance imaging: Coupling of spin relaxation and transport. Magn Reson Med 26: 16-39 (1992).

[Bau96] Bauer WR, Hiller K-H, Roder F, Rommel E, Ertl G, Haase A. Magnetization exchange in capillaries by microcirculation affects diffusion-controlled spin-relaxation: a model which describes the effect of perfusion on relaxation enhancement by intravascular contrast agents. Magn Reson Med 35(1): 43-55 (1996).

[Bau99] Bauer WR, Nadler W, Bock M, Schad LR, Wacker C, Hartlep A, Ertl G. Theory of the BOLD effect in the capillary region: an analytical approach for the determination of T2 in the capillary network of myocardium. Magn Reson Med 41(1): 51-62 (1999).

[Bel98] Belle V, Kahler E, Waller C, Rommel E, Voll S, Hiller K-H, Bauer WR, Haase A. In Vivo Quantitative Mapping of Cardiac Perfusion in Rats Using a Noninvasive MR Spin-Labeling Method, J Magn Reson Imaging 8(6): 1240-1245 (1998).

[Ben02] Bentzen L, Keiding S, Horsman MR, Grönroos T, Hansen SB, Overgaard J. Assessment of hypoxia in experimental mice tumours by [18F]fluoromisonidazole PET and pO2 electrode measurements. Influence of tumour volume and carbogen breathing. Acta Oncol 41(3): 304-312 (2002).

[Ber99] Bernier J, Denekamp J, Rojas A, Trovò M, Horiot JC, Hamers H, Antognoni P, Dahl O, Richaud P, Kaanders J, van Glabbeke M, Piérart M. ARCON: accelerated radiotherapy with carbogen and nicotinamide in non small cell lung cancer: a phase I/II study by the EORTC. Radiother Oncol 52(2): 149-156 (1999).

[Ber00] Bernier J, Denekamp J, Rojas A, Minatel E, Horiot J, Hamers H, Antognoni P, Dahl O, Richaud P, van Glabbeke M, Piérart M. ARCON: accelerated radiotherapy with carbogen and nicotinamide in head and neck squamous cell carcinomas. The experience of the Co-operative group of radiotherapy of the european organization for research and treatment of cancer (EORTC). Radiother Oncol 55(2): 111-119 (2000).

[Bie06] Bieri O, Scheffler K. On the origin of apparent low tissue signals in balanced SSFP. Magn Reson Med 56(5): 1067-1074 (2006).

[Bie09] Bieri O, Scheffler K. SSFP signal with finite RF pulses. Magn Reson Med 62(5): 1232-1241 (2009).

[Bie10] Bieri O. An Analytical Description of Balanced SSFP with Finite RF Excitation. Proceedings ISMRM 2010; #73 (2010).

[Blo46a] Bloch F, Hansen WW, Packard M. Nuclear induction. Phys Rev 69: 127 (1946).

[Blo46b] Bloch F. Nuclear induction. Phys Rev 70(7+8): 460-474 (1946).

[Blu09] Blumhagen JO, Santini F, Weber O, Scheffler K, Bieri O. Impact of Magnetization Transfer on Relaxometry using Transient Steady-State Free Precession Imaging. Proceedings ISMRM 2009; #4501 (2009).

[Bly12] Blystad I, Warntjes JB, Smedby O, Landtblom AM, Lundberg P, Larsson EM. Synthetic MRI of the brain in a clinical setting. Acta Radiol 53(10):1158-1163 (2012).

[Boss06] Boss A, Martirosian P, Schraml C, Clasen S, Fenchel M, Anastasiadis A, Claussen CD, Pereira PL, Schick F. Morphological, contrast-enhanced and spin labeling perfusion imaging for monitoring of relapse after RF ablation of renal cell carcinomas. Eur Radiol 16(6): 1226-1236 (2006).

[Box95] Boxerman JL, Bandettini PA, Kwong KK, Baker JR, Davis TL, Rosen BR, Weisskoff RM. The intravascular contribution to fMRI signal change: Monte Carlo modeling and diffusion-weighted studies in vivo. Magn Reson Med 34(1): 4-10 (1995).

[Bra65] Bratton CB, Hopkins AL, Weinberg JW. Nuclear magnetic resonance studies of living muscle. Science 147(3659): 738-739 (1965).

[Bre01] Breuer F. Darstellung von Oxygenierungs- und Perfusionsänderungen in Tumoren mittels Magnet-resonanz-Tomographie. Diplomarbeit. Physikalisches Institut der Universität Würzburg (2001).

[Bre02] Breuer F, Schmitt P, Kotas M, Zips D, Müller JG, Flentje M, Haase A. Non-invasive monitoring of oxygenation and perfusion changes in tumours while breathing carbogen. ESMRMB 2002, 19th Annual Meeting, Cannes, #38. MAGMA 15, S1, p.13 (2002).

[Brit95] Brittain JH, Hu BS, Wright GA, Meyer CH, Macovski A, Nishimura DG. Coronary angiography with magnetization-prepared T2 contrast. Magn Reson Med 33: 689-696 (1995).

[Broo80] Brooks RA, Di Chiro G, Keller MR. Explanation of cerebral white-gray contrast in computed tomography. J Comput Assist Tomogr 4(4): 489-491 (1980).

[Brow61] Brown RJS. Distribution of fields from randomly placed dipoles: free precession signal decay as result of magnetic grains. Phys Rev 121(5): 1379-1383 (1961).

[Brow79] Brown JM. Evidence for acutely hypoxic cells in mouse tumours, and a possible mechanism of reoxygenation. Br J Radiol 52(620): 650-656 (1979).

[Brow07] Brown GG, Clark C, Liu TT. Measurement of cerebral perfusion with arterial spin labeling: Part 2. Applications. J Int Neuropsychol Soc 13(3): 526-538 (2007).

[Buch12] Buchbender C, Heusner TA, Lauenstein TC, Bockisch A, Antoch G. Oncologic PET/MRI, Part 1: Tumors of the Brain, Head and Neck, Chest, Abdomen, and Pelvis. J Nucl Med 53(6): 928-938 (2012).

[Buck97] Buckley DL, Drew PJ, Mussurakis S, Monson JR, Horsman A. Microvessel density of invasive breast cancer assessed by dynamic Gd-DTPA enhanced MRI. J Magn Reson Imaging 7(3): 461-464 (1997).

[Bus91] Busse RF, Riederer SJ. Steady-state preparation for spoiled gradient echo imaging. Magn Reson Med 45(4): 653-661 (2001).

[Bus99] Bussink J, Kaanders JH, Van der Kogel AJ. Clinical outcome and tumour microenvironmental effects of accelerated radiotherapy with carbogen and nicotinamide. Acta Oncol 38(7): 875-882 (1999).

[Bush86] Bush RS. The significance of anemia in clinical radiation therapy. Int J Radiat Oncol Biol Phys 12(11): 2047-2050 (1986).

[Byd85] Bydder GM, Young IR. MR imaging: Clinical use of the inversion recovery sequence. J Comput Assist Tomogr 9(4): 659-675 (1985).

[Carr52] Carr HY. Free precession techniques in Nuclear Magnetic Resonance. PhD thesis, Harvard University, Cambridge, MA (1952). In: Encyclopedia of Nuclear Magnetic Resonance 1, Wiley and Sons, Hoboken, NJ, USA. (1996).

[Carr54] Carr HY, Purcell EM. Effects of diffusion on free precession in Nuclear Magnetic Resonance experiments. Phys Rev 94(3): 630-638 (1954).

[Carr93] Carr HY. Letter to the editor. Physics Today 46(1): 94 (1993).

[Carr01] Carr JC, Simonetti O, Bundy J, Li D, Pereles S, Finn JP. Cine MR angiography of the heart with segmented true fast imaging with steady-state precession. Radiology 219: 828-834 (2001).

[Cas99] Castillo M. Neuroradiology companion. 2nd edition. Lippincott-Raven Publishers (1999).

[Cha00] Chalela JA, Alsop DC, Gonzalez-Atavales JB, Maldjian JA, Kasner SE, Detre JA. Magnetic resonance perfusion imaging in acute ischemic stroke using continuous arterial spin labeling. Stroke 31(3): 680-687 (2000).

[Chen96] Chen Q, Andersen AH, Zhang Z, Ovadia A, Gash DM, Avison MJ. Mapping drug-induced changes in cerebral by Multiple Gradient Recalled Echo functional MRI. Magn Reson Imag 14(5): 469-476 (1996).

[Chi94] Chien D, Levin DL, Anderson CM. MR gradient echo imaging of intravascular blood oxygenation: T2* determination in the presence of flow. Magn Reson Med 32(4): 540-545 (1994).

[Cho03] Choyke PL, Dwyer AJ, Knopp MV. Functional tumor imaging with dynamic contrast-enhanced Magnetic Resonance Imaging. J Magn Reson Imaging 17: 509-520 (2003).

[Chr11] Christen T, Lemasson B, Pannetier N, Farion R, Segebarth C, Rémy C, Barbier EL. Evaluation of a quantitative blood oxygenation level-dependent (qBOLD) approach to map local blood oxygen saturation. NMR Biomed 24(4): 393-403 (2011).

[Chr12] Christen T, Lemasson B, Pannetier N, Farion R, Remy C, Zaharchuk G, Barbier EL. Is T2* enough to assess oxygenation? Quantitative blood oxygen level-dependent analysis in brain tumor. Radiology 262(2): 495-502 (2012).

[Chu00] Chung HW, Chen CY, Zimmerman RA, Lee KW, Lee CC, Chin SC. T2-Weighted fast MR imaging with true FISP versus HASTE: comparative efficacy in the evaluation of normal fetal brain maturation. Am J Roentgenol 175: 1375-1380 (2000).

[Col97] Collingridge DR, Young WK, Vojnovic B, Wardman P, Lynch EM, Hill SA, Chaplin DJ. Measurement of tumor oxygenation: a comparison between polarographic needle electrodes and a time-resolved luminescence-based optical sensor. Radiat Res 147(3): 329-334 (1997).

[Con92] Constable RT, Anderson AW, Zhong J, Gore JC. Factors influencing contrast in fast spin-echo MR imaging. Magn Reson Imag 10: 497-511 (1992).

[Coo00] Cooper RA, Carrington BM, Loncaster JA, Todd SM, Davidson SE, Logue JP, Luthra AD, Jones AP, Stratford I, Hunter RD, West CM. Tumour oxygenation levels correlate with dynamic contrast-enhanced magnetic resonance imaging parameters in carcinoma of the cervix. Radiother Oncol 57(1): 53-59 (2000).

[Cope69] Cope FW. Nuclear magnetic resonance evidence using D2O for structured water in muscle and brain. Biophys J 9(3): 303-319 (1969).

[Cra87] Crawley AP, Henkelman RM. Errors in T2 estimation using multislice multiple-echo imaging. Magn Reson Med 4(1): 34-47 (1987).

[Cra88] Crawley AP, Wood ML, Henkelman RM. Elimination of transverse coherences in FLASH MRI. Magn Reson Med 8: 248-260 (1988).

[Dam71] Damadian R. Tumor detection by nuclear magnetic resonance. Science 171: 1151-1153 (1971).

[deSou11] de Sousa PL, Vignaud A, Fleury S, Carlier PG. Fast monitoring of T1 , T2 , and relative proton density (M(0)) changes in skeletal muscles using an IR-TrueFISP sequence. J Magn Reson Imaging 33(4): 921-930 (2011).

[Dei91] Deichmann R. Quantifizierung von kernmagnetischen Relaxationszeiten mit Hilfe der Snapshot-FLASH-Bildgebung. Diplomarbeit. Physikalisches Institut der Universität Würzburg (1991).

[Dei92] Deichmann R, Haase A. Quantification of T1 values by snapshot-FLASH NMR imaging. J Magn Reson 96: 608-612 (1992).

[Dei95] Deichmann R. Messung von NMR-parametern mit Schnellbildgebungsexperimenten. Dissertation. Physikalisches Institut der Universität Würzburg (1995).

[Deim94] Deimling M, Heid O. Magnetization prepared true FISP imaging. In: Proceedings SMR, 2nd Annual Meeting, San Francisco, USA; #495 (1994).

[Del08] Dellas K, Bache M, Pigorsch SU, Taubert H et al. Prognostic impact of HIF-1alpha expression in patients with definitive radiotherapy for cervical cancer. Strahlenther Onkol 184: 169-174 (2008).

[Der06] Derakhshan JJ, Blaimer M, Schmitt P, Sunshine JL, Duerk JL, Griswold MA. Inversion-optimized, multi-slice, parallel TOSSI (T-One insensitive Steady State Imaging). Proceedings ISMRM 2006; #2427 (2006).

[Der07] Derakhshan JJ, Sunshine JL, Duerk JL, Griswold MA. Resolution Enhanced TOSSI (T-One insensitive Steady State Imaging). Proceedings ISMRM-ESMRMB 2007; #585 (2007).

[Der12] Derakhshan JJ, Nour SG, Sunshine JL, Griswold MA, Duerk JL. Resolution enhanced T1-insensitive steady-state imaging. Magn Reson Med 68(2): 421-429 (2012).

[Des01] Deshpande VS, Shea SM, Laub G, Simonetti OP, FinnJP, Li D. 3D magnetization-prepared TrueFISP: A new technique for imaging coronary arteries. Magn Reson Med 46: 494-502 (2001).

[Des03] Deshpande VS, Chung Y-C, Zhang Q, Shea SM, Li D. Reduction of transient signal oscillations in TrueFISP using a linear flip angle series magnetization preparation. Magn Reson Med 49: 151-157 (2003).

[Det92] Detre JA, Leigh JS, Williams DS, Koretsky, AP: Perfusion imaging. Magn Reson Med 23(1): 37-45 (1992).

[deVri01] de Vries AF, Griebel J, Kremser C, Judmaier W, Gneiting T, Kreczy A, Ofner D, Pfeiffer KP, Brix G, Lukas P. Tumor microcirculation evaluated by dynamic magnetic resonance imaging predicts therapy outcome for primary rectal carcinoma. Cancer Res 61(6): 2513-2516 (2001).

[Dew90] Dewhirst MW, Sostman HD, Leopold KA, Charles HC, Moore D, Burn RA, Tucker JA, Harrelson JM, Oleson JR. Soft-tissue sarcomas: MR imaging and MR spectroscopy for prognosis and therapy monitoring. Work in progress. Radiology 174(3): 847-853 (1990).

[Dew00] Dewhirst MW, Klitzman B, Braun RD, Brizel DM, Haroon ZA, Secomb TW. Review of methods used to study oxygen transport at the microcirculatory level. Int J Cancer 90(5): 237-255 (2000).

[Die05] Diergarten T, Martirosian P, Kottke R, Vogel U, Stenzl A, Claussen CD and Schlemmer HP. Functional characterization of prostate cancer by integrated magnetic resonance imaging and oxygenation changes during carbogen breathing. Invest Radio 40: 102-199 (2005).

[Dix82] Dixon RL, Ekstrand KE. The physics of proton NMR. Med Phys 9(6): 807-818 (1982).

[Due98] Duerk JL, Lewin JS, Wendt M, Petersilge C. Remember TrueFISP? A high SNR, near 1-second imaging method for T2-like contrast in interventional MRI at 0.2 T. J Magn Reson Imaging 8: 203-208 (1998).

[Dunn99] Dunn TJ, Braun RD, Rhemus WE, Rosner GL, Secomb TW, Tozer GM, Chaplin DJ, Dewhirst MW. The effects of hyperoxic and hypercarbic gases on tumour blood flow. Br J Cancer 80(1-2): 117-126 (1999).

[Dunn02] Dunn JF, O'Hara JA, Zaim-Wadghiri Y, Lei H, Meyerand ME, Grinberg OY, Hou H,. Hoopes PJ, Demidenko E, Swartz HM. Changes in oxygenation of intracranial tumors with carbogen: a BOLD MRI and EPR oximetry study. J Magn Reson Imaging 16: 511-521 (2002).

[Duyn94] Duyn JH, Moonen CT,. van Yperen GH, de Boer RW and Luyten PR. Inflow versus deoxyhemoglobin effects in BOLD functional MRI using gradient echoes at 1.5 T. NMR Biomed 7: 83-88 (1994).

[Duyn97] Duyn JH. Steady state effects in fast gradient echo magnetic resonance imaging. Magn Reson Med 37(4): 559-568 (1997).

[Ear88] Earnest F 4th, Kelly PJ, Scheithauer BW, Kall BA, Cascino TL, Ehman RL, Forbes GS, Axley PL. Cerebral astrocytomas: histopathologic correlation of MR and CT contrast enhancement with stereotactic biopsy. Radiology 166(3): 823-827 (1988).

[Ede80] Edelstein WA. Hutchinson JMS, Johnson G, Redpath T. Spin warp NMR imaging and applications to human whole-body imaging. Phys Med Biol 25: 751-756 (1980).

[Egg75] Eggleston JC, Saryan LA, Hollis DP. Nuclear Magnetic Resonance investigations of human neoplastic and abnormal nonneoplastic tissues. Cancer Res 35: 1326-1332 (1975).

[Ehs12] Ehses P, Seiberlich N, Ma D, Breuer FA, Jakob PM, Griswold MA, Gulani V. IR TrueFISP with a golden-ratio-based radial readout: Fast quantification of T(1) , T(2), and proton density. Magn Reson Med doi: 10.1002/mrm.24225 [Epub ahead of print] (2012).

[Eis95] Eis M, Els T, Hoehn-Berlage M. High resolution quantitative relaxation and diffusion MRI of three different experimental brain tumors in rat. Magn Reson Med 34(6): 835-844 (1995).

[Elk09] Elkady AM, Bowen CV. Diffusion Enhanced Sensitivity of bSSFP Quantification of Micron-Sized Superparamgnetic Iron Oxide. Proceedings ISMRM 2009; #3155 (2009).

[Eng86] Englund E, Brun A, Larsson EM, Györffy-Wagner Z, Persson B. Tumours of the central nervous system. Proton magnetic resonance relaxation times T1 and T2 and histopathologic correlates. Acta Radiol Diagn (Stockh) 27(6): 653-659 (1986).

[Ern66] Ernst RR, Anderson WA. Application of fourier transform spectroscopy to magnetic resonance. Rev Sci Instr 37(1): 93-102 (1966).

[Ess98] Essig M, Hawighorst H, Schönberg SO, Engenhart-Cabillic R, Fuss M, Debus J, Zuna I, Knopp MV, van Kaick G. Fast fluid-attenuated inversion-recovery (FLAIR) MRI in the assessment if intraaxial brain tumors. J Magn Reson Imaging 8: 789-798 (1998).

[Ess99] Essig M, Knopp MV, Debus J, Schönberg SO, Wenz F, Hawighorst H, van Kaick G. Fluid-attenuated-inversion-recovery-(FLAIR-) Bildgebung in der Diagnostik zerebraler Gliome und Metastasen. Radiologe 39: 151-160 (1999).

[Ess03] Essig M, Waschkies M, Wenz F, Debus J, Hentrich HR, Knopp MV. Assessment of brain metastases with dynamic susceptibility-weighted contrast-enhanced MR imaging: initial results. Radiology 228: 193-199 (2003).

[Est33] Estermann I, Stern O. Über die magnetische Ablenkung von Wasserstoffmolekülen und das magnetische Moment des Protons II. Z Physik 85: 17-24 (1933).

[Fat99] Fatouros PP, Marmarou A. Use of magnetic resonance imaging for in vivo measurements of water content in human brain: method and normal values. J Neurosurg 90(1): 109-115 (1999).

[Fau00] Fautz HP, Büchert M, Husstedt H, Laubenberger J, Hennig J. TSE-sequences with spin-echo contrast. Magn Reson Med: 43(4): 577-82 (2000).

[Fel93] Feldmann HJ, Sievers K, Fuller J, Molls M, Lohr E. Evaluation of tumor blood perfusion by dynamic MRI and CT in patients undergoing thermoradiotherapy. Eur J Radiol 16(3): 224-229 (1993).

[Fel98] Feldmann HJ, Molls M, Vaupel P. Clinical investigations ob blood perfusion in human tumors. In: Molls M, Vaupel P (eds). Blood perfusion and microenvironment of human tumors. Springer-Verlag Berlin Heidelberg New York (1998).

[Fel99a] Feldmann HJ: Tumoroxygenierung und Hypoxie; Der Onkologe 5(11): 1000-1007 (1999).

[Fel99b] Feldmann HJ, Molls M, Vaupel P. Blood flow and oxygenation status of human tumors. Strahlenther Onkol 175(1): 1-9 (1999).

[Fen04] Fenchel M, Helber U, Simonetti OP, Stauder NI, Kramer U, Nguyen CN, Finn JP, Claussen CD, Miller S. Multislice first-pass myocardial perfusion imaging: Comparison of saturation recovery (SR)-TrueFISP-two-dimensional (2D) and SR-TurboFLASH-2D pulse sequences. J Magn Reson Imaging 19(5): 555-563 (2004).

[Fox86] Fox PT, Raichle ME. Focal physiological uncoupling of cerebral blood flow and oxidative metabolism during somatosensory stimulation in human subjects. Proc Natl Acad Sci USA 83(4): 1140-1144 (1986).

[Fra87] Frahm J, Hänicke W, Merboldt K-D. Transverse coherence in rapid FLASH NMR imaging. Journal of Magnetic Resonance 72: 307-314 (1987).

[Fre71] Freeman R, Hill HDW. Phase and intensity anomalies in Fourier transform NMR. J Magn Reson 4: 366-383 (1971).

[Fri33] Frisch R, Stern O. Über die magnetische Ablenkung von Wasserstoffmolekülen und das magnetische Moment des Protons I. Z Phys 85: 4-16 (1933).

[Fyl98] Fyles AW, Milosevic M, Wong R, Kavanagh MC, Pintilie M, Sun A, Chapman W, Levin W, Manchul L, Keane TJ, Hill RP. Oxygenation predicts radiation response and survival in patients with cervix cancer. Radiother Oncol 48(2): 149-156 (1998).

[Gai09] Gai ND, Butman JA. Modulated repetition time look-locker (MORTLL): a method for rapid high resolution three-dimensional T1 mapping. J Magn Reson Imaging 30(3): 640-648 (2009).

[Gan04] Ganter C. Off-resonance effects in the transient response of SSFP sequences. Magn Reson Med 52: 368-375 (2004).

[Gan06] Ganter C. Static susceptibility effects in balanced SSFP sequences. Magn Reson Med 56(3): 687-691 (2006).

[Gan09] Ganter C. Analytical solution to the transient phase of steady-state free precession sequences. Magn Reson Med 62(1): 149-164 (2009). Erratum in: Magn Reson Med 63(4): 1135 (2010).

[Gar74] Garroway AN, Grannell PK, Mansfield P. Image formation in NMR by a selective irradiative process. J Phys C: Solid State Phys 7: L457-462 (1974).

[Gil99] Gillies RJ, Schornack PA, Secomb TW, Raghunand N. Causes and effects of heterogeneous perfusion in tumors. Neoplasia 1(3): 197-207 (1999).

[Gil02] Gillies RJ, Raghunand N, Karczmar GS, Bhujwalla ZM. MRI of the tumor microenvironment J Magn Reson Imaging 16: 430-450 (2002).

[Gra86a] Graumann R, Deimling M, Heilmann T, Oppelt A. A new Method for fast and precise T1 determination. In: Proceedings SMRM 1986: 922-923 (1986).

[Gra86b] Graumann R, Oppelt A, Stetter E. Multiple-Spin-Echo imaging with a 2D Fourier method. Magn Reson Med 3: 707-721 (1986).

[Gray53] Gray LH, Conger AD, Ebert M, Hornsey S, Scott OC. The concentration of oxygen dissolved in tissues at the time of irradiation as a factor in radiotherapy. Br J Radiol 26(312): 638-648 (1953).

[Grie97] Griebel J, Mayr NA, de Vries A, Knopp MV, Gneiting T, Kremser C, Essig M, Hawighorst H, Lukas PH, Yuh WT. Assessment of tumor microcirculation: a new role of dynamic contrast MR imaging. J Magn Reson Imaging 7(1): 111-109 (1997).

[Grif97] Griffiths JR, Taylor NJ, Howe FA, Saunders MI, Robinson SP, Hoskin PJ, Powell ME, Thoumine M, Caine LA, Baddeley H. The response of human tumors to carbogen breathing, monitored by Gradient-Recalled Echo Magnetic Resonance Imaging. Int J Radiat Oncol Biol Phys 39(3): 697-701 (1997).

[Grif99] Griffiths JR, Robinson SP. The OxyLite: a fibre-optic oxygen sensor. Br J Radiol 72(859): 627-630 (1999).

[Gris02] Griswold MA, Jakob PM, Heidemann RM, et al. Generalized autocalibrating partially parallel acqusitions (GRAPPA). Magn Reson Med 47: 1202-1210 (2002).

[Gris04] Griswold MA, Schmitt P, Speier P, Nittka M, Gulani V, Jakob PM. Real-Time undersampled radial IR-TrueFISP for fast quantitative T1, T2 & M0 mapping. Proceedings ISMRM 2004, #2661 (2004).

[Gud95] Gudbjartsson H, Patz S. Simultaneous calculation of flow and diffusion sensitivity in steady-state free precession imaging. Magn Reson Med 34: 567-579 (1995).

[Güt31] Güttinger P. Das Verhalten von Atomen im magnetischen Drehfeld. Z Phys 73: 169-184 (1931).

[Gul04] Gulani V, Schmitt P, Griswold MA, Webb AG, Jakob PM. Towards a single-sequence neurologic Magnetic Resonance Imaging examination: Multiple-contrast images from an IR TrueFISP experiment. Invest Radiol 39(12): 767-774 (2004).

[Gyn88] Gyngell ML. The application of steady state free precession in rapid 2DFT NMR imaging: FAST and CE-FAST sequences. Magn Reson Imag 6: 415-419 (1988).

[Haa85] Haase A, Frahm J, Matthaei D, Hänicke W, Merboldt K-D. Rapid images and NMR movies. Proceedings SMR, #980 (1985).

[Haa86] Haase A, Frahm J, Matthaei D, Hänicke W, Merboldt K-D. FLASH imaging. Rapid NMR imaging using low flip-angle pulses. J Magn Reson 67: 258-266 (1986).

[Haa89] Haase A, Matthaei D, Bartkowski R, Dühmke E, Leibfritz D. Inversion recovery snapshot FLASH MR imaging. J Comp Assist Tomogr 13: 1036-1040 (1989).

[Haa90] Haase A. Snapshot FLASH MRI. Applications to T1, T2, and chemical-shift imaging. Magn Reson Med 13(1): 77-89 (1990).

[Haac90] Haacke EM, Wielopolski PA, Tkach JA, Modic MT. Steady-state free precession imaging in the presence of motion: application for improved visualization of the cerebrospinal fluid. Radiology 175: 545-552 (1990).

[Haac97] Haacke EM, Lai S, Reichenbach JR, Kuppusamy K, Hoogenraad FG, Takeichi H, Lin W. In vivo measurement of blood oxygen saturation using magnetic resonance imaging: a direct validation of the blood oxygen level-dependent concept in functional brain imaging. Hum Brain Mapp 5(5): 341-346 (1997).

[Haac99] Haacke EM, Brown RW, Thompson MR, Venkatesan R. Magnetic Resonance Imaging: Physical principles and sequence design. Mosby: St Louis, MO (1999).

[Hahn50a] Hahn EL. Nuclear induction due to free Larmor precession. Phys Rev 77: 297-298 (1950).

[Hahn50b] Hahn EL. Spin echoes. Phys Rev 80(4): 580-594 (1950).

[Hahn60] Hahn EL. Detection of sea-water motion by nuclear precession. J Geophys Res 65(2): 776-777 (1960).

[Har01] Hargreaves BA, Vasanawala SS, Pauly JM, Nishimura DG. Characterization and reduction of the transient response in steady-state MR imaging. Magn Reson Med 46: 149-158 (2001).

[Hawi97] Hawighorst H, Engenhart R, Knopp MV, Brix G, Grandy M, Essig M, Miltner P, Zuna I, Fuss M, van Kaick G. Intracranial meningeomas: time- and dose-dependent effects of irradiation on tumor microcirculation monitored by dynamic MR imaging. Magn Reson Imaging 15(4): 423-432 (1997).

[Hawi98a] Hawighorst H, Bock M, Knopp MV, Essig M, Schoenberg SO, Knapstein PG, Schad LR, van Kaick G. Magnetically labeled water perfusion imaging of the uterine arteries and of normal and malignant cervical tissue: initial experiences. Magn Reson Imaging 16(3): 225-234 (1998).

[Hawi98b] Hawighorst H, Knapstein PG, Knopp MV, Weikel W, Brix G, Zuna I, Schonberg SO, Essig M, Vaupel P, van Kaick G. Uterine cervical carcinoma: comparison of standard and pharmacokinetic analysis of time-intensity curves for assessment of tumor angiogenesis and patient survival. Cancer Res 58(16): 3598-3602 (1998).

[Hawk87] Hawkes RC, Patz S. Rapid Fourier imaging using steady-state free precession. Magn Reson Med 4: 9-23 (1987).

[Haz69] Hazlewood CF, Nichols BF, Chamerlain NF. Evidence for the existence of a minimum of two phases of ordered water in skeletal muscle. Nature 222: 747-750 (1969).

[Henk92] Henkelman RM, Hardy PA, Bishop JE, Poon CS, Plewes DB. Why fat is bright in RARE and fast spin-echo imaging. J Magn Reson Imaging: 2(5): 533-540 (1992).

[Hen03] Henke M, Laszig R, Rübe C, Schäfer U, Haase KD, Schilcher B, Mose S, Beer KT, Burger U, Dougherty C, Frommhold H. Erythropoietin to treat head and neck cancer patients with anaemia undergoing radiotherapy: randomised, double-blind, placebo-controlled trial. Lancet 18; 362(9392): 1255-1260 (2003).

[Henn84] Hennig J, Nauerth A, Friedburg H, Ratzel D. Ein neues Schnellbildverfahren für die Kernspintomographie. Radiologe 24: 579-580 (1984).

[Henn86] Hennig J, Nauerth A, Friedburg H. RARE imaging: A fast imaging method for clinical MR. Magn Reson Med 3: 823-833 (1986).

[Henn88a] Hennig J. Multiecho imaging sequences with low refocusing flip angles. J Magn Reson 78: 397-407 (1988).

[Henn88b] Hennig J, Friedburg H. Clinical applications and methodological developments of the RARE sequence. Magn Reson Imag 6: 391-395 (1988).

[Henn91a] Hennig J. Echoes - how to generate, recognize, use or avoid them in MR imaging sequences. Part I: Fundamental and not so fundamental properties of spin echoes. Concepts Magn Reson 3: 125-143 (1991).

[Henn91b] Hennig J. Echoes - how to generate, recognize, use or avoid them in MR imaging sequences. Part II: Echoes in imaging sequences. Concepts Magn Reson 3: 179-192 (1991).

[Herm99] Hermans R, Lambin P, Van der Goten A et al. Tumoural perfusion as measured by dynamic computed tomography in head and neck carcinoma. Radiother Oncol 53(2): 105-111 (1999).

[Hern10] Hernando CG, Esteban L, Cañas T, Van den Brule E, Pastrana M. The role of magnetic resonance imaging in oncology. Clin Transl Oncol 12: 606-613 (2010).

[Hill96] Hill SA, Pigott KH, Saunders MI, Powell ME, Arnold S, Obeid A, Ward G, Leahy M, Hoskin PJ, Chaplin DJ. Microregional blood flow in murine and human tumours assessed using laser Doppler microprobes. Br J Cancer 74 (Suppl XXVII): 260-263 (1996).

[Hill98] Hill SA, Collingridge DR, Vojnovic B, Chaplin DJ. Tumour radiosensitization by high-oxygen-content gases: influence of the carbon dioxide content of the inspired gas on PO2, microcirculatory function and radiosensitivity. Int J Radiat Oncol Biol Phys 40(4): 943-951 (1998).

[Hil01] Hiller KH, Waller C, Voll S, Haase A, Ertl G, Bauer WR. Combined high-speed NMR imaging of perfusion and microscopic coronary conductance vessels in the isolated rat heart. Microvasc Res 62(3): 327-334 (2001).

[Hin76] Hinshaw WS. Image formation by nuclear magnetic resonance: The sensitive-point method. J Appl Phys 47(8): 3709-3721 (1976).

[Hoe93] Hoeckel M, Knoop C, Schlenger K, Vorndran B, Baussmann E, Mitze M, Knapstein PG, Vaupel P. Intratumoral pO2 predicts survival in advanced cancer of the uterine cervix. Radiother Oncol 26: 45-50 (1993).

[Hoeh92] Hoehn-Berlage M, Tolxdorff T, Bockhorst K, Okada Y, Ernestus RI. In vivo NMR T2 relaxation of experimental brain tumors in the cat: a multiparameter tissue characterization. Magn Reson Imaging 10(6): 935-947 (1992).

[Hoeh94] Hoehn-Berlage M, Bockhorst K. Quantitative magnetic resonance imaging of rat brain tumors: in vivo NMR relaxometry for the discrimination of normal and pathological tissues. Technol Health Care 2(4): 247-254 (1994).

[Hor94] Horsman MR, Nordsmark M, Khalil AA et al. Reducing acute and chronic hypoxia in tumours by combining nicotinamide with carbogen breathing. Acta Oncol 33(4): 371-376 (1994).

[Hor98a] Horsman MR. Measurement of tumor oxygenation. Int J Radiat Oncol Biol Phys; 42(4): 701-704 (1998).

[Hor98b] Horsman MR, Nordsmark M, Overgaard J. Techniques to assess the oxygenation of human tumors. State of the art. Strahlenther Onkol; 174 Suppl 4:2-5 (1998).

[Hor04] Horsman MR, Overgaard J. Preclinical studies on how to deal with patient intolerance to nicotinamide and carbogen. Radiother Oncol 70(3): 301-309 (2004).

[Hos99a] Hoskin PJ, Abdelath O, Phillips H, Gilligan S, Saunders MI, Broderick P, Baddeley H. Inspired and expired gas concentrations in man during carbogen breathing. Radiother Oncol 51(2): 175-177 (1999).

[Hos99b] Hoskin PJ, Saunders MI, Goodchild K, Powell ME, Taylor NJ, Baddeley H. Dynamic contrast enhanced magnetic resonance scanning as a predictor of response to accelerated radiotherapy for advanced head and neck cancer. Br J Radiol 72(863): 1093-1098 (1999).

[Kno99] Knopp EA, Cha S, Johnson G, Mazumdar A, Golfinos JG, Zagzag D, Miller DC, Kelly PJ, Kricheff II. Glial neoplasms: dynamic contrast-enhanced T2*-weighted MR imaging. Radiology 211(3): 791-798 (1999).

[Hou77] Hoult DI. Zeugmatography: A criticism of the concept of a selective pulse in the presence of a field gradient. J Magn Reson 26: 165-167 (1977).

[Howe96] Howe FA, Robinson SP, Griffiths JR. Modification of tumor perfusion and oxygenation monitored by gradient recalled echo MRI and 31P MRS. NMR Biomed 9: 208–216 (1996).

[Howe99] Howe FA, Robinson SP, Rodrigues LM, Griffiths JR. Flow and oxygenation dependent (FLOOD) contrast MR imaging to monitor the repsonse of rat tumors to carbogen breathing. Magn Reson Imag 17(9): 1307–1318 (1999).

[Howe01] Howe FA, Robinson SP, McIntyre DJ, Stubbs M, Griffiths JR. Issues in flow and oxygenation dependent contrast (FLOOD) imaging of tumours. NMR Biomed 14(7-8): 497-506 (2001).

[Hua02] Huang TY, Huang IJ, Chen CY, Scheffler K, Chung HW, Cheng HC. Are TrueFISP images T2/T1-weighted? Magn Reson Med 48: 684-688 (2002).

[Hua07] Huang TY, Liu YJ, Stemmer A, Poncelet BP. T2 measurement of the human myocardium using a T2-prepared transient-state TrueFISP sequence. Magn Reson Med 57: 960-966 (2007).

[Hun02] Hunsche S, Sauner D, Schreiber WG, Oelkers P, Stoeter P. FAIR and dynamic susceptibility contrast-enhanced perfusion imaging in healthy subjects and stroke patients. J Magn Reson Imaging 16(2): 137-146 (2002).

[Hut78b] Hutchinson JMS, Sutherland RJ, Mallard JR. NMR imaging: Image recovery under magnetic fields with large non-uniformities. J Phys E: Sci Instrum 11: 217-222 (1978).

[Jay55] Jaynes ET. Matrix treatment of nuclear induction. Phys Rev 98(4): 1099-1105 (1955).

[Jor00] Jordan FB, Misson P-D, Demeure R, Baudelet C, Beghein N, Gallez B. Changes in tumor oxygenation/perfusion induced by the NO donor, isosorbide dinitrate, in comparison with carbogen: monitoring by EPR and MRI. Int J Radiat Oncol Biol Phys 48(2): 565-570 (2000).

[Just88] Just M, Thelen M. Tissue characterization with T1, T2, and proton density values: results in 160 patients with brain tumors. Radiology 169(3): 779-785 (1988).

[Kaa98] Kaanders JH, Pop LA, Marres HA, Liefers J, van den Hoogen FJ, van Daal WA, van der Kogel AJ. Accelerated radiotherapy with carbogen and nicotinamide (ARCON) for laryngeal cancer. Radiother Oncol 48(2): 115-122 (1998).

[Kaa02a] Kaanders JH, Bussink J, van der Kogel AJ. ARCON: a novel biology-based approach in radiotherapy. Lancet Oncol 3(12): 728-737 (2002).

[Kaa02b] Kaanders JH, Pop LA, Marres HA, Bruaset I, van den Hoogen FJ, Merkx MA, van der Kogel AJ. ARCON: experience in 215 patients with advanced head-and-neck cancer. Int J Radiat Oncol Biol Phys 52(3): 769-778 (2002).

[Kai74] Kaiser R, Bartholdi E, Ernst RR. Diffusion and field-gradient effects in NMR Fourier spectroscopy. J Chem Phys 60(8): 2966-2979 (1974).

[Kal90] Kallinowski F, Zander R, Hoeckel M, Vaupel P. Tumor tissue oxygenation as evaluated by computerized pO2-histography. Int J Radiat Oncol Biol Phys 19: 953-961 (1990).

[Kap76] Kaptein R, Dijkstra K, Tarr CE. A single-scan Fourier Transform method for measuring spin-lattice relaxation times. J Magn Reson 24: 295-300 (1976).

[Ked94] Kedar RP, Cosgrove DO, Smith IE, Mansi JL, Bamber JC. Breast carcinoma: measurement of tumor response to primary medical therapy with color Doppler flow imaging. Radiology: 190(3): 825-830 (1994).

[Kel87] Kelly PJ, Daumas-Duport C, Kispert DB, Kall BA, Scheithauer BW, Illig JJ. Imaging-based stereotaxic serial biopsies in untreated intracranial glial neoplasms. J Neurosurg 66(6): 865-874 (1987).

[Ken94] Kennan RP, Zhong J, Gore JC. Intravascular susceptibility contrast mechanisms in tissues. Magn Reson Med 31(1): 9-21 (1994).

[Kim94] Kim SG, Hendrich K, Hu X, Merkle H and Ugurbil K. Potential pitfalls of functional MRI using conventional gradient-recalled echo techniques. NMR Biomed 7: 69-74 (1994).

[Kim95] Kim S-G. Quantification of relative cerebral blood flow change by flow-sensitive alternating inversion recovery (FAIR) technique: application to functional mapping. Magn Reson Med 34(3): 293-301 (1995).

[Kim07] Kim HS, Kim SY. A prospective study on the added value of pulsed arterial spin-labeling and apparent diffusion coefficients in the grading of gliomas. AJNR Am J Neuroradiol 28(9): 1693-1699 (2007).

[Kje91] Kjellen E, Joiner MC, Collier JM, Johns H, Rojas A. A therapeutic benefit from combining normobaric carbogen or oxygen with nicotinamide in fractionated X-ray treatments. Radiother Oncol 22(2): 81-91 (1991).

[Kno99] Knocke TH, Weitmann HD, Feldmann HJ, Selzer E, Pötter R. Intratumoral pO2-measurements as prediktive assay in the treatment of carcinoma of the uterine cervix. Radiother Oncol 53: 99-104 (1999).

[Kos99] Koshimoto Y, Yamada H, Kimura H, Maeda M, Tsuchida C, Kawamura Y, Ishii Y. Quantitative analysis of cerebral microvascular hemodynamics with T2-weighted dynamic MR imaging. J Magn Reson Imaging 9(3): 462-467 (1999).

[Kot03] Kotas M, Breuer F, Schmitt P, Zips D, Müller JG, Haase A, Flentje M: Nicht-invasive Darstellung von Oxygenierungsänderungen in Tumoren unter Carbogen- und Sauerstoffatmung mittels MR-Bildgebung. 9. Jahreskongress der DEGRO, Essen, #365 (2003).

[Kot09] Kotas M, Schmitt P, Jakob PM, Flentje M. Monitoring of Tumor Oxygenation Changes in Head-and-Neck Carcinoma Patients Breathing a Hyperoxic Hypercapnic Gas Mixture with a Noninvasive MRI Technique. Strahlenther Onkol 185(1): 19-26 (2009).

[Kum75] Kumar A, Welti D, Ernst RR. NMR Fourier zeugmatography. J Magn Reson 18, 69-83 (1975).

[Kur95] Kurki T, Komu M. Spin-lattice relaxation and magnetization transfer in intracranial tumors in vivo: effects of Gd-DTPA on relaxation parameters. Magn Reson Imaging 13(3): 379-385 (1995).

[Lan98] Lanzen JL, Braun RD, Ong AL, Dewhirst MW. Variability in blood flow and pO2 in tumors in response to carbogen breathing. Int J Radiol Biol Phys 42: 855-859 (1998).

[Lau73] Lauterbur PC. Image formation by induced local interactions: examples employing Nuclear Magnetic Resonance. Nature 242: 190-191 (1973).

[Loe09] Loeffler RB, Wu S, van Groningen N, Patay Z, Glass JO, Smeltzer MP, Hillenbrand CM. Accurate T1 and T2 maps obtained with IR-TrueFISP calibrated by a patient driven model. Proceedings ISMRM 2009; #993 (2009).

[Lud00] Ludemann L, Hamm B, Zimmer C. Pharmacokinetic analysis of glioma compartments with dynamic Gd-DTPA-enhanced magnetic resonance imaging. Magn Reson Imaging 18(10): 1201-1214 (2000).

[Lud01] Ludemann L, Grieger W, Wurm R, Budzisch M, Hamm B, Zimmer C. Comparison of dynamic contrast-enhanced MRI with WHO tumor grading for gliomas. Eur Radiol 11(7): 1231-1241 (2001).

[Kwo95] Kwong KK, Cheslar DA, Weisskoff RM, Donahue KM, Davis TL, Ostergaard L, Campbell TA. MR perfusion studies with T1-weighted echo planar imaging. Magn Reson Med 34: 878-887 (1995).

[Lea96] Leadon SA. Reapair of DNA damage produced by ionizing radiation: a minireview. Semin Radiat Oncol 6: 295-305 (1996).

[Leb98a] Lebon V, Brillault-Salvat C, Bloch G, Leroy-Willig A, Carlier PG. Evidence of muscle BOLD effect revealed by simultaneous interleaved gradient-echo NMRI and myoglobin NMRS during leg ischemia. Magn Reson Med 40(4): 551-558 (1998).

[Leb98b] Lebon V, Carlier PG, Brillault-Salvat C, Leroy-Willig A. Simultaneous measurement of perfusion and oxygenation changes using a multiple gradient-echo sequence: application to human muscle study. Magn Reson Imaging 16(7): 721-729 (1998).

[Lee86] Lee JN, Riederer SJ. A modified saturation-recovery approximation for multiple spin-echo pulse sequences. Magn Reson Med 3(1): 132-134 (1986).

[Lee02] Lee VS, Resnick D, Bundy JM, et al. Cardiac function: MR evaluation in one breath hold with real-time true fast imaging with steady-state precession. Radiology 222:835-842 (2002).

[LeR03] Le Roux P. Simplified model and stabilization of SSFP sequences. J Magn Reson 163: 23-37 (2003).

[Li98] Li D, Wang Y, Waight DJ. Blood oxygen saturation assessment in vivo using T2* estimation. Magn Reson Med 39(5): 685-690 (1998).

[Liu07] Liu TT, Brown GG. Measurement of cerebral perfusion with arterial spin labeling: Part 1. Methods. J Int Neuropsychol Soc 13(3): 517-525 (2007).

[Loo70] Look DC, Locker DR. Time saving in measurement of NMR and EPR relaxation times. Rev Sci Instr 41(2): 250-251 (1970).

[Lyng99] Lyng, H, Tanum G, Evensen JF and Rofstad EK. Changes in oxygen tension during radiotherapy of head and neck tumours. Acta Oncol 38: 1037-1042 (1999).

[Lyng01a] Lyng H, Vorren AO, Sundfor K, Taksdal I, Lien HH, Kaalhus O, Rofstad EK. Assessment of tumor oxygenation in human cervical carcinoma by use of dynamic Gd-DTPA-enhanced imaging. J Magn Reson Imaging 14(6): 750-756 (2001).

[Maj32] Majorana E. Atomi orientati in campo magnetico variabile. Nuovo Cimento 9: 43-50 (1932).

[Man73] Mansfield P, Grannel PK. NMR „diffraction“ in solids? J Phys C: Solid State Phys 6: L422-426 (1973).

[Man77] Mansfield P. Multi-planar image formation using NMR spin echoes. J Phys C: Solid State Phys 10: L55-58 (1977).

[Mar10] Martirosian P, Boss A, Schraml C, Schwenzer NF, Graf H, Claussen CD, Schick F. Magnetic resonance perfusion imaging without contrast media. Eur J Nucl Med Mol Imaging 37 (Suppl 1): 52-64 (2010).

[Mayr96] Mayr NA, Yuh WT, Magnotta VA et al. Tumor perfusion studies using fast magnetic resonance imaging technique in advanced cervical cancer: a new noninvasive predictive assay. Int J Radiat Oncol Biol Phys 36(3): 623-633 (1996).

[Mayr99] Mayr NA, Hawighorst H, Yuh WT, Essig M, Magnotta VA, Knopp MV. MR microcirculation assessment in cervical cancer: correlations with histomorphological tumor markers and clinical outcome. J Magn Reson Imaging 10(3): 267-276 (1999).

[Mei58] Meiboom S, Gill D. Modified spin-echo method for measuring nuclear relaxation times. Rev Sci Instrum 29(8): 688-691 (1958).

[Men93] Menon RS, Ogawa S, Tank DW and Ugurbil K. Tesla gradient recalled echo characteristics of photic stimulation-induced signal changes in the human primary visual cortex. Magn Reson Med 30: 380-386 (1993).

[Mill10] Miller KL. Asymmetries of the balanced SSFP profile. Part I: Theory and observation. Magn Reson Med 63(2): 385-395 (2010).

[Milo04] Milosevic M, Fyles A, Hedley D, Hill R. The human tumor microenvironment: invasive (needle) measurement of oxygen and interstitial fluid pressure. Semin Radiat Oncol 14(3): 249-258 (2004).

[Mio96] Miot-Noirault E, Akoka S, Hoffschir D, Pontvert D, Gaboriaud G, Alapetite C, Fetissof F, Le Pape A. Potential of T2 relaxation time measurements for early detection of radiation injury to the brain: experimental study in pigs. AJNR Am J Neuroradiol 17(5): 907-912 (1996).

[Mör10] Mörchel P, Melkus G, Yaromina A, Zips D, Baumann M, Jakob PM, Flentje M. Correlating quantitative MR measurements of standardized tumor lines with histological parameters and tumor control dose. Radiother Oncol 96(1): 123-130 (2010).

[Mol98] Molls M, Vaupel P. The impact of the tumor microenvironment on experimental and clinical radiation oncology and other therapeutic modalitites. In: Molls M, Vaupel P (eds). Blood perfusion and microenvironment of human tumors. Springer-Verlag Berlin Heidelberg New York (1998).

[Mul90a] Mulkern RV, Wong STS, Winalski C, Jolesz FA. Contrast manipulation and artifact assessment of 2D and 3D RARE sequences. Magn Reson Imag 8: 557-566 (1990).

[Mul90b] Mulkern RV, Wong STS, Jakab P, Bleier AR, Sandor T, Jolesz FA. CPMG imaging sequences for high field in vivo transverse relaxation studies. Magn Reson Med 16: 67-79 (1990).

[Mul91] Mulkern RV, Melki PS, Jakab P, Higuchi N, Jolesz FA. Phase-encode order and its effect on contrast and artifact in single-shot RARE sequences. Med Phys 18(5): 1032-1037 (1991).

[Nar86] Naruse S, Horikawa Y, Tanaka C, Hirakawa K, Nishikawa H, Yoshizaki K. Significance of proton relaxation time measurement in brain edema, cerebral infarction and brain tumors. Magn Reson Imaging 4(4): 293-304 (1986).

[Nek92] Nekolla S, Gneiting T, Syha J, Deichmann R, Haase A. T1 maps by k-space reduced snapshot-FLASH MRI. J Comput Assist Tomogr 16(2): 327-332 (1992).

[New05a] Newbould RD, Gold GE, Alley MT, Bammer R. Quantified T1, T2, and PD Mapping in Cartilage with 3D IR-trueFISP. Proceedings ISMRM 2005; #1997 (2005).

[New05b] Newbould RD, Bammer R. Flip Angle Sensitivity in IR-trueFISP T1 and T2 Mapping. Proceedings ISMRM 2005; #2191 (2005).

[New07] Newbould RD, Alley MT, Gold GE, Bammer R. Simultaneous T1, T2, PD, and B1 mapping with dual angle IR-bSSFP (DAIRy-bSSFP). Proceedings ISMRM 2007; #38 (2007).

[New08] Newbould RD, Alley MT, Ropele S, Bammer R. T1 mapping of MT effects in bSSFP. Proceedings ISMRM 2008; #1400 (2008).

[New10] Newbould RD, Skare ST, Alley MT, Gold GE, Bammer R. Three-dimensional T(1), T(2) and proton density mapping with inversion recovery balanced SSFP. Magn Reson Imaging 28(9): 1374-1382 (2010).

[Nis00] Nishimura DG, Vasanawala S. Analysis and reduction of the transient response in SSFP imaging. Proceedings ISMRM 2000; #301 (2000).

[Nor96] Nordsmark M, Overgaard M, Overgaard J: Pretreatment oxygenation predicts radiation response in advanced squamous cell carcinoma of the head and neck. Radiother Oncol 41(1): 31-39 (1996).

[Nor97] Nordsmark M, Maxwell RJ, Horsman MR, Bentzen SM, Overgaard J. The effect of hypoxia and hyperoxia on nucleoside triphosphate/inorganic phosphate, pO2 and radiation response in an experimental tumour model. Br J Cancer 76(11): 1432-1439 (1997).

[Nor00] Nordsmark M, Overgaard J. A confirmatory prognostic study on oxygenation status and loco-regional control in advanced head and neck squamous cell carcinoma treated by radiation therapy; Radiother Oncol 57(1): 39-43 (2000).

[Noz96] Nozue M, Lee I, Yuan F, Teicher BA, Brizel DM, Dewhirst MW, Milross CG, Milas L, Song CW, Thomas CD, Guichard M, Evans SM, Koch CJ, Lord EM, Jain RK, Suit HD. Interlaboratory variation in oxygen tension measurement by Eppendorf "Histograph" and comparison with hypoxic marker. J Surg Oncol 66(1): 30-38 (1997).

[Oga90a] Ogawa S, Lee TM, Nayak AS, Glynn P. Oxygenation-sensitive contrast in magnetic resonance image of rodent brain at high magnetic fields. Magn Reson Med 14: 68–78 (1990).

[Oga90b] Ogawa S, Lee TM, Kay AR, Tank DW. Brain magnetic resonance imaging with contrast dependent on blood oxygenation. Proc Natl Acad Sci USA 87: 9868–9872 (1990).

[Oga92] Ogawa S, Tank DW, Menon R, Ellermann JM, Kim SG, Merkle H, Ugurbil K. Intrinsic signal changes accompanying sensory stimulation: functional brain mapping with magnetic resonance imaging. Proc Natl Acad Sci USA 89(13): 5951-5955 (1992).

[Oga93] Ogawa S, Menon RS, Tank DW, Kim SG, Merkle H, Ellermann JM, Ugurbil K. Functional brain mapping by blood oxygenation level-dependent contrast magnetic resonance imaging. A comparison of signal characteristics with a biophysical model. Biophys J 64(3) :803-812 (1993).

[Oli01] Olive PL, Banath JP, Aquino-Parsons C. Measuring hypoxia in solid tumours - is there a gold standard? Acta Oncol 40(8): 917-923 (2001).

[Opp86] Oppelt A, Graumann R, Barfuss H, Fischer H, Hartl W, Schajor W. FISP – a new fast MRI sequence. Electromedica 54: 15-18 (1986).

[Pad02] Padhani AR. Dynamic contrast-enhanced MRI in clinical oncology: current status and future directions. J Magn Reson Imaging 16: 407-422 (2002).

[Pard94] Pardo FS, Aronen HJ, Kennedy D, Moulton G, Paiva K, Okunieff P, Schmidt EV, Hochberg FH, Harsh GR, Fischman AJ, et al. Functional cerebral imaging in the evaluation and radiotherapeutic treatment planning of patients with malignant glioma. Int J Radiat Oncol Biol Phys 30(3): 663-669 (1994).

[Parr74] Parrish RG, Kurland RJ, Janese WW, Bakay L. Proton relaxation rates of water in brain and brain tumors. Science 183: 438-439 (1974).

[Part01] Partridge SE, Aquino-Parsons C, Luo C, Green A, Olive PL. A pilot study comparing the intratumoral oxygenation using the COMET assay following 2.5% and 5% carbogen and 100% oxygen. Int J Radiat Oncol Biol Phys 49: 575-580 (2001).

[Patz89] Patz S. Steady-state free precession, an overview of basic concepts and applications. In: Feig E, ed. Advances in Magnetic Resonance Imaging, Volume 1, Norwood, New Jersey, Ablex, p. 73-102 (1989).

[Pau24] Pauli W. Zur Frage der theoretischen Deutung der Satelliten einiger Spektrallinien und ihrer Beeinflussung durch magnetische Felder. Naturwissenschaften 12(37): 741-743 (1924).

[Pau36] Pauling L, Coryell CD. The magnetic properties and structure of hemoglobin, oxyhemoglobin and carbonmonoxyhemoglobin. Proc Natl Acad Sct USA 22: 210-216 (1936).

[Pau91] Pauly JM, Le Roux P, Nishimura DG, Macovski A. Parameter relations for the Shinnar-Le Roux selective excitation pulse design algorithm. IEEE T Med Imaging 10(1): 53-65 (1991).

[Paul04] Paul D, Hennig J. Comparison of different flip angle variation functions for improved signal behavior in SSFP sequences. Proceedings ISMRM 2004; #2663 (2004).

[Paul06] Paul D, Markl M, Fautz HP, Hennig J. T2-weighted balanced SSFP imaging (T2-TIDE) using variable flip angles. Magn Reson Med 56: 82-93 (2006).

[Pet06] Petersen ET, Zimine I, Ho YC, Golay X. Non-invasive measurement of perfusion: a critical review of arterial spin labelling techniques. Br J Radiol 79(944): 688-701 (2006).

[Petr00] Petrella JR, Provenzale JM. MR perfusion imaging of the brain: techniques and applications. AJR Am J Roentgenol 175(1): 207-219 (2000).

[Pir95] Pirhonen JP, Grenman SA, Bredbacka AB, Bahado-Singh RO, Salmi TA. Effects of external radiotherapy on uterine blood flow in patients with advanced cervical carcinoma assessed by color Doppler ultrasonography. Cancer: 76(1): 67-71 (1995).

[Poon92] Poon CS, Henkelman RM. Practical T2 quantitation for clinical applications. J Magn Reson Imaging 2(5): 541-553 (1992).

[Pop98] Poptani H, Puumalainen AM, Gröhn OH, Loimas S, Kainulainen R, Ylä-Herttuala S, Kauppinen RA. Monitoring thymidine kinase and ganciclovir-induced changes in rat malignant glioma in vivo by nuclear magnetic resonance imaging. Cancer Gene Ther 5(2): 101-109 (1998).

[Pos99] Postema S, Pattynama PM, van Rijswijk CS, Trimbos JB. Cervical carcinoma: can dynamic contrast-enhanced MR imaging help predict tumor aggressiveness? Radiology 210(1): 217-220 (1999).

[Pow96] Powell ME, Hill SA, Saunders MI, Hoskin PJ, Chaplin DJ. Effect of carbogen breathing on tumour microregional blood flow in humans. Radiother Oncol 41(3): 225-231 (1996).

[Pow99] Powell ME, Collingridge DR, Saunders MI, Hoskin PJ, Hill SA, Chaplin DJ. Improvement in human tumour oxygenation with carbogen of varying carbon dioxide concentrations. Radiother Oncol 50(2): 167-171 (1999).

[Pra97] Prasad PV, Chen Q, Goldfarb JW, Epstein FH, Edelman RR. Breath-hold R2* mapping with a multiple gradient-recalled echo sequence: application to the evaluation of intrarenal oxygenation. J Magn Reson Imaging 7: 1163-1165 (1997).

[Pre01] Preibisch C, Haase A. Perfusion imaging using spin-labeling methods: contrast-to-noise comparison in functional MRI applications. Magn Reson Med 46(1): 172-182 (2001).

[Pru99] Pruessmann KP, Weiger M, Scheidegger MB, et al. SENSE: sensitivity encoding for fast MRI. Magn Reson Med 42:952-962 (1999).

[Pun98] Punwani S, Ordidge RJ, Cooper CE, Amess P, Clemence M. MRI measurements of cerebral deoxyhaemoglobin concentration [dHb] - correlation with near infrared spectroscopy (NIRS). NMR Biomed 11: 282-289 (1998).

[Pur46a] Purcell EM, Torrey HC, Pound RV. Resonance absorption by nuclear magnetic moments in a solid. Phys Rev 69(1-2): 37-38 (1946).

[Pur46b] Purcell EM, Bloembergen N, Pound RV. Resonance absorption by nuclear magnetic moments in a single crystal of CaF_2. Phys Rev 70: 988 (1946).

[Rabi38] Rabi II, Zacharias JR, Millman S, Kusch P. A new method of measuring nuclear magnetic moment. Phys Rev 53: 318 (1938).

[Rabi39] Rabi II, Millman S, Kusch P, Zacharias JR. The molecular beam resonance method for measuring nuclear magnetic moments. Phys Rev 55: 526-535 (1939).

[Rai76] Raichle ME, Eichling JO, Straatmann MG, Welch MJ, Larson KB, Ter-Pogossian MM. Blood-brain barrier permeability of 11C-labeled alcohols and 15O-labeled water. Am J Physiol 230(2): 543-552 (1976).

[Rei97] Reichenbach JR, Venkatesan R, Yablonskiy DA, Thompson MR, Lai S, Haacke EM. Theory and application of static field inhomogeneity effects in gradient-echo imaging. J Magn Reson Imaging 7(2): 266-279 (1997).

[Reim10] Reimer P, Parizel PM, Meaney JFM, Stichnoth FA (Editors). Clinical MR imaging: A practical approach. Third Edition, Springer-Verlag Berlin, Heidelberg (2010).

[Reis08] Reiser MF, Semmler W, Hricak H (Editors). Magnetic Resonance Tomography. Springer-Verlag Berlin Heidelberg (2008).

[Res01] Ressel A, Weiss , Feyerabend T. Tumor oxygenation after radiotherapy, chemotherapy, and/or hyperthermia predicts tumor free survival. Int J Rad Oncol Biol Phys 49(4): 1119-1125 (2001).

[Ric02] Richter E, Feyerabend T. Grundlagen der Strahlentherapie. 2. Auflage. Springer-Verlag Berlin Heidelberg New York (2002).

[Rij02] Rijpkema M, Kaanders JH Schuuring J, Joosten FBM, van der Kogel AJ, Heerschap A. Effects of breathing a hyperoxiy hypercapnic gas mixture on blood oxygenation and ascularity of head and neck tumors as measured by magnetic resonance imaging. Int J Radiation Oncol Biol Phys 53: 1185-1191 (2002).

[Rij04] Rijpkema M, Schuuring J, Bernsen PL, Bernsen HJ, Kaanders JH, van der Kogel AJ, Heerschap A. BOLD MRI response to hypercapnic hyperoxia in patients with meningiomas: correlation with Gadolinium-DTPA uptake rate. Magn Reson Imaging 22: 761-767 (2004).

[Rin1995] Rinck PA (Editor). The rational use of magnetic resonance imaging. Blackwell Wissenschafts-Verlag and European magnetic resonance forum foundation, Oxford (1995).

[Robe00] Roberts HC, Roberts TP, Brasch RC, Dillon WP. Quantitative measurement of microvascular permeability in human brain tumors achieved using dynamic contrast-enhanced MR imaging: correlation with histologic grade. AJNR Am J Neuroradiol 21(5): 891-899 (2000).

[Robe01] Roberts HC, Roberts TP, Bollen AW, Ley S, Brasch RC, Dillon WP. Correlation of microvascular permeability derived from dynamic contrast-enhanced MR imaging with histologic grade and tumor labeling index: a study in human brain tumors. Acad Radiol 8(5): 384-391 (2001).

[Robi95] Robinson SP, Howe FA, Griffiths JR. Noninvasive monitoring of carbogen-induced changes in tumor blood flow and oxygenation by functional magnetic resonance imaging. Int J Radiat Oncol Biol Phys 33(4): 855-859 (1995).

[Robi97] Robinson SP, Rodrigues LM, Ojugo AS, McSheehy PM, Howe FA, Griffiths JR. The response to carbogen breathing in experimental tumour models monitored by gradient-recalled echo magnetic resonance imaging. Br J Cancer 75(7): 1000-1006 (1997).

[Robi99] Robinson SP, Collingridge DR, Howe FA, Rodrigues LM, Chaplin DJ, Griffiths JR. Tumor response to hypercapnia and hyperoxia monitored by FLOOD magnetic resonance imaging. NMR Biomed 12: 98-106 (1999).

[Robi00] Robinson SP, Howe FA, Stubbs M, Griffiths JR. Effects of nicotinamide and carbogen on tumour oxygenation, blood flow, energetics and blood glucose levels. Br J Cancer 82(12): 2007-2014 (2000).

[Robi01] Robinson SP, Rodrigues LM, Howe FA, Stubbs M and Griffiths JR. Effects of different levels of hypercapnic hyperoxia on tumour R2* and arterial blood gases. Magn Reson Imaging 19: 161-166 (2001).

[Robi03] Robinson SP, Rijken PF, Howe FA, McSheehy PM, van der Sanden BP, Heerschap A, Stubbs M, van der Kogel AJ, Griffiths JR. Tumor vascular architecture and function evaluated by non-invasive susceptibility MRI methods and immunohistochemistry. J Magn Reson Imaging 17(4): 445-454 (2003).

[Roj91] Rojas A. Radiosensitization with normobaric oxygen and carbogen. Radiother Oncol 20 Suppl 1: 65-70 (1991):

[Roj96] Rojas A, Hirst VK, Calvert AS, Johns H. Carbogen and nicotinamide as radiosensitizers in a murine mammary carcinoma using conventional and accelerated radiotherapy. Int J Radiat Oncol Biol Phys 34(2): 357-365 (1996).

[Ros94] Rostrup E, Larsson HB, Toft PB, Garde K, Thomsen C, Ring P, Søndergaard L, Henriksen O. Functional MRI of CO2 induced increase in cerebral perfusion. NMR Biomed 7(1-2): 29-34 (1994).

[Rud00] Rudat V, Vanselow B, Wollensack P, Bettschneider C, Osman-Ahmet S, Eble MJ, Dietz A: Repeatability and prognostic impact of the pretreatment pO2 histography in patients with advanced head and neck cancer. Radiother Oncol 57(1): 31-37 (2000).

[Run97] Runge VM, Muroff LR, Wells JW. Principles of contrast enhancement in the evaluation of brain diseases: an overview. J Magn Reson Imaging 7: 5-13 (1997).

[Ryd95] Rydberg JN, Riederer SJ, Rydberg CH, Jack CR. Contrast optimization of fluid-attenuated inversion recovery (FLAIR) imaging. Magn Reson Med 34: 868-877 (1995).

[Sau10] Sauer R. Strahlentherapie und Onkologie. 5. Auflage. Elsevier GmbH, Urban & Fischer Verlag München.

[Sche01a] Scheffler K, Hennig J. T1 quantification with inversion recovery TrueFISP. Magn Reson Med 45:720-723 (2001).

[Sche01b] Scheffler K, Heid O, Hennig J. Magnetization preparation during the steady state: fat-saturated 3D TrueFISP. Magn Reson Med 45: 1075-1080 (2001).

[Sche03a] Scheffler K, Hennig J. Is TrueFISP a gradient-echo or a spin-echo sequence? Magn Reson Med 49: 395-397 (2003).

[Sche03b] Scheffler K. On the transient phase of balanced SSFP sequences. Mag Reson Med 49: 781-783 (2003).

[Sche03c] Scheffler K, Lehnhardt S. Principles and applications of balanced SSFP techniques. Eur Radiol 13: 2409-2418 (2003).

[Schm01] Schmitt P, Weigel M, Jakob PM, Kotas M, Flentje M, Haase A. Dynamic Monitoring of T2* and Perfusion Changes induced by Oxygen or Carbogen Breathing. Proceedings ISMRM-ESMRMB 2001; #1572 (2001).

[Schm02] Schmitt P, Griswold MA, Fidler F, Jakob PM, Kotas M, Flentje M, Haase A. Quantification of both T1 and T2 values with IR TrueFISP experiments. Proceedings of the 19th Annual Meeting of the ESMRMB, Cannes, France, 2002; #469 (2002). MAGMA 15, Suppl 1 (2002).

[Schm03a] Schmitt P, Kotas M, Tobermann A, Haase A and Flentje M. Quantitative tissue perfusion measurements in head and neck carcinoma patients before and during radiation therapy with a non-invasive MR imaging spin-labeling technique. Radiother Oncol 67: 27-34 (2003).

[Schm03b] Schmitt P, Jakob PM, Haase A, Griswold MA: T-One insensitive Steady State Imaging (TOSSI): Obtaining TrueFISP images with pure T2 contrast. Proceedings ISMRM 2003; #551 (2003).

[Schm04a] Schmitt P, Griswold MA, Jakob PM, Kotas M, Flentje M, Haase A: Inversion Recovery TrueFISP: Quantification of T1, T2 and spin density. Magn Reson Med 51: 661-667 (2004).

[Schm04b] Schmitt P, Kotas M, Flentje M, Haase A, Jakob PM, Griswold MA: TOSSI (T-One insensitive Steady State Imaging): Sequence optimization and first results in tumor patients. Proceedings ISMRM 2004; #2085 (2004).

[Schm06] Schmitt P, Griswold MA, Gulani V, Haase A, Flentje M, Jakob PM. A simple geometrical description of the TrueFISP ideal transient and steady-state signal. Magn Reson Med 55: 177-186 (2006).

[Schm12] Schmitt P, Jakob PM, Kotas M, Flentje M, Haase A, Griswold MA. T-one insensitive steady state imaging: A framework for purely T2-weighted TrueFISP. Magn Reson Med 68(2): 409-420 (2012).

[Schn83] Schneiders NJ, Post H, Brunner P, Ford J, Bryan RN, Willcott MR. Accurate T2 NMR images. Med Phys 10(5): 642-645 (1983).

[Schr01] Schreiber WG, Schmitt M, Kalden P, Horstick G, Gumbrich T, Petersen S, Mohrs O, Kreitner KF, Voigtlander T, Thelen M. Perfusion MR imaging of the heart with TrueFISP. Rofo 173(3): 205-210 (2001).

[Schu02] Schuuring J, Rijpkema M, Bernsen H, Bernsen P, van der Maazen R, Kaanders J, van der Kogel A and Heerschap A. Effect of breathing a hyperoxic hypercapnic gas mixture on the oxygenation of meningiomas; preliminary results. J Neurooncol 57: 127-132 (2002).

[Schu06] Schuuring J, Bussink J, Bernsen H, Peeters W and van der Kogel A. Effect of carbogen breathing on the radiation response of a human glioblastoma xenograft. Strahlenther Onkol 182: 408-414 (2006).

[Schw96] Schwarzbauer C, Morrissey SP, Haase A. Quantitative Magnetic Resonance Imaging of perfusion using magnetic labeling of water proton spins within the detection slice. Magn Reson Med 35(4): 540-546 (1996).

[Sek87] Sekihara K. Steady-state magnetizations in rapid NMR imaging using small flip angles and short repetition intervals. IEEE Trans Med Imag 6(2): 157-164 (1987).

[Shea02] Shea SM, Deshpande VS, Chung YC, Li D. Three-dimensional true-FISP imaging of the coronary arteries: improved contrast with T2-preparation. J Magn Reson Imaging 15: 597-602 (2002).

[Shin02] Shin JH, Lee HK, Kwun BD, Kim JS, Kang W, Choi CG, Suh DC. Using relative cerebral blood flow and volume to evaluate the histopathologic grade of cerebral gliomas: preliminary results. AJR Am J Roentgenol 179(3): 783-789 (2002).

[Sie94] Siemann DW, Horsman MR, Chaplin DJ. The radiation response of KHT sarcomas following nicotinamide treatment and carbogen breathing. Radiother Oncol 31(2): 117-122 (1994).

[Sil00a] Silva AC, Lee SP, Iadecola C, Kim S-G. Early temporal characteristics of cerebral blood flow and deoxyhemoglobin changes during somatosensory stimulation. J Cereb Blood Flow Metab 20(1): 201-206 (2000).

[Sil00b] Silva AC, Kim S-G, Garwood M. Imaging blood flow in brain tumors using arterial spin labeling. Magn Reson Med 44(2): 169-173 (2000).

[Sil03] Silvennoinen MJ, Kettunen MI, Kauppinen RA. Effects of hematocrit and oxygen saturation level on blood spin-lattice relaxation. Magn Reson Med 49(3): 568-571 (2003).

[Sol98] Soltanian-Zadeh H, Windham JP, Peck DJ, Mikkelsen T. Feature space analysis of MRI. Magn Reson Med 40(3): 443-453 (1998).

[Spi72] Spiessl B. Prinzipien der TNM-Klassifizierung. Z. Krebsforsch 78: 31-41 (1972).

[Spu02] Spuentrup E, Bornert P, Botnar RM, Groen JP, Manning WJ, Stuber M. Navigator-gated free-breathing three-dimensional balanced fast field echo (TrueFISP) coronary magnetic resonance angiography. Invest Radiol 37: 637-642 (2002).

[Stab99] Stables LA, Kennan RP, Anderson AW, et al. Density matrix simulations of the effects of J coupling in spin echo and fast spin echo imaging. J Magn Reson 140: 305-314 (1999).

[Stad99] Stadler P, Becker A, Feldmann HJ, Hansgen G, Dunst J, Wurschmidt F, Molls M. Influence of the hypoxic subvolume on the survival of patients with head and neck cancer. Int J Radiat Oncol Biol Phys 44(4):749-754 (1999).

[Steh07] Stehning C, Winkelmann S, Dahnke H. Simultaneous T1, T2 and spin density quantification in 5 seconds using inversion recovery SSFP. Proceedings ISMRM 2006; #1719 (2006).

[Steh08] Stehning C, S. Winkelmann S, Sénégas J, Dahnke H. Volumetric Simultaneous T1, T2, T2* and Proton Density Mapping in One Minute Using Interleaved Inversion Recovery SSFP and Multi Gradient Echo Imaging. Proceedings ISMRM 2008; #241 (2008).

[Ster21] Stern O. Ein Weg zur experimentellen Prüfung der Richtungsquantelung im Magnetfeld. Z Phys 7: 249-253 (1921).

[Stü98] Stüben G, Stuschke M, Knühmann K, Horsman MR, Sack H. The effect of combined nicotinamide and carbogen treatments in human tumour xenografts: oxygenation and tumour control studies. Radiother Oncol 48(2): 143-148 (1998).

[Tho00] Thomas DL, Lythgoe MF, Pell GS, Calamante F, Ordidge RJ. The measurement of diffusion and perfusion in biological systems using magnetic resonance imaging. Phys Med Biol 45(8): R97-138 (2000).

[Thu82] Thulborn KR, Waterton JC, Matthews PM, Radda GK. Oxygenation dependence of the transverse relaxation time of water protons in whole blood at high field. Biochim Biophys Acta 714(2): 265-270 (1982).

[Tof99] Tofts PS, Brix G, Buckley DL, Evelhoch JL, Henderson E, Knopp MV, Larsson HB, Lee TY, Mayr NA, Parker GJ, Port RE, Taylor J, Weisskoff RM. Estimating kinetic parameters from dynamic contrast-enhanced T1-weighted MRI of a diffusable tracer: standardized quantities and symbols. J Magn Reson Imaging 10(3): 223-232 (1999).

[Tof03] Tofts P (Editor). Quantitative MRI of the Brain: Measuring Changes Caused by Disease. John Wiley & Sons Inc., Hoboken, NJ, USA (2003).

[Tou08] Tourdias T, Rodrigo S, Oppenheim C, Naggara O, Varlet P, Amoussa S, Calmon G, Roux FX, Meder JF. Pulsed arterial spin labeling applications in brain tumors: practical review. J Neuroradiol 35(2): 79-89 (2008).

[Tovi93] Tovi M. MR imaging in cerebral gliomas analysis of tumour tissue components. Acta Radiol Suppl 384: 1-24 (1993).

[Tre12] Treglia G, Giovannini E, Di Franco D, Calcagni ML, Rufini V, Picchio M, Giordano A. The role of positron emission tomography using carbon-11 and fluorine-18 choline in tumors other than prostate cancer: a systematic review. Ann Nucl Med (Epub ahead of print, 2012).

[Twi83] Twieg DB. The k-trajectory formulation of the NMR imaging process with applications in analysis and synthesis of imaging methods. Med Phys 10(5): 610-621 (1983).

[Utz86] Utz JA, Herfkens RJ, Glover G, Pelc N. Three second clinical NMR images using a gradient recalled acquisition in a study state mode (GRASS). Proceedings SMRI 1986; Magn Reson Imag 4(2): 106 (1986).

[Van05] Vance CJ, Newbould RD, Ames BN, Bammer R. Placental Imaging and Relaxation Parameter Mapping at 1.5 Tesla. Proceedings ISMRM 2005; #537 (2005).

[VanD99] Van der Sanden BP, Heerschap A, Hoofd L, Simonetti AW, Nicolay K, van der Toorn A, Colier WN, van der Kogel AJ. Effect of carbogen breathing on the physiological profile of human glioma xenografts. Magn Reson Med 42(3): 490-499 (1999).

[VanW96] Van Waesberghe JH, Castelijns JA, Weerts JG, Nijeholt GJ, Hillegers JP, Polman CH, Barkhof F. Disappearance of multiple sclerosis lesions with severely prolonged T1 on images obtained by a FLAIR pulse sequence. Magn Reson Imag 14: 209–213 (1996).

[Vau89] Vaupel P, Kallinowski F, Okunieff P. Blood flow, oxygen and nutrient supply, and metabolic microenvironment of human tumors. A review. Cancer Res 49: 6449-6465 (1989).

[Vau90] Vaupel P. Oxygenation of human tumors. Strahlenther Onkol 166: 377-386 (1990).

[Vau98a] Vaupel P. Tumor blood flow. In: Molls M, Vaupel P (eds). Blood perfusion and microenvironment of human tumors. Springer-Verlag Berlin Heidelberg New York (1998).

[Vau98b] Vaupel P, Höckel M. Oxygenation of human tumors. In: Molls M, Vaupel P (eds). Blood perfusion and microenvironment of human tumors. Springer-Verlag Berlin Heidelberg New York (1998).

[Vau98c] Vaupel P, Kelleher DK, Thews O. Modulation of tumor oxygenation.Int J Radiat Oncol Biol Phys; 42(4): 843-848 (1998).

[Vau01a] Vaupel P, Kelleher DK, Höckel M. Oxygenation status of malignant tumors: pathogenesis and significance for tumor therapy. Semin. Oncol. 28 (Suppl 8): 29-35 (2001).

[Vau01b] Vaupel P, Thews O, Höckel M. Treatment resistance of solid tumors. Role of hypoxia and anaemia. Medical Oncology 18: 243-259 (2001).

[Vin90] Vinitski S, Mitchell DG, Szumowski J, Burk DL Jr, Rifkin MD. Variable flip angle imaging and fat suppression in combined gradient and spin-echo (GREASE) techniques. Magn Reson Imaging 8(2): 131-139 (1990).

[Vym95] Vymazal J, Hajek M, Patronas N, Giedd JN, Bulte JW, Baumgarner C, Tran V, Brooks RA. The quantitative relation between T1-weighted and T2-weighted MRI of normal gray matter and iron concentration. J Magn Reson Imaging 5(5): 554-560 (1995).

[Wac99] Wacker CM, Bock M, Hartlep AW et al. Changes in Myocardial Oxygenation and Perfusion Under Pharmalogical Stress With Dipyridamole: Assessment Using T2* and T1 Measurements. Magn Reson Med 41(4): 686-695 (1999).

[Walk09] Walker-Samuel S, Orton M, Baker LC, Boult JK, Robinson SP. Dual-relaxation, temporally-constrained, dynamic contrast-enhanced MRI using inversion recovery TrueFISP. Proceedings ISMRM 2009; #2289 (2009).

[Wall00] Waller C, Kahler E, Hiller KH et al. Myocardial perfusion and intracapillary blood volume in rats at rest and with coronary dilatation: MR imaging in vivo with use of a spin-labeling technique. Radiology 215(1): 189-197 (2000).

[Wang90] Wang HZ, Riederer SJ. A spoiling sequence for suprresion of residual transverse magnetization. Magn Reson Med 15: 175-191 (1990).

[Wang07] Wang Y, Wu KC, Kitagawa K, Murthy V, Lorenz CH. Myocardial T1 Mapping Using Inversion Recovery SSFP Cine. Proceedings ISMRM 2007; #2575 (2007).

[War03] Warmuth C, Gunther M, Zimmer C. Quantification of blood flow in brain tumors: comparison of arterial spin labeling and dynamic susceptibility-weighted contrast-enhanced MR imaging. Radiology 228(2): 523-532 (2003).

[War07] Warntjes JB, Dahlqvist O, Lundberg P. Novel method for rapid, simultaneous T1, T*2, and proton density quantification. Magn Reson Med 57(3): 528-537 (2007).

[War08] Warntjes JB, Leinhard OD, West J, Lundberg P. Rapid magnetic resonance quantification on the brain: Optimization for clinical usage. Magn Reson Med 60(2): 320-329 (2008).

[Wau70] Waugh JS. Sensitivity in Fourier Transform NMR spectroscopy of slowly relaxing systems. J Mol Spectrosc 35: 298-305 (1970).

[Weh84] Wehrli FW, MacFall JR, Shutts D, Breger R, Herfkens RJ. Mechanisms of contrast in NMR imaging. J Comput Assist Tomogr 8: 369-380 (1984).

[Weh92] Wehrli FW. The origins and future of Nuclear Magnetic Resonance Imaging. Physics Today 45(6): 34-42 (1992).

[Weid05] Weidensteiner C, Rausch M, McSheehy PM, Allegrini PR. DCE-MRI using Inversion Recovery TrueFISP for quantitative permeability measurements in rat tumors. Proceedings ISMRM 2005; #2059 (2005).

[Weid06] Weidensteiner C, Rausch M, McSheehy PM, Allegrini PR. Quantitative dynamic contrast-enhanced MRI in tumor-bearing rats and mice with inversion recovery TrueFISP and two contrast agents at 4.7 T. J Magn Reson Imaging 24(3): 646-656 (2006).

[Wei72] Weisman ID, Bennett LH, Maxwell LR, Woods MW, Burk D. Recognition of cancer in vivo by Nuclear Magnetic Resonance. Science 178: 1288-1290 (1972).

[Wei92] Weisskoff RM, Kiihne S. MRI susceptometry: image-based measurement of absolute susceptibility of MR contrast agents and human blood. Magn Reson Med 24(2): 375-383 (1992).

[Wei94] Weisskoff RM, Zuo CS, Boxerman JL, Rosen BR. Microscopic susceptibility variation and transverse relaxation: theory and experiment. Magn Reson Med 31(6): 601-610 (1994).

[Weig00a] Weigel M, Schmitt P, Jakob PM, Hermann A, Kotas M, Flentje M, Haase A. Dynamic Measurement of T2* Changes while breathing Carbogen. ESMRMB `00, 17th Annual Meeting in Paris, MAGMA 11, Suppl.1, 262 (2000).

[Weig00b] Weigel M. Dynamische NMR-Messungen zur Gehirnfunktion bei variablem Sauerstoffangebot. Diplomarbeit. Physikalisches Institut der Universität Würzburg (2000).

[Wenz96] Wenz F, Rempp K, Hess T, Debus J, Brix G, Engenhart R, Knopp MV, van Kaick G, Wannenmacher M. Effect of radiation on blood volume in low-grade astrocytomas and normal brain tissue: quantification with dynamic susceptibility contrast MR imaging. AJR Am J Roentgenol 166(1): 187-93 (1996).

[Whi97] Whittall KP, MacKay AL, Graeb DA, Nugent RA, Li DK, Paty DW. In vivo measurement of T2 distributions and water contents in normal human brain. Magn Reson Med 37(1): 34-43 (1997).

[Wilm93] Wilmes LJ, Hoehn-Berlage M, Els T, Bockhorst K, Eis M, Bonnekoh P, Hossmann KA. In vivo relaxometry of three brain tumors in the rat: effect of Mn-TPPS, a tumor-selective contrast agent. J Magn Reson Imaging 3(1): 5-12 (1993).

[Woe61] Woessner DE. Effects of diffusion in Nuclear Magnetic Resonance spin-echo experiments. J Chem Phys 34(6): 2057-2061 (1961).

[Wolf07] Wolf RL, Detre JA. Clinical neuroimaging using arterial spin-labeled perfusion magnetic resonance imaging. Review. Neurotherapeutics 4(3): 346-359 (2007).

[Wong00] Wong JC; Provenzale JM; Petrella JR. Perfusion MR imaging of brain neoplasms. Am J Roentgenol 2000; 174(4): 1147-1157.

[Wood87] Wood ML, Silver M, Runge VM. Optimization of spoiler gradients in FLASH MRI. Magn Reson Imag 5(6): 455-463 (1987).

[Wood88] Wood ML, Runge VM. Artifacts due to residual magnetization in three-dimensional magnetic resonance imaging. Med Phys 15(6): 825-831 (1988).

[Wou02] Wouters BG, Weppler SA, Koritzinsky M, Landuyt W, Nuyts S, Theys J, Chiu RK, Lambin P. Hypoxia as a target for combined modality treatments. Eur J Cancer 38(2): 240-257 (2002).

[Wri57] Wright EA, Howard-Flanders P. The influence of oxygen on the radiosensitivity of mammalian tissues. Acta Radiol 48(1): 26-32 (1957).

[Wri91] Wright GA, Hu BS, Macovski A. Estimating oxygen saturation of blood in vivo with MR imaging at 1.5 T. J Magn Reson Imaging 1(3): 275-283 (1991).

[Wu08] Wu WC, Wang J. In vivo blood T1 mapping using inversion recovery TrueFISP. Proceedings ISMRM 2008; #3080 (2008).

[Yab94] Yablonskiy DA, Haacke EM. Theory of NMR signal behavior in magnetically inhomogeneous tissues: the static dephasing regime. Magn Reson Med 32(6): 749-763 (1994).

[Ye96] Ye FQ, Pekar JJ, Jezzard P, Duyn J, Frank JA, McLaughlin AC. Perfusion imaging of the human brain at 1.5T using a single-shot EPI spin tagging approach. Magn Reson Med 36(2): 219-224 (1996).

[Yut08] Yutzy SR, Duerk JL. Pulse sequences and system interfaces for interventional and real-time MRI. J Magn Reson Imaging 27: 267-275 (2008).

[Zho98] Zhong J, Kennan RP, Fulbright RK, Gore JC. Quantification of intravascular and extravascular contributions to BOLD effects induced by alteration in oxygenation or intravascular contrast agents. Magn Reson Med 40(4): 526-536 (1998).

[Zips04] Zips D, Adam M, Flentje M, Haase A, Molls M, Mueller-Klieser W, Petersen C, Philbrook C, Schmitt P, Thews O, Walenta S, Baumann M. Impact of hypoxia and the metabolic microenvironment on radiotherapy of solid tumors. Introduction of a multi-institutional research project. Strahlenther Onkol 180(10): 609-615 (2004).

[Zips07] Zips D, Yaromina A, Schütze C, Wüllrich K, Krause M, Krause M, Hessel F, Eicheler W, Dörfler A, Brüchner K, Menegakis A, Zhou X, Bergmann R, van den Hoff J, Beuthien-Baumann B, Baumann M. Experimental evaluation of functional imaging for radiotherapy. Strahlenther Onkol 183: Spec No2: 41-2 (2007).

[Zur87] Zur Y, Bendel P. Elimination of the steady state transverse magnetization in short TR imaging. Proceedings SMR 1987; #440 (1987).

[Zur88] Zur Y, Stokar S, Bendel P. An analysis of fast imaging sequences with steady-state transverse magnetization refocusing. Magn Reson Med 6: 175-193 (1988).

[Zur90] Zur Y, Wood ML, Neuringer LJ. Motion-insensitive, steady-state free precession imaging. Magn Reson Med 16: 444-459 (1990).

[Zur91] Zur Y, Wood ML, Neuringer LJ. Spoiling of transverse magnetization in steady-state sequences. Magn Reson Med 21: 251-263 (1991).

Acknowledgements

This work would not have been possible without the help and support of numerous people, and I would like to take the opportunity to thank them in this section.

First, I would like to thank my supervisor **Prof. Dr. Peter M. Jakob** for all his guidance and help, during my time at the University of Würzburg and afterwards. His knowledge of MR techniques is unmatched, and he is not only highly disciplined, dedicated and inspiring scientist and teacher, but also has a great sense of humor. I do not take the late submission of this thesis for granted, and I am very grateful to him for encouraging me to finalize it. To make a long story short - “langer Rede kurzer Sinn”: Thank you very much, PeJa!

Prof. Dr. Axel Haase founded and built the EP5 lab, turning it into an excellent working environment. He established and nourished a unique spirit in the lab, characterized by self-responsibility, scientific curiosity and creativity. He initiated the project I worked on, and he always gave me the freedom to pursue my research in directions that were of particular interest to me. Unforgotten highlights of my Ph.D. time were the EP5 seminar weeks and pool parties. I would like to express my sincere gratidude for all his support and for taking the time to serve as a reviewer of this thesis and as an examiner in my defense.

Most results in this thesis would not have been possible without close collaboration between physicists and clinicians. I am very grateful to **Prof. Dr. Michael Flentje** for starting this thesis project together with Prof. Haase, and for continuously providing his clinical input and valuable advice. Prof. Flentje was always very enthusiastic about our collaboration, and he was a great source of motivation and encouragement.

I am indebted to the **IZKF Würzburg** for providing financial support. The IZKF has not only ensured that I could pay my breakfast rolls, but also funded bizarre hardware items such as plastic respiratory face masks, strange gas mixtures, and data CDs (!).

The contributions and importance of **Prof. Dr. Mark A. Griswold** for this work have been enormous. Many parts of this work would not have been accomplished without his ingenious ideas, positive and visionary thinking, unwaning enthusiasm, continuous encouragement and practical advice. I cannot thank him enough for all his help, for his friendship, and also for kicking my *** to make me finalize this thesis.

It has been a wonderful piece of luck that **Prof. Dr. Dr. Vikas Gulani** decided to spend a year abroad at EP5 in Germany and happened to be allocated a desk next to mine. He combines a deep medical engineering knowledge with a vast medical experience and unique scientific skills. The year with Vikas as my office mate will always remain a very special one for me. I regularly think back on the long evenings we spent in the lab, enjoying our projects

and having great discussions. These discussions were not only about MR sequences and image contrasts or small currents in thin wires, but also about the myriad of ways to be “out” in a strange sport called cricket (I will never get it – can it be sports at all if the players have tea breaks with cucumber sandwiches?), about differences between the Swabian dialect and the German language, and many other important aspects of life. It has also been extremely helpful of Vikas to have reviewed most parts of this thesis and corrected my worst “Genglish” expressions. I am grateful for all his assistance and for his friendship.

I have been fortunate to have had the opportunity to collaborate with **Dr. Felix Breuer** and **Dr. Matthias Weigel** on their diploma projects. Both were excellent students, and I learned a lot from working with them - about MR, about different yet efficient ways of going about projects, and about myself. In addition, Felix has done a fantastic job in proof-reading this thesis. I would like to thank both of them very much for all their efforts and help.

My clinical collaborators at the Department of Radiation Oncology were **Dr. Markus Kotas** and **Dr. Anja Tobermann**. They provided important clinical know-how, sacrificed significant amounts of their scarce time for our common research activities, and recruited and instructed all the patients who participated in our studies. For all these and many other valuable contributions, I send them a sincere “thank you”.

I thank my office mates, particularly **Dr. Volker Behr**, **Dr. Daniel Haddad** and **Dr. Florian Fidler**, for the pleasant atmosphere in our room, for all the helpful discussions, for their generous support, and many enjoyable disctractions. Special thanks to Volker, who knows essentially everything one might want to know about computers (if not, he’ll find out for you in a minute) and who is one of the smartest, kindest and most helpful persons I know.

I spent quite some time with **Dr. Sascha Köhler**, **Dr. Silvia Olt**, **Dr. Andreas Greiser**, and **Dr. Martin Blaimer** - during the time at work and in between, with activities such as running, cycling, playing soccer or just chatting or having a beer. Sascha helped me a lot by thoroughly proofreading this manuscript. I want to express my thanks to all of them for sharing their expertise in various situations, for many helpful discussions about both work and life, for the wonderful time at EP5 and for their friendship.

Sabine Voll, **Elsbeth Fekete**, **Irene Ramoz** and **Anna Schmidt** took care of so many aspects in the lab, obvious and less obvious ones, and have always been very obliging. For me, Sabine was the heart and soul of the lab. She often infected those around her with her good mood, and she has been a great source of encouragement for me.

The **Department of Experimental Physics 5** has been a unique place to work at - in particular because of the people I had the opportunity to become acquainted and to collaborate with. Looking back now, I realize more and more how much I have learned during my time in the lab and what a wonderful period of my life this was. Many thanks to everybody who accompanied me during my time at EP5 and to all the current members of EP5, who joined the defense of this thesis and the subsequent get-together, and thus contributed to making this final step a pleasant event.

I am indebted to **Daniela Sturm-Kirchgassner** who provided a great amount of help for the submission of this dissertation and for the organization of its defense - far in excess of just standard support. Many thanks for this!

Dr. Carmel Hayes has contributed a very useful last-minute review - thank you!

My parents **Wilma and Paul Schmitt** have always encouraged me, believed in me and supported me, and they have been with me whenever I needed their help.

Anna and Nikolas, my children, often had to accept that I seemed to prefer sitting at my desk and working on this thesis instead of spending time with them. I would like to thank them for their patience during this time and in general for making my life rich, vivid, and colorful.

Finally, I would like to thank my dear wife **Claudia** for all her empathy and understanding during stressful times, for her continuous support and for her love.